

---

# COSMOLOGY BETWEEN QUAD AND THE CMB

---

Abigail Turner

A THESIS SUBMITTED TO  
CARDIFF UNIVERSITY  
FOR THE DEGREE OF  
DOCTOR OF PHILOSOPHY

20 OCTOBER 2009

UMI Number: U585291

All rights reserved

INFORMATION TO ALL USERS

The quality of this reproduction is dependent upon the quality of the copy submitted.

In the unlikely event that the author did not send a complete manuscript and there are missing pages, these will be noted. Also, if material had to be removed, a note will indicate the deletion.



UMI U585291

Published by ProQuest LLC 2013. Copyright in the Dissertation held by the Author.  
Microform Edition © ProQuest LLC.

All rights reserved. This work is protected against  
unauthorized copying under Title 17, United States Code.



ProQuest LLC  
789 East Eisenhower Parkway  
P.O. Box 1346  
Ann Arbor, MI 48106-1346

**Author:** Abigail Turner

**Title:** Cosmology between QUaD and the CMB

**Date of submission:** 20 October 2009

Permission is granted to Cardiff University to circulate and to have copied for non-commercial purposes, at its discretion, the above title upon the request of individuals or institutions. The author reserves other publication rights, and neither the thesis nor extensive extracts from it may be printed or otherwise reproduced without the author's written permission.

Copyright © 2010 by Abigail Turner



# ABSTRACT

QUaD is a ground based bolometric polarimeter which observed the cosmic microwave background (CMB) at 100 and 150 GHz for three austral winters. Two different techniques; field differencing and ground template subtraction, were used to analyze the data providing highly accurate maps and power spectra of both temperature and polarization. These measurements were then used to constrain cosmological parameters and in conjunction with the results of several other experiments further our knowledge and understanding of cosmology in the early universe.

This thesis presents an investigation into the astrophysical phenomena in the foreground of QUaD's observation region. Although an area with minimal foreground was selected for the experiment, nevertheless between QUaD and the CMB there are various sources of millimeter radiation that could potentially contaminate the measurements. Template temperature maps of the dust and synchrotron radiation in the region are extrapolated to CMB frequencies and correlated with QUaD's maps to quantify the extent of any structure similarity detected. These are compared with the correlation expected by chance in a single universe to confirm the cleanliness of the field and highlight the robustness of the published CMB results.

The residual signal persistently observed in the difference spectrum between QUaD's 100 GHz and 150 GHz frequency data is fitted against template spectra for the far infrared background (FIRB) and the Sunyaev-Zel'dovich (SZ) effect. The fitting analysis serves to constrain the parameters,  $b$  (the galaxy clustering bias), and  $\sigma_8$  (the rms mass fluctuations in a  $8h^{-1}$  Mpc sphere) upon which the amplitudes of the template spectra are dependent. The contribution to the power from the predicted background of radio point sources is subtracted before a simultaneous fit to the two parameters is carried out. It is found that  $\sigma_8 = 1.11_{-0.06}^{+0.04}$  and  $b = 3.27_{-0.23}^{+0.18}$ . Whilst these values are shown to be consistent with other recent astronomical results, the amplitudes of the FIRB and SZ effect they imply are, once extrapolated to high- $\ell$ , incompatible with the QUaD data on these angular scales. This suggests that some other factors; perhaps instrumental systematics, features in the analysis pipeline, or indeed other astrophysical phenomena could also be responsible for the signal seen in the frequency difference spectrum.

## ACKNOWLEDGEMENTS

Firstly I would like to thank my supervisor Professor Walter Gear at Cardiff University. He has overseen my entire PhD research project and provided lots of useful background information. For more specific help on the foreground analysis, giving his up time to discuss progress each week and allowing me to visit him at the Laboratoire AstroParticule Cosmologie in Paris I thank Ken Ganga. The rest of the QUaD collaboration have also provided much valuable support and advice. In particular I note Nutan for getting me started with it all, Michael for his assistance explaining the analysis and hosting me in Cambridge, Ed for his much needed computational help and Sujata for many useful discussions. For providing the suite of Infrared galaxy simulations I acknowledge Guilaine Lagache at the Institut d'Astrophysique Spatiale in Orsay. Within the department at Cardiff I am very grateful to Richard for perpetually fixing my computers, Bruce for his IDL knowledge, Rob for being a great friend and comedian, and Pete for the times when only red wine and cake could help!

I have many great friends to which I owe a huge amount of thanks. Tess especially for her daily emails and continual efforts to keep happy and motivated. Charlotte as we struggled through our PhDs together drinking a lot of coffee and tea in Marks and Spencer's café. Matt, Ruth, Ginger, Chris and the many other people who have, probably without even knowing it, helped me along the way. I also am very thankful to all those who create Star Trek and Lost, to Patricia Cornwell and Tess Gerritson, and to the people who make Puzzler Collection.

A big thank you goes to my Mum and Dad. They have always been interested in what I am doing, listened to me talk about it and were keen to read my thesis, no matter how little they might actually understand. They have been a huge support in so many ways and I never want to take that for granted.

Over the last year Simon has been a huge encouragement to me. I thank him for being so special and making me so much happier than I was during the second year. Trying to explain the project to him via an analogy with soup has helped make the picture clearer in my own head!

Finally, but most significantly, I praise God for carrying me across the sand.

# CONTENTS

<b>Abstract</b>	<b>v</b>
<b>Acknowledgements</b>	<b>vi</b>
<b>List of Tables</b>	<b>xi</b>
<b>List of Figures</b>	<b>xii</b>
<b>1 Introduction</b>	<b>1</b>
1.1 Big Bang Cosmology . . . . .	1
1.2 Structure Formation . . . . .	2
1.2.1 Inflation Theory . . . . .	3
1.2.2 Gravitational Instability . . . . .	4
1.2.3 Angular Formalism . . . . .	6
1.3 Temperature Power Spectrum . . . . .	6
1.4 Cosmological Model and Parameters . . . . .	8
1.5 Temperature Power Spectrum Limitations . . . . .	11
1.6 Polarization . . . . .	11
1.6.1 Polarization Power Spectra . . . . .	14
1.6.2 Secondary Polarization . . . . .	15
1.7 Thesis Outline . . . . .	17
<b>2 QUaD</b>	<b>19</b>
2.1 QUaD Instrumentation . . . . .	19
2.1.1 From the CMB Through the Atmosphere and Telescope to the Fo- cal Plane... . . . .	19
2.1.2 ... and onto the Detectors . . . . .	20
2.1.3 Optical Efficiency . . . . .	23
2.1.4 Noise . . . . .	23
2.1.5 Polarimetry Errors . . . . .	26
2.1.6 PSB Failures . . . . .	26
2.1.7 Cryogenics . . . . .	26
2.1.8 Calibrations . . . . .	27
2.2 QUaD Observations . . . . .	33
2.2.1 Observing Strategy . . . . .	33
2.2.2 Low Level Data Processing . . . . .	35
2.3 Other Instruments . . . . .	36

2.3.1	ACBAR . . . . .	37
2.3.2	BOOMERanG . . . . .	37
2.3.3	CBI . . . . .	37
2.3.4	DASI . . . . .	38
2.3.5	MAXIPOL . . . . .	38
2.3.6	WMAP . . . . .	38
2.3.7	Planck . . . . .	38
2.3.8	SPIDER . . . . .	39
2.3.9	QUIET . . . . .	40
<b>3</b>	<b>Analysis</b>	<b>41</b>
3.1	Maps . . . . .	41
3.1.1	Field Differencing . . . . .	41
3.1.2	Ground Template Removal . . . . .	42
3.1.3	Map-making . . . . .	43
3.1.4	Temperature Maps . . . . .	44
3.1.5	Polarization Maps . . . . .	45
3.1.6	Jackknife Maps . . . . .	48
3.2	Power Spectra . . . . .	49
3.2.1	Power Spectrum Estimation . . . . .	49
3.2.2	Signal Simulations . . . . .	51
3.2.3	Noise Simulations . . . . .	52
3.2.4	Signal plus Noise Simulations . . . . .	53
3.2.5	Transfer Function . . . . .	53
3.2.6	Band Power Window Functions . . . . .	54
3.2.7	Power Spectra Results . . . . .	55
3.2.8	Chi-Square Statistics . . . . .	58
3.2.9	Band Power Deviations . . . . .	59
3.3	Parameter Estimation . . . . .	62
3.3.1	Likelihood Theory . . . . .	62
3.3.2	Computation . . . . .	63
3.3.3	Results . . . . .	64
<b>4</b>	<b>Dust</b>	<b>67</b>
4.1	Foregrounds . . . . .	67
4.2	Dust Models . . . . .	68
4.2.1	Intensity Models . . . . .	69
4.2.2	Polarization . . . . .	71
4.3	Looking for Dust in QUaD Data . . . . .	72
4.3.1	Statistical Correlations . . . . .	74
4.3.2	Correlation Results and Discussion . . . . .	77
4.3.3	Cross Correlations . . . . .	78
4.3.4	Polarization Correlations . . . . .	79

<b>5</b>	<b>Synchrotron</b>	<b>83</b>
5.1	Synchrotron Radiation . . . . .	83
5.1.1	Intensity Models . . . . .	84
5.1.2	Extrapolation to CMB Frequencies . . . . .	86
5.1.3	Polarization . . . . .	87
5.2	Looking for Synchrotron Radiation in QUaD Data . . . . .	88
5.2.1	Statistical Correlations . . . . .	91
5.2.2	Cross Correlations . . . . .	92
5.2.3	Polarization Correlations . . . . .	94
<b>6</b>	<b>Far Infrared Background</b>	<b>97</b>
6.1	Galaxy Clustering . . . . .	97
6.1.1	Infrared Galaxies . . . . .	97
6.1.2	Clustering of Infrared Galaxies . . . . .	100
6.2	Bias . . . . .	100
6.3	Far Infrared Background Anisotropies . . . . .	101
6.3.1	Power Spectrum . . . . .	101
6.3.2	Observations . . . . .	104
6.3.3	Bias Measurements . . . . .	105
6.4	QUaD's Frequency Jackknife . . . . .	105
6.5	Looking for the FIRB in QUaD's Frequency Jackknife . . . . .	108
6.5.1	FIRB Frequency Difference . . . . .	108
6.5.2	Linear Fits . . . . .	108
6.5.3	$\ell$ -range . . . . .	109
6.5.4	Bias Results . . . . .	109
6.6	Infrared Galaxy Simulations . . . . .	111
6.6.1	Unit Conversion . . . . .	112
6.6.2	Beam Convolution . . . . .	113
6.6.3	Repixelization . . . . .	114
6.6.4	Maps and Power Spectra . . . . .	114
6.6.5	Bias Results with Simulated Spectra . . . . .	115
<b>7</b>	<b>Sunyaev-Zel'dovich Effect</b>	<b>117</b>
7.1	The Thermal Sunyaev-Zel'dovich Effect . . . . .	117
7.1.1	Frequency Dependence . . . . .	117
7.1.2	Temperature Distortion of the CMB . . . . .	118
7.1.3	Kinetic Sunyaev Zel'dovich Effect . . . . .	120
7.2	Thermal SZ Effect Power Spectrum . . . . .	120
7.2.1	Analytic Prediction . . . . .	120
7.2.2	Dependence on Cosmological Parameters . . . . .	121
7.3	Observations and $\sigma_8$ Measurements . . . . .	123
7.4	Looking for the SZ Effect in QUaD's Frequency Jackknife . . . . .	124
7.4.1	SZ Frequency Difference . . . . .	124
7.4.2	Linear Fits . . . . .	125

7.4.3	$\sigma_8$ Results . . . . .	126
7.5	Radio Point Sources . . . . .	128
7.5.1	Radio Point Source Spectra . . . . .	128
7.5.2	$\sigma_8$ Results After Correcting for Residual Point Sources . . . . .	130
7.6	Simultaneously Fitting the FIRB and the SZ Effect . . . . .	131
7.6.1	Discussion of Results . . . . .	133
7.6.2	Including Variation of $\sigma_8$ in the FIRB Spectrum . . . . .	136
7.6.3	Results in the Context of QUaD's high- $\ell$ Data . . . . .	137
<b>8</b>	<b>Conclusions and Future Work</b>	<b>141</b>
8.1	Summary of Key Results . . . . .	141
8.1.1	Dust . . . . .	142
8.1.2	Synchrotron . . . . .	142
8.1.3	Far Infrared Background . . . . .	143
8.1.4	Sunyaev-Zel'dovich Effect . . . . .	144
8.1.5	FIRB and the SZ effect . . . . .	145
8.2	Future Work . . . . .	145
<b>A</b>	<b>Polarization Map Extraction</b>	<b>147</b>

# LIST OF TABLES

3.1	QUaD Cosmological Parameters . . . . .	65
4.1	QUaD and Dust Linear Fits . . . . .	77
4.2	Polarization QUaD and Dust Linear Fits . . . . .	81
5.1	QUaD and Synchrotron Linear Fits . . . . .	92
5.2	Polarization QUaD and Synchrotron Linear Fits . . . . .	95
6.1	Bias Results . . . . .	110
6.2	Bias Results using Simulated FIRB Spectra . . . . .	116
7.1	$\sigma_8$ Results . . . . .	126
7.2	$\sigma_8$ Results with Radio Correction . . . . .	130

# LIST OF FIGURES

1.1	Timeline of the Universe . . . . .	3
1.2	Baryonic Oscillations . . . . .	4
1.3	COBE Sees Lumps in the Primeval Soup . . . . .	5
1.4	The Temperature Power Spectrum . . . . .	7
1.5	Physical Baryon Density . . . . .	9
1.6	Curvature . . . . .	10
1.7	Thomson Scattering . . . . .	12
1.8	Polarization Patterns . . . . .	13
1.9	Scalar Perturbations . . . . .	14
1.10	Tensor Perturbations . . . . .	15
2.1	QUaD's Optical Path . . . . .	20
2.2	The Focal Plane Layout . . . . .	22
2.3	QUaD . . . . .	24
2.4	Time Series for the Elevation Nods . . . . .	29
2.5	Calibration Comparison . . . . .	32
2.6	QUaD's Observing Region . . . . .	34
2.7	Observing Strategy and Timestream Data . . . . .	35
2.8	WMAP . . . . .	39
3.1	Ground Subtraction Technique . . . . .	43
3.2	Temperature Maps . . . . .	46
3.3	Polarization Maps . . . . .	48
3.4	Band Power Window Functions . . . . .	54
3.5	100 GHz Power Spectra . . . . .	55
3.6	150 GHz Power Spectra . . . . .	56
3.7	Cross Frequency Power Spectra . . . . .	57
3.8	Chi-Square Statistics . . . . .	58
3.9	Band Power Deviation Plots . . . . .	60
3.10	Comparison Plot . . . . .	61
4.1	WMAP Foreground Amplitudes . . . . .	68
4.2	All-Sky Dust Map . . . . .	69
4.3	Dust Map at 94 GHz . . . . .	72
4.4	Field Differenced CMB and dust maps . . . . .	73
4.5	Dust Scatter Plots . . . . .	75
4.6	QUaD Sized Regions Around the Sky . . . . .	76

4.7	Correlation Histograms . . . . .	77
4.8	Cross Power Spectrum . . . . .	78
4.9	Dust Band Power Deviations . . . . .	79
4.10	Polarization Scatter Plots . . . . .	80
5.1	All-Sky Synchrotron Map . . . . .	85
5.2	All-Sky Synchrotron Map . . . . .	87
5.3	Synchrotron Radiation . . . . .	88
5.4	Polarization Fraction . . . . .	89
5.5	Synchrotron Map at 100 GHz . . . . .	89
5.6	Field Differenced CMB and synchrotron maps . . . . .	90
5.7	Synchrotron Scatter Plots . . . . .	91
5.8	Cross Power Spectrum . . . . .	93
5.9	Synchrotron Band Power Deviations . . . . .	93
5.10	Polarization Correlation . . . . .	94
6.1	Cosmic Backgrounds . . . . .	98
6.2	The Far Infrared Sky Before and After Subtraction of Foregrounds . . . . .	99
6.3	Contribution to the FIRB Power Spectrum from Geometrical Effects . . . . .	102
6.4	The Mean Infrared Galaxy Emissivity . . . . .	103
6.5	The Far Infrared Background Spectrum . . . . .	104
6.6	Frequency Jackknife Power Spectrum . . . . .	106
6.7	Frequency Jackknife Band Power Deviations . . . . .	107
6.8	FIRB Frequency Difference Spectrum . . . . .	109
6.9	Linear Fit to the FIRB Model . . . . .	110
6.10	Scaled FIRB Spectra . . . . .	111
6.11	Infrared Galaxy Simulations . . . . .	112
6.12	Convolved Infrared Galaxy Simulations . . . . .	113
6.13	Repixelized Convolved IR galaxy Simulations . . . . .	114
6.14	QUaD Simulated IR Galaxy Maps . . . . .	115
6.15	FIRB Power Spectrum from Simulations . . . . .	115
6.16	Scaled Simulated FIRB Spectra . . . . .	116
7.1	Inverse Compton Scattering . . . . .	118
7.2	Frequency Dependence of the SZ Effect . . . . .	119
7.3	The Sunyaev Zel'dovich Spectrum . . . . .	122
7.4	QUaD's Small Angular Scale Temperature Power Spectra . . . . .	123
7.5	SZ Effect Frequency Difference Spectrum . . . . .	125
7.6	Linear Fit to the SZ Effect template . . . . .	127
7.7	Scaled SZ Effect Spectra . . . . .	127
7.8	Radio Point Source Corrections . . . . .	128
7.9	Radio Point Source White Spectra . . . . .	129
7.10	Theoretical Residual Radio Point Source Spectra . . . . .	130
7.11	Scaled SZ Effect Spectra Using Point Source Corrected Results . . . . .	131
7.12	SZ Effect and FIRB Amplitude Likelihoods . . . . .	132
7.13	$\sigma_8$ and $b$ Likelihoods . . . . .	133

7.14	One Dimensional Likelihood Slices . . . . .	134
7.15	$\sigma_8$ and $b$ Results . . . . .	135
7.16	New SZ effect and FIRB Amplitudes . . . . .	136
7.17	New $\sigma_8$ and $b$ . . . . .	137
7.18	Results Compared to QUaD's High- $\ell$ Temperature Data . . . . .	138

# 1 INTRODUCTION

---

“YOU STRETCH OUT THE STARRY CURTAIN OF THE HEAVENS.”

PSALM 104 v2

## 1.1 BIG BANG COSMOLOGY

Once upon a time the universe was a hot, dense primeval soup. It has been expanding and cooling for 13.7 billion years (Dunkley et al., 2009) since. We still do not know what exactly happened but it is commonly believed that the universe as we see it today exploded into existence from a single point in both space and time before which neither existed. This is the theory first proposed as the ‘hypothesis of the primeval atom’ in 1927 by George Lemaître, and independently by Alexander Friedman. A mathematical model was later advocated and developed in the 1950’s by George Gamov after Hubble’s observations of receding galaxies suggested an expanding universe and was unintentionally coined the ‘Big Bang Theory’ by Fred Hoyle describing it with effect on the radio!

Initially this soup would have been an opaque plasma of electrons, protons, helium nuclei and neutrinos. Photons would not have been able to travel very far without being scattered by free electrons. As it expanded over time, the universe cooled and eventually, at a temperature of about 3000K, protons and electrons coalesced into neutral atoms. The photons were now free to travel across a transparent universe and hence this epoch of recombination, as it is known, is as far back in time as we are able to see electromagnetically. Since it was the last time the photons were scattered by the electrons it is also known as the surface of last scattering and can be thought of as the surface of the soup. The photons from this time, approximately 380,000 years after the Big Bang, have been redshifted just like the light from the stars Hubble observed. The radiation today has a temperature of 2.73K peaking at millimeter wavelengths, but was actually first detected in the microwave region hence giving rise to the name Cosmic Microwave Background (CMB), a thermal afterglow

remaining from the Big Bang.

When the CMB was measured for the first time in 1965 (Penzias & Wilson, 1965) it provided very encouraging evidence to support the Big Bang theory. At a first glance it is uniform across the whole sky; homogeneous (the same everywhere) and isotropic (the same in all directions). In 1992, the COsmic Background Explorer (COBE) satellite found it to be the most perfect black-body spectrum known (Mather et al., 1994). The geometry of such a homogeneous space-time can be characterized as a simple function of time,  $t$ , with a scalar factor,  $a(t)$ , describing its expansion:

$$ds^2 = g_{\mu\nu}dx^\mu dy^\nu = -dt^2 + a(t)^2d(x)^2 \quad (1.1)$$

$g_{\mu\nu}$  here is the space-time metric and  $ds$  the co-ordinate interval between two space-time events, related to the proper time,  $\tau$ , between them by  $ds^2 = -d\tau^2$ .

Based on this we know that objects in the universe are separated by a distance proportional to the scale factor, and redshifts will be proportional to  $1/a(t)$ . Whilst this homogeneity is true averaged over cosmological scales, the planets, stars, galaxies, and even our very existence prove otherwise. The large-scale structure we see today must have originated as some inhomogeneities in the early universe and scientists have put a lot of effort into developing a theory to explain these primordial seeds and how they might have evolved into the phenomena we can now observe.

## 1.2 STRUCTURE FORMATION

Light travels at a finite velocity of  $3 \times 10^8 \text{ ms}^{-1}$  and special relativity tells us that no information is permitted to travel faster than this. As such there exists a maximum separation of two regions of space that were in causal contact at the time of recombination. Despite this we find the CMB to be uniform across much larger scales; scales with no apparent way to establish a thermal equilibrium. In fact the CMB should consist of about  $10^4$  causally disconnected regions (Baumann & Peiris, 2008), not the remarkably near-homogeneous temperature we observe. This so called ‘horizon problem’ is just one of the puzzles of the otherwise very successful standard theory of the Big Bang. The other particularly significant problem is that of the flatness of the universe. The geometry of the universe is dependent upon its matter content and is flat if its total energy density is equal to a critical density:

$$\rho_c = \frac{3H^2}{8\pi G} \quad (1.2)$$

Any greater and the universe becomes positively curved like the surface of a sphere and any

lower results in saddle-shaped negative curvature. Observations indicate that the universe is actually very close to being exactly flat. The trouble with this is that any deviation from flatness, however slight, in the initial moments after the Big Bang would either have grown over time creating a very non-flat universe today or have caused a rapid collapse. The near flatness seen today requires an incredibly delicate tuning of conditions in the early universe or an alternative mechanism by which this geometry arose, hence the ‘flatness problem’.

### 1.2.1 INFLATION THEORY

The theory of inflation (Guth, 1981) is the most currently accepted of many theories (such as brane cosmology or plasma cosmology) proposed to provide a solution to these and other issues in the original theory. The basic concept is that the universe expanded exponentially during its first  $10^{-43}$ s, faster than the growth of the causal horizon. During this period of rapid expansion the universe was driven as close to flat as we observe today and regions initially in thermal contact were stretched beyond the horizon, hence solving both the flatness and the horizon problems, even if further questions are introduced by the idea, such as the cause of the acceleration.



Figure 1.1: Timeline of the Universe

After inflation the universe was dominated by radiation until recombination took place  $\sim 400,000$  years after the Big Bang. It then became matter dominated with stars, galaxies and solar system forming in due course over the aeons.

(Image: Rhys Taylor - <http://planck.cf.ac.uk>)

Inflation theory is also able to explain the large scale structure observed throughout space when combined with some quantum mechanics. It suggests that before either matter or radiation, the very early universe was filled with an unidentified scalar field, termed the ‘inflaton’ field,  $\phi$ . If Bosonic, the Bosons would have had zero spin and energies  $\sim 10^{15}$  GeV. Under no obligation to obey the Fermi-exclusion principle they could all settle into the zero-point solution of Schrödinger’s equation. Just as the zero-point fluctuations of a one-dimensional harmonic oscillator induce a non-zero variance in oscillation amplitude, tiny quantum fluctuations would be induced in the inflaton field creating slight over and under densities throughout space, along with fluctuations in background space-time. These would be characterized by a Gaussian random distribution which would be preserved as inflation occurred; the small regions of over and under density would be stretched over cosmic proportions and the space-time fluctuations translated into a stochastic background of gravitational waves.

### 1.2.2 GRAVITATIONAL INSTABILITY

Gravitational potential wells formed in the places of over density into which matter, both baryonic and dark, would fall. As matter fell into the wells its temperature would increase, and consequently the pressure inside would also increase. Dark matter can only interact gravitationally, but the baryonic matter would be rebounded by the driving force set up by this pressure increase. Between the opposing forces of gravity and pressure, sound wave oscillations were established in the photon-baryon fluid. These oscillations can be thought of as a spring compressing in the wells under gravity whilst rarefying over potential hills as illustrated in Figure 1.2.

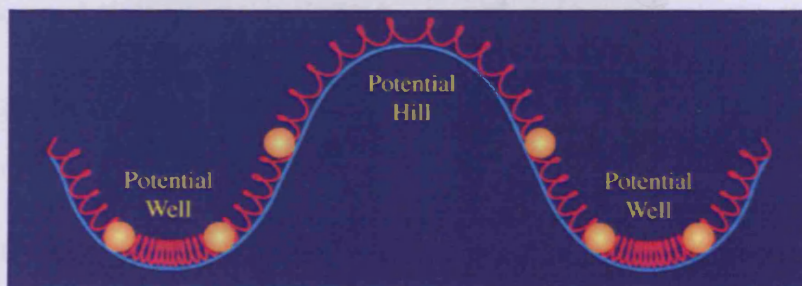


Figure 1.2: Baryonic Oscillations

Regions of high density generate potential wells and regions of low density generate potential hills.

(Image: Wayne Hu - <http://background.uchicago.edu/~whu/intermediate/intermediate.html>)

As the whole universe cooled upon expansion the tops of the potential hills, being fractionally cooler, would reach recombination temperature a short while before the bottoms of the wells. The epoch of recombination was thus not an instantaneous event, but occurred over a finite time, during which we can say that the universe is neither opaque nor transparent, but semi-transparent. The oscillatory motion of the baryons is frozen at this point and the effect is manifested as slight temperature anisotropies in the CMB we observe.

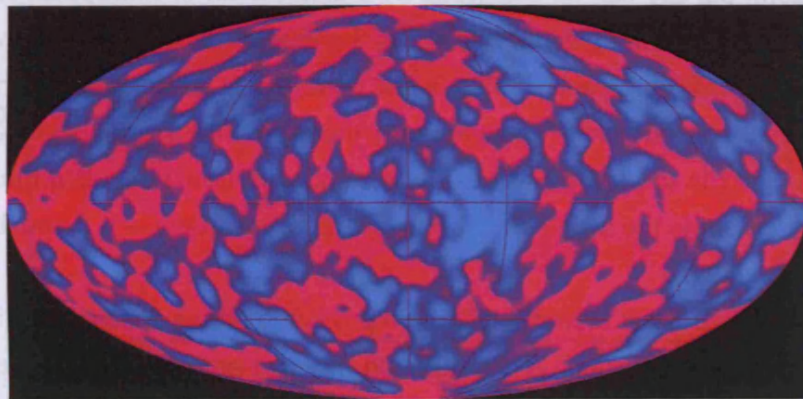


Figure 1.3: COBE Sees Lumps in the Primeval Soup

COBE observed temperature variations of 1 part in 100,000, providing the first evidence of these tiny density fluctuations (Smoot et al., 1992).

(Image: NASA - [http://lambda.gsfc.nasa.gov/product/cobe/dmr\\_image.cfm](http://lambda.gsfc.nasa.gov/product/cobe/dmr_image.cfm))

Consistent with their sound wave like behaviour, these baryonic oscillations were moving at the speed of sound for a relativistic plasma ( $c/\sqrt{3}$ ). If there is an initial spectrum of fluctuations then just as an oscillating musical instrument generates several harmonic modes above a fundamental mode, so will the baryons. The fundamental mode is that which in the 380,000 years following the Big Bang underwent a single compression. As the universe has expanded since the time of recombination we find this mode now equates to a radius of approximately 1 Gpc in the present epoch, roughly the size of a supercluster and hence compatible with being the explanation for large scale structure formation in the cosmos. Above this are many different modes all caught in different phases of their oscillation. Photons undergoing a compression correspond to cold spots in the CMB as they would have lost energy climbing out of the potential well. On the other hand those in a rarefaction are now seen as hot spots with a temperature slightly above that of the mean.

### 1.2.3 ANGULAR FORMALISM

Taking Fourier transforms of the photon distribution we can obtain an almost continuous spectrum of wave-number ( $k$ ) modes (inverse wavelengths). The spatial inhomogeneities at recombination that are described by their wave-number are observed looking out into the sky and so they have become angular anisotropies projected onto the surface of a sphere. It is therefore better to use spherical harmonic transforms rather than Fourier analysis to comprehend the CMB as we see it from Earth. Much like the quantum orbital states of an atom, the sky can be described by a discrete set of multipoles called  $\ell$  modes ( $\ell = 0, 1, \dots, \infty$ );  $\ell = 0$  being a monopole,  $\ell = 1$  a dipole etc. . . . In analogy with magnetic quantum number  $m$ , for each multipole  $\ell$  value there exists a subset of spherical harmonic orders  $m = -\ell, \dots, \ell$ . For each  $\ell$  there are only therefore  $2\ell + 1$  possible measurements so a fundamental limit is set, known as cosmic variance, on how well each multipole can be measured. For example the dipole  $\ell = 1$  has just three  $m$ -orders  $-1, 0$  and  $1$  so this mode will not be well-known.

The perturbations at recombination are projected onto a sphere at a distance  $D$  that the radiation has since travelled. A perturbation of wave-number  $k$  will have an angle  $1/\ell$  on the sky. The fundamental mode of oscillations, that undergoing a single compression since the big bang, projected onto this distance  $D$  hence corresponds to a particular angle across the sky. Cosmology predicts this mode to be that for which  $k = \ell/D$  giving a fundamental angular wave-number of  $\ell = 200$ , equivalent to the 1 Gpc mentioned above. This was confirmed by BOOMERANG's measurements (Masi et al., 2003) and since then a number of other ground, balloon and space-based missions have not only supported the result but have attempted to make measurements of the angular fluctuations to higher and higher degrees of precision, out to smaller and smaller angular scales (higher  $\ell$ ).

## 1.3 TEMPERATURE POWER SPECTRUM

All the CMB data from a map of the sky can be summarized by a power spectrum ( $C_\ell$ ) as a function of multipole, where the power is the square of the mean amplitude fluctuation. If all the modes were received from the same plane we would see a simple series of spikes, however arriving from across all planes results in a wave shaped curve with peaks and troughs. The exact shape of the spectrum and the location of these peaks depends on various cosmological parameters of the universe, hence the better we map the CMB, the better we understand the cosmos. Modes caught in a maximum compression or a maximum rarefaction at recombination correspond to peaks in the temperature power spectra, whilst the troughs are the result of photons caught at maximum velocity either falling into or

coming up out of a potential well. Velocity is consequently out of phase with respect to the density by  $\pi/2$ .

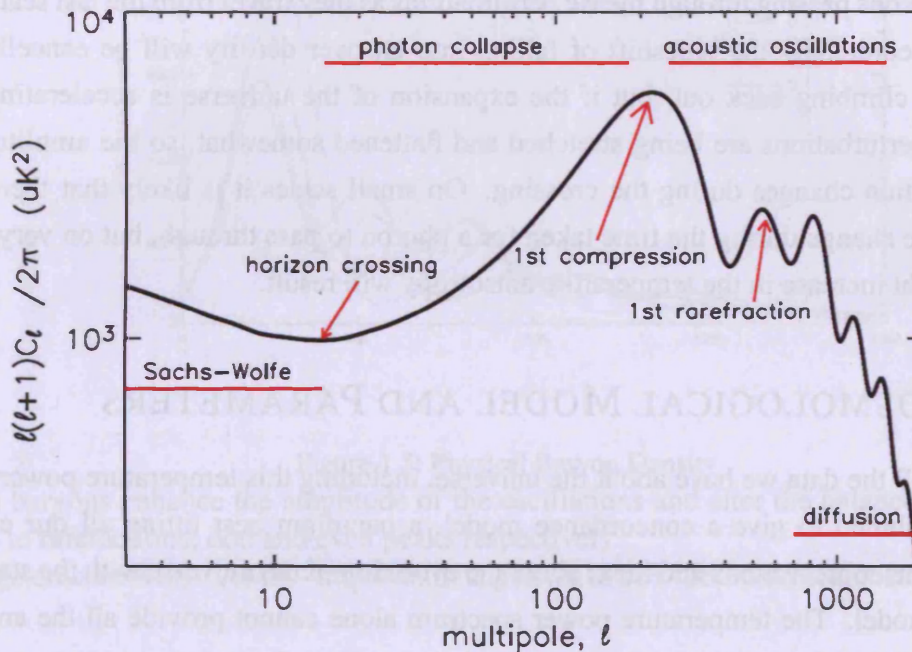


Figure 1.4: The Temperature Power Spectrum

Various different physical effects determine the exact shape of the peaks and their position (Bowden, 2003).

A model of the temperature power spectrum consistent with theory and within the error bars of data acquired from several CMB experiments, such as WMAP (Bennett et al., 2003a) and BOOMERANG is presented in Figure 1.4 which shows its various distinctive features. At low multipoles the spectrum is flat since the modes are larger than the horizon size. After crossing over into scales within the horizon the spectrum increases until the first peak corresponding to the fundamental mode in which the baryons have reached the first maximal compression. The second peak is then the mode for which there has been one compression and one rarefaction, the third a compression, a rarefaction, and a second compression, and so on for subsequent peaks. Although the exact shape of these peaks depends on several cosmological parameters, there is a general decrease in amplitude as peaks reach higher multipoles. This is due to silk damping (Silk, 1968) - an effect due to photons moving a finite mean-free-path in the finite time recombination takes, causing a damping of the fluctuations on small scales. Another effect, which results in a slight rise in the power spectrum at low  $l$ , is the Sachs-Wolfe effect (Sachs & Wolfe, 1967). This is due to those photons that are suddenly free to travel across space needing to initially climb

out of the potential well where they have been coupled with the baryons. This would have used energy and hence redshifted the photons slightly.

Linked to this is the so-called Integrated Sachs-Wolfe (ISW) effect which is the net effect of photons passing through metric perturbations as they travel from the last scattering surface. Theoretically the blueshift of falling into an over density will be cancelled by the redshift climbing back out, but if the expansion of the universe is accelerating this means the perturbations are being stretched and flattened somewhat, so the amplitude of the perturbation changes during the crossing. On small scales it is likely that there will be negligible change during the time taken for a photon to pass through, but on very large scales a slight increase in the temperature anisotropy will result.

## 1.4 COSMOLOGICAL MODEL AND PARAMETERS

At present all the data we have about the universe, including this temperature power spectrum is combined to give a concordance model, a paradigm best fitting all our current measurements, observations and ideas about the evolution of the universe with the standard Big Bang model. The temperature power spectrum alone cannot provide all the answers but alongside data from weak lensing, large scale structure and supernova experiments and observations, the model can be built up. Its most fundamental features are that we live in a flat universe, expanding at an accelerating rate and of the total energy density only about 4% is ordinary baryonic matter. The remainder is believed to be about 1/3 dark matter (material that only interacts gravitationally) and about 2/3 dark energy (a hypothetical energy permeating space, exerting a negative pressure against gravity causing the acceleration of the universe).

The details of the CMB temperature power spectrum relate to various aspects of this model. The position of the first peak is an indication of curvature, with measurements currently revealing that our universe is very close to being spatially flat, with a total density (matter + energy) of unity. The exact flatness is also dependent upon the amount of dark matter present, for which we gain some insight from the higher peaks. The second peak tells us about the amount of baryons in the universe; more baryons means more mass and hence deeper potential wells and enhanced compressions. This results in a relative suppression of this peak and the extra mass also slows the oscillations shifting the peak to slightly higher multipoles. The higher peaks are dependent upon the ratio of dark matter to radiation, hence if the amount of radiation is known from the CMB temperature then we learn about dark matter from these peaks. More dark matter causes damping to occur at lower  $\ell$  since it decreases the driving force behind the oscillations.

If the universe did indeed undergo inflation we expect the truly random quantum

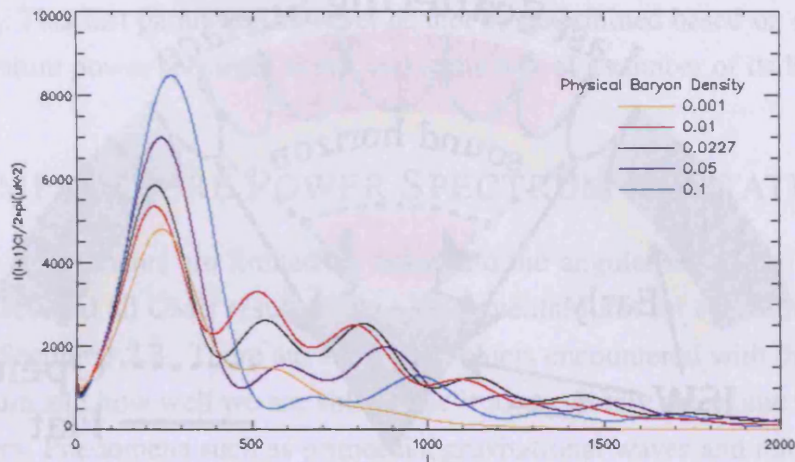


Figure 1.5: Physical Baryon Density

More baryons enhance the amplitude of the oscillations and alter the balance of compressions to rarefactions; odd and even peaks respectively.

(Image created with CAMB - [http://lambda.gsfc.nasa.gov/toolbox/tb\\_camb\\_form.cfm](http://lambda.gsfc.nasa.gov/toolbox/tb_camb_form.cfm))

fluctuations that were stretched in the process to conserve this randomness and the associated Gaussian distribution. Testing the Gaussianity of the measurements is a test of standard inflation theory and any non-Gaussianity found may signify some other processes at work in the early universe. Non-gaussianity can arise if there are correlations in the data and care must be taken to ensure that no artifacts of the experiment or analysis are responsible before declaring new physics. There are alternative inflation theories with non-uniform expansion of the universe or temperature gradients which permit non-Gaussianity, an ekpyrotic universe (the idea that our universe was created by the collision of two others) for example (Khoury et al., 2001).

There are lots of potential parameters that could characterize our universe but the number essential to alone provide a successful cosmological model is debatable, between 5 and 7 (Liddle, 2004). CMB experiments in general attempt to determine seven of the most fundamental parameters. Hubble's constant in his famous equation relating the recession velocity of galaxies to their distance,  $v = H_0 d$ , is more commonly expressed as  $h$ , the constant in units of 100 km/s/Mpc. We expect Hubble's constant to be changing over time, since it is a measure of the expansion of the universe, which is known to be accelerating. Estimates of the age of the universe can be made by extrapolating the changes in the expansion rate, though it is believed that the age is close to simply  $1/H_0$ . Parameters  $\Omega_b h^2$  and  $\Omega_m h^2$  are the baryon density and the matter (baryonic and dark) density. The quantities  $\Omega_b$  and  $\Omega_m$  are the ratios of the physical density to the critical density which we

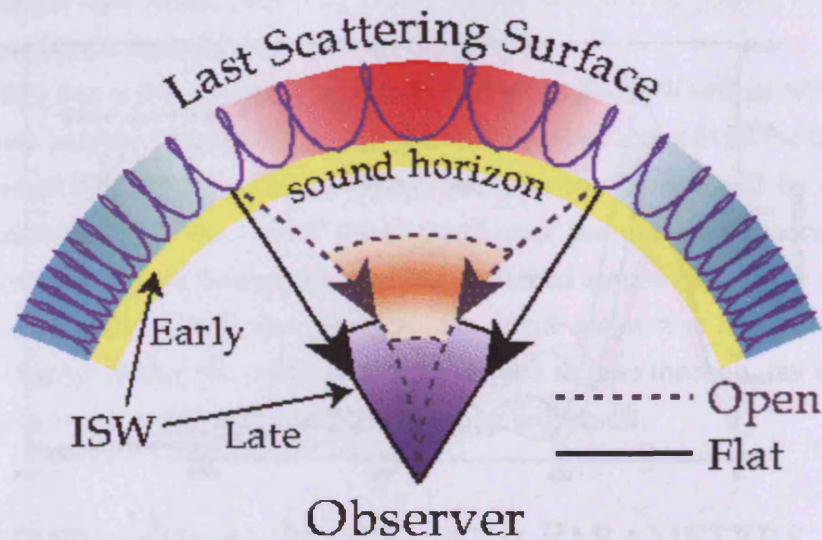


Figure 1.6: Curvature

The metric of spacetime since recombination will determine the distance to the last scattering surface and manifest itself in the position of the peaks in the spectrum.  
 (Image: Wayne Hu - <http://background.uchicago.edu/~whu/physics/tour.html>)

saw to be a function of  $h^2$  in equation 1.2 hence the density parameters are traditionally given in the form  $\Omega_i h^2$  such that they are proportional to the physical density. The amount of baryonic matter will determine the sound horizon size at recombination, which modes are oscillating and how fast, therefore setting the amplitude and the phase of each mode in the distribution. The position of the peaks will depend on the angular scale over which these modes are projected, which is set by the distance to the last scattering surface. As the horizon lines in Figure 1.6 illustrate this will have been affected by the curvature of the universe, as well as the total matter density and the Hubble constant which have all played a role in the expansion of the universe since recombination.

$\tau$  is the optical depth to reionization - a time when the universe became once again reionized, possibly by quasars or early stars at around  $z \sim 10 - 15$  (Komatsu et al., 2009). This is a parameter which gives the probability that a CMB photon has been Thomson scattered off a free electron and therefore actually originated in a different direction to that from which it appears. This serves to smear out the features in the CMB spectrum on small scales; suppressing the peaks by a factor  $e^{-\tau}$ . The overall normalization of the power spectra is quantified by the parameter  $A$ , the amplitude of density fluctuations. The scalar spectral index,  $n_s$  is a measure of the tilt of the spectrum, dependent upon the relative ratio of small to large scale power. A seventh parameter needed to complete the current concordance model is the tensor to scalar ratio,  $r$ . This is the amplitude of the tensor

fluctuations (gravitational waves predicted by inflation) compared to the scalar (density) perturbations. This last parameter however cannot be determined based on measurements of the temperature power spectrum alone, and is the first of a number of its limitations.

## 1.5 TEMPERATURE POWER SPECTRUM LIMITATIONS

All telescope experiments are limited by noise and the angular resolution of the instrument being used and all CMB results have a fundamental limit set by cosmic variance as described in Section 1.2.3. There are further problems encountered with the temperature power spectrum and how well we are able to use it to accurately determine the cosmological parameters. Phenomena such as primordial gravitational waves and reionization from the first stars may adjust the spectrum in a similar way to the parameters under consideration. Also there are various combinations of parameters which will give the same pattern, signifying the need for additional data in order to break these degeneracies.

The geometric degeneracy is that existing between curvature of the universe and the matter density. Almost the same power spectrum pattern can be obtained by varying the curvature to compensate for changes in  $\Omega_m$  and  $h$ , given a set of initial perturbations with  $n_s$  and  $A$  (Efstathiou & Bond, 1999). The Integrated Sachs-Wolfe effect can help to some extent but this suffers its own issues with cosmic variance, so usually information from other astronomical observations is used to constrain one or the other parameter.

There is a degeneracy between  $n_s$  and the density parameters, because changes to the height of the first few peaks can be reproduced by changes in either parameter. Changes to the reionization optical depth simply move the temperature spectrum up and down and this can be mimicked by a change in amplitude, hence there is also a degeneracy between  $A$  and  $\tau$ . Inclusion of tensor-to-scalar ratio analysis increases the uncertainty on the other parameters by affecting the power spectrum in a similar fashion to that of the ISW and hence it is no longer able to help with the geometric degeneracy described above. In order to break these degeneracies and obtain more precise data for constraining the cosmological parameters we can make use of another feature of the CMB as well as the temperature anisotropies - its polarization.

## 1.6 POLARIZATION

Although it was first predicted back in 1968 that the CMB would be polarized (Rees, 1968), a detection was not actually made until 2002 (Kovac et al., 2002) by an instrument called DASI (Degree Angular Scale Interferometer) at the South Pole.

The Thomson scattering of the CMB photons at recombination generates a polarization as electrons preferentially re-emit radiation with a polarization orthogonal to the scattering direction. The temperature anisotropies set up during recombination create a quadrupole distribution with hot peaks separated from cold peaks by  $90^\circ$ . This results in a net polarization of about 10% after scattering. Figure 1.7 illustrates the process with the blue lines representing hot radiation and the red lines indicating cold regions. There are five independent components to a quadrupole moment, which in terms of a multipole decomposition of the radiation field via spherical harmonics are given by  $\ell = 2$  with  $m = 0, \pm 1$  and  $\pm 2$ .

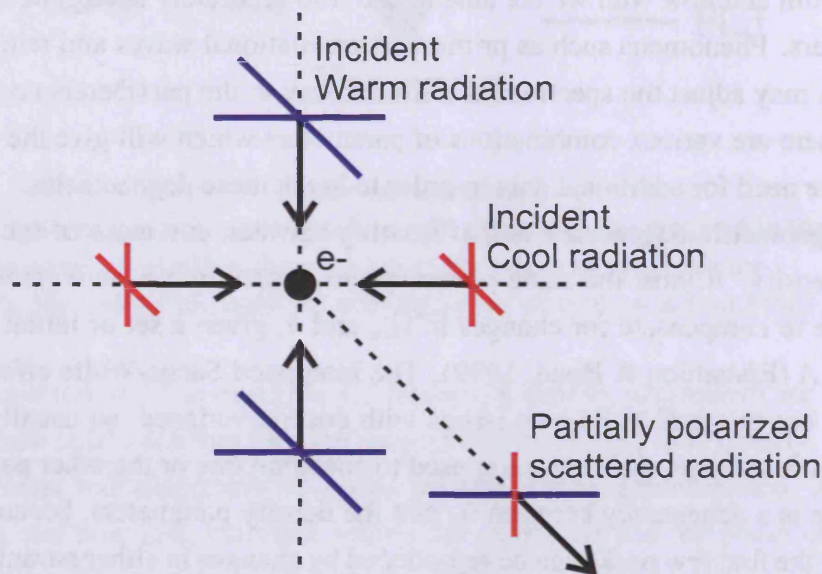


Figure 1.7: Thomson Scattering

Polarization of the CMB arises because of Thomson scattering within a temperature anisotropy (Hinderks, 2005).

Polarization is quantified by Stokes parameters:  $I$ ,  $Q$  and  $U$ . ( $V$  is not needed in this case as the CMB is not circularly polarized.)  $I$  corresponds to the total intensity (the temperature) and  $Q$  and  $U$  are co-ordinate dependent quantities describing the directionality of linear polarization. If two polarimeters are perpendicularly oriented along the  $x$  and  $y$  directions, each will detect part of the total intensity  $I = \langle E^2 \rangle$  (where the angled brackets mean time averages).  $E$  here is the amplitude of the electric field vector at an angle  $\chi$  to the reference  $x$  direction:

$$I_x = \langle E^2 \cos^2 \chi \rangle \quad (1.3)$$

$$I_y = \langle E^2 \sin^2 \chi \rangle \quad (1.4)$$

Parameter  $Q$  is defined as the difference between these intensities and  $U$  is the difference between the intensities measured if the co-ordinate system were rotated through  $45^\circ$ :

$$Q = I_x - I_y = I \cos 2\chi \quad (1.5)$$

$$U = I_{x(45)} - I_{y(45)} = I \sin 2\chi \quad (1.6)$$

$Q$  and  $U$  are therefore related to the total polarized intensity  $I_p$  by:

$$I_p^2 = Q^2 + U^2 \quad (1.7)$$

These quantities can be redefined in terms of rotationally invariant quantities  $E$  and  $B$  via decomposition into the grad of a scalar plus the curl of a vector. If  $\theta_\ell$  is the angle between the  $x$ -axis and the polarization direction:

$$E(\ell) = Q(\ell) \cos(2\theta_\ell) + U(\ell) \sin(2\theta_\ell) \quad (1.8)$$

$$B(\ell) = -Q(\ell) \sin(2\theta_\ell) + U(\ell) \cos(2\theta_\ell) \quad (1.9)$$

$E$  polarization is either parallel or perpendicular to the direction in which the polarization strength is changing most rapidly, i.e. it shows divergence (circular) patterns around the peak polarization areas.  $B$  on the other hand is at  $45^\circ$  to the  $E$  field, so it shows rotational (spiral) patterns.

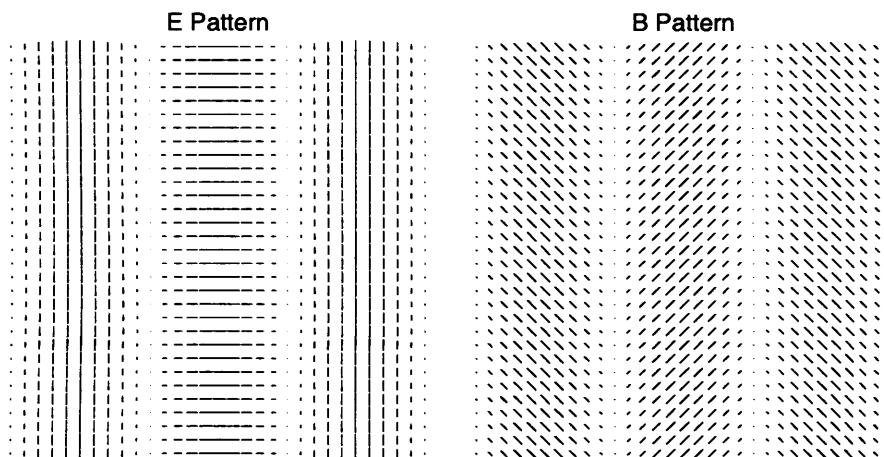


Figure 1.8: Polarization Patterns

Divergence patterns are generated by pure  $E$  fields (left) whilst rotational patterns are generated by pure  $B$  fields (right) (Hinderks, 2005).

These two quantities are spin-2 meaning they are headless vectors looking the same after a  $180^\circ$  rotation. A reversal in the sign of the temperature fluctuation results in a  $90^\circ$  rotation of the polarization patterns. Whilst the temperature anisotropy cannot differentiate between the three contributions being made to the quadrupole at recombination, they each lead to a different geometry in the polarization as it has a “handedness”. The sources are scalars, vectors and tensors, corresponding to  $m = 0, \pm 1$  and  $\pm 2$  respectively. The scalar polarization patterns ( $m = 0$ ) are due to density fluctuations; the quadrupole created causes a polarization either perpendicular or parallel to the direction in which the perturbation is changing, thus giving rise to only  $E$  modes.

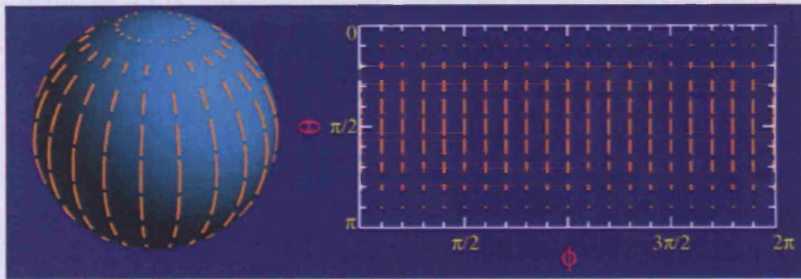


Figure 1.9: Scalar Perturbations  
Only  $E$  modes are generated by a scalar perturbation.

Vector polarization patterns ( $m = 1$ ) are due to vorticity (circular motion in a fluid) but they are not enhanced by gravitational collapse and hence are damped relative to those of the scalar and tensors. Tensor patterns ( $m = 2$ ) result from the transverse traceless perturbations of a gravitational wave for example. The stretching and squeezing of the wavelength produces a quadrupole temperature variation which generates both  $E$  and  $B$  modes.

Observations of a  $B$  mode signature could potentially provide the first direct evidence for primordial gravitational waves, however the  $B$  mode anisotropy is at least an order of magnitude smaller than the  $E$  mode which is already just 10% of the temperature anisotropy. There is the additional problem that polarized dust and other astrophysical phenomena between the CMB and the telescope is also detected contaminating the results. Much of this thesis is devoted to investigating these foregrounds so see later chapters for details.

### 1.6.1 POLARIZATION POWER SPECTRA

With both temperature and polarization measurements the CMB is therefore able to be characterized by four types of correlations. Autocorrelations of temperature,  $E$  modes

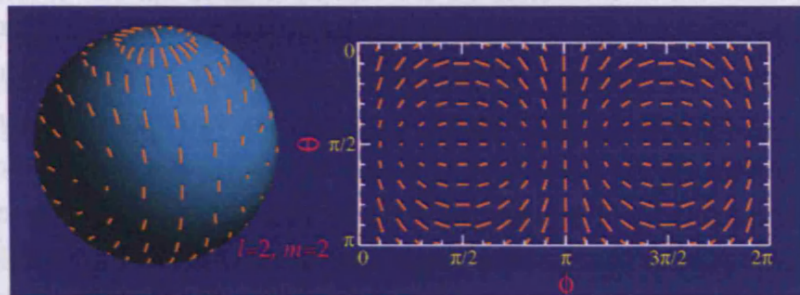


Figure 1.10: Tensor Perturbations

Both  $E$  and  $B$  modes are generated by a tensor perturbation.

(Images: Wayne Hu - <http://background.uchicago.edu/~whu/intermediate/intermediate.html>)

and  $B$  modes give us  $TT_{\ell m}$ ,  $EE_{\ell m}$ ,  $BB_{\ell m}$ , and a cross correlation between temperature and  $E$  modes gives  $TE_{\ell m}$ . Due to the opposite parity between  $B$  and  $E$ ,  $BE_{\ell m} = 0$  and likewise the opposite parity between  $B$  and  $T$  means  $BT_{\ell m} = 0$ .

The  $TE$  and  $EE$  power spectra will show the same series of acoustic peaks as that of  $TT$ , however the peaks will be in different places. The perturbations in the quadrupole are not directly coupled to the overall density perturbations but to those of the velocity of the fluid. The baryonic velocity is greatest down the slopes of the potential wells hence the peaks in the polarization spectra are out of phase with the temperature peaks. The  $EE$  spectrum therefore shows peaks at the position of the dips in the  $TT$  spectrum. A quadrupole can only be created over scales for which photons have sufficient time to meet. On large scales there isn't sufficient time but on smaller scales the amplitude of the temperature perturbation and hence quadrupole is smaller, thus the polarization spectrum shows a peak at  $\ell = 1000$ , but is only a fraction of the magnitude of the temperature peak.

### 1.6.2 SECONDARY POLARIZATION

The polarization anisotropies created at the surface of last scattering are referred to as primary. Secondary polarization anisotropies are subsequently generated and are also observed in the spectra. When the universe is reionized, Thomson scattering occurs and polarization is produced. This leads to a second peak on larger angular scales than the CMB peak known as the reionization bump. The optical depth,  $\tau$ , determines the height of the bump. For a greater optical depth more photons will have been able to last scatter since reionization and hence give a larger amplitude to the bump. Its position will depend upon the time when reionization occurred. Further back in time means reionization took place across a smaller scale and therefore is seen at higher  $\ell$ .

Large scale structures throughout space will cause gravitational lensing which affects the polarization from the CMB. It also leads to the conversion of  $E$  modes into  $B$  modes. Large galaxies will gravitationally influence the CMB photons, causing them to deflect slightly as they propagate through space. This has the effect of smearing out sharp features in the power spectra of both temperature and polarization, but it is more noticeable in the  $EE$  spectrum because the peaks are sharper. Lensing has an even more severe effect on the  $BB$  spectrum, since it does not simply change the amplitude of a polarized signal, but also mixes the different polarization modes. Upon deflection a pure  $E$ -mode polarization field will generate a  $B$ -mode component. Although this lensing effect, occurring over small scales, is only significant at high  $\ell$ , it nevertheless imposes a minimum on the value of  $r$  measured and contaminates a true measurement of primordial  $B$ -modes. Recently there have been some proposals for de-lensing using information from weak lensing galaxy surveys (Marian & Bernstein, 2007; Smith et al., 2008).

Gravitational lensing though, despite being a considered contamination in the context of measuring  $B$ -modes actually contains useful cosmological information. Gravitational lensing takes place during the time when the universe is dominated by dark energy, which influences the rate of expansion of the universe. Therefore measuring the lensing gives us an insight into the growth of large scale structures, the acceleration of the universe's expansion and the dark energy causing it. Neutrinos will suppress clustering of dark matter on small scales dependent upon their mass. The gravitational force is not able to overcome the pressure due to the neutrino velocity dispersion, hence measurements of lensing can constrain the neutrino mass. Galaxy redshift surveys and measurements of weak lensing on the shapes of galaxies tell us about the large scale clustering of galaxies at redshifts  $z < 2$ , but the  $B$ -mode signal created by lensing can provide us with this information at higher redshifts,  $z > 2$ .

Not only does measuring polarization as well as temperature allow for an alternative fundamental check of the cosmological parameters but it can be used to break degeneracies which occur if only the temperature data is used. Since the peaks in the polarization spectrum are out of phase with those of the temperature spectrum, changes to the density parameters will cause the two spectra to move in opposite directions at each scale thus providing a distinction between a change in the amplitude of the peaks being due to  $n_s$  or  $\Omega_m$ . The reionization bump in the polarization spectrum allows for a constraint upon  $\tau$ , hence breaking its degeneracy encountered in the temperature spectrum with  $A$ , and therefore permitting a more precise estimation of the amplitude. By the polarization data providing vital information about the tensor-to-scalar ratio,  $r$ , the tensor component of the temperature spectrum will be better understood and thus no longer limiting the accuracy with which the parameters are constrained, or inhibiting the use of the ISW to aid analysis.

Therefore, to use the CMB to further our understanding of the history of the universe and more accurately determine these cosmological parameters which describe it, we need an experiment which can not only measure the temperature power spectrum to a high degree of precision, but which also makes polarization measurements of a similar quality.

## 1.7 THESIS OUTLINE

QUaD is one such project undertaken to make a major step forward in precision CMB measurements, particularly polarization. Having introduced the theory behind the CMB and how it is used to probe cosmology I will now move onto describing QUaD. The project is run by a collaboration of scientists from around the world, with various members involved with its different aspects, from the planning to the construction and implementation, to the data analysis. Joining the team in its later stages my work has focussed on the data analysis, though for completeness I will review the instrument itself and the observation strategy employed along with all the analysis techniques from the output data through to cosmological parameters.

In Chapter 2 I describe the experiment, the observations and how they are initially processed. I also briefly summarize some of the other past, present and future CMB instruments. Chapter 3 then proceeds to explain how we obtain maps, power spectra and parameter estimations from the data. Much of the coding for the various stages of the analysis was written prior to my arrival, but I have nevertheless not only been able to run all stages of the pipeline, but also to make modifications to them, allowing the unique work of Chapter 4 onwards to be carried out. As such through the analysis chapter, unless otherwise stated, the maps and plots are my own creation.

My contribution to the project has been to explore in depth the presence of any astrophysical foregrounds in QUaD's data. There are various different phenomena which could present a source of contamination so each of these are investigated in turn. Chapter 4 looks at dust, employing various statistical correlation techniques which are then also used in Chapter 5 in considering synchrotron radiation. These chapters both use field differencing techniques and CMB results published in Pryke et al. (2009). Chapter 6 turns to the Far Infrared Background and finally the Sunjaev-Zel'dovich effect is explored in Chapter 7, both with the improved results of Brown et al. (2009). Chapter 8 then summarizes the conclusions from these analyses and gives a discussion of future work.



## 2 QUAD

---

“TIMELINE? THIS IS NO TIME TO ARGUE ABOUT TIME. WE DON’T HAVE THE TIME!”

DEANNA TROI - STAR TREK: FIRST CONTACT

### 2.1 QUAD INSTRUMENTATION

#### 2.1.1 FROM THE CMB THROUGH THE ATMOSPHERE AND TELESCOPE TO THE FOCAL PLANE...

The name QUaD is in fact an acronym of acronyms! It comes from QUEST (Q and U Extra-galactic Survey Telescope) at DASl (Degree Scale Inferometer) (Church et al., 2003), so called because the QUEST telescope was put on an existing mount at the South Pole originally used for DASl (Leitch et al., 2002). This is an azimuth-elevation mount with a third axis allowing the entire telescope to be rotated around the line of sight and observations made at two so called ‘deck’ angles,  $-3^\circ$  and  $57^\circ$ . QUaD operated for three austral winters from 2005 before being decommissioned in November 2007. The telescope featured a Cassegrain design as shown in Figure 2.1 with a large 2.6 m primary mirror focussing radiation onto a smaller secondary mirror, which in turn reflected the light back through a hole in the centre of the primary mirror and on to the detectors. This design was chosen for its large field of view and its axial symmetry so that any spurious polarization signal arising from the instrument would be symmetrically distributed. Two lenses were used to position the focus behind the primary mirror along with cold stops to prevent any off-axis rays from reaching the focal plane.

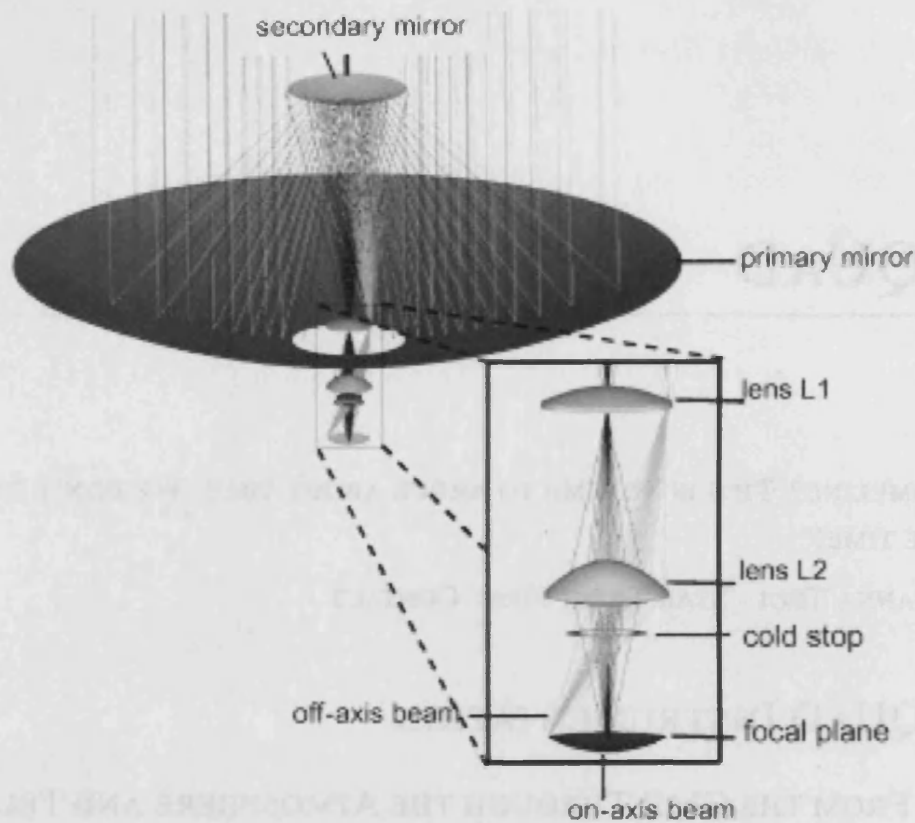


Figure 2.1: QUAD's Optical Path

The rays follow the Cassegrain design reflecting off the 2.6m primary mirror, then off a secondary mirror and onto the focal plane (O'Sullivan et al., 2008).

### 2.1.2 ... AND ONTO THE DETECTORS

Upon the focal plane the beam formed a diffraction pattern consisting of a central spot with surrounding faint rings. From there feedhorns transmitted and focussed the radiation down onto an array of Polarization Sensitive Bolometers (PSBs) (Jones et al., 2003). Two operating frequencies, chosen to match windows in the atmosphere at millimeter wavelengths were mapped simultaneously. Pairs of PSBs aligned orthogonally absorbed radiation at 100 GHz and 150 GHz. Initially 12 detectors at 100 GHz and 19 at 150 GHz were set up, however over the course of the observations some of these malfunctioned leading to slightly fewer being used in the analysis. The feedhorns coupling the radiation to the detectors were fashioned so as to create a Gaussian beam on the sky. These beams can be quantified by their Full-Width Half-Maximum (FWHM), that is the width of the beams on the sky at the point where the intensity is half its value at the Gaussian's maximum. QUAD made some special observations of a bright quasar (QSO PKS0537 – 441) to determine

mean FWHMs of 5.0' at 100 GHz and 3.5' at 150 GHz. A more detailed analysis of the quasar data revealed the presence of some sidelobe structure. Sidelobes are smaller amplitude beams away from the main beam, often of radiation in undesired directions. Their maximum value relative to the main beam, the sidelobe level, is another important parameter in beam characterization. QUaD's sidelobe level was found to be just below  $-20$  dB. The uncertainty on these parameters is  $+5/ - 2\%$ , due to daily fluctuations in the weather causing thermal contractions or expansions of the telescope optical assembly and therefore the focus.

The position and orientation of the 31 detectors on the focal plane were considered in detail before the final layout was decided upon (Bowden, 2003). For Stokes parameters  $Q$  and  $U$  to be determined from the total signal, at least two measurements of each frequency are needed of each particular point on the sky. Also to avoid any atmospheric or instrumental changes occurring between these measurements the focal plane was set up such that at least two feeds with different orientations observed the same position on the sky during each scan. Towards the edges of the focal plane there would be more severe optical aberrations and the instrumental polarization signal would be more significant. The detectors therefore needed to be packed as tight as possible away from the edges. Additionally the feeds were arranged to optimize the evenness of their sky coverage at both frequencies simultaneously. Oversampled regions would need to be downweighted in the subsequent analysis and hence would have been a waste of some integration time.

On arrival at the PSB, the radiation is intercepted by an absorber of heat capacity  $C$ , thermally linked with a conductivity  $G$ , to a heat sink. This heats a semi-conductor thermistor that is thermally linked in series to a high resistance load resistor. A bias voltage is applied across the two components and the voltage across the thermistor is measured. With an increase in incident power, the thermistor is heated and its resistance increases. Since the current across the thermistor is maintained at a constant value by the load resistor, its output voltage changes. We define the responsivity,  $S$ , of the bolometer to be the output voltage per unit change in power. The temperature change occurring in the PSB is proportional to the change in power and hence the output voltage measured, but the response is not instantaneous. To any change in power there is an exponential response function:

$$T_{bol} = T_{av} + \Delta T(1 - e^{-t/\tau}) \quad (2.1)$$

in which  $T_{av}$  is the bolometer temperature with no fluctuations,  $t$  the time since the fluctuation and  $\tau$  the bolometer time constant. This is the time taken for the thermistor to change by a temperature  $\Delta T(1 - 1/e)$  and is found from the bolometer parameters as  $\tau = C/G$ . The non-instantaneous response of the bolometers means they act as a low pass filter and

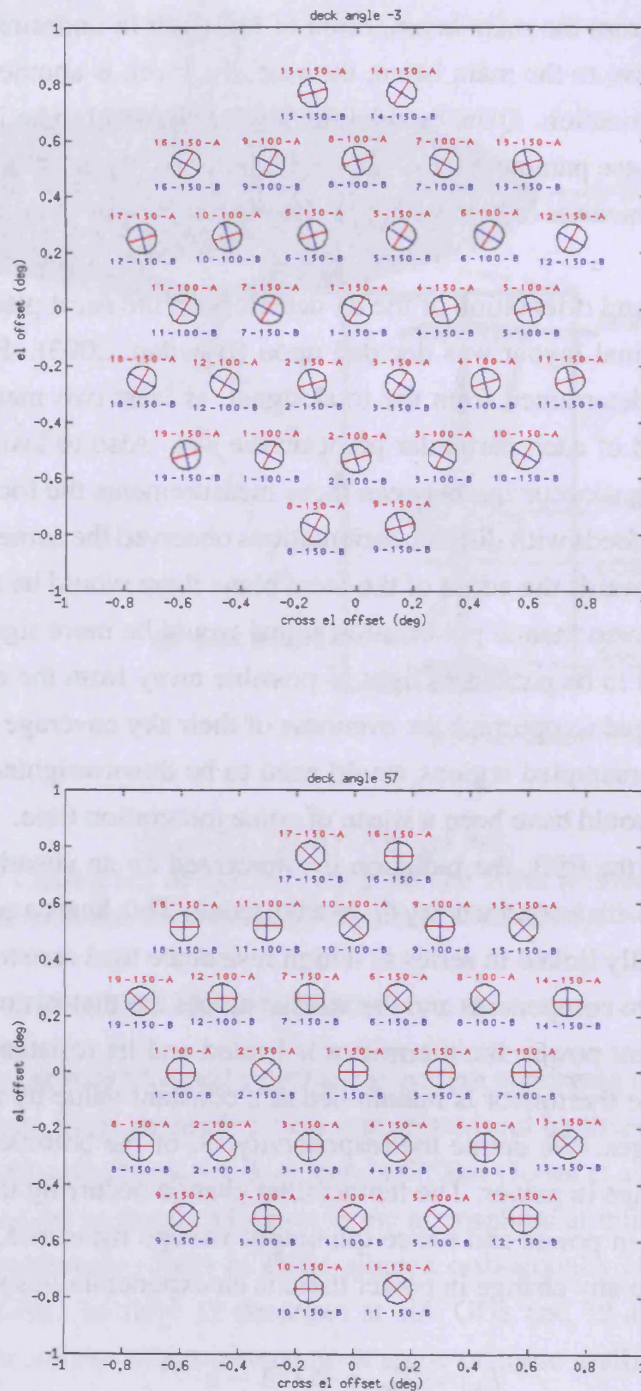


Figure 2.2: The Focal Plane Layout

This figure shows the focal plane layout at the two deck angles; the distribution of the different frequency detectors and their orientation. Deck angle  $-3^\circ$  is on top and  $57^\circ$  is on the bottom.

accurate knowledge of the time constants is required to reform the original data timestream. Investigations of the temporal responses found several of the bolometers to be better described by a dual time constant model, that is a second constant was needed for a good fit. For a few bolometers even this was not a reasonable fit and they were rejected from the analysis.

By having the PSBs set up in pairs, one coated along only the horizontal and the other only along the vertical axis of the grid, allowing just the component of the electric field in these directions to be absorbed, Stokes parameters may be determined. Unpolarized light is split equally between the two thereby permitting removal of this 'common mode signal' by differencing the outputs from each pair.

The support structure for the instrument was designed for maximum rigidity and minimal thermal conductivity. The supports also provided convenient places to attach wiring and this helped to reduce mechanical vibrations that would generate an electrical signal. A cone surrounded the secondary mirror, which expanded and contracted with external temperature changes. This cone was made of foam because it does not reflect or absorb at millimeter wavelengths. The focus, however remained slightly better in warmer conditions. The mirrors were set so that as many beams as possible were optimally focussed with data uncorrelated to the temperature of the environment. The telescope was skirted by a ground shield which served to reflect rays up into the sky, reducing stray signals from the ground. Problems arose, nevertheless, when snow entered the ground shield and the team at the South Pole spent many an hour shovelling out snow!

### 2.1.3 OPTICAL EFFICIENCY

Optical efficiency is the fraction of in-band power on the receiver that is actually detected by the bolometer. Reflection and absorption losses reduce this efficiency to a typical maximum of about 40% for mm wavelengths. The central group of 7 feedhorns were found to be the more efficient, however this was expected since the best ones from initial testing were positioned centrally. Tests of QUAD's optical efficiency revealed values, for the complete optical chain, of approximately 30% at 100 GHz and 35% at 150 GHz.

### 2.1.4 NOISE

However ideal the instrumentation, the true CMB signal will be hidden amongst a number of sources of noise. Some of these are non-time varying and so create a constant, removable, background level. Others are variable, they cannot be predicted, and set a fundamental limit on the accuracy to which we can measure the CMB. Any noise which is generated

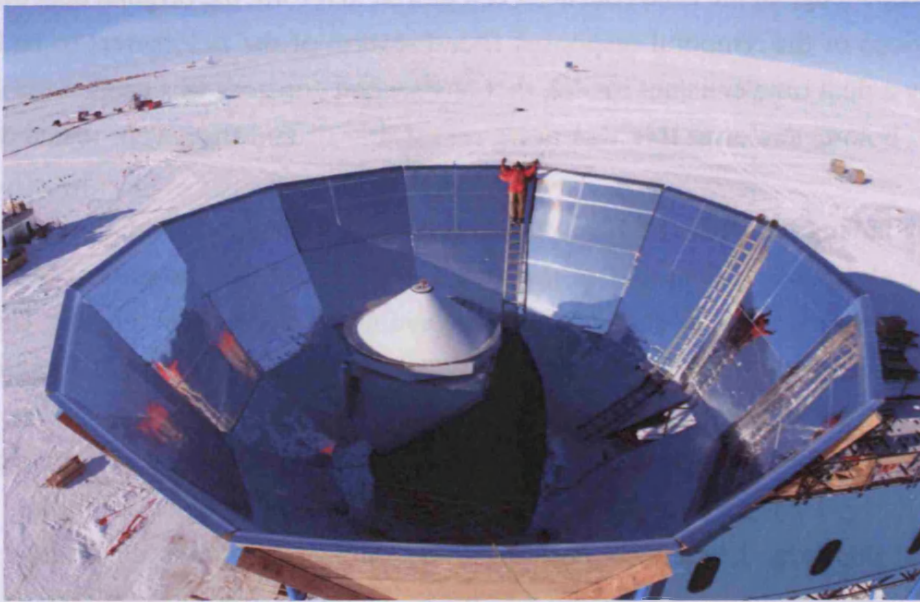


Figure 2.3: QUaD

A panoramic photograph of QUaD at the South Pole  
(Image: Robert Schwarz - <http://www.antarctic-adventures.de>)

by a completely random uncorrelated process is referred to as white noise, in analogy with white light. By taking more and more measurements, however, the mean value of this random noise will ultimately reach zero, hence the longer the integration time, the more accurate the results.

As the radiation passes through the optical chain some of the common mode signal (that reaching both bolometers in a pair) becomes polarized resulting in instrumental polarization. The electronics of the detector systems means there may be some gain difference between bolometers in a pair, which upon differencing may mean that some contribution from the common mode signal remains. Transmission to the detectors also adds some different electronic (Johnson) noise to each bolometer which again is not removed by the differencing process. There is white noise from the read-out electronics, shot noise from the statistical fluctuations in the number of photons received along with boson bunching noise and thermal noise from the emissions of the optical chain and detectors themselves.

In general, noise is quantified as a Noise Equivalent Power (NEP) which is the incident optical power required to generate an output voltage equal to the root-mean-square (RMS) noise voltage. It is useful to characterize the noise in terms of the brightness of a source, defining a noise equivalent temperature (NET) and likewise NEQ and NEU (generally equal) for polarization measurements. To determine these quantities the bolometers

are run in their normal modes for a period of time with the telescope parked. The white noise from this yields the NEP from which NET can be calculated by means of an absolute calibration factor converting the units from Volts into Kelvin. In Hertz the NEP is the amplitude of the one-sided power spectrum, i.e. the noise in a half second integration time and so a division by  $\sqrt{2}$  is required to convert from  $\mu\text{KHz}^{-1/2}$  into  $\mu\text{Ksec}^{1/2}$ . Qualitatively the NET for a particular detector is the amplitude of the temperature fluctuation measureable in one second with a unitary signal-to-noise ratio. NEQ is then computed as:

$$NEQ = \frac{NET}{\sqrt{2}(1 - \epsilon)} \quad (2.2)$$

where the factor of  $\sqrt{2}$  is introduced because there are two bolometers in a pair effectively doubling the integration time and  $\epsilon$  is cross-polarization between the two bolometers in a pair.

White noise fluctuations arise because of the fact that energy is quantized, that is it is confined to discrete packets. The quanta of energy does not flow at a constant rate and light, like energy is also quantized. The number of photons, wave packets of light, the PSB will detect in any given time period will vary randomly and not be the same in any particular period of time. We can therefore merely predict the probability that a certain number are detected based on the known parameters of the bolometer. Photons are bosons and these show a somewhat bizarre behaviour in their arrival at a detector. Immediately after the detection of one photon the probability of detecting another is increased. This is part of the quantum mechanical Bose-Einstein theory describing photons and adds some boson-bunching component to the photon noise. The photon NEP is therefore given by a two component equation (Lamarre, 1986):

$$NEP_{photon}^2 \approx 2h\nu P_{tot} + \frac{P_{tot}^2}{\Delta\nu} \quad (2.3)$$

with  $P_{tot}$  the total power incident on the detector and  $\Delta\nu$  the optical bandwidth. The first term quantifies the Bose-Einstein bunching effects and the second term gives the Possionian fluctuations of the photon flux per unit bandwidth.

Within the detector electronics there are free electrons moving around in a random fashion. At any instant in time there might happen to be more electrons in one particular place than another and this distribution will fluctuate randomly. The voltage measured across the thermistor will therefore also fluctuate from moment to moment, creating Johnson noise. Its contribution will depend on the temperature of the bolometer, its resistance and responsivity. The same idea applies to all aspects of the instrumentation. The thermal energy transferred from the bolometer to the heat sink creates phonon noise dependent upon its conductivity, as the energy flow, just as that within the detector electronics, is not

constant. Knowing the probability distribution of each source of white noise allows the total NEP to be calculated from the individual variances of the quantum noise signals.

Advances in detector design can serve to reduce detector and amplifier noise, whilst photon noise can be reduced by the site choice of the South Pole and decreasing emissions from the filters and telescope.

### 2.1.5 POLARIMETRY ERRORS

In addition to the sources of noise described above, the polarization measurements will suffer from various effects of systematic errors introduced by the instrument. One polarization state can be slightly enhanced over the other as a result of partially polarized emissions from the telescope. Diffraction, oblique reflection and birefringence within the telescope and optics may polarize some of the unpolarized incident radiation converting  $T$  into  $Q$  and  $U$ , possibly even some  $V$ .

Some depolarization effects or cross polar leakage can occur as well, reducing the measured  $Q$  and  $U$  intensities. The biggest problem in polarimetry is that of cross polarization; power from one state of polarization is converted to the orthogonal state. It is also known as  $Q \leftrightarrow U$  mixing, and it leads to  $E \leftrightarrow B$  mixing, deforming the final power spectra and causing a loss in sensitivity to the polarized fraction of incident radiation. QUaD shows levels of 5% and 8% cross polar leakage for 150 GHz and 100 GHz respectively.

These errors can be accounted for in the analysis software if known, suitable polarized and unpolarized sources are studied and if the polarizing efficiency of the detector is known. Typically it is found to be  $> 99.9\%$

### 2.1.6 PSB FAILURES

There are a number of reasons why a PSB might fail during an observation. If a bad set of transistors are used there will be random discrete jumps in voltage in an effect called ‘popcorn’ noise. Bad wire bonding may mean the electrical connection open during thermal cycling, or any connection between the two PSBs in a pair will cause a thermal short and a high measured cross polar leakage. Cosmic ray hits and glitches in the PSBs are recorded with the data so they may be accounted for in the data analysis.

### 2.1.7 CRYOGENICS

Instrumental thermal noise is reduced through the cooling of detectors. This is accomplished via a cryostat consisting of two toroidal tanks. The outer is filled with liquid nitrogen at 77K and the inner with liquid helium at 4K. Between each stage there is a vacuum

shield minimizing thermal losses and the outer tank itself provides a shield for the colder inner one. A three-stage sorption fridge is then used for cooling to 250mK. Cryopumps cool liquid helium (both  $^3\text{He}$  and  $^4\text{He}$ ) by reducing vapour pressure at the surface. Each day the cryogens are refilled, the fridge is cycled and any routine maintenance in the cryogenic systems is carried out. The bias circuit, which passes a current through the thermistor and resistor ensuring a constant current such that only the voltage is altered with the incoming radiation, is housed within the cryostat. A read-out circuit passes the voltage measurement onto the warm electronics where its signal is amplified, filtered and demodulated. The DC offset is removed and then a digital signal is produced which can be stored.

### 2.1.8 CALIBRATIONS

It is imperative that the data acquired from QUaD may be compared with that from other experiments, and also that within the QUaD experiment itself, data from each detector must be comparable with all the others. This requires two types of calibrations to be performed; relative - those within the experiment, and absolute - in order to convert the outputs into real thermodynamic temperatures that permit such comparisons.

Sensitivity is affected by both atmospheric absorption and emissions, so QUaD carried out various calibrations each day to quantify these effects. A measure of the atmosphere, optical depth  $\tau$ , characterizes how opaque it is to radiation. Optical depth is defined as:

$$d\tau = \kappa\rho dz \quad (2.4)$$

in which  $\kappa$  is the opacity of the medium, in this case the atmosphere,  $\rho$  is its density and  $z$  is the optical path.  $\tau$  is then found by integrating along the line of sight. Transmission through the atmosphere at a particular frequency,  $\nu$ , varies with zenith angle (angle around from straight up) according to a decreasing exponential function with optical depth as the constant:

$$Tr_{atm,\nu} = e^{-\tau_\nu A} \quad (2.5)$$

Airmass,  $A = \sec \theta$ , with  $\theta$  the zenith angle is the path through the atmosphere. Working down from zenith the optical loading increases, becoming infinite along the horizon. (This is a somewhat simplified model, realistically things become more complex below about  $\theta = 60^\circ$ .) The apparent brightness of an astronomical source therefore decreases accordingly as the telescope is tipped down. The total load temperature on the telescope is given by:

$$T_{load}(\theta) \approx T_{tot} + \tau T_{atm} \sec \theta \quad (2.6)$$

where  $T_{tot}$  is a constant total temperature offset incorporating both loading from the telescope and the non-varying component of the atmosphere. This equation tells us that  $\tau$  and  $T_{atm}$  are inseparable. At the South Pole in an adjacent building there is a tipper which measured optical depth every 12.7 minutes at a wavelength of  $350\mu\text{m}$ , along with the atmospheric temperature at the time,  $T_{atm}$ . Because values of  $\tau$  are very large at this wavelength the two values are able to be determined separately in this case and every two hours independent data is reported. QUAD measured  $\tau T_{atm}$  by performing a sky-dip. Once a day the telescope was tipped to a known elevation, the atmospheric emission as a function of zenith angle measured using the tipper's  $T_{atm}$  data to break the degeneracy in equation 2.6, and the properties of the bolometers deduced. Such measurements could then be used to recalibrate the bolometers and compensate for their overall gain drifts due to changes in the weather or elevation angle. Slightly more variation occurs with 150 GHz detectors as they are more affected by a water vapour line at 182 GHz.

To counter any mismatch in the gain between two bolometers in a pair we conducted a simple, quick and well-understood calibration called an elevation nod. This calibration is necessary because in the analysis the signals from the two bolometers are summed and differenced to give temperature and polarization time series respectively, and any gain difference would appear as spurious signal. After every 5 scans of the CMB a sky-dip of  $1.35^\circ$  was executed and the subsequent change in airmass generated a 1V signal according to:

$$\frac{\partial T_{load}}{\partial \theta} \propto \frac{\partial \sec \theta}{\partial \theta} = \sec \theta \tan \theta \quad (2.7)$$

Thus for a small change in angle at a zenith angle  $\theta \lesssim 50^\circ$ , the change in airmass becomes proportional to the change in optical loading with a constant of proportionality  $g_{ed}$ :

$$\delta T_{load} \approx g_{ed} \sec \theta \quad (2.8)$$

The elevations are recorded during the nods and corrections applied to account for the offsets of each particular PSB on the focal plane array. The airmass at each of these elevations can then be found. A line is fit to the bolometer time series during the nod expressed as a linear function of the airmass. The slope of this linear fit gives the constant of proportionality; the relative gain of the bolometer.

Separate fits are made for the up and down parts of the elevation nod and so as not to include regions during which the telescope is accelerating the first and last 200 readings are neglected. The average of these two slopes is then computed and the average of all the

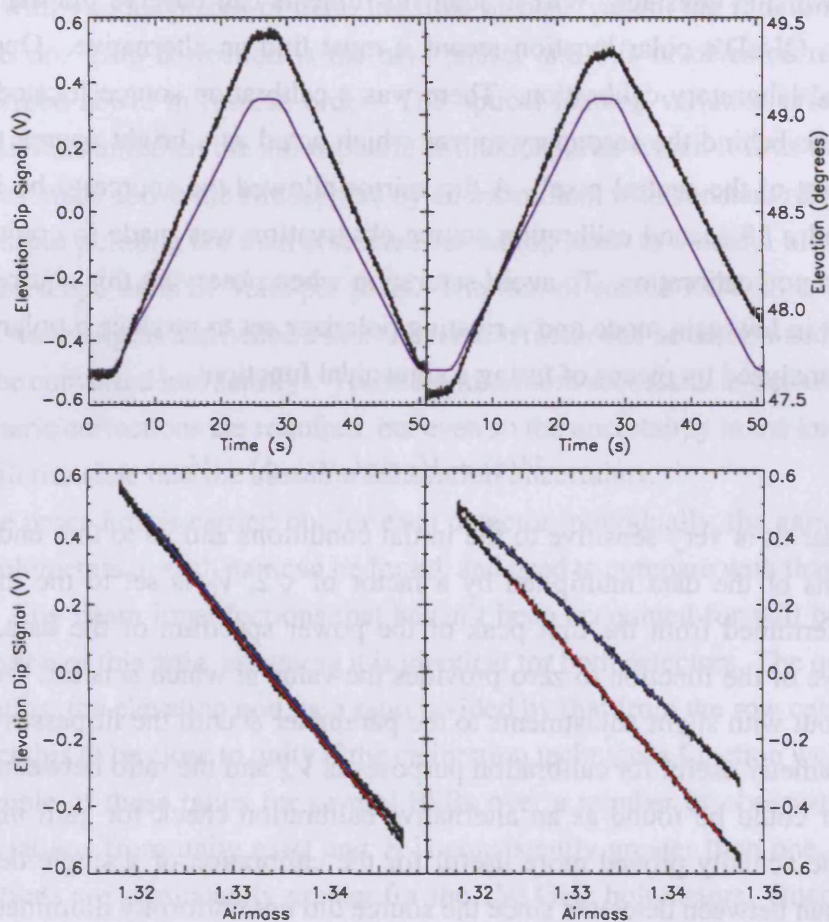


Figure 2.4: Time Series for the Elevation Nodes

The upper panel shows the bolometer voltage measurements along with the elevation at each time in blue. Below is the same bolometer voltages plotted as a function of airmass with a linear fit applied (Zemcov, 2006).

elevation nodes carried out each day for a particular PSB. The A/B gain ratio of a bolometer pair was then found by dividing the average from one PSB by the other in the pair. The detector gain ratios on the whole were found to be fairly stable in the short term except in instances of very bad weather, but over longer time some of the channels demonstrated ramping, as in the right hand side graphs of Figure 2.4. Such bolometers experienced a decrease in responsivity, possibly due to a poor thermal connection with the heat sink, after each reset of the bias current. In general these detectors were simply excluded from the final analysis. Again, for the same reasons as above, we found there to be less stability with the 150 GHz bolometers.

The voltage measurements QUaD recorded need to be converted into flux by means

of a conversion constant. Whilst other instruments can observe planets to calibrate this constant, QUAD's polar location meant it must find an alternative. One option was an analytical laboratory calibration. There was a calibration source located inside QUAD's foam cone behind the secondary mirror which acted as a bright source to determine the gain offset of the central pixel. A flip mirror allowed the source to be injected into the beam and a 10 second calibration source observation was made in conjunction with the elevation nod calibration. To avoid saturation when observing this source the bolometers were put in low gain mode and a rotating polarizer set to produce a polarization vector at 1.7 Hz, analyzed by means of fitting a sinusoidal function:

$$V(t) = V_A \sin(\omega t + \phi) + V_0 \quad (2.9)$$

The linear fit is very sensitive to the initial conditions and so to that end  $V_A$  is set to the mean rms of the data multiplied by a factor of  $\sqrt{2}$ ,  $V_0$  is set to the mean of the data,  $\omega$  is determined from the first peak of the power spectrum of the data, and setting the derivative of the function to zero provides the value at which  $\phi$  is set. Iterations are then carried out with slight adjustments to the parameter  $\phi$  until the fit passes a statistical test. The parameter useful for calibration purposes is  $V_A$  and the ratio between two bolometers in a pair could be found as an alternative calibration check for gain mismatches. This technique actually proved more useful for the calibration of a single detector over time rather than between detectors since the source did not uniformly illuminate the focal plane each bolometer would have seen something slightly different. The polarizer also reflected up to 40% of the light, so to a certain extent the detectors were seeing themselves.

Another part of QUAD's daily routine was the row calibration. Four times a day each of the seven rows of the focal plane were scanned back and forth across a bright source called RCW38 giving two blips in the time series. If there were no atmosphere and both the source and telescope were ideal there would be a constant integral under each blip. Nevertheless the blips are affected by the atmosphere, the telescope beam pattern and by any complex structure surrounding the source. On top of adding noise to the data, the atmosphere creates a varying optical load changing the responsivity of the bolometers, and also extinguishes some of the source flux. The telescope's pointing needs to be accurate so that it passes over the middle of the source and the brightness of the main lobe of the source isn't suppressed. The exact shape of the blip is determined by the telescope beam shape. Working backwards through a three stage process these factors can be undone to yield a model image of the source which is then used for absolute calibrations.

The first part is blip extraction in which the blips are initially located and then fit to a one dimensional Gaussian. The heights and widths,  $V_{blip}$  and  $\sigma_{blip}$ , of the fits are

recorded along with various pieces of data; the time of observation, the rotation angle of telescope and so on. Blip correction is the next phase, and this involves correcting for the effects described above in reverse order. The optical loading variation affecting the detector responsivities and then the atmospheric extinction, after which it is as though the measurement was made above the atmosphere by an instrument with constant responsivity. The beam shape and pointing are then corrected for which leads to a model of the image normalized to telescope units of Volts per pixel. The flux of source RCW38 is known at both of QUaD's wavelengths and hence a flux conversion factor can be determined allowing a time series to be converted into Janskys. The method is more successful at 100 GHz where smaller atmospheric corrections are required, but even so the uncertainty in the known flux, at about 10% will translate into the absolute calibration uncertainty.

Since the procedure is carried out for each detector individually, the gain ratio between the two bolometers in each pair can be found, and used to compare with that from the elevation nods. Any beam imperfections that haven't been accounted for will be divided out upon calculation of this ratio, assuming it is identical for both detectors. The quantity  $R$  is the ratio of ratios; the elevation nod gain ratio divided by that from the row calibrations. We would expect this to be close to unity if the calibration techniques function well. Figure 2.5 shows a sample of these ratios for several PSBs over a number of observation days. We see that deviations from unity exist and  $R$  is consistently greater than one. Furthermore, the deviations are significantly greater for the 150 GHz bolometers. Quantitatively these deviations are of order  $\sim 5\%$  for 100 GHz and as high as 15 – 18% in the 150 GHz bolometers.

There are several potential explanations for the difference between the calibration results. Since the optical chains are identical the differences must therefore arise within the horn bolometers and the horns themselves. Bolometers operating at both frequencies are affected by the various sources of noise described previously. Also the analysis assumes the beams are identical in both members of a pair but in reality there may be some mismatch. If there is a warp in the primary mirror this would cause an asymmetry in QUaD's optics, although the feedhorns should ensure that the detectors do not suffer from this optical aberration. There could also be some birefringence (splitting of light into two unequal waves) in the polyethylene lenses. This asymmetry is difficult to quantify since it is the result of plastic imprinting as it cools. Perhaps therefore neither of these calibration techniques are ideal for absolute calibrations and are better suited for internal consistency checks.

The method by which the most accurate attempt at determining an absolute calibration factor is through the comparison of QUaD's results with those from other experiments after maps have been made. The sun moves around the galaxy creating a dipole in the CMB from the doppler shift of its motion. The FIRAS instrument on COBE measured this dipole

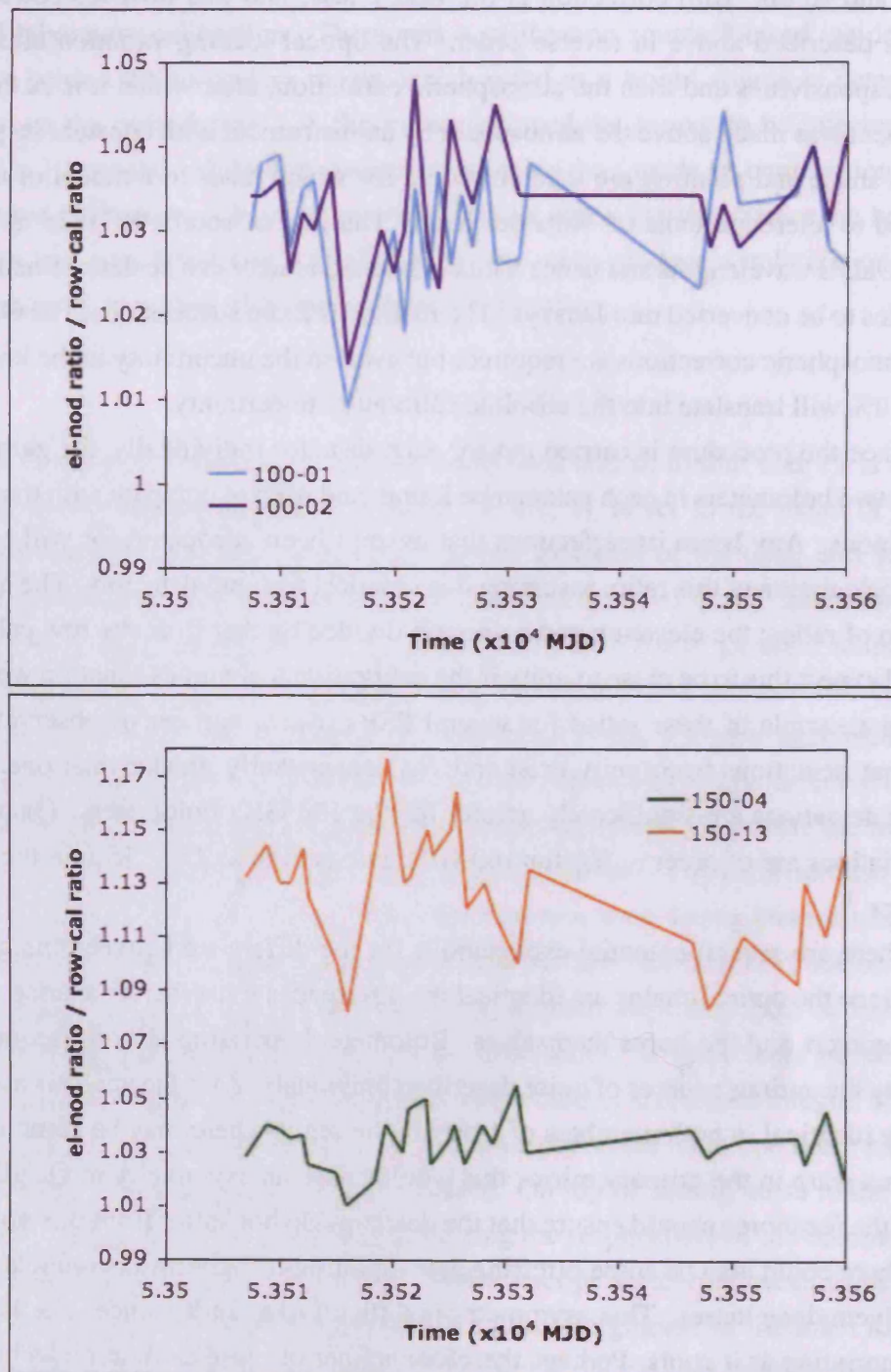


Figure 2.5: Calibration Comparison

Ratio between the elevation nod and row calibration techniques for 100 GHz PSBs (top) and 150 GHz PSBs (bottom).

to be  $3.369 \pm 0.004$  mK (Fixsen et al., 1996). QUaD, because its observation patch of sky is so small, is unable to directly measure the dipole and calibrate accordingly but WMAP and other experiments are able to make use of the dipole for their calibration. Hinshaw et al. (2003) reported an uncertainty of 0.5% in the absolute calibration of WMAP based upon this method. In principle QUaD's maps could then be compared with those of WMAP and calibrated accordingly, but again because WMAP maps the entire sky with a large angular resolution and QUaD surveys less than 1% of the sky there is only a very small overlap in  $\ell$  space. BOOMERanG's B03 145 GHz maps were calibrated to an accuracy of 1.8% with WMAP (Masi et al., 2006) and so QUaD can be calibrated via these which are of intermediate survey size and angular resolution, and hence cover a similar  $\ell$  range.

Combining several calibration techniques is no doubt the best way to ensure no major errors have occurred and to check things are self-consistent. Altogether they permit the instrument to make measurements of the CMB with many detectors which can all be translated into comparable data in Volts, which can subsequently be converted into Kelvin and compared alongside results from other experiments.

## 2.2 QUAD OBSERVATIONS

### 2.2.1 OBSERVING STRATEGY

At the South Pole every 24 hours the celestial sphere rotates about the zenith. The observations were therefore organized such that each day they began at a fixed Local Sidereal Time (LST) just after the chosen field had passed the laboratory building. The region of sky selected for QUaD observations was an area of approximately 60 square degrees directed away from known dusty regions and the Galactic plane. Its partial overlap with the *B2K* field allowed for the absolute calibration technique described in section 2.1.8 and the 3 point sources contained within permitted other calibrations to be conducted. The size of the region was a compromise between high signal-to-noise ratio and good sensitivity to the low- $\ell$  region.

The observations were divided into two 8 hour blocks with various special calibration tests run immediately before and after. Between the blocks the entire telescope was rotated through a 'deck angle' of  $60^\circ$ , from  $-3^\circ$  to  $57^\circ$ , about the line of sight and there was a half hour break to allow thermal stabilization. To this end 19 hours each day were spent completing this observation schedule and the remaining time was used for fridge cycling.

These two 8 hour blocks were then split into 16 half hours. At the start of each half hour the internal calibration source was observed and an elevation nod performed. The observing field is cut into two adjacent equal areas called the lead and trail field. For

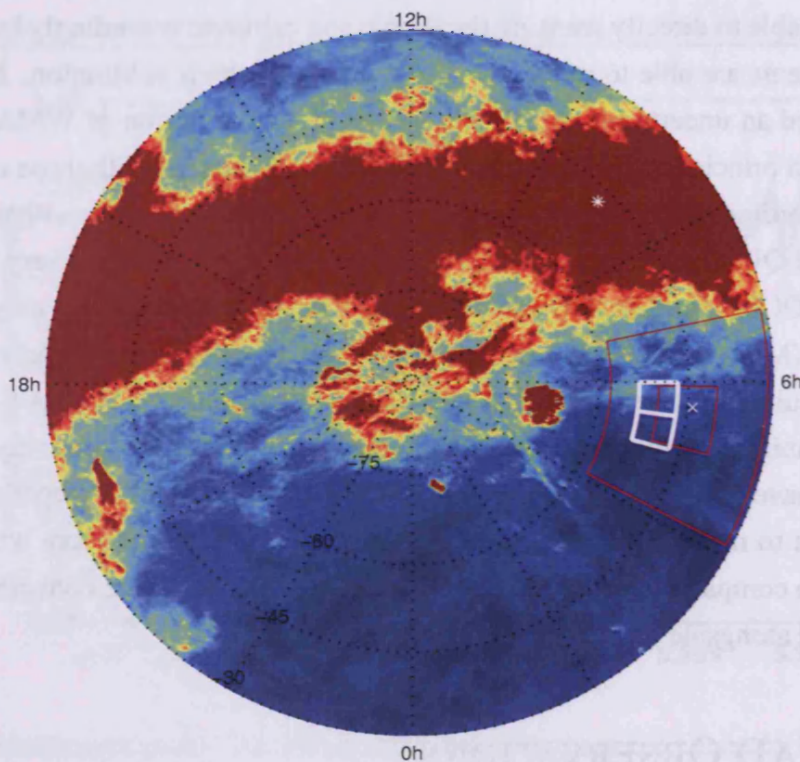


Figure 2.6: QUaD's Observing Region

The white boxes are the two fields QUaD observed shown on a 150 GHz dust map (Finkbeiner et al., 1999) along with the B03 regions and the locations of point sources RCW38 (asterisk) and *PKS0537 – 441* (cross).

the first half hour the telescope would scan back and forth five times across the lead field, be stepped up by  $0.02^\circ$  in declination and the process repeated four times. This amounted to 40 half-scans each of 30 seconds. Then an identical set of observations would be made during the next half hour, but this time of the trail field. In this way by subtracting the lead and trail field data any signal coming from the ground which is constant over the half hour will cancel.

For the eight hour block the observations continued in this manner, increasing in declination so that a  $0.64^\circ$  region was covered. The declination was reset before the second block at the alternative deck angle was commenced. The next day an adjacent  $0.64^\circ$  region would be observed until the entire survey area had been covered. This was all repeated over and over with a slight offset in declinations such that the joins were not in the same place each time and no sections were uncovered on account of bad weather or telescope malfunctions.

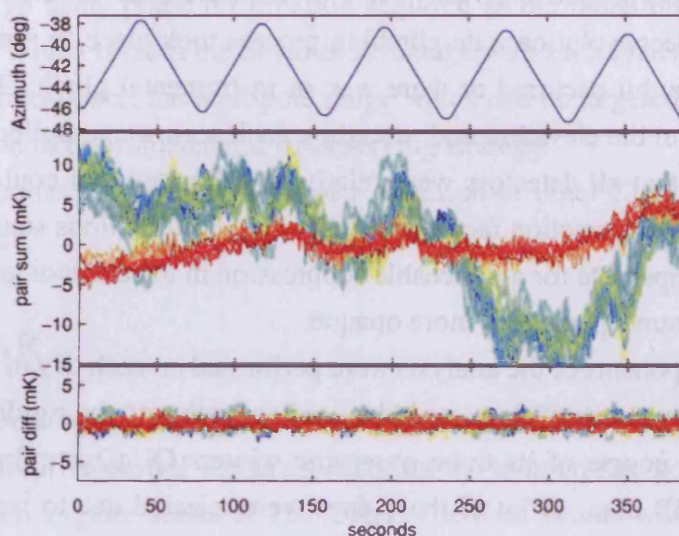


Figure 2.7: Observing Strategy and Timestream Data

The top panel shows how QUaD scans back and forth in azimuth over 30 second periods. This gives TOD streams at both 100 GHz (red/orange) and 150 GHz (blue/green) which amongst the pairs of PSBs leads to summed (middle panel) and differenced (bottom panel) data. A relative gain calibration has been applied along with a scaling to temperature units and a low pass filter to  $< 1$  Hz (Pryke et al., 2009).

### 2.2.2 LOW LEVEL DATA PROCESSING

The data analysis procedure followed is referred to as a pipeline and within this pipeline there are three distinct stages. Map-making and the construction of power spectra from them, and parameter estimation and its interpretation in a cosmological context follow on from the first stage of preprocessing the time ordered data (TOD) stream.

Section 2.1.2 described the non-instantaneous response of the bolometers to the changes in the incident optical power and hence the initial step in the data reduction process was a deconvolution of the detector time constants. The dual time constant model was used to undo the detector response function and its associated filtering effects, and recover the original data waveform. Those detectors which do not fit the model well, along with a couple of others which also misbehave, were rejected from the analysis at this stage. 9 out of 12 100 GHz bolometers remained with 18 out of the 19 150 GHz ones.

During each scan the telescope moved across with a constant velocity after an initial acceleration, then a deceleration before turning around and performing the process in reverse to scan back to the original position, as illustrated in Figure 2.7. Only the data recorded during the constant velocity phases of the scanning are retained because there is spurious signal generated by the accelerations. 600 samples were taken per scan, decimated

from a rate of 100 per second since only every 5<sup>th</sup> measurement was significantly different.

After the deconvolution a de-glitching process took place to remove scans during which a cosmic ray hit occurred or there was an instrumental glitch. The normalization factors derived from the elevation nod preceding each scan were applied to the half-scans individually such that all detectors were relatively calibrated and could be analyzed together. An additional correction factor derived from the calibrations source measurements was applied to compensate for a noticeable suppression in the detector gains during poorer weather when the atmosphere was more opaque.

These components of the analysis were performed on each day of data separately so that after this different sets of days could be used according to the rigidity of the rejection criteria. Over the course of its three observing winters QUAD acquired more than 300 days worth of CMB data. A lot of these days were rejected due to very bad weather or instrumental problems. A further set of days were rejected because of moon contamination creating stripes in the maps. After these cuts 67 days were used from the 2005 season to provide a first set of data published in Ade et al. (2008) and 143 days which led to the second and third season spectra in Pryke et al. (2009). The data have not been combined into 210 day set because between the first and second season there was re-focussing of the telescope, some faulty bolometers were replaced and the scan strategy changed slightly.

The map-making and power spectrum techniques used in the analysis of the data leading to these papers is described in the next chapter. Firstly though I will briefly review some other CMB instrumentation.

## 2.3 OTHER INSTRUMENTS

There are a variety of instruments designed to measure both the temperature and polarization of the CMB; some currently in operation, some under construction and others planned for the future. The nature of the detection differs for each according to the frequency range desired. While bolometers may be the most suitable for the high frequencies at which QUAD observed, for lower frequencies the instruments make use of coherent systems borrowing radio astronomy techniques. The latter measures both phase and amplitude whereas bolometers only measure the total intensity. Also the detectors used can operate at room temperature, and even the amplifiers can work at 20K, much higher and therefore easier to attain than the 300mK needed for bolometers. Polarimetry is carried out by splitting the incoming radiation with an orthomode transducer or a polarizing grid (better for higher frequencies) into orthogonally polarized components. Interferometers, used a great deal in radio astronomy, can be formed by coherent systems. A pair of telescopes combine the

signals they receive using phase information acquired as the radiation reaches each telescope separately. Whilst there is the obvious advantage with such systems of a much better rejection of the atmosphere, the multipole range which can be targeted may be limited by the baselines of the interferometer and its observing strategy.

Here are some short descriptions of a selection of other CMB experiments, past, present and future:

### 2.3.1 ACBAR

The Arcminute Cosmology Bolometer Array Receiver (ACBAR) operated at the South Pole for five consecutive austral winters measuring the temperature power spectrum very accurately on small angular scales at 150 GHz. The final results were published in Reichardt et al. (2009a).

Website:- <http://cosmology.berkeley.edu/group/swlh/acbar/>.

### 2.3.2 BOOMERANG

BOOMERanG (Balloon Observations OF Millimetric Extragalactic RAdiation aNd Geophysics) was a balloon-borne experiment, which flew around the Antarctic in 1998, initially measuring the peaks in the CMB temperature power spectrum. The flight has since been repeated (in 2003) after the instrument was upgraded with PSBs and polarizing wire grids. A good detection was made of the  $E$ -mode fitting with existing measurements and models (Montroy et al., 2006). This was the first time a detection of polarization was made using bolometers, boding well for QUaD and other such experiments also conducting bolometric polarimetry.

Website:- <http://cmb.phys.cwru.edu/boomerang/>

### 2.3.3 CBI

The Cosmic Background Imager (CBI) is a 13 element 30 GHz interferometer situated in Chile, observing on small angular scales ( $400 < \ell < 3000$ ) by means of large baselines. Again this was originally a temperature experiment upgraded to make polarized observations (Readhead et al., 2004) which provided strong  $E$ -mode detections consistent with those from other experiments. The latest results from Sievers et al. (2009) have combined five years of observations into a single temperature power spectrum.

Website:- <http://www.astro.caltech.edu/~tjp/CBI/>

### 2.3.4 DASI

QUaD's predecessor at the South Pole mount was the first instrument to detect the polarization of the CMB (Kovac et al., 2002) using 13 feed-horns in an interferometric array operating from 26 GHz up to 36 GHz. Initially built as a small scale temperature experiment, waveguide polarizers were inserted to allow measurements of  $E$ -mode polarization too.

Website:- <http://astro.uchicago.edu/dasi/>

### 2.3.5 MAXIPOL

MAXIPOL is another balloon-borne experiment and the first to use a rotating half-wave plate to measure polarization. This additional apparatus was added onto the experiment MAXIMA (Millimeter-Wave Anisotropy eXperiment Array) which had measured temperature anisotropies (Balbi et al., 2001). After surveying an area of 8 square degrees with 12 polarimeters centered around 140 GHz and analyzing up to  $\ell \sim 700$ , it found weak evidence for an  $E$ -mode power consistent with standard cosmology (Wu et al., 2007).

Website:- <http://groups.physics.umn.edu/cosmology/maxipol/>

### 2.3.6 WMAP

Eight years after its launch the latest results from the Wilkinson Microwave Anisotropy Probe (WMAP) reported in Hinshaw et al. (2009) incorporate five years of data. It uses differential radiometers which measure the difference between two telescope beams, from 1.4 and 1.6 primary mirrors sat upon a 5m diameter solar panel keeping it in the shadows. Operating in space at L2, WMAP surveys the whole sky in five discrete radio frequency bands spanning 23 GHz to 94 GHz. The first data release in 2003 (Hinshaw et al., 2003) was simply temperature, but since then WMAP has gone on to take polarization measurements as well, with many improvements to the analysis along the way and it probably provides the most accurate data we have of the CMB on large angular scales ( $\ell < 1000$ ), at least until Planck's results are announced.

Website:- <http://map.gsfc.nasa.gov/>

### 2.3.7 PLANCK

Planck is a satellite with a similar sensitivity and the same detectors as QUaD, launched in May 2009. It is designed to map the entire sky (except for the galactic plane) and hence will measure down to low multipoles like WMAP. By using both PSBs and HEMT



Figure 2.8: WMAP

The WMAP spacecraft.

(Image: NASA - <http://map.gsfc.nasa.gov/resources/wmapsc.html>)

(High Electron Mobility Transistor) amplifiers, Planck will be able to work over a range of frequencies, from 30 GHz all the way up to 353 GHz.

Website:- [www.esa.int/planck/](http://www.esa.int/planck/)

While Planck may be able to measure the  $E$ -mode power spectrum to a similar degree of accuracy as that currently known of the temperature power spectrum, the next big challenge facing CMB cosmologists is measuring the  $B$ -mode signal. This will require advances in detector power as a far greater sensitivity is needed. A number of experiments are being planned to undertake this goal, although unfortunately due to the current economic situation the major UK  $B$ -mode project, Clover (North et al., 2008), has had to be cancelled.

### 2.3.8 SPIDER

A balloon-borne experiment planned to fly from Australia in 2010, Spider has been designed to study the CMB polarization with six telescopes at frequencies ranging from 70 GHz to 300 GHz and large format bolometer arrays (Crill et al., 2008).

Website:- [http://palquest.org/~lgg/spider\\_front.htm](http://palquest.org/~lgg/spider_front.htm)

### 2.3.9 QUIET

A proposal to upgrade CBI with an array of about 1000 polarimeters which will take measurements of  $Q$  and  $U$  simultaneously at 40 and 90 GHz, the  $Q/U$  Imaging Experiment (QUIET) aim will be to measure the  $B$ -mode spectrum over a multipole range  $40 < \ell < 2500$ .

Website:- <http://quiet.uchicago.edu/>

There are many others which have all contributed to a greater or lesser extent to our present knowledge of the CMB, along with lots of proposals for future experiments, some of which will see light, potentially adding to our current understanding of the field, perhaps even revolutionizing the cosmological theories entirely.

## 3 ANALYSIS

---

“THE REAL GOAL OF PHYSICS IS TO COME UP WITH AN EQUATION THAT COULD EXPLAIN THE UNIVERSE BUT STILL BE SMALL ENOUGH TO FIT ON A T-SHIRT.”

LEON LEDERMAN

### 3.1 MAPS

After the low-level processing the next stage in the data analysis pipeline is that of making CMB maps from the timestream. Chapter 2 described the lead-trail scheme employed in the scanning strategy which permits removal of the ground pickup by field differencing. An alternative method also investigated with QUaD data is that of ground template removal. Regardless of the technique used it is imperative that the map-making procedure begins by a mitigation against the ground contamination otherwise it produces obvious artifacts in the maps.

#### 3.1.1 FIELD DIFFERENCING

In the field differencing process the assumption is made that the ground signal, whilst obviously changing over longer periods of time, is constant on half hour timescales to a sufficiently accurate level. The differencing is carried out on a point by point basis subtracting each half-scan from its partner a half hour later leaving a timestream which is, in principle, clean of ground pickup. Since we expect the CMB to be a Gaussian random field the power spectrum which will result from a differenced field is simply twice that of the non-differenced field. Whilst highly successful in removing the ground signal, and not changing the signal-to-noise, the disadvantage to this method is that the effective sky area is halved and this creates an increase of  $\sim 40\%$  ( $\Delta C_{fd} = \sqrt{2}\Delta C_{nfd}$ ) on the uncertainties of the power spectrum measurements on all angular scales.

### 3.1.2 GROUND TEMPLATE REMOVAL

In addition to the lead-field scheme providing a means by which to remove the ground contamination, there exists another feature of the observation strategy which can be taken advantage of for ground pickup mitigation. During each scan set the CMB field moves across the sky. There are 6 minutes between the time when a given sky pixel is first visited on the first half-scan of a set to when it is last visited on the tenth half-scan, and the sky rotates by  $1.6^\circ$  during this time. It is therefore possible to separate the signal on the sky which moves around from the signal on the ground which stays put, over scales smaller than  $1.6^\circ$ . Combining the data from both the lead field and the trail field (which will be completely fresh sky but the same ground) adds to the successful achievement of this separation. This is just slightly increasing upon the 30 minute assumption made with the field differencing, by suggesting that the ground signal remains constant over the time from the start of the lead scan-set to the end of the trail scan-set, which is 36 minutes.

We can say that the time ordered data (TOD) is given by:

$$d_i = S_i(\theta) + G(\alpha) + n_i + o_{scan} \quad (3.1)$$

with  $S_i(\theta)$  the sky signal,  $G(\alpha)$  the ground signal as a function of azimuth  $\alpha$ ,  $n_i$  the random noise and  $o_{scan}$  a constant offset for each half-scan. Removing this offset prevents  $1/f$  atmospheric noise dominating when the ground templates are constructed. This offset is found simply as the mean of the data within each scan, from the region where all the half-scans overlap. The ground is divided up into azimuth bins and the ground templates then come from summing all the data from both the lead and trail scan-sets which fall into each bin. The sums per bin are then normalized by dividing by the number of times each bin is hit during the scan, see Figure 3.1. The size of these bins does not seem to perceptibly alter the ultimate maps indicating that the ground varies quite smoothly in azimuth. It was set at  $0.1^\circ$ . Obviously these sums contain signal from both random noise and the CMB as well as the ground. For perfectly random noise and an ideal scan strategy these terms would average to zero, but instead the filtering of the CMB and noise signal this method introduces are taken into account later.

The templates are subtracted from the TOD to leave a timestream that should be free from ground contamination and the map-making process continues in the same way as that for the field differenced timestream.

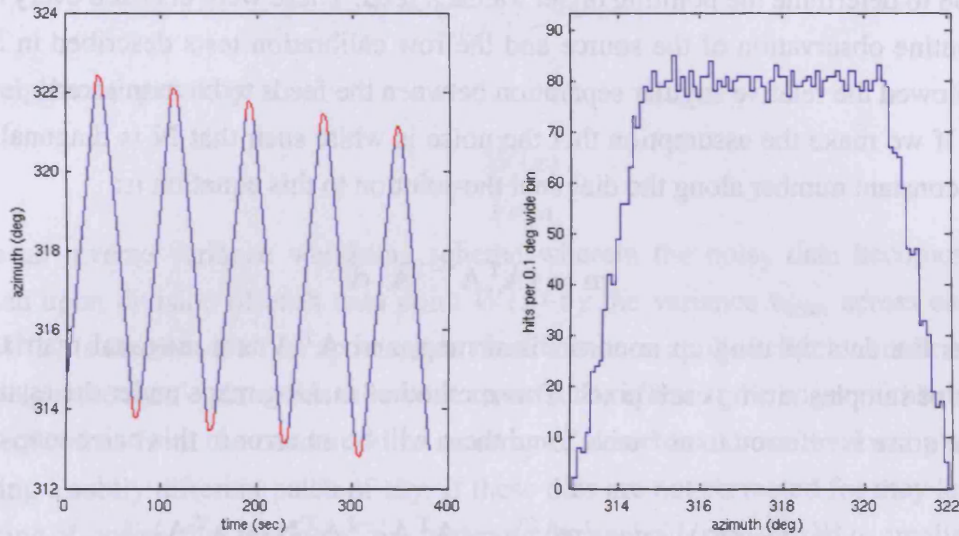


Figure 3.1: Ground Subtraction Technique

On the left we see how the sky rotates slightly between each half-scan allowing data from several scans falling into a particular azimuth bin on the ground to be collected together forming a template. The right hand plot shows the number of constant velocity (blue) hits each  $0.1^\circ$  azimuth bin received each scan.

### 3.1.3 MAP-MAKING

Whatever the means by which the TOD is cleaned from ground contamination the same procedure and map-making equations will now apply. The process begins with the subtraction of a polynomial (typically of third order) from each half-scan for each bolometer whilst using a source mask to hide any bright point-like sources. In doing this subtraction a substantial amount of atmospheric variation is removed. The maps are constructed on a per day per bolometer basis and later coadded. For each PSB pair the data is both summed and differenced to yield temperature and polarization TOD and so from here on the pipeline bifurcates to produce separate temperature (T) maps, and polarization (Q and U) maps.

The principal equation used is:

$$\mathbf{A}^T \mathbf{N}^{-1} \mathbf{A} \mathbf{m} = \mathbf{A}^T \mathbf{N}^{-1} \mathbf{d} \quad (3.2)$$

$\mathbf{A}$  is a ‘pointing’ matrix indicating the pixel being observed on the sky for each TOD sample.  $\mathbf{N}$  is the noise matrix,  $\mathbf{m}$  the map being made and  $\mathbf{d}$  the input data. The application of the pointing matrix  $\mathbf{A}$  puts the data into pixellized bins. The overall telescope pointing came from a nine parameter pointing model handled by the telescope control computer

and approximately one day each month was devoted to making a map of the bright source *RCW38* to determine the pointing offset for each feed. These were checked every 8 hours by a routine observation of the source and the row calibration tests described in Section 2.1.8 allowed the relative angular separation between the feeds to be monitored.

If we make the assumption that the noise is white such that  $\mathbf{N}$  is diagonal with a single, constant number along the diagonal the solution to this equation is:

$$\mathbf{m} = (\mathbf{A}^T \mathbf{A})^{-1} \mathbf{A}^T \mathbf{d} \quad (3.3)$$

$\mathbf{A}^T$  bins the data creating an unnormalized map, and  $\mathbf{A}^T \mathbf{A}$  is a diagonal matrix of the number of samples hitting each pixel. This method of making maps under the assumption of white noise is referred to as ‘naive’, and there will be an error in this naive map of:

$$\langle (\mathbf{m} - \langle \mathbf{m} \rangle) (\mathbf{m} - \langle \mathbf{m} \rangle)^T \rangle = (\mathbf{A}^T \mathbf{A})^{-1} \mathbf{A}^T \mathbf{N} \mathbf{A} (\mathbf{A}^T \mathbf{A})^{-1} \quad (3.4)$$

For a more complicated map an estimate of the noise power spectrum is needed. The possibilities then include using ‘brute force’, Jacobi solvers or conjugate gradient methods. Having acquired maps, by whichever technique for individual bolometers per day they can then be integrated into one final map,  $\mathbf{c}$ , using:

$$\mathbf{c} = (\mathbf{B}^T \mathbf{s}^{-1} \mathbf{B})^{-1} \mathbf{B}^T \mathbf{S}^{-1} \mathbf{s} \quad (3.5)$$

where  $\mathbf{B}$  is a vector composed of all the pointing matrices:

$$\mathbf{B} = (\mathbf{A}_0, \mathbf{A}_1, \mathbf{A}_2, \dots, \mathbf{A}_{n-1}) \quad (3.6)$$

$\mathbf{S}$  is constructed in a similar way to represent all the noise matrices and  $\mathbf{s}$  is a vector of all the maps:

$$\mathbf{s} = \begin{pmatrix} \mathbf{m}_0 \\ \mathbf{m}_1 \\ \mathbf{m}_2 \\ \vdots \\ \mathbf{m}_{n-1} \end{pmatrix} \quad (3.7)$$

### 3.1.4 TEMPERATURE MAPS

Maps of the CMB temperature are built from the summed data with a simple weighting applied:

$$T = \frac{1}{\sum_i \omega_i} \sum_i \omega_i s_i \quad (3.8)$$

with weights,  $\omega_i$ , given by:

$$\omega_i = \frac{W(x)}{\nu_{scan}} \quad (3.9)$$

This is an inverse variance weighting scheme wherein the noisy data becomes down-weighted upon division of each data point  $W(x)$  by the variance  $\nu_{scan}$  across each half-scan.  $W(x)$  is the data after an apodization mask has been applied. Such a mask serves to downweight the scan ends which otherwise create a tile effect at the edges of the map. The tile effect comes from the coaddition of an array of detectors across the focal plane each observing a subtly different patch of sky. If these tiles are not corrected for they lead to an up-mixing of power, that is power from large angular scales is transferred to smaller scales creating a falsely high level in the damping tail region of the spectrum.

QUaD temperature maps have been produced and published using both the field difference technique (Pryke et al., 2009) and the ground subtraction technique (Brown et al., 2009) at both 100 and 150 GHz. The excellent spatial correlation between the patterns in the maps at the two frequencies is evidence of a very high signal to noise in the maps and three discrete sources showed up weakly detected in the maps.

There are two different ways in which the maps may be presented. The first is a straightforward flat sky approximation pixelizing the sky on a two dimensional cartesian grid of 1.2 arcmin pixels. The other, used throughout my work, employs a pixelization scheme called HEALPix (Górski et al., 2005) to show the maps with the correct degree of spherical curvature for the declination at which the observations were made. The acronym HEALPix stands for Hierarchical Equal Area isoLatitude Pixelization; a clever system designed to divide the sphere up into equal regions according to the desired resolution. The grid of pixels is then set up such that the centres form rings at constant latitude and they can be numbered in either rings or nests depending on what you are trying to achieve with the software. The resolution is described by a parameter  $N_{side}$  where the number of pixels over the sky is then given by  $12N_{side}^2$ . QUaD's maps were made using a resolution of  $N_{side} = 2048$  which means the whole sphere is divided into 50, 331, 638 equally big pixels of size 1.7 arcmin.

### 3.1.5 POLARIZATION MAPS

The process of producing polarization maps is a little more involved than that for the temperature ones; equation 3.2 requires some modification to incorporate the polarization data.

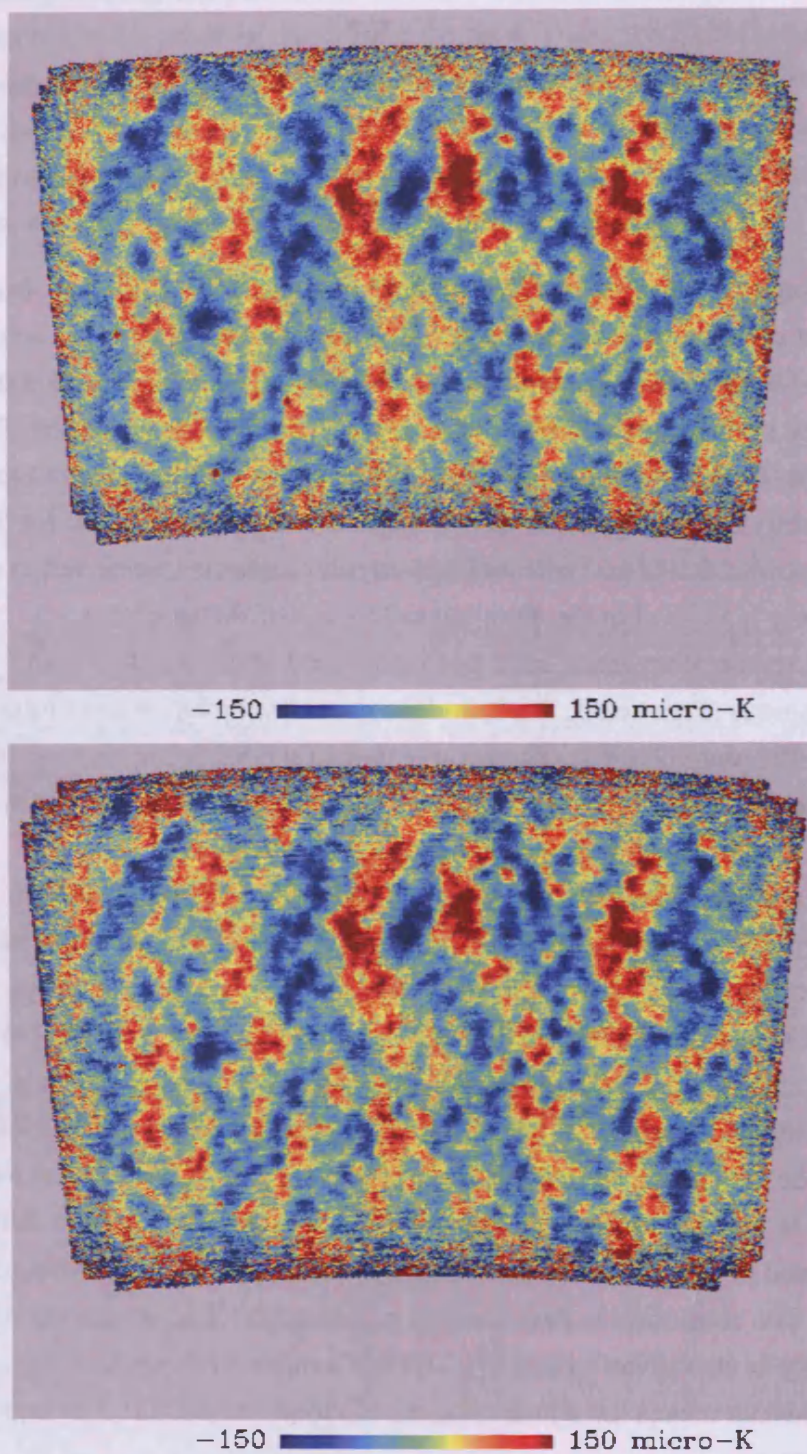


Figure 3.2: Temperature Maps

Since the ground subtraction technique is an improvement upon that of field differencing, with double the effective sky area and the fact that the sky is actually curved, it could be argued that the best maps are the HEALPix ones from the template removal method. (100 GHz top and 150 GHz bottom)

The simplest way is by merely making maps using the difference between detector pairs separately for each telescope rotation angle and bolometer orientation since they are linear combinations of  $Q$  and  $U$ . Without the assumptions of the PSBs being aligned perfectly at  $90^\circ$  or cross polarization being zero, however, the map-making depends on some more complex mathematics. The angle between bolometer  $A$  and its pair  $B$  is  $\pi/2 + \delta\alpha_h$  for a particular horn,  $h$ . The cross-polar leakage, if the cross polarization is  $\epsilon_{h,d}$  for detector  $d$  in horn  $h$ , is given by:

$$\gamma_{h,d} = \frac{1 - \epsilon_{h,d}}{1 + \epsilon_{h,d}} \quad (3.10)$$

This cross polar leakage is not temperature to polarization leakage, but rather a small loss of efficiency in measuring the polarization by means of pair differencing arises because of slight misalignment. The effective angle of the bolometer is defined as:

$$\tan(2\beta_h) = \frac{(\gamma_{h,A} - \gamma_{h,B}) \sin(\delta\alpha_h)}{(\gamma_{h,A} + \gamma_{h,B}) \cos(\delta\alpha_h)} \quad (3.11)$$

The effective angle is added to the nominal angle  $\alpha_h$ , resulting in a nominal polarization angle of  $a_h = \alpha_h + \beta_h$ , since half of the difference is assigned to each leg of the pair.

Chi-square statistics can be used as a measure of fitness to the theoretical expected data. It is defined from the difference maps,  $M_{h,\alpha_h}$ , as:

$$\chi^2 = \sum_{h,\alpha_h} \omega_{h,\alpha_h} (M_{h,\alpha_h} - Q \cos(2a_h) - U \sin(2a_h))^2 \quad (3.12)$$

In this equation,  $\omega_{h,\alpha_h}$  is a weighting function, a characterization of the importance of each map. The same inverse variance,  $1/\sigma^2$ , weighting as for the temperature can be used, or alternatively the weights can be uniform such that all the maps are weighted equally or set to zero to ignore a map. The weights are normalized to total unity. In order to find the values of  $Q$  and  $U$  for each pixel  $p$  that best fit the difference map, the chi-squared function can be differentiated with respect to both  $Q$  and  $U$  and then each set to zero. Combining the two equations obtained by this procedure and rearranging to determine  $Q$  and  $U$  gives a  $2 \times 2$  matrix, as detailed in Appendix A:

$$\begin{pmatrix} Q_p \\ U_p \end{pmatrix} = \begin{pmatrix} \sum_{h,\alpha_h} w_{h,\alpha_h} \cos(2a_h) \cos(2a_h) & \sum_{h,\alpha_h} w_{h,\alpha_h} \cos(2a_h) \sin(2a_h) \\ \sum_{h,\alpha_h} w_{h,\alpha_h} \sin(2a_h) \cos(2a_h) & \sum_{h,\alpha_h} w_{h,\alpha_h} \sin(2a_h) \sin(2a_h) \end{pmatrix}^{-1} \times \begin{pmatrix} \sum_{h,\alpha_h} w_{h,\alpha_h} \cos(2a_h) M_{h,\alpha_h,p} \\ \sum_{h,\alpha_h} w_{h,\alpha_h} \sin(2a_h) M_{h,\alpha_h,p} \end{pmatrix} \quad (3.13)$$

The exact weighting scheme used is of less importance for the polarization maps compared to that of the temperature case in equation 3.8 because the vast majority of the atmospheric noise is removed by differencing the data from PSB pairs. The tiling edge effects due to the overlapping sky coverage are also less apparent with polarization.

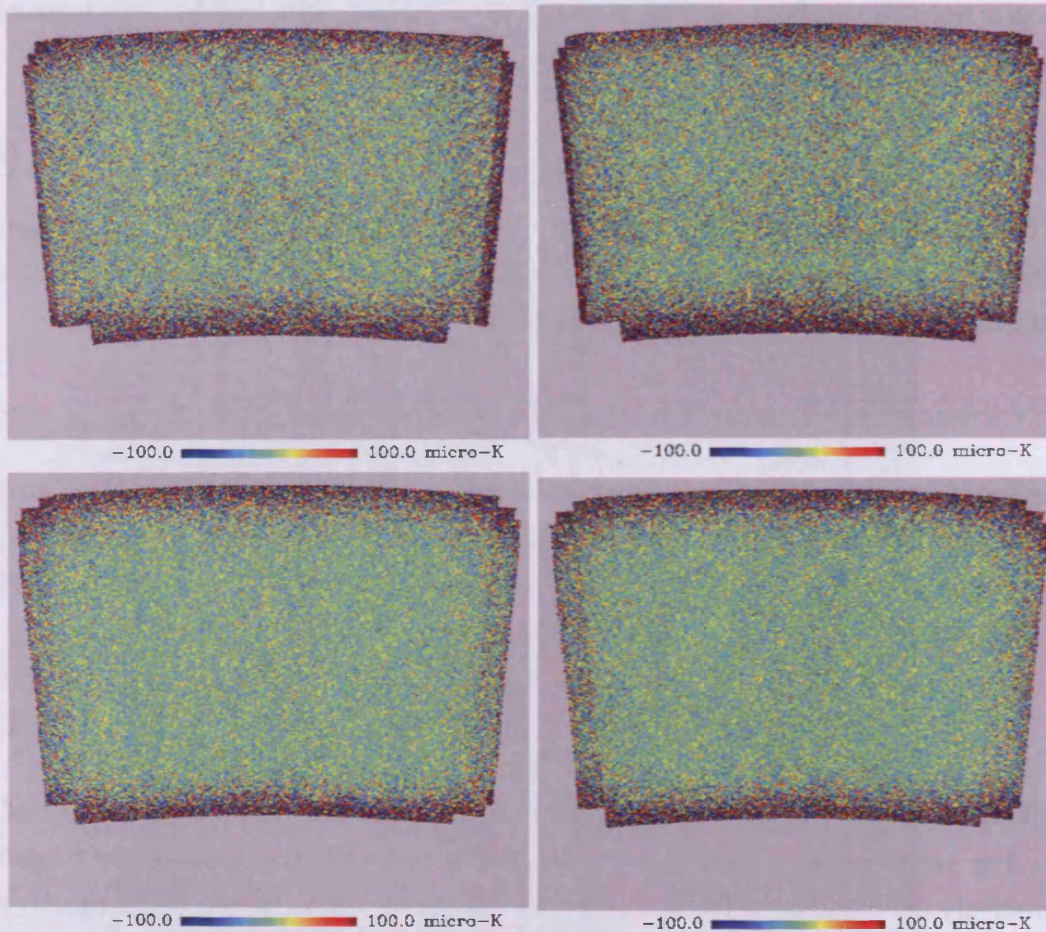


Figure 3.3: Polarization Maps

Whilst no polarization structure is visible to the naked eye in these  $Q$  (left) and  $U$  (right) maps, there is a great deal of polarized CMB hidden amongst the noise. (100 GHz top and 150 GHz bottom)

### 3.1.6 JACKKNIFE MAPS

As a probe for systematic contamination a battery of jackknife tests are performed. These involve dividing the timestream approximately in half in a particular fashion such that each should contain identical sky signal. Upon subtracting one half from the other this same sky

signal will disappear but any differing contamination will remain. A map is constructed in the same way as above for each relevant component of the timestream and then the subtraction from its partner is made and the resulting map is divided by two. There are four data splits which QUaD uses for its jackknife tests; deck angle, scan direction, split season and focal plane.

The deck jackknife is all the data taken at deck  $-3^\circ$  subtracted from that at deck  $57^\circ$ . The observation strategy not only means there is a  $60^\circ$  rotation of the entire telescope between these two halves but the data is taken over completely different azimuth ranges. The sets therefore are different in time, azimuth angle and detector polarization angle and it is consequently unlikely that some source of contamination would be common to both.

The scan direction jackknife divides the data into that from the forward scans and that from the backward scans. Something varying rapidly or something which is scan synchronous, such as motions of the liquid cryogen, would result in a non-zero map being produced in this test. It is therefore a good check of internal instrumental effects and requires successful deconvolution of the detector channel temporal responses.

The split season jackknife is simply taking the difference between the first half of the list of days and the second half. This is a check for significant shifts in the absolute calibration over time, or anything which might gradually change over the year.

The focal plane jackknife splits the data into that from the detectors aligned with one orientation angle and that from those set at  $45^\circ$  to this. Both deck angles are still included so each detector has still made observations at two polarization angles, thereby still permitting the polarization maps. This test might reveal some problems with false instrumental signals, but since this would probably also show up in the deck jackknife, this is perhaps the least useful test.

## 3.2 POWER SPECTRA

### 3.2.1 POWER SPECTRUM ESTIMATION

As was illustrated in Figure 1.4, a power spectrum is a means of summarizing all of the statistical properties of the CMB anisotropies. We assume the anisotropies to have a Gaussian distribution and thus all the information within the CMB maps can be represented as an angular power spectrum by taking the spherical harmonic transform of the map:

$$C_\ell = \frac{1}{2\ell + 1} \sum_{m=-\ell}^{\ell} |a_{\ell m}|^2 \quad (3.14)$$

As opposed to a noise-less complete sky however, QUaD, and indeed most of the other

instruments, observes only a noisy fraction of the full sky. Spherical harmonic transforms of our cut-sky maps yield so called pseudo-power spectra. Correlations are introduced among the measured  $C_{\ell}$ s and the variance is increased. This is to say that the pseudo- $C_{\ell}$ s, ( $\tilde{C}_{\ell}$ s), are a mixture of the ‘true’  $C_{\ell}$ s over an  $\ell$  range. The extent of the mixing is dependent primarily on the map-size (Magneville & Pansart, 2007), yet is not particularly influenced by its shape unless vastly elongated. The technique employed by our data analysis pipeline follows the MASTER method (Hivon et al., 2002) extended to polarization (Brown et al., 2005).

The pseudo power spectra  $\tilde{C}_{\ell}$ s are estimated from the maps using fast spherical harmonic transforms via the anafast program of the HEALPix package. These are then corrected for the effects of the cut sky, noise, timestream filtering, beam suppression and additional filtering arising if the ground subtraction technique was used to obtain the true  $C_{\ell}$ s with the equation:

$$\mathbf{C}_{\ell} = \frac{1}{\mathbf{F}_{\ell}} \mathbf{M}_{\ell\ell'}^{-1} (\tilde{\mathbf{C}}_{\ell} - \langle \tilde{\mathbf{N}}_{\ell} \rangle_{MC}) \quad (3.15)$$

Here,  $\mathbf{F}_{\ell}$  is a transfer function describing the effect of the polynomial filtering, the telescope’s beam pattern on the data and filtering due to ground template removal. This correction is derived by means of running signal-only simulations.  $\langle \tilde{\mathbf{N}}_{\ell} \rangle_{MC}$  is the pseudo power spectra from noise-only simulations, averaged so that the noise is not too noisy!  $\mathbf{M}_{\ell\ell'}$  is a mode-mode coupling matrix dependent purely on the survey geometry describing the effects of the mixing occurring amongst the  $C_{\ell}$ s due to a small finite sky area. The matrix is found following the recipes in Hivon et al. (2002) and Brown et al. (2005) using spherical harmonics on a window weighting function set to 0 outside of the observing region and values up to 1 inside. Since it is only the size of the sky cut which determines the matrix with no factors dependent upon angular scales on the sky or the initial spectrum, the width of the peaks does not vary with the angular size,  $\ell$ , but they merely become wider as the map size decreases. Thus the smaller the region of sky being observed, the more mixing takes place from other  $\ell$ s into the one being considered.

With the width of the peak being nearly constant with  $\ell$  the coupling matrix is almost band diagonal (Magneville & Pansart, 2007, Figure 4). The upshot of this is that  $\mathbf{M}_{\ell\ell'}$  becomes uninvertible and so it is necessary to bin the power spectrum estimates. A binning operator  $\mathbf{P}_{b'b}$  is used along with a binned coupling matrix  $\mathbf{M}_{bb'}^{-1}$  (Brown et al., 2005) incorporating the filtering and beam corrections. The bin size is chosen such that the matrix becomes invertible without loss of information in making the assumption that the power spectrum is piecewise constant. The equation to be solved now becomes:

$$\mathbf{P}_b = \sum_{b'} \mathbf{M}_{bb'}^{-1} \sum_{\ell} P_{b'\ell} (\tilde{\mathbf{C}}_{\ell} - \langle \tilde{\mathbf{N}}_{\ell} \rangle_{MC}) \quad (3.16)$$

with the binned coupling matrix given by:

$$\mathbf{M}_{bb'} = \sum_{\ell} P_{b\ell} \sum_{\ell'} \mathbf{M}_{\ell\ell'} F_{\ell} Q_{\ell'b'} \quad (3.17)$$

$Q_{\ell'b'}$  is the inverse operator of the binning one,  $P_{b\ell}$ , serving to unfold a band power back into individual  $C_{\ell}$ s.

Just as the maps could be presented with either the curvature of sky incorporated or under the approximation of a flat sky, the power spectrum can also be produced with this approximation in place. In this case two dimensional Fourier transforms are used to estimate the power spectra and no correction is applied for the mode-mixing arising due to the sky cut. Instead this pipeline makes power spectrum estimations according to:

$$\mathbf{P}_b = F_b^{-1} \sum_{\ell} P_{b\ell} (\tilde{\mathbf{C}}_{\ell} - \langle \tilde{\mathbf{N}}_{\ell} \rangle_{MC}) \quad (3.18)$$

with  $F_b$  the binned equivalent of the per-multipole transfer function  $F_{\ell}$ .

Whichever method is used for the spectral band powers, their error bars are found from the square roots of the diagonal elements in the covariance matrix,  $\mathbf{C}_{bb'}$ . A covariance matrix is the inverse of a Fisher information matrix; a matrix communicating the amount of information one parameter carries about another. In this case we are seeing how well we can determine the power spectra despite instrumental noise:

$$\mathbf{C}_{bb'} = \langle \Delta \mathbf{P}_b \Delta \mathbf{P}_b' \rangle \quad (3.19)$$

We calculate this from the scatter amongst the power spectra measured from the simulations containing both signal and noise, which I now go on to describe.

### 3.2.2 SIGNAL SIMULATIONS

The WMAP5 parameters from Hinshaw et al. (2009) are fed into the CAMB (Code for Anisotropies in the Microwave Background) software (Lewis et al., 2000) to generate model  $\Lambda$ CDM power spectra. A modification of the synfast software in the HEALPix package is then used to yield curved sky maps of Temperature, and Q and U polarization with an nside of 8192, translating to 0.4 arcmin pixels. These simulated maps are then projected onto a two-dimensional grid and convolved with the QUaD beams. The QUaD data (except the signal) is then read in per detector per day, and for each the sky map,  $M$ ,

that would be observed given the detector angles, polarization efficiencies and model input  $T$ ,  $Q$  and  $U$  maps is calculated as:

$$M = \frac{1}{2} \left( T + \frac{1 - \epsilon}{1 + \epsilon} (Q \cos 2\theta + U \sin 2\theta) \right) \quad (3.20)$$

$\epsilon$  being the cross polar leakage and  $\theta$  the detector polarization angle. A signal-only simulated timestream is then reconstructed from this map according to the pointing information for each detector. Injected into this is some scatter amongst the nominal polarization angles and efficiencies of  $1^\circ$  and 0.015 respectively, along with a small pointing wander set by the generation of Gaussian random numbers of mean zero and variance 0.5 arcmin in RA and dec.

### 3.2.3 NOISE SIMULATIONS

The real TOD is made up of noise along with CMB and ground signal. Given that the instantaneous signal-to-noise is negligible, the CMB can be ignored when measuring the noise power spectra, but the ground, however, cannot. If the ground subtraction procedure were to be first carried out on the TOD, whilst being a successful technique for real data, the noise properties are left non-uniform. This is because the azimuth bins strategy in the ground template construction procedure results in noisier scan ends compared with the middle region, as Figure 3.1 illustrates. The noise is therefore measured from the field differenced TOD which adequately removes the ground signal since power spectra from differenced data are simply a factor of two times undifferenced spectra this technique may be used in conjunction with a pipeline where the rest employs ground template subtraction methods.

The noise power spectra could be obtained as the power spectra per each lead-trail set after field differencing, then divided by two and assigned to both corresponding lead and trail scans of undifferenced data. There are certain times, however, particularly amongst the temperature data when such a simple procedure is not satisfactory and so a more complex noise simulation method incorporating correlations between the detectors was developed.

In this case longer pieces of timestream are generated and then cut down to half-scan length when the map construction takes place. To begin with the TOD from a complete five scan set with turnarounds included is Fourier transformed. The covariance matrix between detectors is taken of these Fourier modes for each of a series of logarithmically spaced frequency bins.

Cholesky decomposition (Press et al., 2007) is a technique commonly used with Monte Carlo simulations when there are multiple correlated variables. The covariance matrix for each frequency bin is Cholesky decomposed. The possible correlations between

real and imaginary parts of the Fourier modes between detectors are able to be preserved, but we are assuming no correlations between modes. The result of the decomposition is applied to a vector of uncorrelated random numbers to model the observed degree of covariance among detectors. Once all frequency bins have undergone this process the resulting sets of modes are inverse Fourier transformed to give a simulated timestream. This noise timestream yielded can now be field differenced and maps produced as before. The sufficiently low instantaneous signal-to-noise means there is no need to first subtract the signal.

Sets (500-600 are used in the published results, but the more the better) of such signal-only and noise-only simulated timestreams are then run through the usual map-making pipeline. Either ground subtraction or field differencing, and polynomial filtering is applied as for the real data to obtain  $T$ ,  $Q$  and  $U$  maps of the CMB as would be observed with QUaD's detectors, beams and pointing in the absence of noise along with maps of just the noise, both fully accounting for the effects of filtering.

### 3.2.4 SIGNAL PLUS NOISE SIMULATIONS

Simulated maps containing both signal and noise could be obtained by summing the signal-only and the noise-only timestreams and running this through the map-making pipeline. However, since all the data processing steps are linear, the results of this are identical to those obtained by simply adding the simulated signal-only maps to the noise-only ones, which is more efficient computationally. Just as for the real data, the noise bias is removed from each of these simulations by subtraction of the mean of the ensemble of noise-only simulations, and they are also then corrected for the beam and filtering with the transfer function.

### 3.2.5 TRANSFER FUNCTION

The signal-only simulations are used to estimate the transfer function according to the equation:

$$\langle \tilde{\mathbf{C}}_{\ell} \rangle_{MC} = \sum_{\ell'} \mathbf{M}_{\ell\ell'} F_{\ell'} \mathbf{C}_{\ell'} \quad (3.21)$$

in which  $\mathbf{C}_{\ell'}$  is the model spectra input to the simulations.  $\mathbf{M}_{\ell\ell'}$  is the mode-mode coupling matrix previously described, necessary because of QUaD's small survey size.

### 3.2.6 BAND POWER WINDOW FUNCTIONS

It was also mentioned before that the power spectra are measured not as individual  $C_\ell$ s but rather as band powers (Bond, 1995). A binning strategy is employed to give the average power spectrum through a filter called a window function (Knox, 1999). A set of band power window functions are used as a weighting applied to the theory spectrum in order to find its expected value in each  $\ell$ -range bin; its band power. These window functions,  $W_{b\ell}$  are defined by:

$$\langle P_b \rangle = \sum_{\ell} \frac{W_{b\ell}}{\ell} \langle C_\ell \rangle \quad (3.22)$$

and found from:

$$W_{b\ell} = \sum_{b'} M_{bb'}^{-1} \sum_{\ell'} P_{\ell'\ell} M_{\ell'\ell} F_\ell \quad (3.23)$$

QUaD divides the data into bins of angular size  $\delta\ell = 80$ . Figure 3.4 shows the band power window functions for 23 of the bins from  $\ell \sim 200 - 2000$  each normalized to total unity.

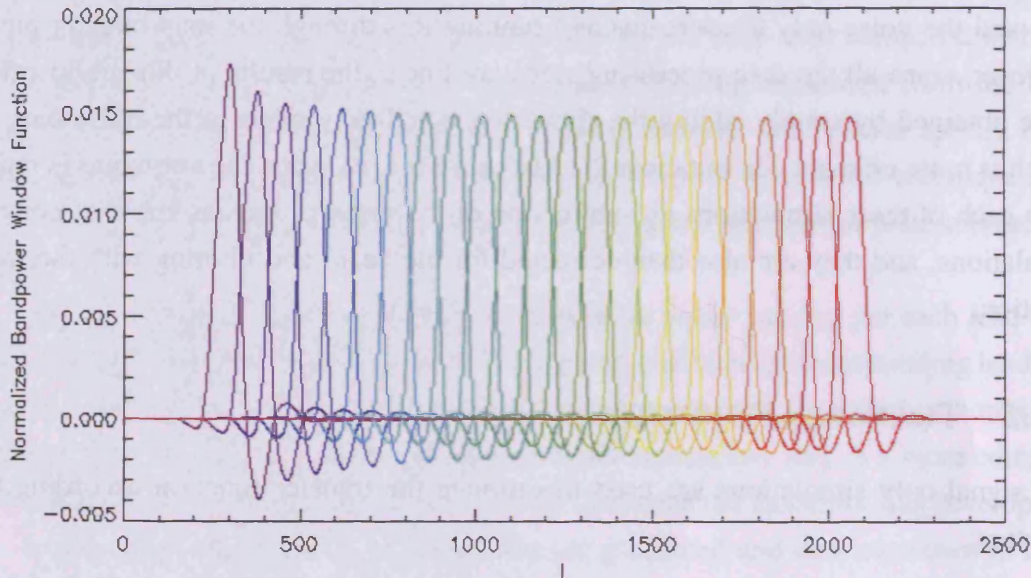


Figure 3.4: Band Power Window Functions

For each bin the function extends across the whole  $\ell$  range filtering the power spectrum to give its average within that bin. Negative values arise as a consequence of applying the mode-mode coupling matrix described in Section 3.2.1. These are for the TT cross frequency spectrum.

## 3.2.7 POWER SPECTRA RESULTS

After all the simulations are completed, the signal-only ones used to find the filter transfer function and the noise-only to correct for the the noise contribution, equation 3.16 can be solved to give the power spectra, along with error bars derived from the scatter amongst signal plus noise simulations. Spectra are calculated separately for 100 GHz and 150 GHz and also cross spectra between the two frequencies. With both temperature and polarization data the six spectra described in Section 1.6.1 can be found;  $TT$ ,  $EE$ ,  $BB$ ,  $TE$ ,  $TB$  and  $EB$ , giving a total of 18.

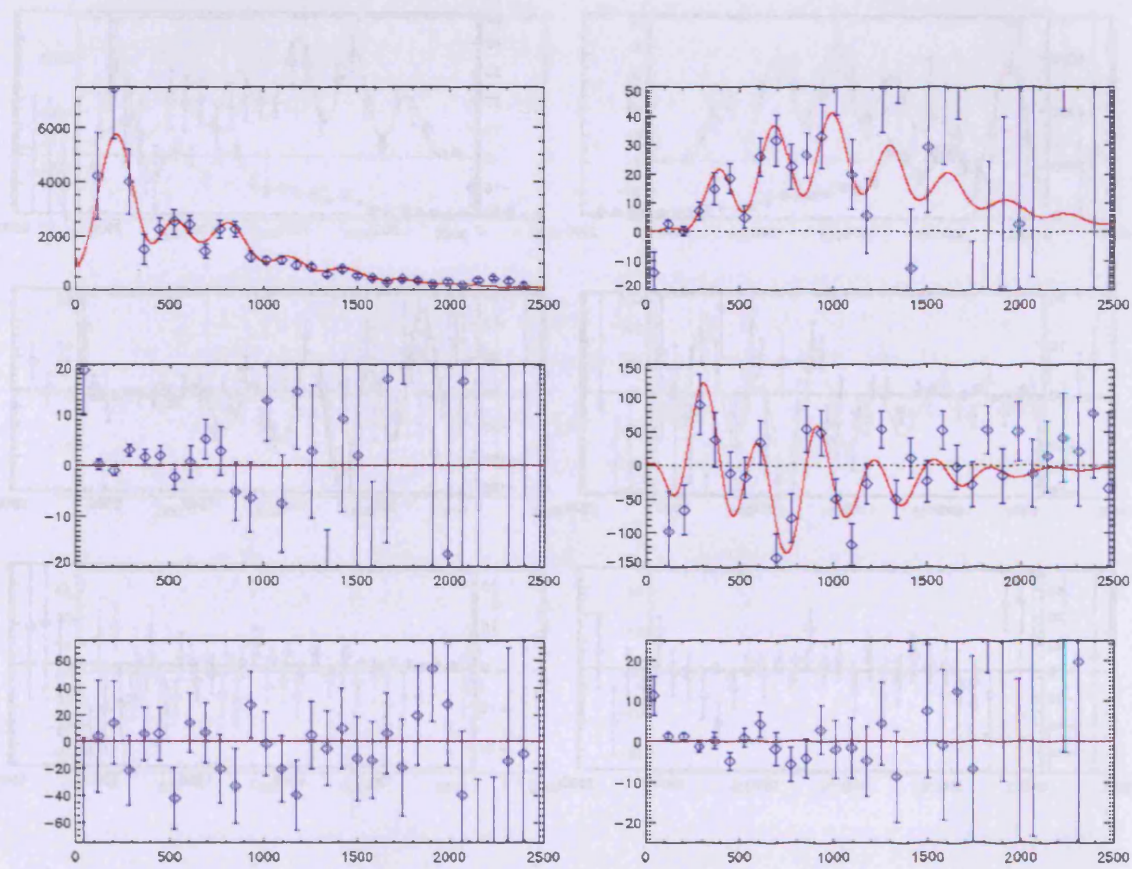


Figure 3.5: 100 GHz Power Spectra

Clockwise from top left:  $TT$ ,  $EE$ ,  $TE$ ,  $EB$ ,  $TB$ ,  $BB$ .

The same set of 18 power spectra are produced for each jackknife map too, allowing various systematics to be checked according to the split made. To quantify the extent to which the jackknife tests are passed and the extent to which our power spectra agree with theory a statistical chi-square analysis is performed.

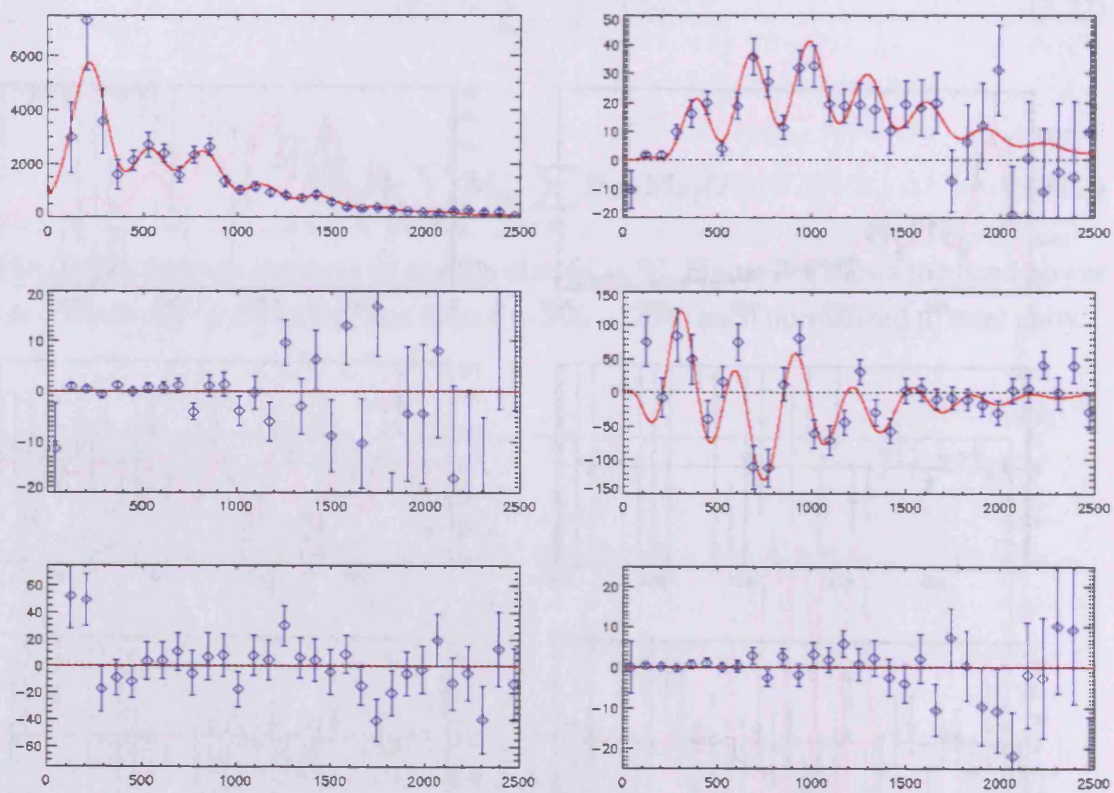


Figure 3.6: 150 GHz Power Spectra  
 Clockwise from top left:  $TT$ ,  $EE$ ,  $TE$ ,  $EB$ ,  $TB$ ,  $BB$ .

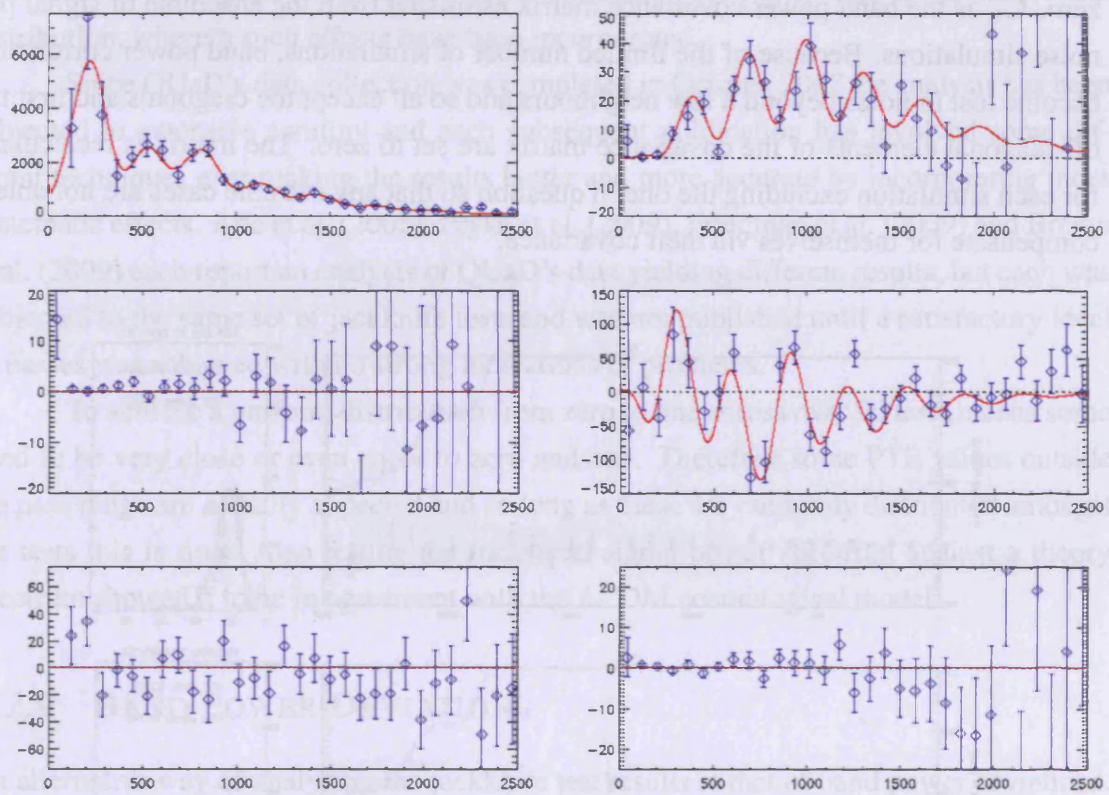


Figure 3.7: Cross Frequency Power Spectra  
 Clockwise from top left: *TT*, *EE*, *TE*, *EB*, *TB*, *BB*.

### 3.2.8 CHI-SQUARE STATISTICS

The chi-square statistic is calculated using the equation:

$$\chi^2 = \sum_{ij} (P_i - P_i^{th}) C_{ij}^{-1} (P_j - P_j^{th}) \quad (3.24)$$

Here  $P_i$  is the measured band power and  $P_i^{th}$  is the expected value of the  $i^{th}$  band power being tested. The band power window functions are used to bin the model  $\Lambda$ CDM spectrum for testing the signal against theory and for the jackknife tests the expected values are zero.  $C_{ij}$  is the band power covariance matrix estimated from the ensemble of signal plus noise simulations. Because of the limited number of simulations, band power correlations become lost in noise beyond a few neighbours and so all except the diagonals and first two off-diagonal elements of the covariance matrix are set to zero. The matrix is recalculated for each simulation excluding the one in question so that any extreme cases are not able to compensate for themselves via their covariance.

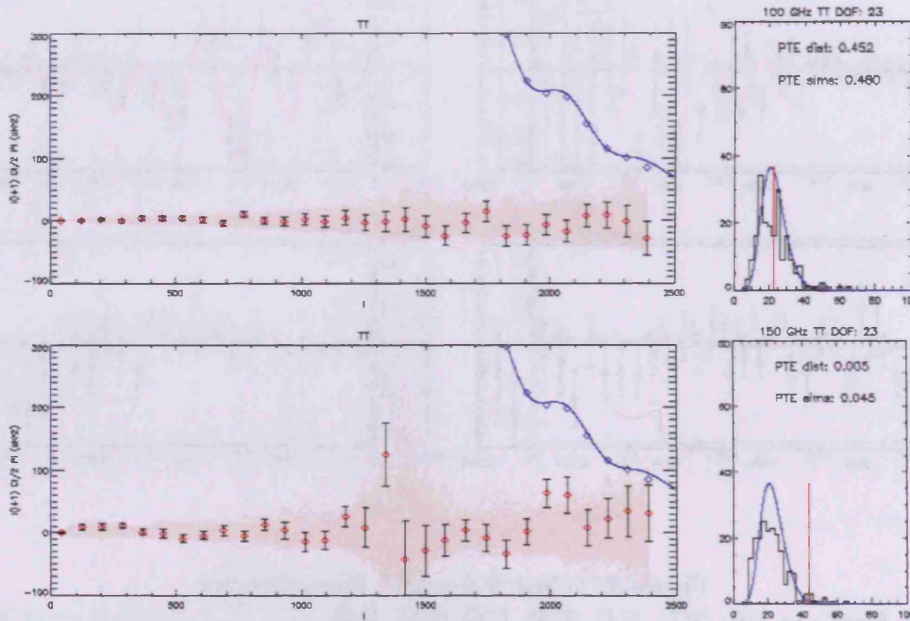


Figure 3.8: Chi-Square Statistics

Two examples of the scan direction jackknife test TT spectra and chi-square plots: 100 GHz which passes the jackknife test (top) and 150 GHz which fails (bottom).

The  $\chi^2$  values for the simulations should follow a  $\chi^2$  distribution with  $N$  degrees of freedom, where  $N$  is the number of band powers used in the analysis. Plots such as those in Figure 3.8 can be made as a histogram of  $\chi^2$  values measured from the simulations,

along with a curve displaying the corresponding theoretical distribution and the position of the  $\chi^2$  value given by the actual data (the red line). We can therefore compare the measured  $\chi^2$  values from the data to the distribution measured from the set of signal plus noise simulations and calculate the probability of a  $\chi^2$  value being greater by chance than that of the real data. We refer to this as a ‘probability to exceed’ (PTE) and ideally the values would be distributed uniformly from zero to one. A test is considered to be a pass if its PTE value lies between 0.05 and 0.95. Since a perfect cancellation isn’t necessarily expected for all the jackknives because of the polynomial filtering and the scan strategy, the PTEs are calculated with respect to the simulation set rather than to the theoretical distribution, wherein such effects have been incorporated.

Since QUaD’s data collection was completed in October 2007 the analysis has been subjected to extensive scrutiny and each subsequent publication has involved some different techniques ever making the results better and more accurate by incorporating more systematic effects. Ade et al. (2008), Pryke et al. (2009), Friedman et al. (2009) and Brown et al. (2009) each report an analysis of QUaD’s data yielding different results, but each was subjected to the same set of jackknife tests and was not published until a satisfactory level of passes was achieved with no strong indications of problems.

To achieve a uniform distribution from zero to one across over 90 tests means some need to be very close or even equal to zero and one. Therefore some PTE values outside the pass range are actually expected and so long as these are randomly distributed amongst the tests this is fine. Also testing the measured signal power spectrum against a theory spectrum showed it to be in agreement with the  $\Lambda$ CDM cosmological model.

### 3.2.9 BAND POWER DEVIATIONS

An alternative way of analyzing the jackknife test results is that of band power deviations. These show the extent to which each band power is contributing to the overall  $\chi^2$  statistic and come from dividing each spectral point by its error bar. In this way if there is a jackknife failure the particular bin(s) or  $\ell$ -range responsible can be identified. Furthermore if a number of failures occur within a single jackknife test but the band power deviation plots show it to be caused by a different band power in each case, then it is likely the failures are due to chance rather than some systematic contamination.

Band power deviations from the successful jackknife tests have the majority of their values within  $\pm 1\sigma$  of mean value amongst the simulations, i.e. between the two blue lines in Figure 3.9. Those from a failure have some more extreme values in particular bins. If these are even distributed along the  $\ell$ -axis as is the case for the plot shown, there is less cause for concern than a cluster over a defined  $\ell$ -range.

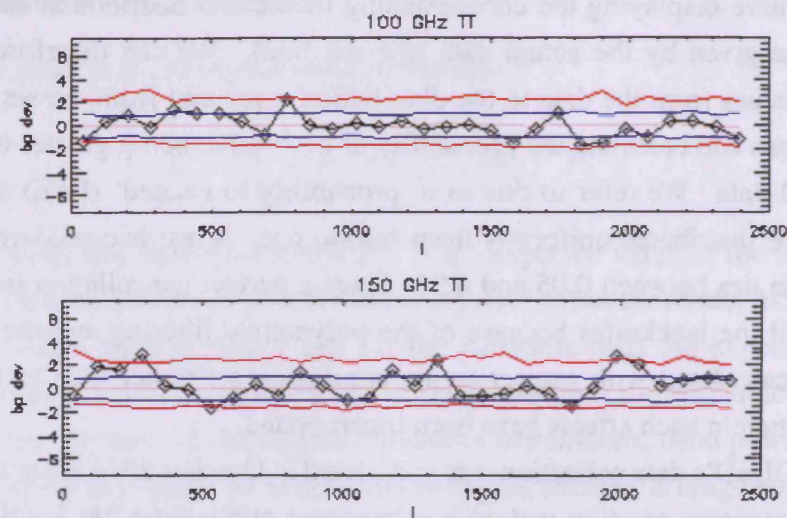


Figure 3.9: Band Power Deviation Plots

The band power deviations corresponding to the scan direction jackknife tests of Figure 3.8. The red lines indicate the positions of 2.3% and 97.7% of the distribution of signal plus noise simulation band power deviation values, the blue lines 15.9% and 84.1% and the grey line 50%.

After the spectra have been produced to a satisfactory degree of accuracy and possibilities of significant systematic contamination ruled out via jackknife tests and the statistical results from them, they made be compared with those from other experiments and used both by themselves and in conjunction with the others to carry out parameter estimation.

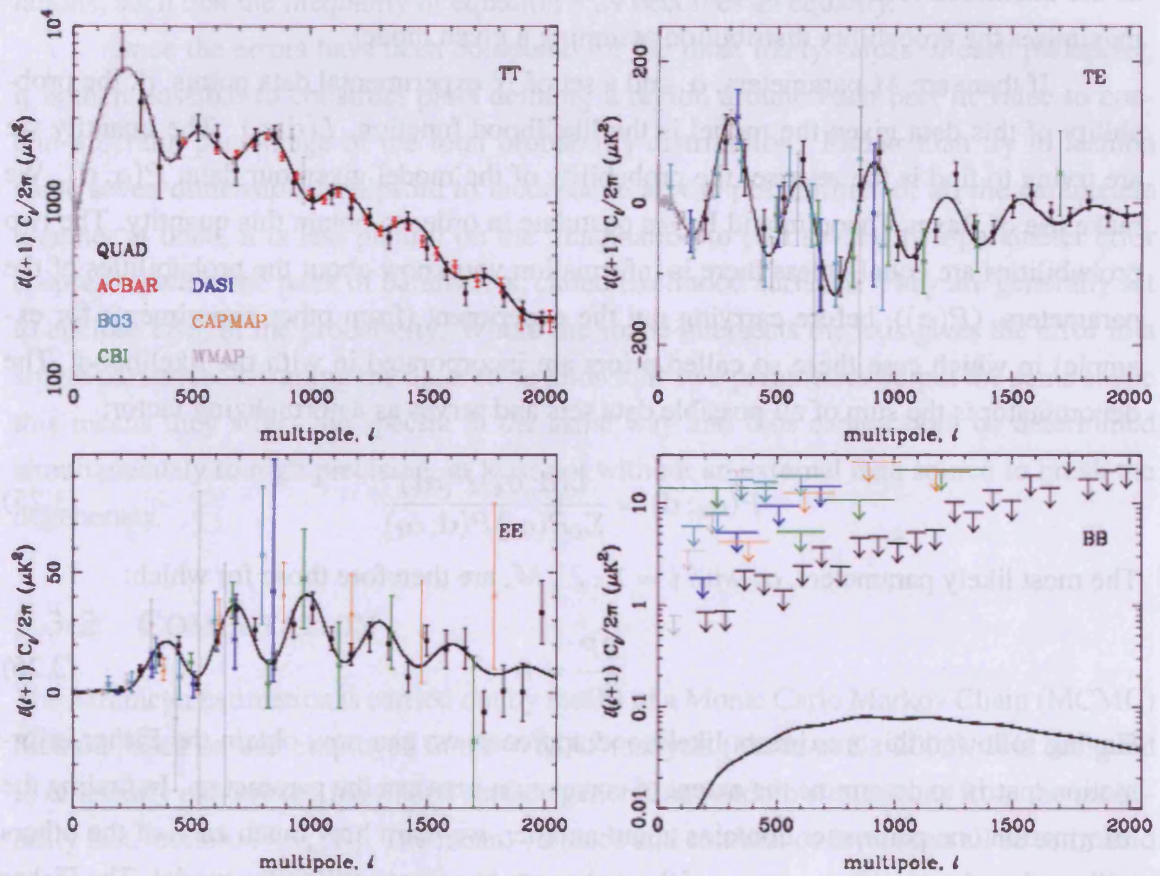


Figure 3.10: Comparison Plot  
 QUAD's data with that from other recent surveys (Brown et al., 2009).

### 3.3 PARAMETER ESTIMATION

#### 3.3.1 LIKELIHOOD THEORY

As discussed in the introduction, the ultimate aim of CMB experiments is to better the accuracy with which we know each of the cosmological parameters describing the universe and its properties and thereby increase our understanding of it. The idea is to find the combination of parameters making the best fit to the data. This is accomplished by means of the likelihood function; the most likely set of parameters given the data is that which maximises the probability distribution assuming a given model.

If there are  $M$  parameters,  $\alpha$ , and a set of  $N$  experimental data points,  $\mathbf{d}$ , the probability of this data given the model is the likelihood function,  $L(\mathbf{d}; \alpha)$ . The quantity we are trying to find is the reverse; the probability of the model given our data,  $P(\alpha; \mathbf{d})$ . We make use of Bayes Theorem and Bayes postulate in order to obtain this quantity. The two probabilities are equal unless there is information you know about the probabilities of the parameters, ( $P(\alpha)$ ), before carrying out the experiment (from other experiments for example) in which case these so called priors are incorporated in with the likelihood. The denominator is the sum of all possible data sets and serves as a normalizing factor:

$$P(\alpha_k; \mathbf{d}) = \frac{L(\mathbf{d}; \alpha_k)P(\alpha_k)}{\sum_{\ell} P(\alpha_{\ell})P(\mathbf{d}; \alpha_{\ell})} \quad (3.25)$$

The most likely parameters,  $\alpha_i$  with  $i = 1, \dots, M$ , are therefore those for which:

$$\frac{\partial P}{\partial \alpha_i} = 0 \quad (3.26)$$

Having followed this maximum likelihood approach we can now obtain the Fisher information matrix to determine the extent of correlation between the parameters. In finding the information one parameter contains about another, we learn how much each of the others will need to change when any one of them changes in order to still fit the model. The Fisher information matrix is evaluated at the maximum likelihood values of the parameters, with  $\mathcal{L} = -\ln L$ , from:

$$F_{ij} = \left\langle \frac{\partial^2 \mathcal{L}}{\partial \alpha_i \partial \alpha_j} \right\rangle \quad (3.27)$$

The covariance matrix is then computed as the inverse of this Fisher information matrix:

$$C_{ij} = F_{ij}^{-1} \quad (3.28)$$

In this matrix the diagonal elements are the variances of each parameter, with the errors on them therefore having a value at least as high as the square roots of the diagonals according

to the Cramér-Rao inequality (Press et al., 2007):

$$\Delta\alpha_i \geq 1/\sqrt{F_{ij}} \quad (3.29)$$

From the off-diagonal elements we find the correlation coefficients between the parameters. For no correlation we would expect values of zero, whereas positive or negative values would indicate a positive or negative correlation respectively. The smallest errors are yielded when the maximum likelihood parameters are found and if there are no correlations, such that the inequality of equation 3.29 becomes an equality.

Once the errors have been computed for the most likely values of each parameter, it is then possible to construct plots defining a region around each best fit value to contain a certain percentage of the total probability distribution. Rather than try to fashion some seven dimensional ellipsoid to incorporate all the possibilities of all the parameters together at once, it is less painful on the imagination to plot several two-parameter error ellipses between the pairs of parameters, called likelihood surfaces. They are generally set to enclose 68% of the probability. Where the shape intersects the axis gives the error in a single parameter assuming the other to be known. If two parameters output the same shape this means they affect the spectra in the same way and thus cannot both be determined simultaneously to high precision; at least not without an external data source to break the degeneracy.

### 3.3.2 COMPUTATION

The parameter estimation is carried out by means of a Monte Carlo Markov Chain (MCMC) method based on that employed in the WMAP analysis (Verde et al., 2003). It is designed to efficiently explore the likelihood surface generating random simulations from the probability distribution,  $P(\alpha_k; \mathbf{d})$ . The mean, variance and confidence levels can all be estimated from the simulation samples obtained. The chain does not depend on its starting location and will eventually have covered all the target distribution. A judgement must be made to determine when there is sufficient convergence as for any finite chain there will be areas which have not been visited but there comes a point where a reasonable sample of the surface has been taken. In the event of the likelihood surface not being fully explored the results will yield wrong cosmological parameters.

The procedure begins with a burn-in period, which is removed after around 100,000 steps have been completed to leave at least 80,000. To obtain at least 4 chains of such length within a reasonable amount of time various techniques are employed to improve the efficiency of the analysis. Some of the parameter combinations are degenerate which causes a

slowing of convergence, but since there is little point in exploring areas of the surface affected by the degeneracy a set of re-parameterizations is used to control this. A covariance matrix is used which takes into account all of the correlations between the parameters. The input priors,  $P(\alpha_k)$ , are chosen such that the parameter space is optimal without having an effect on the outcome and the chain shouldn't hit the imposed boundaries. QUaD used the same priors and re-parameterizations as WMAP, along with the same convergence/mixing test to check the completion of sufficient coverage of the likelihood surface. The chain is further optimized by careful selection of a step-size and by calculating the parameter covariance matrix after an initial run. Extra terms are added to the band power covariance matrix to compensate for the beam and calibration uncertainties. Therefore the more accurately we are able to understand these features of the experiment the smaller the uncertainties on them will be and consequently the errors on our parameters will be smaller.

### 3.3.3 RESULTS

Parameter estimation results from the first season of QUaD data were published together with the power spectra results in Ade et al. (2008). The parameters reported came from the convergence of four chains each with around 50,000 steps. This analysis was a six parameter constraint using only the polarization spectra ( $TE$ ,  $EE$  and  $BB$ ). It was found that: 'For all the parameters our 68% confidence limit enclosed the WMAP3 expectation value.'

A more in depth parameter estimation analysis was performed following the second and third season spectra of Pryke et al. (2009) and published in a separate paper Castro et al. (2009). In this analysis not only was the standard six parameter estimation performed for temperature-only, polarization-only and temperature plus polarization but also an extension to include isocurvature modes. The scalar primordial perturbations of the CMB responsible for large scale structure formation are due to density fluctuations. An adiabatic model suggests that these density fluctuations were present initially, but they could also have been generated by stresses within the matter pushing matter around. We call this isocurvature and there are four possible modes: baryon density, cold dark matter, neutrino density and neutrino velocity. Their phase is different from that of adiabatic modes and there are various features in the polarization spectra which provide insight into the isocurvature constraints.

This time the QUaD temperature data was found to be in good agreement with WMAP5 expectations but the polarization results were less so, the baryon density parameter,  $\Omega_b h^2$ , in particular being much higher. This appeared to have resulted from the  $TE$  spectrum and it was concluded that either some new physics were responsible, some remaining residual systematics or that the results arose by chance. Then it was left to see

Parameter	Symbol	Value
Baryon Density	$\Omega_b h^2$	0.0243 $^{+0.0025}_{-0.0025}$
Cold Dark Matter Density	$\Omega_c h^2$	0.119 $^{+0.0253}_{-0.0250}$
Acoustic Peak Scale	$\theta$	1.041 $^{+0.005}_{-0.005}$
Optical depth	$\tau$	$< 0.54$ 95% <i>C.L.</i>
Scalar fluctuation amplitude	$\ln(10^{10} A_s)$	3.58 $^{+0.28}_{-0.30}$
Scalar fluctuation index	$n_s$	0.804 $^{+0.098}_{-0.098}$
Age	(GYr)	13.5 $^{+0.4}_{-0.4}$
Dark Energy Density	$\Omega_\Lambda$	0.68 $^{+0.14}_{-0.14}$
Matter Density	$\Omega_m$	0.32 $^{+0.14}_{-0.14}$
Reionization Depth	$z_{re}$	23.9 $^{+8.1}_{-9.0}$
Hubble Constant	$H_0$	71.1 $^{+10.9}_{-10.9}$
Linear Mass Perturbation	$\sigma_8$	0.98 $^{+0.15}_{-0.15}$

Table 3.1: QUaD cosmological parameter results from the improved temperature and polarization spectra.

if future polarization experiments or the improved QUaD analysis would show the same trend. In investigating the isocurvature modes QUaD was able to provide some improvement on the fractional cold dark matter density mode parameter over WMAP5 but nothing significant.

Upon developing the ground subtraction technique and re-analysing QUaD data to provide improved measurements of the temperature and polarization of the CMB (Brown et al., 2009), the parameter estimation was repeated. The results from this analysis were then reported in Gupta et al. (2009), again with temperature-only, polarization-only and combined temperature - polarization sets. They each provide tight constraints on the parameters consistent with those from WMAP5 and other CMB data, with the only exception being a lower preferred value for the scalar fluctuation index,  $n_s$  (0.804 compared with 0.967 in the WMAP5 analysis). In addition to the standard six parameters a number of other derived parameters were calculated and presented in the paper. Table 3.1 lists the complete temperature plus polarization results from Gupta et al. (2009).

Gupta et al. (2009) also contains results from a tensor analysis, providing a constraint on the parameter  $r$ , the ratio of tensor to scalar perturbation assuming the tensor tilt,  $n_t$  is related to the tensor and scalar amplitudes via  $n_t = -A_t/(8A_s)$ . The constraint achieved by QUaD is  $r < 0.32$  to 95% confidence; the strongest limit to date on the tensors from the CMB alone.

Whilst adding polarization data to temperature does break some degeneracies amongst the parameters allowing a more accurate estimation to be made, they can be even further

constrained by the addition of other cosmological data. Observations of galaxy clustering, supernovae, baryon acoustic oscillations and large scale-structure along with the Hubble Space Telescope data from deep field surveys and CMB data from other experiments probing different  $\ell$ -regions, can all be added to QUaD's data.

Castro et al. (2009) added to QUaD the WMAP5 data set from the LAMBDA website<sup>1</sup> and large scale structure data from SDSS Luminous Red Galaxies fourth data release (Tegmark et al., 2006). Brown et al. (2009) investigated the effect of adding QUaD to the WMAP5 data, the SDSS data and also the final results from the ACBAR experiment (Reichardt et al., 2009a), whilst Gupta et al. (2009) additionally included results from CBIPol (Sievers et al., 2009) and BICEP (Chiang et al., 2009).

Since WMAP has measured the low- $\ell$  region, in particular the first peak, to such a high degree of accuracy, QUaD's contribution comes in tightening the errors on parameters more dependent on the high- $\ell$  peaks and their relative heights; the baryon and matter densities. Adding QUaD to the datasets from several previous CMB experiments as well as throwing galactic data into the mix allows as much information as possible to be included and the parameters derived the most accurate to fit all this data, making for a stronger constraining power than any dataset alone might permit and providing the best tightening of parameter space towards the best description of cosmology.

---

<sup>1</sup>LAMBDA website: <http://lambda.gsfc.nasa.gov/>

## 4 DUST

---

“SINCE EVERY PIECE OF MATTER IN THE UNIVERSE IS IN SOME WAY AFFECTED BY EVERY OTHER PIECE OF MATTER IN THE UNIVERSE, IT IS POSSIBLE TO EXTRAPOLATE THE WHOLE OF CREATION - EVERY SUN, EVERY PLANET, THEIR ORBITS, THEIR COMPOSITION AND THEIR ECONOMIC AND SOCIAL HISTORY FROM, SAY, ONE SMALL PIECE OF FAIRY CAKE.”

DOUGLAS ADAMS - THE RESTAURANT AT THE END OF THE UNIVERSE

### 4.1 FOREGROUNDS

Between QUaD and the CMB lies much more than just empty space. Although an observation region through minimal foreground was chosen, nevertheless any astrophysical phenomena emitting at millimeter wavelengths will have been included along with the CMB in QUaD's measurements. A foreground can be defined as anything between the surface of last scattering and the telescope. A constant foreground, such as the atmosphere, would simply be an addition to the total background power, increasing photon noise and therefore decreasing sensitivity. Unfortunately however, the foreground fluctuates over the sky adding spurious signal into the CMB fluctuations. We rely on the differing spectral and spatial distributions of the foreground components in order to separate them from the CMB, however it is entirely possible that by chance there is a correspondence of large scale structures between the two (Chiang et al., 2008).

The area of sky observed by QUaD was directed away from the galactic plane but the extended emissions to high galactic latitude are unavoidable. Galactic foreground sources include dust, synchrotron and free-free emissions. We may also encounter contamination from the extra-galactic emissions of radio and infra-red galaxies, and high energy electrons from galaxy clusters may distort the CMB via the Sunyaev-Zel'dovich effect.

Bennett et al. (2003a) reported on the foregrounds measured by WMAP after its first

year and more recently Kogut et al. (2007) and Gold et al. (2009) for the third and fifth year WMAP data respectively. WMAP mapped the entire sky at five frequency values ranging from 23 GHz to 94 GHz and used masks to block those regions in which the foreground signal dominated over the CMB (i.e. the Galactic plane and point sources). In the range 30 - 150 GHz and at galactic latitudes above  $\sim 15^\circ$  the CMB is dominant, with the other components dependent upon frequency according to Figure 4.1.

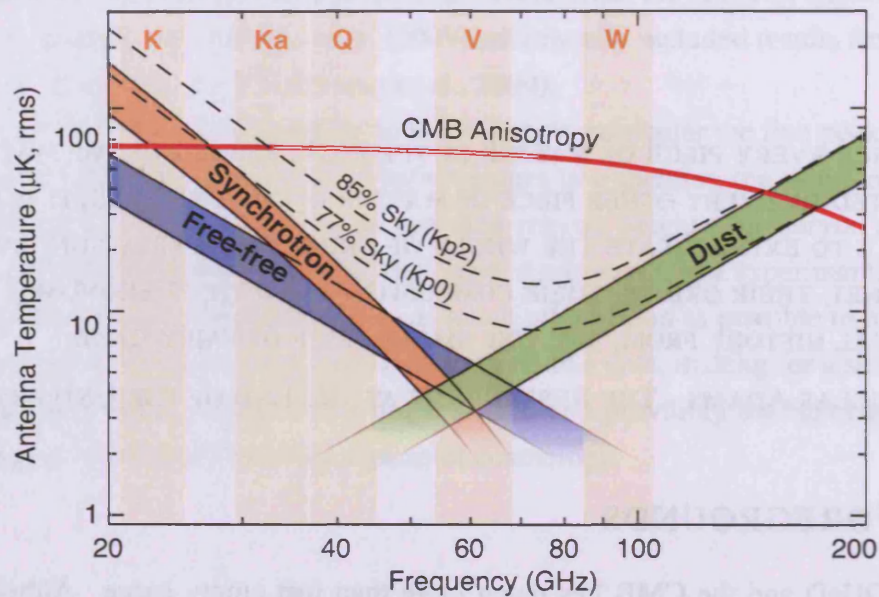


Figure 4.1: WMAP Foreground Amplitudes

CMB Anisotropy compared to Galactic emissions on a  $1^\circ$  angular scale (Bennett et al., 2003a).

We therefore see that at frequencies lower than 30 GHz the synchrotron emissions become more dominant whilst at higher frequencies the dust takes over. If observations are made at the frequencies where these components do dominate then templates can be made of their contribution at CMB frequencies by extrapolation. A model of frequency dependence is required for this, which comes from using two or more maps at similar frequencies and fitting a theoretical model.

## 4.2 DUST MODELS

Dust makes up 1% by mass of the interstellar medium. Since we exist within this interstellar medium our view of the universe is always obscured by dust to some extent. Dust consists

of small grains that can be made up of Carbon, Nitrogen, Oxygen, Aluminium, Silicon, Magnesium or Iron, with a composition largely dependent on the Carbon-Oxygen ratio in the local environment upon formation (e.g. Desert et al., 1990). It forms in the outer atmosphere of red giants and is then blown out by radiation pressure. It can also be found in the ejecta from Wolf-Rayet (helium) stars, planetary nebula, novae and supernovae. There is an upper limit on the size of a dust grain since to be ejected it must permit radiation pressure to overcome gravity.

Trumpler discovered dust in 1930 as the explanation for the paradox of clusters appearing bigger and brighter than their distance from us would suggest. In fact the interstellar dust was causing the extinction of light from the cluster making them seem further away than they truly were. Dust grains absorb photons from starlight which excite vibrational modes within them and are then re-emitted at a lower frequency. The peak of dust emissions occurs at about 3000 GHz ( $100 \mu\text{m}$ ), therefore we expect QUaD to see a higher level at 150 GHz than at 100 GHz.

#### 4.2.1 INTENSITY MODELS

Finkbeiner et al. (1999) used data from the FIRAS and DIRBE instruments on COBE along with IRAS results to create a detailed map of dust in the universe extrapolated to CMB frequencies with the resulting prediction (shown in Figure 4.2) at 94 GHz made publicly available<sup>2</sup>.

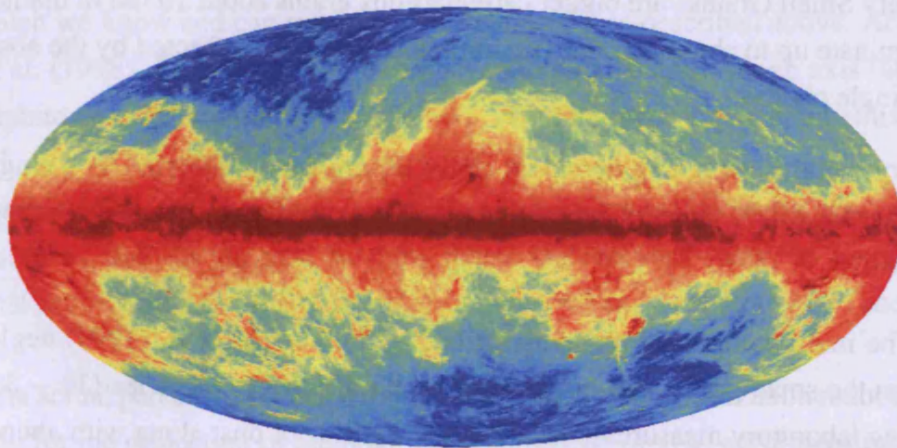


Figure 4.2: All-Sky Dust Map

An extrapolation of surveys by FIRAS, DIRBE and IRAS to 94 GHz.

<sup>2</sup>[http://lambda.gsfc.nasa.gov/product/foreground/fg\\_fds\\_get.cfm](http://lambda.gsfc.nasa.gov/product/foreground/fg_fds_get.cfm)

The extrapolation to lower frequencies is sensitive to the composition and the emissivity of the dust grains. For a simple model dust can be treated as a grey body with a particular temperature and emissivity. The emission is then dependent on frequency according to:

$$I_\nu = \frac{\nu^\alpha B(\nu, T_{dust})}{\nu_0^\alpha B_0(\nu, T_{dust})} \quad (4.1)$$

where  $B(\nu, T)$  is the Planck function at temperature  $T$  and frequency  $\nu$ . Schlegel et al. (1998) assumed this naive model finding  $\alpha = 2$  as the best fit to the 100  $\mu\text{m}$  DIRBE and IRAS data used to generate the initial dust map. However, it turns out that this single power law emissivity function is not an accurate fit at all frequencies. When correlated with the FIRAS data, Finkbeiner et al. (1999) found an  $\alpha = 1.5$  profile to be better at low frequencies whilst an  $\alpha = 2.2$  emissivity proved better for higher frequencies.

They suggested, against earlier predictions, that different types of dust grains within the interstellar medium might obey differing emissivity laws, with particular species becoming more dominant at certain frequencies. Dust particles can be divided into three main groups based on their size and composition:

- Polycyclic Aromatic Hydrocarbons are the smallest, dominating at high frequencies with characteristic C-C and C-H vibrations creating characteristic emission lines between 3 and 17  $\mu\text{m}$ . A single energetic photon can heat them to a high temperature since they are so small.
- “Very Small Grains” are bigger carbonaceous grains about 10 nm in diameter which dominate up to about 80  $\mu\text{m}$ . Their temperature is also affected by the absorption of a single photon.
- Larger grains becoming dominant above 80  $\mu\text{m}$  are not affected by a single photon, rather they have an equilibrium temperature dependent on the surrounding environment.

The multi-component model described by Finkbeiner et al. (1999) neglects emissions from the small grains that are insignificant at FIRAS frequencies (30 – 3000 GHz). Combining laboratory measurements of various species of dust along with abundances revealed through observations of molecular cloud cores, they propose models in which each component can be characterized by an emissivity power law,  $\alpha$ , a power fraction,  $f$ , and a ratio of thermal emission to optical opacity,  $q$ . The best fitting two component model is found to be one with  $\alpha_1 = 1.67$ ,  $\alpha_2 = 2.70$ ,  $f_1 = 0.0363$  and  $\frac{q_1}{q_2} = 13.0$ . Physically this means there is a component of dust (with  $\alpha = 1.67$ ) that only makes up 3.63% of the dust

but which has an opacity ratio 11.2 times higher than the dominant species of dust. This component has a temperature of 9.4K whilst the dominant component is at 16.2K. With this model the equivalent extrapolation to that of equation 4.1 is:

$$I_\nu = \frac{\sum_k f_k q_k \nu^\alpha B(\nu, T_{dustk})}{\sum_k f_k q_k \nu_0^\alpha B_0(\nu, T_{dustk})} \quad (4.2)$$

in which  $k$  is the dust component. This is a slight approximation as there is also a weak dependence upon grain size but it is quite reasonable to neglect this under the assumption that each component has a single temperature within a small locale. In fact over the small frequency interval observed by QUaD it is likely that one single component will dominate, nevertheless the best fit model by Finkbeiner et al. (1999) extrapolated to 94 GHz is convenient for our use.

#### 4.2.2 POLARIZATION

Magnetic fields can cause dust grains to become aligned, and this results in polarization of the dust emission. Generally the grains have a non-spherical shape and they will emit preferentially along their longest axis. With a random distribution this will lead to no net polarization but if the long axes become aligned there will be a polarized fraction of the overall emission. To understand the distribution of the polarized dust we need information about the intrinsic dust polarized emissivity, the strength and direction of the magnetic field and the polarization reduction factor.

The intrinsic polarized emissivity depends upon the type and shape of the dust grains which we know and can model to a certain extent as described above. According to Prunet et al. (1998) if the grains are an oblate spheroidal shape with an axis ratio  $\sim 2/3$ , and a graphite to silicate ratio of  $\sim 0.25 - 0.5$  then the intrinsic polarized emissivity will be  $\sim 30\%$ .

They also describe the great uncertainty with which we know the relative direction of the magnetic field to the dust but how recent observations show, in agreement with theory, that the alignment of the dust grains is independent of the strength of the magnetic field.

The actual percentage of polarization is lessened by a ‘polarization reduction factor’ accounting for the projection of the polarization direction onto a two dimensional plane of the sky and in summing the contributions of various different directions of polarization along each line of sight.

A three-dimensional model of the dust polarization is thus made under the assumption that it is correlated with HI emissions and then integrated along the line of sight, taking into account the polarization reduction effects, to create a two-dimensional map. Results

from this suggest a polarization percentage of  $\sim 3 - 5\%$  and that the corresponding power spectra has a spectral index of  $1.3 - 1.4$ . Measurements by ARCHEOPS (Benoît et al., 2004) of the polarized dust emission agree with this, suggesting a  $4 - 5\%$  polarized signal.

A somewhat simpler model is proposed in Baccigalupi (2003) making the assumption of a perfect correlation between total and polarized intensity with a  $5\%$  degree of polarization. Also because they assume the Galactic magnetic field to be completely efficient at imprinting a polarization pattern to both dust and synchrotron, they take the dust polarization angle map to be the same as that of synchrotron emission. They found this to be in good agreement with the model of Prunet et al. (1998).

### 4.3 LOOKING FOR DUST IN QUAD DATA

QUaD surveyed a particular patch of the sky centred at RA  $5.5\text{h}$ , Dec  $-50^\circ$ . We can extract the relevant section of the full sky dust map in Figure 4.2 to obtain a prediction of the dust in our observing region.

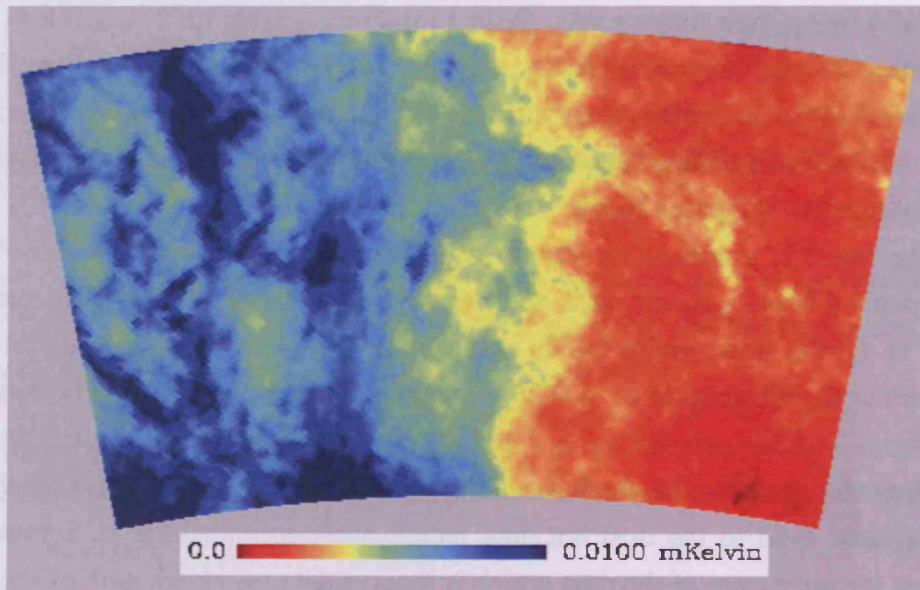


Figure 4.3: Dust Map at 94 GHz

The all-sky dust map trimmed to QUaD's observing region.

This trimmed map, shown in Figure 4.3, can then be put through the same map-making pipeline (my specifically adapted version of the codes) as that of the simulated CMB maps described in Section 3.2.2. From this we obtain a map of the dust as if it had been obtained with QUaD's observing strategy. The pointing information from the 143

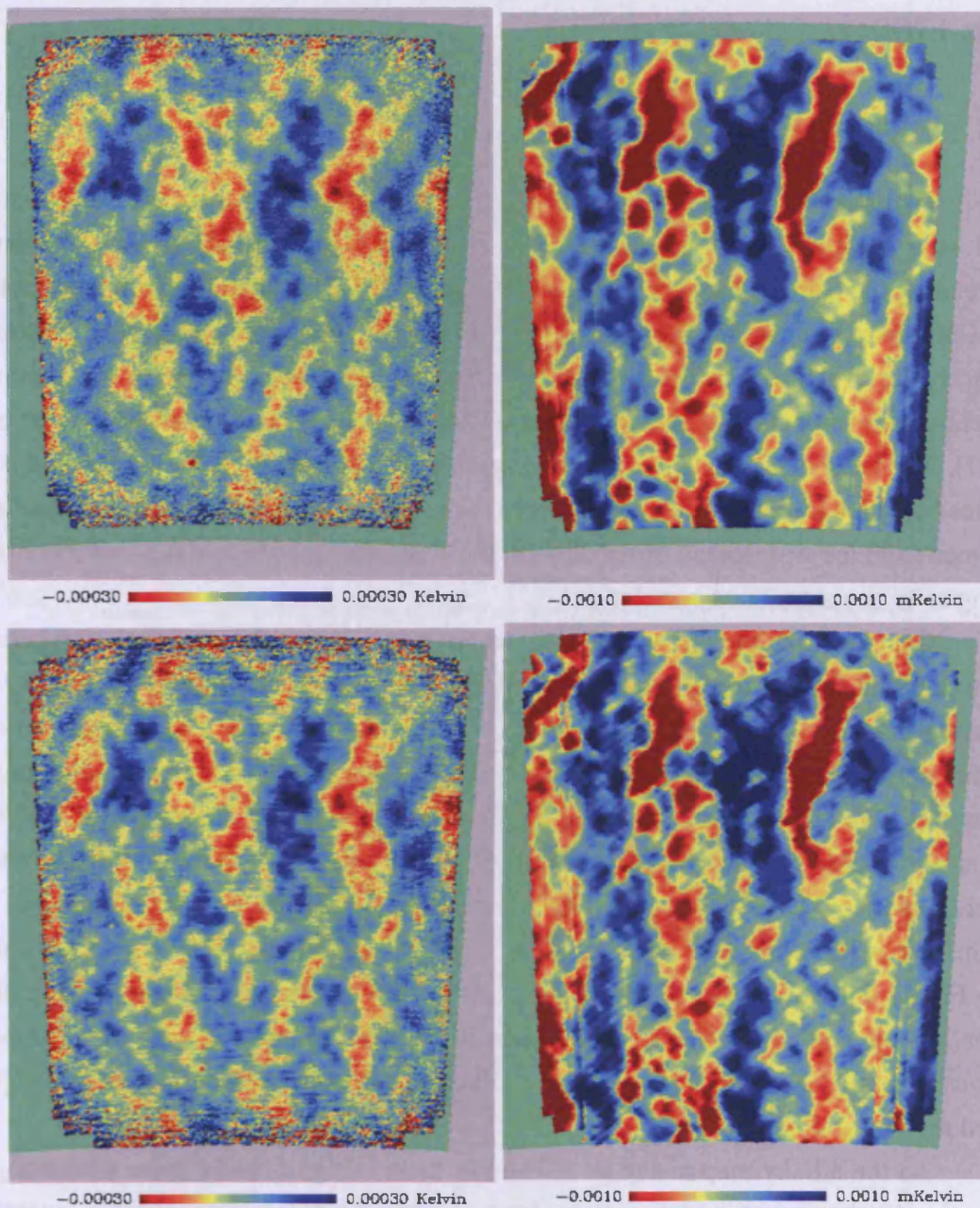


Figure 4.4: Field Differenced CMB and dust maps

Being run through the same map-making pipeline allows the CMB maps (left) to be directly compared with maps of the dust prediction in QUAD's region (right) at both 100 GHz (top) and 150 GHz (bottom)

good days of QUaD's actual data is used, along with beam convolutions, inverse variance weights, third order polynomial filtering and field-differencing. The maps outputted are then identical in both size and resolution to those the pipeline produced of the CMB with the real TOD.

### 4.3.1 STATISTICAL CORRELATIONS

Whilst a visual comparison can be made using Figure 4.4 there are various statistical ways in which the maps may be more quantitatively compared. A simple means of correlating the pairs of maps is to make scatter plots pixel by pixel; the temperature from the CMB map against that from the dust map. A linear fit algorithm can then be used to quantify the level of any correlation therein. Two such algorithms are one which minimizes the chi-square error statistic and one that uses a least absolute deviation method (Press et al., 2007). The latter is less sensitive to outlying data. The gradients of these linear fits is one means by which level of correlation between the maps can be quantified. It is immediately obvious from the widespread distribution in the scatter plots of Figure 4.5 that there is not going to be any significant correlation.

Over an ensemble of universes we would expect there to be no correlation between the true CMB and the foreground, however one particular sky pattern (such as ours) may generate non-zero correlations by chance. It is therefore necessary to quantify an error on any correlation value obtained introduced by the possibility of a chance alignment of structures. We can do this by comparing the results to those of situations for which we definitely wouldn't expect any correlation except by chance. Different but equally sized patches of the all sky dust map can be correlated with the QUaD maps in the same way as the real section of the dust map. If we imagine that we have a cookie cutter shaped like Figure 4.3 we can work our way around the sky in longitude whilst staying at the same latitude cutting out maps to use. Then flipping to the same latitude in the opposite hemisphere and again working around the sphere in longitude provides a total of 37 QUaD sized regions of dust.

As the all-sky map in Figure 4.2 shows there is significantly more dust along the galactic plane so we should stay away from this. In the galactic co-ordinate system the galactic plane runs across the centre and locations are defined with galactic latitudes,  $l$ , and longitudes,  $b$ . QUaD, however, uses the equatorial co-ordinate system with its pointing information given in terms of right ascension (RA) and declination (Dec). Figure 4.6 illustrates in both co-ordinate frames the arrangement of the 37 regions along with the location of QUaD.

Each of these maps is then treated in the same way as before to give maps similar

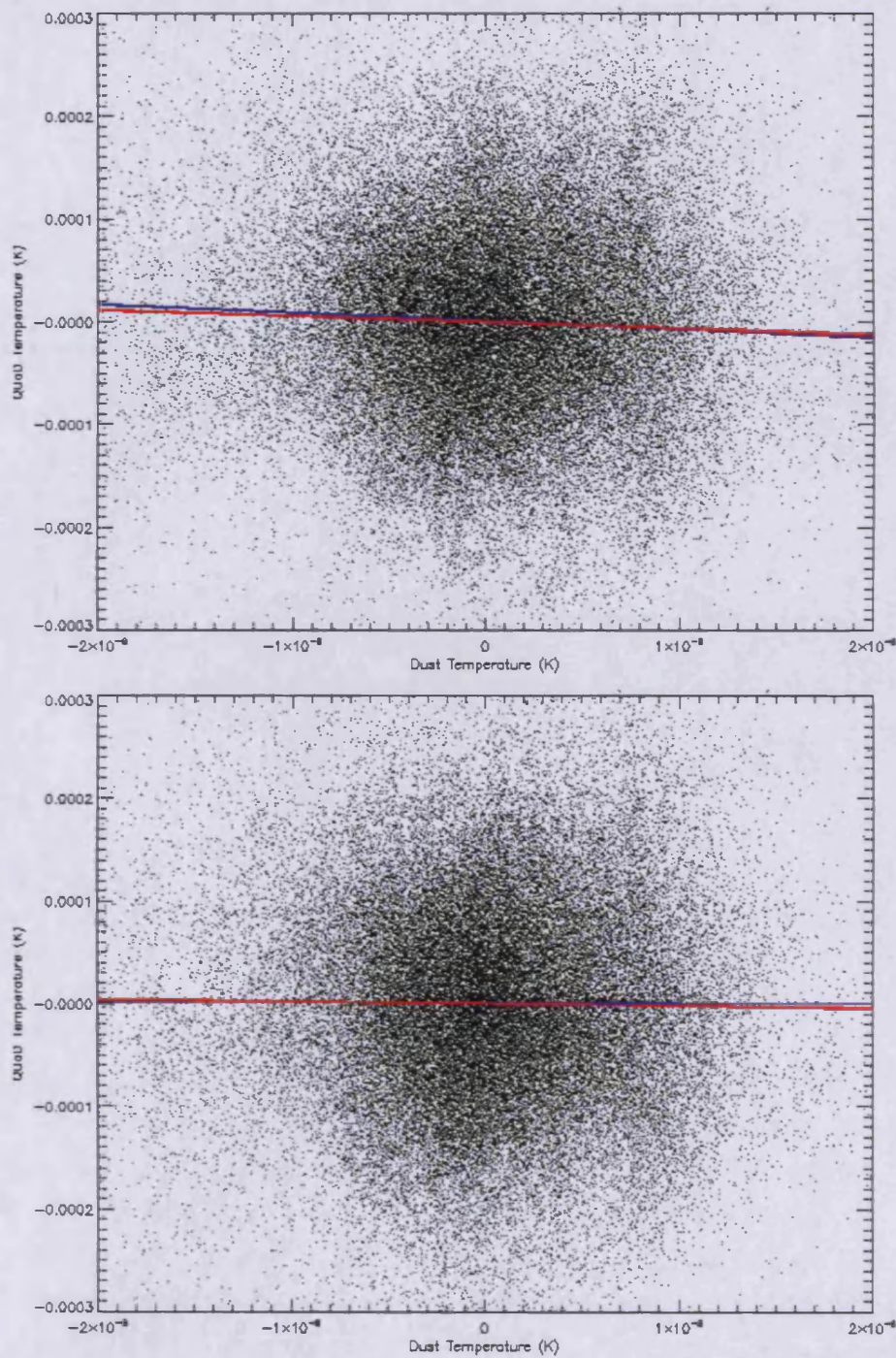


Figure 4.5: Dust Scatter Plots

Pixel by pixel correlations between QUaD CMB maps and dust maps at 100 GHz (top) and 150 GHz (bottom) with a least chi-square linear fit (blue) and a least absolute deviation fit (red) overplotted.

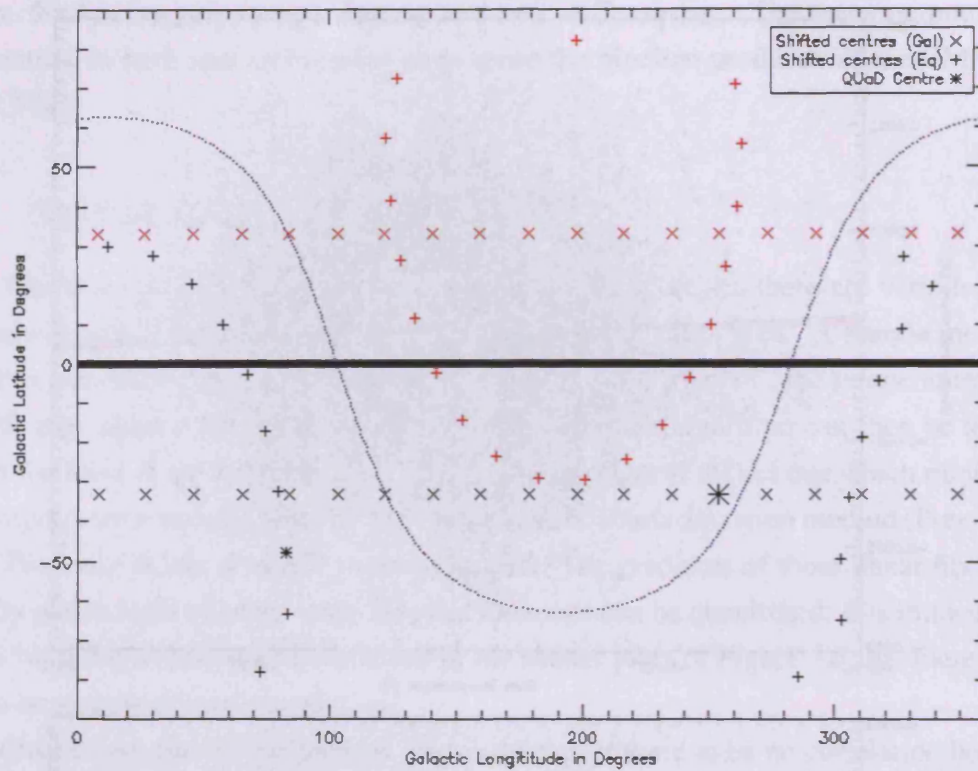


Figure 4.6: QUaD Sized Regions Around the Sky

The Galactic Plane shown as the thick black line in the galactic co-ordinate system translates to the dotted line in the Equatorial frame. The centre of QUaD's observing region is marked with an asterisk and the 37 identically sized alternative regions are marked with crosses and plus signs in the two co-ordinate systems.

to those in Figure 4.4 and scatter plots like those in Figure 4.5. The standard deviation amongst the alternative foreground regions can then be taken as the errors on the linear fit gradients as given in Table 4.1.

Correlations and covariances are defined as measures of strength between two or more sets of random variates. Cosmic covariance (Chiang et al., 2008), in analogy with cosmic variance, is a limitation arising as a consequence of our single sky preventing us from being sure that any correlation between the CMB and the foreground is accurate. This cosmic covariance can be expressed via a cosmic correlation coefficient, a value between  $-1$  and  $1$  quantifying the level of similarity amongst the temperatures. Positive or negative unity indicates a perfect correlation whilst zero means there is no correlation. The coefficient,  $x_{cmb,F}$ , is calculated from the temperatures of the CMB and foreground,  $T_{cmb}$  and  $T_F$  respectively, according to:

$$x_{cmb,F} = \frac{\langle T_{cmb} T_F \rangle - \langle T_{cmb} \rangle \langle T_F \rangle}{\sigma_{cmb} \sigma_F} \quad (4.3)$$

where the angled brackets denote averages and  $\sigma$  the variance. Again an error can be found on this coefficient by calculating its value for each shifted region and taking the standard deviation from the results.

### 4.3.2 CORRELATION RESULTS AND DISCUSSION

The cosmic correlation coefficient results with their errors are summarized in the table below along with those from the linear fits:

	100 GHz	150 GHz
Least chi-square linear fit	$-7.89 \pm 8.00$	$-0.33 \pm 7.18$
Least absolute deviation fit	$-5.89 \pm 7.34$	$-1.92 \pm 7.00$
Cosmic correlation coefficient	$-0.042 \pm 0.063$	$-0.001 \pm 0.037$

Table 4.1: Results from the linear fits and the correlation coefficient between QUaD's CMB maps and the dust predicted in its observing region.

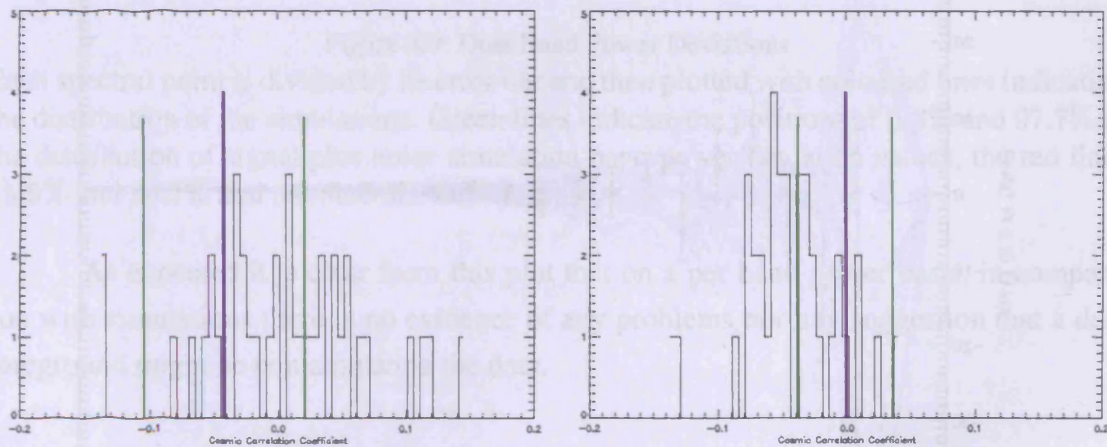


Figure 4.7: Correlation Histograms

The scatter amongst the 37 shifted region CMB-dust correlation coefficient is shown with QUaD's correlation coefficient (purple line) at 100 GHz (left) and 150 GHz (right).

Histogram plots can be made illustrating the scatter seen in the correlations among the 37 alternative regions. The QUaD correlation value is shown in purple with green lines marking one standard deviation either side.

Whilst interesting that the statistical tests result in a negative correlation, it is clearly not significant in light of the errors which are all greater than the value of the correlations themselves. The histogram is tending towards a Gaussian shape albeit with a slightly negative mean. Both histograms show the zero point encompassed within the two green lines which are the  $1\sigma$  error boundaries, and thus to within  $1\sigma$  there is no significant correlation. We can therefore conclude that the negative correlation observed is more likely due to a chance matching of morphology rather than actual foreground contamination.

### 4.3.3 CROSS CORRELATIONS

In Section 3.2.7 it was mentioned that power spectra could be calculated between the two frequencies; a cross frequency spectrum. The same principles can be applied to obtain a cross power spectrum between the QUaD CMB maps and the dust map, rather than between the 100 GHz and 150 GHz CMB maps. Error bars on this can be found as the scatter amongst a set of cross spectra produced from signal plus noise CMB simulations (see Section 3.2.4) and the dust map. In QUaD's analysis the first two band powers are ignored because the CMB isn't measured well on these large angular scales, hence these are shown fainter in the plot, Figure 4.8.

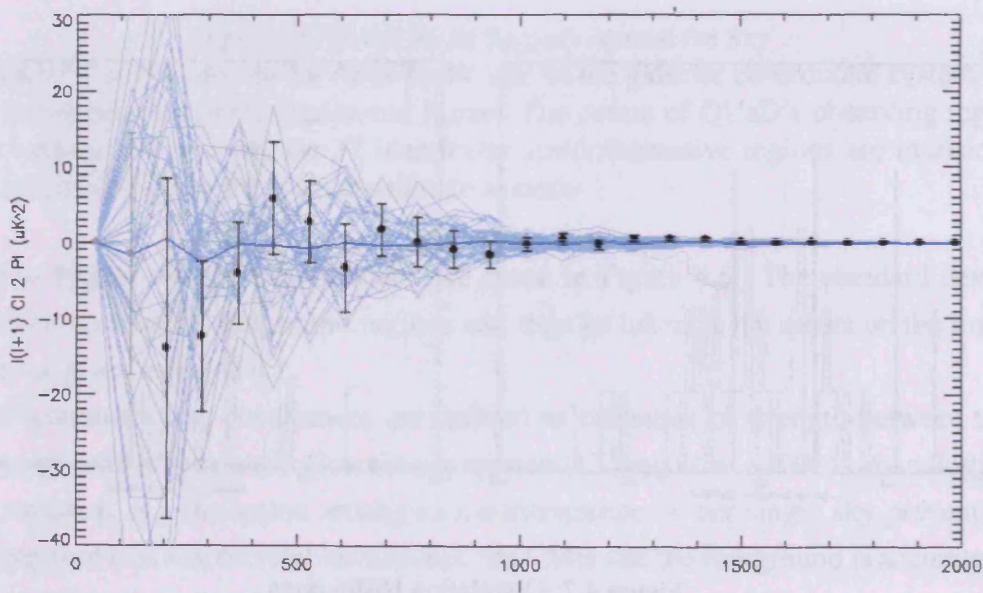


Figure 4.8: Cross Power Spectrum

The power spectrum obtained between QUaD's CMB map and the dust map. The results of the same cross spectrum performed with simulated CMB maps are shown in light blue with their average as the blue line.

It can be seen that all of the points, inclusive of their error bars, lie within the spread of simulations with not a single band power showing any extreme behaviour. As a further clarification of this result we can take this cross power spectrum and use it to create a band power deviation plot in exactly the same way as Section 3.2.9 described.

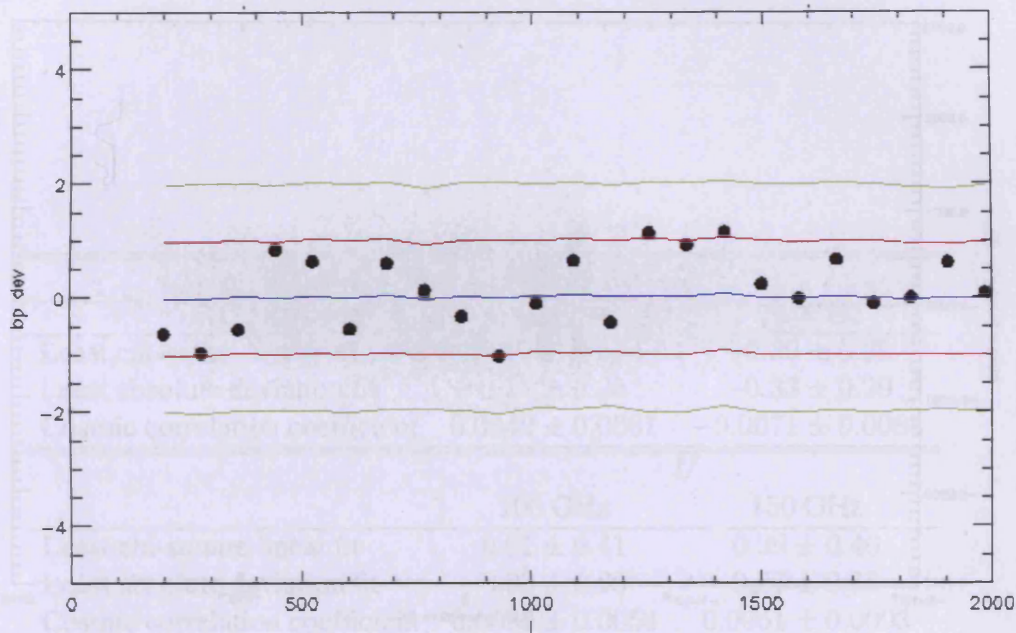


Figure 4.9: Dust Band Power Deviations

Each spectral point is divided by its error bar and then plotted with coloured lines indicating the distribution of the simulations. Green lines indicate the positions of 2.3% and 97.7% of the distribution of signal plus noise simulation band power deviation values, the red lines 15.9% and 84.1% and the blue line 50%.

As expected it is clear from this plot that on a per band power basis, in comparison with simulations there is no evidence of any problems nor any suggestion that a dust foreground might be contaminating the data.

#### 4.3.4 POLARIZATION CORRELATIONS

Section 4.2.2 concluded that a simple yet robust model of the dust polarization was to assume a perfect correlation between the dust's total intensity and its polarized intensity, just with 5% the strength. Under this assumption it is therefore satisfactory to test for polarized dust foreground contamination via correlations between the dust temperature maps and QUaD's polarization ones. We can use both the  $Q$  and  $U$  maps as well as constructing total polarization ones from equation 1.7:

$$I_p^2 = Q^2 + U^2 \quad (4.4)$$

Error bars on linear fits and cosmic correlation coefficients calculated may be obtained in the same way as for the temperature.

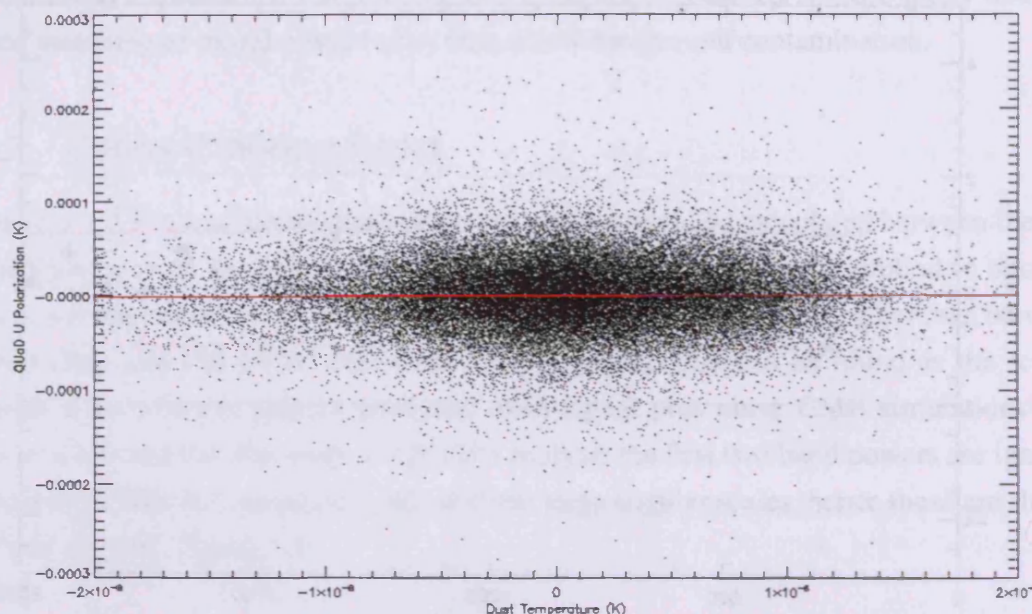


Figure 4.10: Polarization Scatter Plots

Pixel by pixel correlation between QUaD's 150 GHz  $U$  CMB map and the dust map with a least chi-square linear fit (blue) and a least absolute deviation fit (red) overlotted.

Figure 4.10 is just one example of the polarization scatter plots. All the results from  $Q$ ,  $U$  and total polarization intensity,  $P$ , at both frequencies are summarized in Table 4.2

Overall, despite a few instances in which this isn't true, the error bars are bigger than the value of the fits or correlations. There is no particular polarization state or frequency showing a significant correlation across all three tests, indicating that QUaD's polarization data is clean of any dust contamination.

The conclusion that neither QUaD's temperature nor its polarization data is tainted by a dusty foreground might seem like quite a boring result from a foreground science point of view. It is nevertheless very good news for QUaD, confirmation that a good choice of dust-free observing region was chosen and one step towards proving the robustness of our CMB results.

	$Q$	
	100 GHz	150 GHz
Least chi-square linear fit	$0.41 \pm 0.41$	$-0.39 \pm 0.29$
Least absolute deviation fit	$0.11 \pm 0.25$	$-0.33 \pm 0.29$
Cosmic correlation coefficient	$0.0042 \pm 0.0061$	$-0.0071 \pm 0.0084$
	$U$	
	100 GHz	150 GHz
Least chi-square linear fit	$0.91 \pm 0.41$	$0.29 \pm 0.40$
Least absolute deviation fit	$0.08 \pm 0.20$	$0.37 \pm 0.38$
Cosmic correlation coefficient	$0.0093 \pm 0.0054$	$0.0051 \pm 0.0093$
	$P$	
	100 GHz	150 GHz
Least chi-square linear fit	$1.02 \pm 1.35$	$0.59 \pm 1.03$
Least absolute deviation fit	$8.45 \pm 4.91$	$7.63 \pm 4.16$
Cosmic correlation coefficient	$0.0083 \pm 0.017$	$0.0078 \pm 0.027$

Table 4.2: Polarization linear fits and correlation coefficient results between QUaD's CMB polarization maps and the dust map.



# 5 SYNCHROTRON

---

“SCIENTISTS HAVE DISCOVERED A NOISE MADE JUST PRIOR TO THE BIG BANG THAT SOUNDS SOMETHING LIKE ‘OOPS’! ”

CULLY ABRELL

## 5.1 SYNCHROTRON RADIATION

Having established through various statistical analyses and cross correlation studies that dust did not contaminate either QUaD’s temperature or polarization data to any significant level we can now turn our attention to another potential foreground candidate. Figure 4.1 illustrates that whilst dust is the dominant foreground component at higher frequencies, below around 50 GHz synchrotron emissions become more significant. At QUaD’s 100 and 150 GHz frequencies, however, the expected levels of synchrotron radiation are very low. We can nevertheless perform the same tests to ensure this is the case and that no problems are revealed.

When cosmic ray electrons are accelerated in a magnetic field they emit synchrotron radiation. This often occurs in association with type Ib (Wolf-Rayet stars which have lost almost all of their hydrogen in a heavy solar wind to a companion star) and type II (single very massive stars) supernovae. The Galactic magnetic field accelerates relativistic electrons released in a supernova causing them to emit synchrotron radiation dependent upon the electron energy distribution and the strength of the magnetic field. The frequency of the emission for electrons with a relativistic gamma  $\gamma \gg 1$  is given by:

$$\omega = \frac{qB}{\gamma mc} \quad (5.1)$$

with  $B$  the magnetic field strength, and  $q$  and  $m$  the charge and mass of an electron respectively. In the extremely relativistic case, beaming will occur, bunching the radiation, and resulting in an emission spectrum with a characteristic critical frequency:

$$\omega_c = \frac{3\gamma^2 qB}{2mc} \sin \alpha \quad (5.2)$$

$\alpha$  being pitch angle; the angle between the electron's velocity vector and the magnetic field.

### 5.1.1 INTENSITY MODELS

As Figure 4.1 demonstrated, synchrotron radiation is most dominant at radio wavelengths and this therefore means we can use radio maps to create templates of the synchrotron radiation and in a similar way as for the dust extrapolate it up to CMB frequencies. For this again we need to know how the emission scales with frequency. A simple power law is most commonly used for the frequency dependence with a spectral index  $\alpha$ :

$$T(\nu) = T(\nu_*) \left(\frac{\nu}{\nu_*}\right)^{-\alpha} \quad (5.3)$$

in which  $\nu_*$  is the reference radio frequency and  $T$  is the thermodynamic temperature (proportional to intensity), as opposed to the antenna temperature more commonly used in long wavelength astronomy, which follows a power law with a different spectral index.  $\alpha$  in turn depends upon the cosmic ray electron energy distribution, also expressed as a power law with an index  $\gamma$ :

$$N(E) \propto E^{-\gamma} \quad (5.4)$$

The intensity spectral index,  $\alpha$ , is related to this energy spectral index by  $\alpha = (\gamma - 1)/2$  and takes values  $0.5 < \alpha < 1.1$  based on  $2.0 < \gamma < 3.2$ .

Data from four separate surveys (Jodrell Bank MkI, Bonn 100 meter, Parkes 64 meter and Jodrell Bank MkIA telescopes) were combined to yield a full sky radio continuum brightness map at 408 MHz (Haslam et al., 1981, 1982). Whilst this map, Figure 5.1, has an angular resolution of  $0.85^\circ$  there are still sufficiently large enough errors associated with it to warrant a significant uncertainty in an extrapolation to a higher frequency, and also there is no comparable all-sky map with which to investigate the spectral index. Smoot (1999) describes other incomplete sky radio maps of varying angular resolutions and levels of uncertainty which ultimately reveal our general lack of understanding of the true spectral index.

It was suggested in Bennett et al. (2003b) that only  $\sim 10\%$  of synchrotron radiation comes from the electrons trapped in the magnetic fields of discrete supernova remnants. The remaining 90% is from the diffuse emissions of cosmic ray electrons spread across the galaxy. These two components have very different spectral indices (Lisenfeld & Völk, 2000) which also vary over frequency range. The spectral shape of the diffuse synchrotron

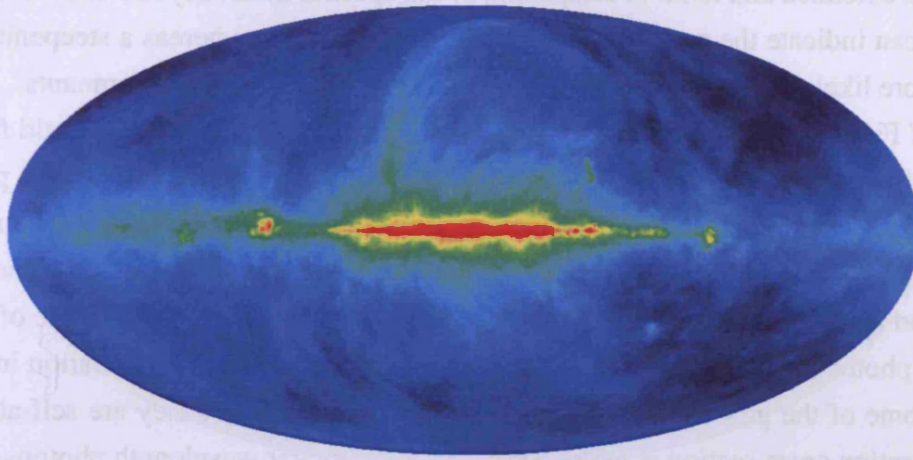


Figure 5.1: All-Sky Synchrotron Map  
Radio continuum brightness map at 408 MHz from 4 separate surveys.  
(Image: NASA - [http://lambda.gsfc.nasa.gov/product/foreground/f\\_images.cfm](http://lambda.gsfc.nasa.gov/product/foreground/f_images.cfm))

emission is determined by the physical processes affecting the propagation of the cosmic ray electrons. Propagation by diffusion or by convection, energy losses occurring via synchrotron radiation, inverse Compton scattering, adiabatic loss, or free-free emission, and the confinement of the electrons within a galaxy will all characterize the spectrum.

A steep spectral index ( $\alpha > 0.9$ ) indicates that cosmic ray electrons are largely confined to their host galaxies and lose a lot of their energy before they escape from the galaxy halo, whereas a flatter spectral index ( $\alpha < 0.7$ ) suggests the cosmic rays are free to leave the halo before they lose energy. The secondary energy losses occurring among the cosmic ray electrons particularly affect the synchrotron spectrum at higher frequencies. Propagation via diffusion involves scattering of the electrons by magnetic field irregularities, whereas convection is an outward systematic movement of the electrons. The extent to which the mechanism for propagation affects the spectral index is dependent on the confinement and energy losses. In the case of strong confinement with a substantial energy loss it makes little difference, but if considerable energy losses do not occur and the cosmic ray electrons may freely escape from the galaxy, then the means of their transmission plays a bigger role because unlike diffusion, convection is an energy independent process.

Whilst observations of the spectral indices of galaxies might reveal information about the degree of confinement as described above, no further firm conclusions regarding the nature of the propagation are able to be drawn, but a very flat spectral index is a sign of strong convection (Bennett et al., 2003b). Galactic halo observations can help to diagnose the importance of the energy losses, but these can be difficult to obtain because the haloes

tend to be extended and faint. A steepening of the spectral index beyond about 3kpc above the disk can indicate the presence of dominant energy losses, whereas a steepening below this is more likely due to the contribution of radiation from supernova remnants.

If Figure 4.1 were to be extended down to lower frequencies, we would find there is a low frequency cut-off to the synchrotron emissions, and hence a peak at a particular frequency defined by the critical frequency of equation 5.2, dependent upon the magnetic field strength of the environment. The cut-off at low frequencies arises because of self-absorption and free-free absorption. In propagating towards the observer some of the synchrotron photons may scatter off the electrons which are emitting the radiation in the first place. Some of the photon energy is lost to the electrons, hence they are self-absorbing. The absorption cross-section is larger for low energy, longer wavelength photons, thus explaining the decrease in flux and ultimate cut-off at low frequencies.

Fortunately at frequencies above  $\sim 70$  GHz we expect the synchrotron emission to be significantly below the CMB emission and at QUaD's frequencies the predicted power in our observing region a negligible  $0.03 \mu\text{K}$  (Pryke et al., 2009). Gold et al. (2009) found with the five year WMAP data that fixing the synchrotron spectral index had no influence on their cosmological conclusions because of the low levels involved.

### 5.1.2 EXTRAPOLATION TO CMB FREQUENCIES

Miville-Deschênes et al. (2008) reports on a synchrotron estimation made on the basis of an extrapolation of the Haslam 408 MHz data (Figure 5.1) with a spatially varying spectral index. They used the three year 23 GHz WMAP temperature and polarization data (Page et al., 2007; Hinshaw et al., 2007) along with models of the magnetic field in the galaxy obtaining a mean spectral index of  $\alpha = 0.96$ . The Haslam map is extrapolated to any frequency,  $\nu$  in GHz, via:

$$T_\nu = T_{408} \left( \frac{\nu}{0.408} \right)^{-\alpha} \quad (5.5)$$

in accordance with equation 5.3. Various models for  $\alpha$  are considered but the one used by the Planck collaboration in their foreground prediction models is Model 3 of Miville-Deschênes et al. (2008). In this one the assumption is made that the 23 GHz WMAP intensity,  $I_{23}$  (after subtraction of the CMB), is composed of synchrotron radiation,  $S_{23}$ , free-free emissions,  $F_{23}$ , and some anomalous emissions which are well correlated with the dust column density,  $E(B - V)$ , thus permitting  $\alpha$  to be calculated by:

$$\alpha = -0.248 \log \left( \frac{I_{23} - F_{23} - aE(B - V)}{T_{408}} \right) \quad (5.6)$$

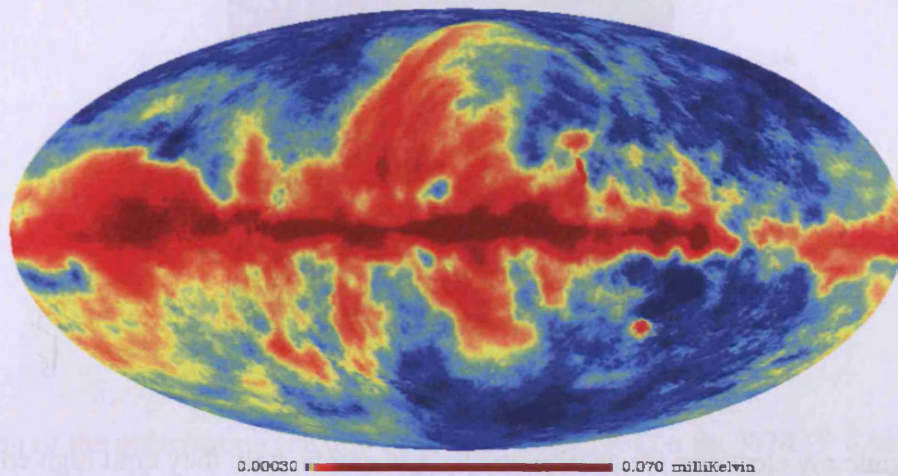


Figure 5.2: All-Sky Synchrotron Map

The Planck Sky Model was used to create a prediction of the synchrotron foreground at 100 GHz based upon an extrapolation of the Haslam map.

where  $a$  is taken to be 0.65 mK/mag and the factor 0.248 comes from  $1/\log(23/0.408)$ . This model therefore enables an all-sky map to be made of the synchrotron intensity at any frequency wherein the spectral index will vary spatially with the WMAP distribution. The free-free template used also comes from the WMAP estimations (Hinshaw et al., 2007).

The ‘Planck Sky Model’ is an IDL package developed for predicting the sky emission in the frequency range 10 – 1000 GHz based upon this method. I have used their software to make predictions of the sky’s synchrotron emissions at each of QUaD’s frequencies. There is not a significant amount of difference between that at 100 and at 150 GHz just as expected a slightly higher power at 100 GHz, shown in Figure 5.2.

### 5.1.3 POLARIZATION

Synchrotron emission is characteristically polarized because the magnetic field direction serves to organize the radiation into the plane of acceleration, as illustrated in Figure 5.3.

As in the case of dust we can make the assumption of correlation between the total and polarized intensity and therefore simply take a constant fraction of the total synchrotron intensity.

The degree of linear polarization could be as high as 75%, but this will usually be reduced to  $< 20\%$  by the magnetic field orientations varying along any particular line of sight (Bennett et al., 2003b). In addition the polarization plane of the radiation may be

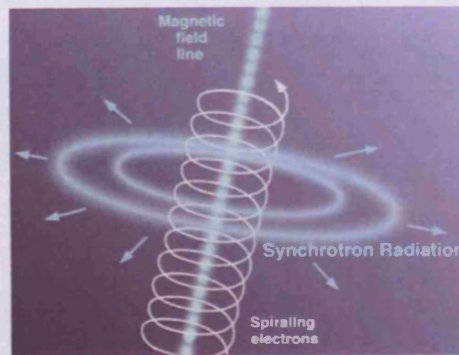


Figure 5.3: Synchrotron Radiation

When cosmic ray electrons are accelerated by a magnetic field they emit high energy photons linearly polarized in the plane of acceleration.

Image: Astronomy Online - <http://astronomyonline.org>

rotated along its transmission under the influence of parallel magnetic fields via the Faraday effect. This will also serve to lessen the polarized fraction. The actual polarization fraction,  $P(\nu)$ , may therefore be given by:

$$\frac{P(\nu)}{T(\nu)} = f_s g \quad (5.7)$$

$f_s$  being the intrinsic polarization fraction of 75% and  $g$  a geometrical reduction factor reflecting the extent to which magnetic field fluctuations about the line of sight result in depolarization.  $g$  takes a value between 0 and 1 and will depend upon the structure of the magnetic field and the distribution of the cosmic ray electrons.

Since free-free and anomalous emissions are assumed to be unpolarized, the 23 GHz WMAP polarization data (Hinshaw et al., 2007) is therefore likely to be dominated by synchrotron polarization. It can thus be used to constrain parameters of the magnetic field and a model of  $g$  across the sky is created. Miville-Deschênes et al. (2008) gives maps of the polarization fraction across the sky for their different models. Figure 5.4 shows the result from Model 3. In QUaD's observing region the level of synchrotron polarization is  $\sim 10 - 15\%$ .

## 5.2 LOOKING FOR SYNCHROTRON RADIATION IN QUAD DATA

Analysis from the all-sky map of Figure 5.2 can then proceed in much the same way as for the dust foreground detailed in Section 4.3 in the previous chapter. Firstly the relevant

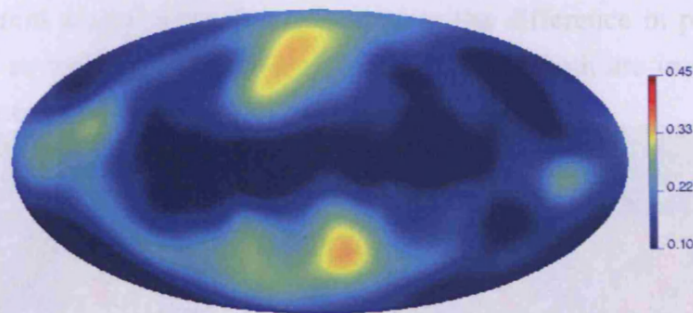


Figure 5.4: Polarization Fraction

Estimation of the polarization fraction across the sky based on the WMAP 3 year 23 GHz polarization data and models of the magnetic field (Miville-Deschênes et al., 2008).

section of the full sky map at each frequency is cut out to leave maps just over QUaD's observing region and the 'cookie cutter' used to provide 37 QUaD sized regions around the sphere for quantifying errors.

Following the same methods as before these two trimmed maps were then put through QUaD's map-making pipeline to yield template maps of the synchrotron radiation as if observed with QUaD's pointing, beams etc... which can be directly compared with those of the CMB.

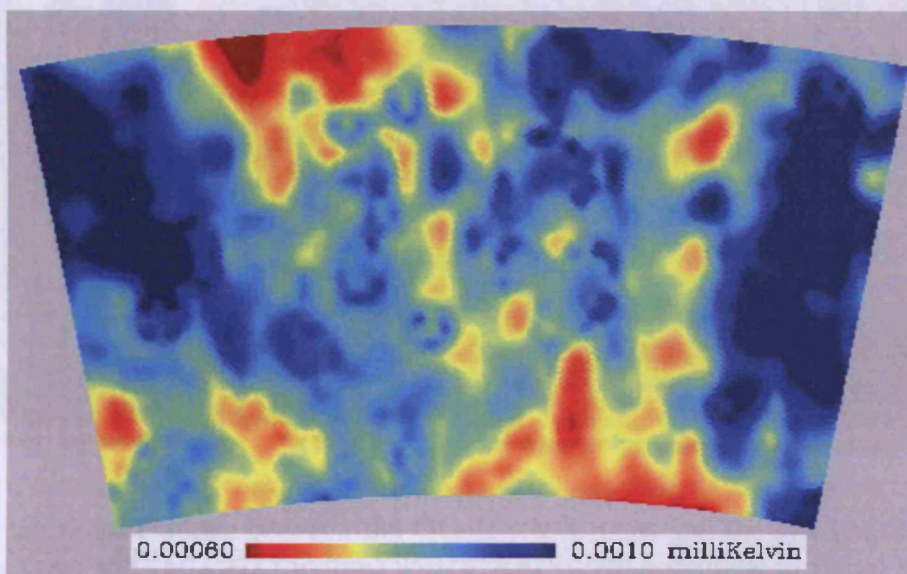


Figure 5.5: Synchrotron Map at 100 GHz

The all-sky synchrotron map trimmed to QUaD's observing region.

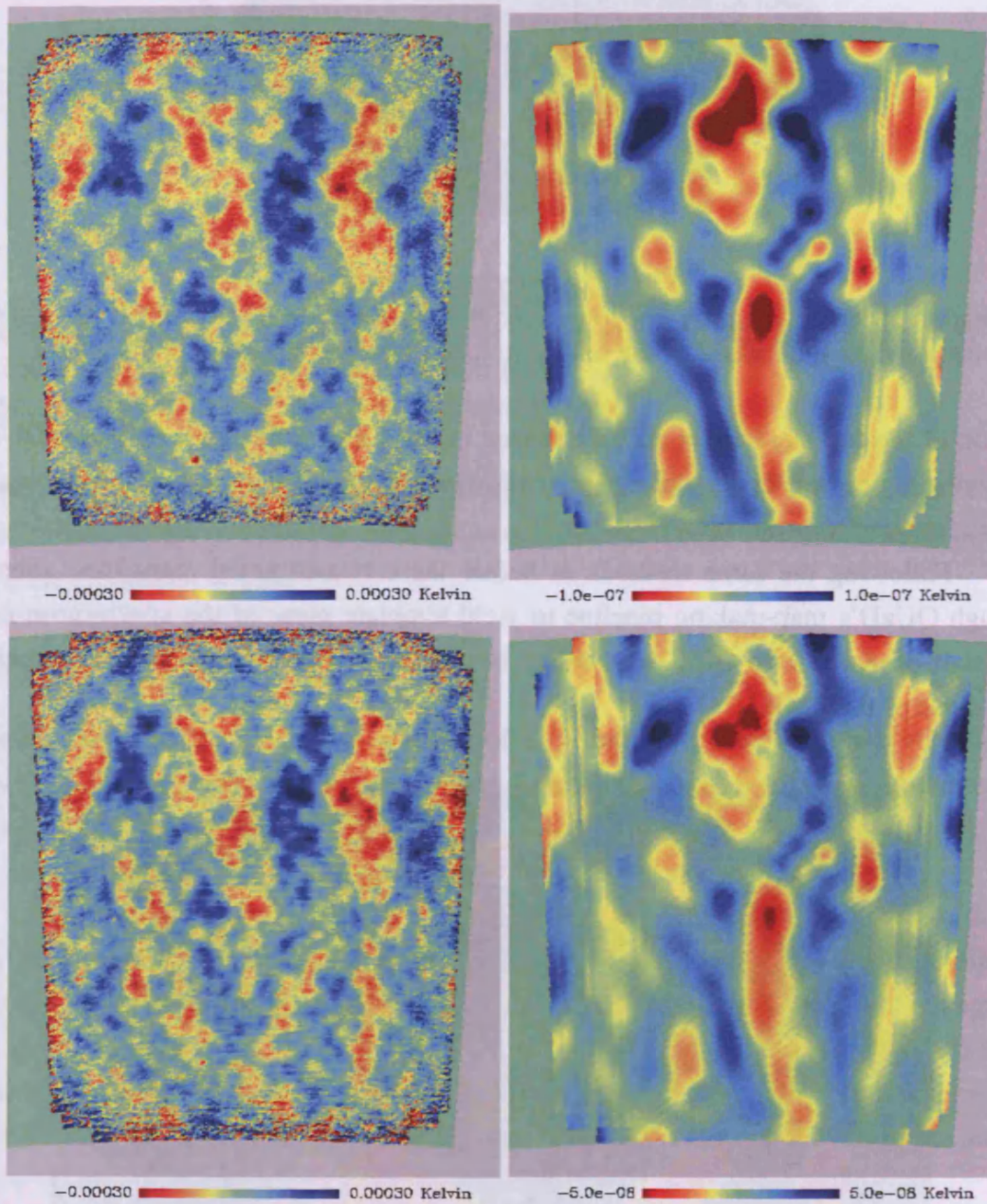


Figure 5.6: Field Differenced CMB and synchrotron maps

In the same way as the dust maps of Figure 4.4 these maps (right) came from the synchrotron prediction being run through QUaD's map-making pipeline and so can be directly compared with the CMB maps (left) at 100 GHz (top) and 150 GHz (bottom).

The different scales on these maps indicate the difference in power between the two frequencies, as well as highlighting how much lower both are in comparison to the temperature anisotropies we see in CMB maps.

### 5.2.1 STATISTICAL CORRELATIONS

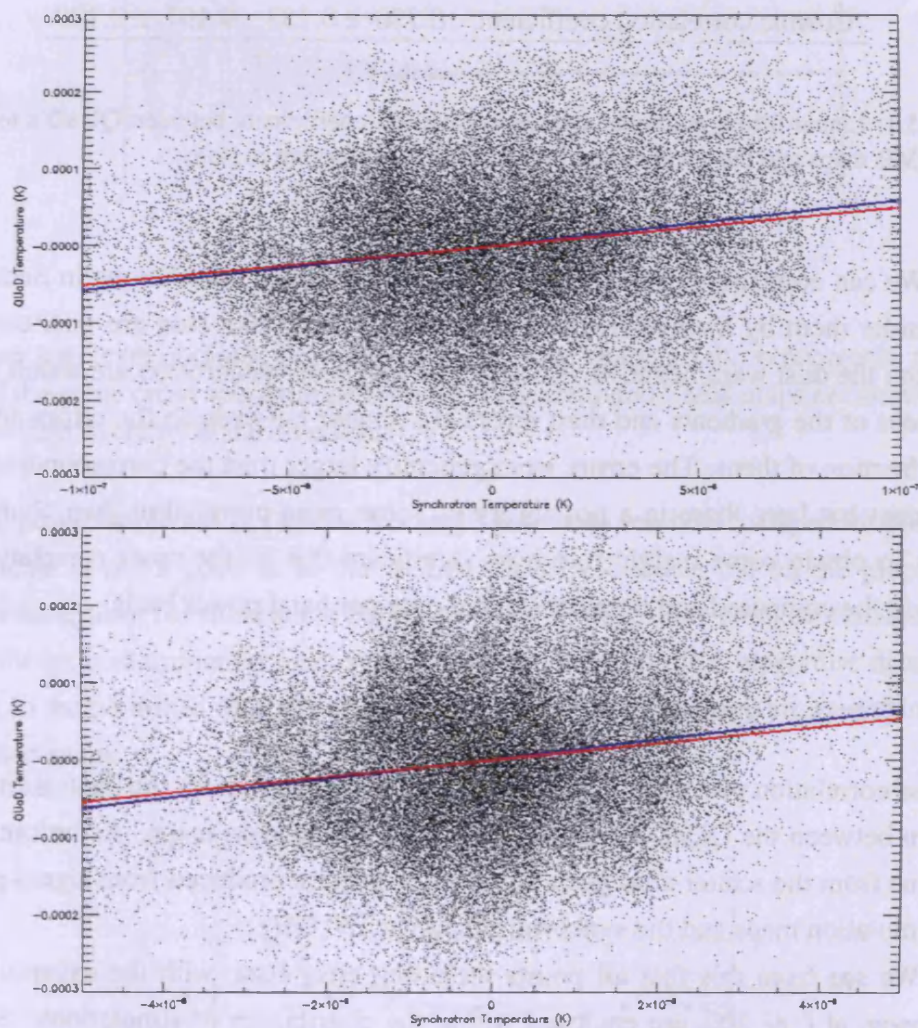


Figure 5.7: Synchrotron Scatter Plots

Pixel by pixel correlations between the QUaD CMB maps and the synchrotron maps at 100 GHz (top) and 150 GHz (bottom) with a least chi-square linear fit (blue) and a least absolute deviation fit (red) overplotted.

Next we make scatter plots equivalent to those in Section 4.3.1 where each pixel in the maps are individually plotted according to their CMB temperature and corresponding predicted synchrotron temperature. At each frequency two linear fits are carried out and

the cosmic correlation coefficient calculated with errors provided by the standard deviation amongst the same fits performed on regions shifted about the synchrotron map. Results are tabulated in Table 5.1 below.

	100 GHz	150 GHz
Least chi-square linear fit	$589 \pm 96$	$1275 \pm 207$
Least absolute deviation fit	$509 \pm 83$	$1084 \pm 176$
Cosmic correlation coefficient	$0.230 \pm 0.138$	$0.197 \pm 0.129$

Table 5.1: Linear fitting gradients and the correlation coefficients between QUaD's temperature CMB maps and the synchrotron predicted in its observing region.

We can compare these results to those from the dust correlations in Section 4.3.2 and consider them by themselves. All the correlations in this case are positive whereas those from the dust were negative. Because the levels of synchrotron are much lower the magnitudes of the gradients and their errors are greater but even so the errors are a much smaller fraction of them. The errors were generally larger than the corresponding statistic for the dust but here there is a possibility of some more correlation than chance might permit. To obtain some insight into how significant this is, the cross correlation power spectra can be computed and then considered on a per band power basis.

## 5.2.2 CROSS CORRELATIONS

The cross correlation plot of Figure 5.8 is the equivalent to that for the dust; a cross power spectrum between the QUaD CMB maps and the synchrotron maps. As before the error bars come from the scatter amongst a set of cross spectra produced from signal plus noise CMB simulation maps and the synchrotron map at 100 GHz.

We see from this that all points including error bars, with the exception of one band power, at  $\ell \sim 200$ , are enclosed within the distribution of simulations. So it must therefore be this one point pulling all the correlations to a value so much larger than the error. This band power itself has a large error associated with it, but by considering the band power deviations; each spectral point divided by its error bar, we can quantify its level of significance.

Although of greater significance than any of the band power deviations found in the dust investigation, this one point (along with two others to a lesser extent at higher  $\ell$ ) are still enclosed within the  $2\sigma$  line. This results suggests that we should not trust the QUaD CMB temperature band power at  $\ell \sim 200$  as much as we might the rest. In fact looking

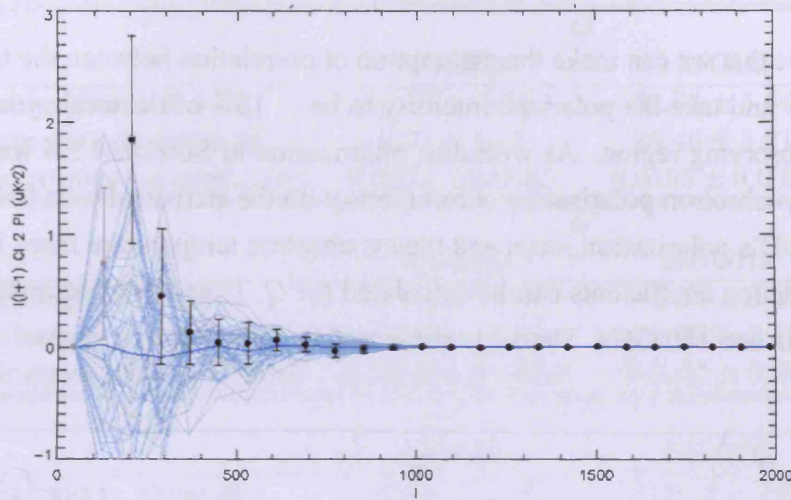


Figure 5.8: Cross Power Spectrum

The power spectrum obtained between QUAD's CMB map and the synchrotron map. The results of the same cross spectrum performed with simulated CMB maps are shown in light blue with their average as the blue line.

at the TT power spectrum in Figures 3.5 and 3.6 we can see how the spectral point at this angular scale is not a good fit to the  $\Lambda$ CDM model plotted in red on the graph. Aside from this exception, for subsequent band powers,  $l \gtrsim 250$ , there is no evidence to suggest any significant contamination from synchrotron radiation in the temperature data. We can now turn to the polarized data and check for synchrotron foreground emissions in QUAD's polarization maps.

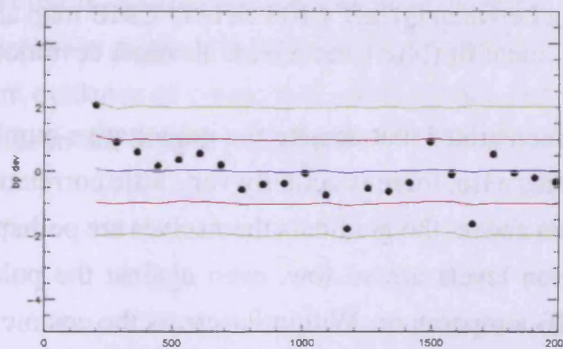


Figure 5.9: Synchrotron Band Power Deviations

Each band power from the cross spectrum is divided by its error bar. The lines indicate the distribution of the simulations: green lines indicate the positions of 2.3% and 97.7%, the red lines 15.9% and 84.1% and the blue line 50%.

### 5.2.3 POLARIZATION CORRELATIONS

We saw above that we can make the assumption of correlation between the total and polarized intensity and take the polarized intensity to be  $\sim 15\%$  of the total synchrotron intensity in our observing region. As with dust polarization in Section 4.3.4 we can therefore investigate synchrotron polarization correlations with the statistical tests being carried out between QUaD's polarization maps and the synchrotron temperature map. Linear fits and cosmic correlation coefficients can be calculated for  $Q$ ,  $U$  and total polarization intensity,  $P$ , at 100 GHz and 150 GHz. These are presented in Table 5.2.

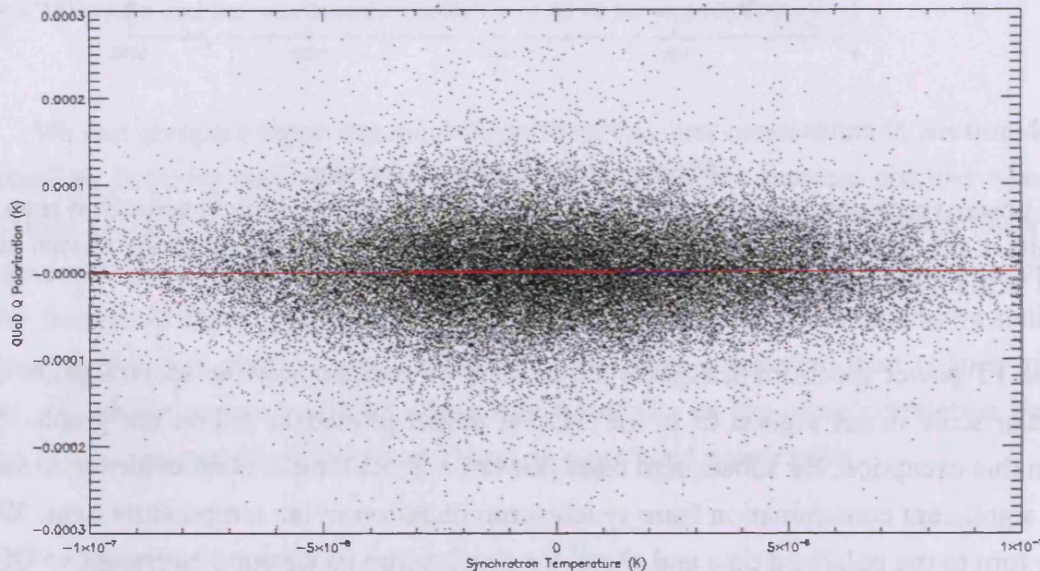


Figure 5.10: Polarization Correlation

An example scatter plot between QUaD's 100 GHz  $Q$  CMB map and the synchrotron map with a least chi-square linear fit (blue) and a least absolute deviation fit (red) overplotted.

Figure 5.10 demonstrates that despite the quantitative numbers of the linear fits in Table 5.2 suggesting otherwise, there is actually very little correlation present. As with the temperature scatter plots above, the gradients themselves are perhaps so large in magnitude because the synchrotron levels are so low, even against the polarization data which is  $\sim 10\%$  that of the CMB temperature. Within  $2\sigma$  errors the cosmic correlation coefficients are insignificant and considering the range of possible values with magnitudes 0 to 1, where 1 is a perfect correlation, such low values as these indicate only a very slight hint of a correlation.

A conclusion can be made therefore that, excluding the band power at  $\ell = 200$ ,

	$Q$	
	100 GHz	150 GHz
Least chi-square linear fit	$11.79 \pm 1.91$	$34.86 \pm 5.66$
Least absolute deviation fit	$6.93 \pm 1.12$	$36.46 \pm 5.91$
Cosmic correlation coefficient	$0.0073 \pm 0.0065$	$0.0155 \pm 0.0083$
	$U$	
	100 GHz	150 GHz
Least chi-square linear fit	$-28.41 \pm 4.61$	$-3.52 \pm 0.57$
Least absolute deviation fit	$-34.79 \pm 5.64$	$-0.979 \pm 0.157$
Cosmic correlation coefficient	$-0.0120 \pm 0.0089$	$-0.0021 \pm 0.0053$
	$P$	
	100 GHz	150 GHz
Least chi-square linear fit	$-79.84 \pm 12.95$	$-141.4 \pm 22.9$
Least absolute deviation fit	$-288.0 \pm 37.0$	$-404.8 \pm 65.7$
Cosmic correlation coefficient	$-0.039 \pm 0.021$	$-0.045 \pm 0.031$

Table 5.2: Results from the linear fits and correlation coefficient calculations between QUaD's CMB polarization maps and the synchrotron map.

there is no significant contamination from synchrotron emissions in the QUaD's temperature and polarization CMB data. Although there are a few hints of slightly more correlations amongst large scale structures in the maps these are by far not significant enough, with such a low level of synchrotron power in the field, to present any problems or lead to any doubt that a synchrotron foreground might be affecting our results above  $\ell \sim 250$ .

The conclusions from the template cross correlations presented in this and the previous chapter were reported in Section 8 of Pryke et al. (2009). The paper states that although a non-zero correlation might arise as a result of chance, our investigations have highlighted no significant evidence of contamination from dust and also that the predicted level of synchrotron power in our field is negligible.





# 6 FAR INFRARED BACKGROUND

---

“DOES EVERYTHING IN LIFE HAVE TO HAVE A PERFECTLY REASONABLE EXPLANATION; ALL GROUNDED IN CLEAR SCIENTIFIC REASON; NO MAGIC LEFT IN THE UNIVERSE?”

CLARK KENT - LOIS AND CLARK

## 6.1 GALAXY CLUSTERING

Chapter 1 explored the theory of gravitational instability causing the growth of density perturbations in an expanding universe and how this leads to the large scale structures we observe today. One component of the theory is the idea that galaxies are the result of baryonic matter accreting into dark matter potential wells, known as halos. Surveys reveal the presence of galaxies throughout the cosmos from around  $z \sim 2-3$ , yet despite a wealth of observations, the processes governing galaxy formation and therefore their distribution are poorly understood. If they followed the patterns set by the dark matter potential wells then all galaxies would show a similar spatial arrangement. Be that as it may, it appears in fact that the various types of galaxies cluster in different ways suggesting that in fact they are not perfect tracers of the underlying dark matter. More luminous galaxies show more correlation than fainter ones for example, whilst older ones are more correlated than their younger counterparts (Dressler, 1980). The properties of infrared galaxies make them sensitive to the role of galaxy formation and subsequent evolution, and as such they are ideal candidates to study in the context of clustering.

### 6.1.1 INFRARED GALAXIES

Infrared galaxies are characterized by their high dust content and star formation rates. It is their dustiness which makes them more efficient at star formation as it cools the collapsing

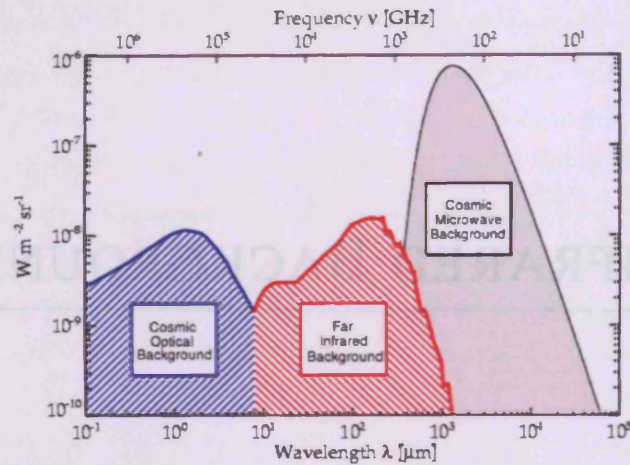


Figure 6.1: Cosmic Backgrounds

Spectral energy distributions with frequency of the cosmic optical, far infrared and cosmic microwave backgrounds (Dole et al., 2006).

protostars. The dust absorbs the ultra-violet (UV) and optical photons emitted by stars, active galactic nuclei (AGN) and starbursts within the galaxy, re-emitting them as infrared (IR) radiation, shifting the spectrum to longer wavelengths. The far infrared region of the electromagnetic spectrum covers the wavelength range  $25 \mu\text{m}$  to  $350 \mu\text{m}$ , hence emitting in this region, and up to millimeter wavelengths, with a peak at  $170 \mu\text{m}$ , the emissions from these galaxies make up what is called the Far Infrared Background (FIRB).

Such a background radiation that would trace the initial stages of galaxy formation was predicted over 40 years ago in Partridge & Peebles (1967) and subsequently models of the FIRB (e.g. Desert & Puget, 1990) have been developed following the first observations of infrared galaxies. The Infrared Astronomical Satellite (IRAS), in particular, provided a lot of new information regarding IR galaxies via an all sky survey at wavelengths 12, 25, 60 and  $100 \mu\text{m}$  (Soifer & Neugebauer, 1985). For the first time a calculation of the luminosity function of IR galaxies was possible at  $z < 0.25$ .

For a long time the FIRB remained hidden amongst strong foregrounds and only permitted upper limits to be determined. In 1996, however, the first tentative detections were made. As reported in Puget et al. (1996) the Far InfraRed Absolute Spectrometer (FIRAS), a Michelson interferometer on COBE, completed a whole sky survey over wavelengths  $105 \mu\text{m}$  to  $5 \text{mm}$ . Interplanetary and interstellar dust components, along with the CMB were measured and removed leaving a clear excess at submillimeter wavelengths that could not be explained as either dust or galactic components. Figure 6.2 shows the diffuse glow of the FIRB after foregrounds have been subtracted from the entire far infrared sky.

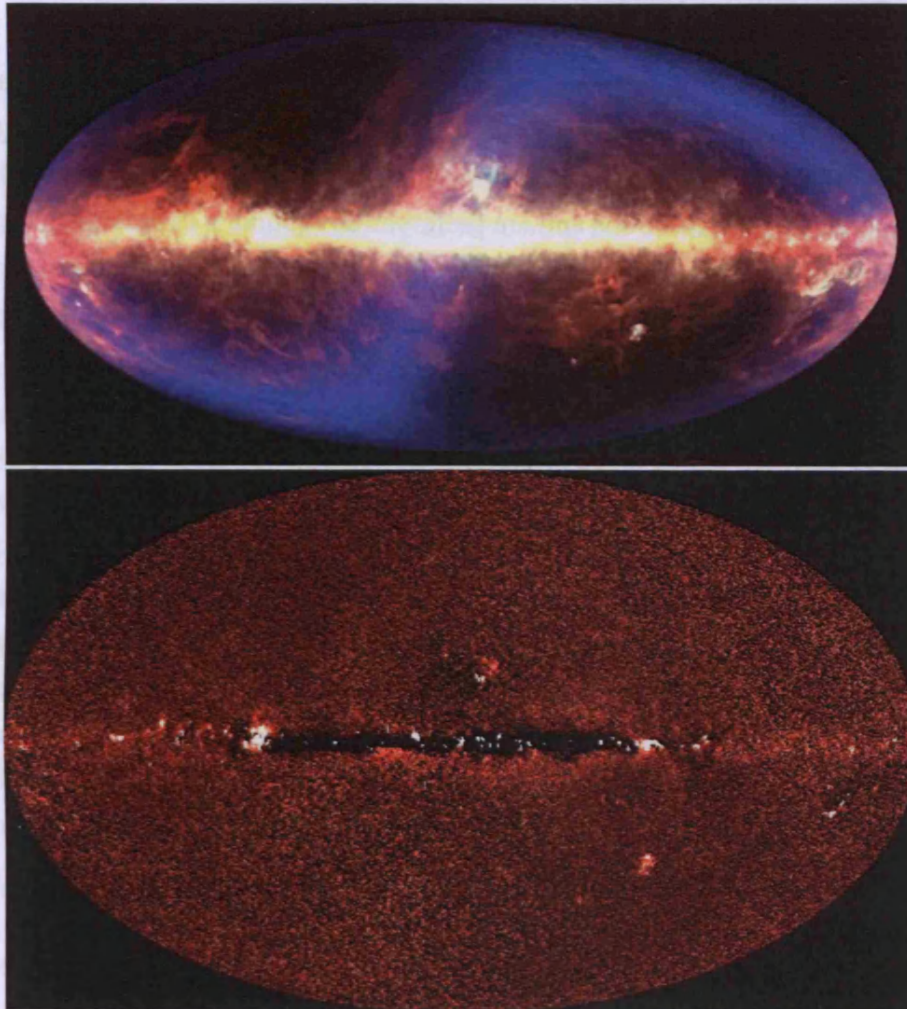


Figure 6.2: The Far Infrared Sky Before and After Subtraction of Foregrounds

The top image shows the entire sky in the far infrared with contributions from our Solar System, the Milky Way and the universe. After the dusty foreground contributions are removed a diffuse background glow remains.

(Images: NASA - <http://antwrp.gsfc.nasa.gov/apod/>)

After its initial detection with FIRAS, another instrument aboard COBE, the Diffuse InfraRed Background Experiment (DIRBE) provided confirmation and measurements at several wavelengths (Hauser, 1998). Since then contributions from many other surveys have added to our knowledge about the IR universe.

### 6.1.2 CLUSTERING OF INFRARED GALAXIES

The clustering strength of a given galaxy population depends on the typical mass of the extended halos hosting the population. A more massive halo supports a more clustered population. Infrared galaxies, especially the more luminous ones, are frequently associated with mergers and interactions and are preferentially found in overdense environments. Their clustering strengths are therefore greater than those of other populations.

## 6.2 BIAS

The extent of correlation between the infrared galaxy distribution and the large scale dark matter density field may be quantified by a bias parameter,  $b$ . When it was realized in the mid-80's that galaxy clusters themselves show clustering properties, Kaiser (1984) introduced the concept of bias. His paper focussed on the Abell clusters (groups of a least 50 galaxies within 1.5 Mpc), explaining how such structures might form in regions where the primordial density enhancement was unusually large. The idea is that the baryonic oscillations causing the CMB were superposed on underlying larger scale, smaller amplitude density fluctuations. Such fluctuations would have been created by the total matter content of the universe, of which a large component is dark matter. Galaxies would form where the overdensity was beyond a critical threshold, with clusters then forming in the regions of extra-enhanced density.

The bias parameter is defined as the ratio in overdensities,  $\delta = \Delta\rho/\bar{\rho}$ , between the galaxies and total mass:

$$b = \frac{\delta_{gal}}{\delta_m} \quad (6.1)$$

where  $\bar{\rho}$  denotes the mean level and the densities are per comoving unit volume.

This is a somewhat simplistic definition of the parameter suggesting a trivial correlation between the spatial distributions of dark matter and galaxies. It is likely to be more complex than this; perhaps depending upon spatial frequency,  $k$ , redshift,  $z$ , radiation frequency,  $\nu$ , galactic masses and so on. On small scales there will be pairs of galaxies within a single dark matter halo, whilst on large scales the halos themselves will cluster, hence resulting in a dependency upon spatial frequency, with some transition region between these

two extremes. The different spectral energy distribution of different galaxies will mean that at different frequencies the galaxies will exhibit different clustering properties accordingly, while the redshift dependency arises from independent evolutions of the dark matter and the infrared galaxies. An alternative definition of the bias incorporating these effects is:

$$\frac{\delta\rho_{gal}(k, \nu, z)}{\bar{\rho}_{gal}(k, \nu, z)} = b(k, \nu, z) \frac{\delta\rho_m(k, z)}{\bar{\rho}_m(k, z)} \quad (6.2)$$

$\delta\rho$  being the fluctuation in density from the mean  $\bar{\rho}$ .

A value of  $b = 1$  implies an unbiased universe in which matter exactly follows the pattern of light on large-scales, whereas higher values mean a biased universe with total mass more widely dispersed than the light, following the underlying dark matter density distribution.

Both simulations and observations have been used to verify the ideas of bias and to gain more of an understanding about its dependency on various factors. Weinberg et al. (2004) ran hydrodynamic simulations of galaxies and dark matter to determine that the bias should increase with  $z$ . Observationally the bias has been measured more at optical and radio wavelengths where there more are sources seen than in the far-IR and submillimeter. Evidence has been found in both spectral bands that bias increases with redshift (Marinoni et al., 2006; Brand et al., 2003), but it does not necessarily follow that the same applies in the infrared. In 2007 Spitzer data was used to provide a constraint on the bias at the far infrared wavelength 160  $\mu\text{m}$  by measuring fluctuations in the FIRB (Lagache et al., 2007).

## 6.3 FAR INFRARED BACKGROUND ANISOTROPIES

The discrete nature of far infrared sources and the correlations between these sources, mean we expect the FIRB to be anisotropic on both small and large scales respectively.

### 6.3.1 POWER SPECTRUM

Knox et al. (2001) presents the angular power spectrum of the FIRB anisotropies at frequency  $\nu$  as:

$$C_\ell^\nu = \int \frac{dz}{r^2} \frac{dr}{dz} a^2(z) \bar{j}^{-2}(\nu, z) b^2(k, \nu, z) P_M(k)|_{k=\ell/r} G^2(z) \quad (6.3)$$

There are lots of terms in this equation to consider.  $\frac{dz}{r^2} \frac{dr}{dz} a^2(z)$  is geometrical and independent of both radiation frequency and spatial frequency,  $k$ .  $r$  is the co-ordinate distance from our position and  $a$  the scale factor. Each one is a decreasing function with respect to redshift,  $z$ .  $G^2(z)$  is the linear theory growth function (Peebles, 1980), which describes

the effect on the power spectrum due to our living in an expanding universe. Expansion causes the matter density to decrease hence slowing down the accretion of matter, but it is not straight-forward and requires a suppression factor,  $g$ , dependent on both the matter and dark energy densities,  $\Omega_m$  and  $\Omega_\Lambda$ , both now and as functions of redshift:

$$G^2(z) = \frac{1}{(1+z)^2} \frac{g^2(\Omega_m(z), \Omega_\Lambda(z))}{g^2(\Omega_{m0}, \Omega_{\Lambda0})} \quad (6.4)$$

Combining the geometrical terms we obtain the function shown in Figure 6.3 wherein  $r^{-2}$  is the most dominating effect causing the very steep decrease with redshift at low  $z$ .

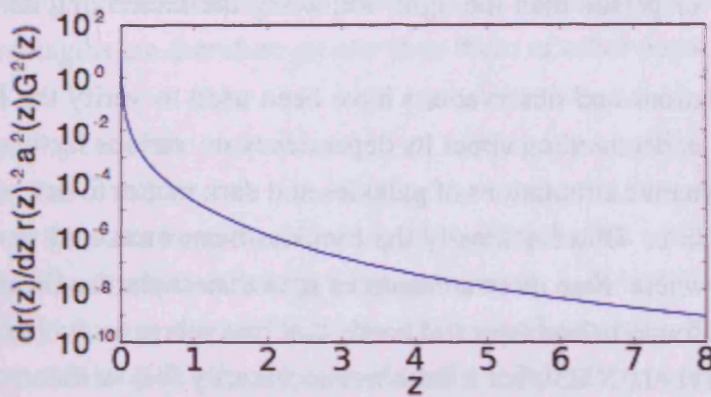


Figure 6.3: Contribution to the FIRB Power Spectrum from Geometrical Effects

The first term of equation 6.3 is the combination of various geometrical functions of redshift, which combined with the linear growth factor characterizing the universe's expansion, results in the function shown here.

The next term in equation 6.3,  $\bar{j}^2(\nu, z)$ , is the mean IR galaxy emissivity per co-moving unit of volume,  $W/Mpc^3/Hz/sr$ . This is the integral over the number of sources at each luminosity multiplied by the appropriately redshifted luminosity. This is largely dependent on the Spectral Energy Distribution (SED) of the IR galaxies. The SED of a galaxy summarizes many of its physical properties into a single function with contributions coming from many different regions within a galaxy each with different temperatures and densities. Section 4.2.1 discussed the various types of dust present in the interstellar medium. Since IR galaxies are largely composed of dust, their SED is made up of contributions from these different dust particles; large grains, very small grains and polycyclic aromatic hydrocarbons. In addition there is a contribution from stellar emissions. The assumption is made that the SED is only dependent on the bolometric luminosity, that is the total energy across all wavelengths, and the resulting emissivity functions at various

frequencies are shown in Figure 6.4.

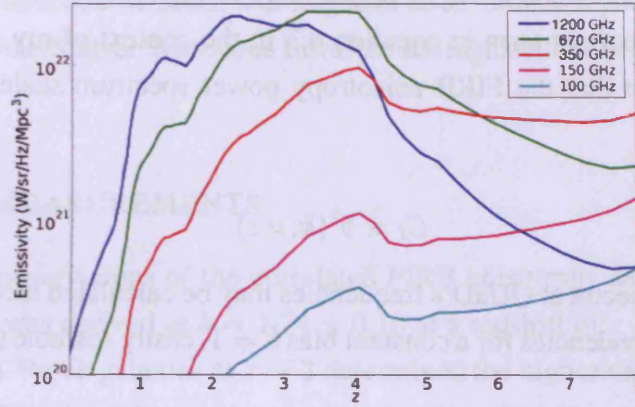


Figure 6.4: The Mean Infrared Galaxy Emissivity

Emissivities per comoving volume as a function of redshift at various frequencies with QUaD's 100 GHz in light blue and 150 GHz in purple.

$P_M(k)|_{k=\ell/r}$  is the power spectrum of the dark matter density fluctuations. There are various phenomena affecting the amplitude of the power spectrum on different spatial scales. A transfer function,  $T(k, t)$ , (Peebles, 1980; Bardeen et al., 1986) describes how self-gravity, pressure and damping from diffusion and free-streaming dark matter particles have a combined effect as a function of spatial frequency,  $k$  and time,  $t$ . For small  $k$  there is very little effect but on large scales the growth of structures is damped. Defined at  $k = \ell/r$ , the present,  $z = 0$ , dark matter power spectrum is:

$$P_M(k) \propto kT^2(k) \quad (6.5)$$

Whilst this transfer function determines the shape and evolution of the power spectrum, it does not set its normalization since the origin of the density fluctuations are not explained. The normalization typically chosen is the cosmological parameter  $\sigma_8$ .  $\sigma_8$  is defined by an integral of the power spectrum with a window function corresponding to a radius of 8 Mpc:

$$\sigma^2(R) = \frac{1}{(2\pi)^2} \int_0^\infty k^2 W_k^2(R, k) P_M(k, 0) dk \quad (6.6)$$

where  $R$  is set to  $8h^{-1}$  Mpc, and  $W_k$  is the Fourier transform of the window. A top-hat filter function is typically used for the window function defined as:

$$W = \frac{3V}{4\pi R^3} \begin{cases} 1 & \text{if } r < R \\ 0 & \text{otherwise.} \end{cases} \quad W_k = 3 \left[ \frac{\sin(kR)}{(kR)^3} - \frac{\cos(kR)}{(kR)^2} \right] \quad (6.7)$$

Hence the density fluctuations are effectively smoothed on these scales. In this chapter  $\sigma_8$  is set to 0.8, the value typically used in astronomy derived from large scale structure and cosmology results (e.g. Seljak et al., 2006; Dunkley et al., 2009).

The most important term in equation 6.3 in the context of my work is  $b^2(k, \nu, z)$ , from which we learn that the FIRB anisotropy power spectrum scales according to the square of the bias:

$$C_\ell \propto b^2(k, \nu, z) \quad (6.8)$$

The angular power spectra at QUaD's frequencies may be calculated incorporating all these components and dependencies for a constant bias  $b = 1$ , easily scalable to alternative biases given equation 6.8.

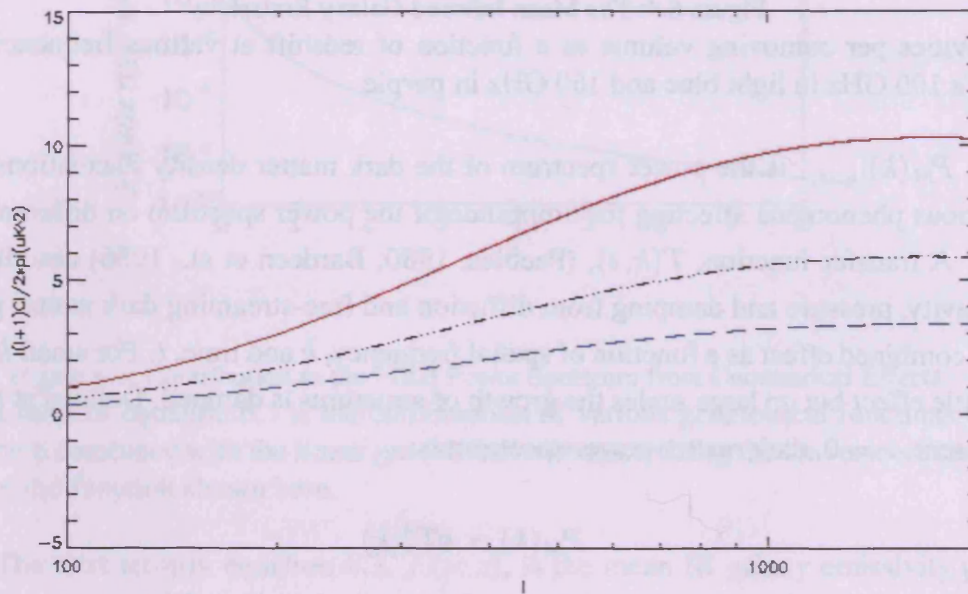


Figure 6.5: The Far Infrared Background Spectrum

Power spectra for the FIRB assuming  $b = 1$  at QUaD's frequencies; 100 GHz in blue, 150 GHz in red and the cross frequency spectrum in black.

### 6.3.2 OBSERVATIONS

Aboard the Infrared Space Observatory (ISO) launched in 1995, the PHOTo-polarimeter (ISOPHOT) made the first detections of the FIRB fluctuations at  $170 \mu\text{m}$ . This was a detection of the fluctuations due to discrete unresolved extra-galactic sources (Lagache &

Puget, 2000). The first detection of the larger scale correlated anisotropies was sometime later by the Multiband Imaging Photometer for Spitzer (MIPS), an instrument on the Spitzer Space Telescope launched in 2003. As Lagache et al. (2007) reported, the observations made were part of the Spitzer Wide-area InfraRed Extragalactic (SWIRE) survey and made at  $160 \mu\text{m}$ .

### 6.3.3 BIAS MEASUREMENTS

From the Spitzer observations of the correlated FIRB anisotropy described above, a constraint on the bias was derived as  $b = 1.74 \pm 0.16$  at a redshift of  $z \sim 1$ . Optical observations of the Lyman-Break galaxies at  $z \sim 3$  determined the higher values of  $b \sim 2 - 6$  (e.g. Steidel et al., 1998). The Infrared Astronomy Satellite (IRAS) measured a lower bias at redshift  $z < 0.05$  (Saunders et al., 1992), which is expected based on the low levels of starburst activity in local universe dark matter halos, and consistent with the findings at optical and radio wavelengths that bias increases with redshift. In addition the Sloan Digital Sky Survey (SDSS) reported a low value ( $b \sim 1.1$ ) at a redshift  $z \sim 0.1$  (Tegmark et al., 2006), confirming that in the local universe IR galaxies are not biased tracers of the mass. As time progresses therefore, from a redshift of  $\sim 1$  to the present, it seems the galaxies become less biased tracers of the mass density field. Environmental effects such as gas stripping and merging events may be triggering star formation and clustering in places which otherwise would not be showing clustering given the underlying dark matter distribution in the vicinity.

Although for obvious reasons, since it is a CMB experiment, QUaD observes the CMB power swamping over any expected FIRB at its frequencies, it may nevertheless still be possible to probe its presence with a method that effectively eliminates the CMB.

## 6.4 QUAD'S FREQUENCY JACKKNIFE

Section 3.1.6 described how various systematic contamination checks are carried out by means of jackknife tests. In each of these tests the timestream is in some way split in half and differenced such that in the ideal case the identical sky signals would subtract out leaving zero. Since QUaD observes at both 100 and 150 GHz, a fifth jackknife test permitted is a frequency jackknife. This is somewhat different in the sense that the true sky brightness may actually differ between them and any cancellation failure encountered may indicate an astrophysical foreground rather than an instrumental systematic. In fact if all instrumental effects have been correctly simulated then any residual in the difference

map should be due to such a real foreground signal. As with the other jackknife power spectra this one is also formed by taking the difference of the two maps; the 100 GHz and the 150 GHz maps in this case, dividing by two, and taking the resulting map through to power spectrum estimation. Error bars are obtained from the scatter among an ensemble of frequency jackknived signal plus noise simulations.

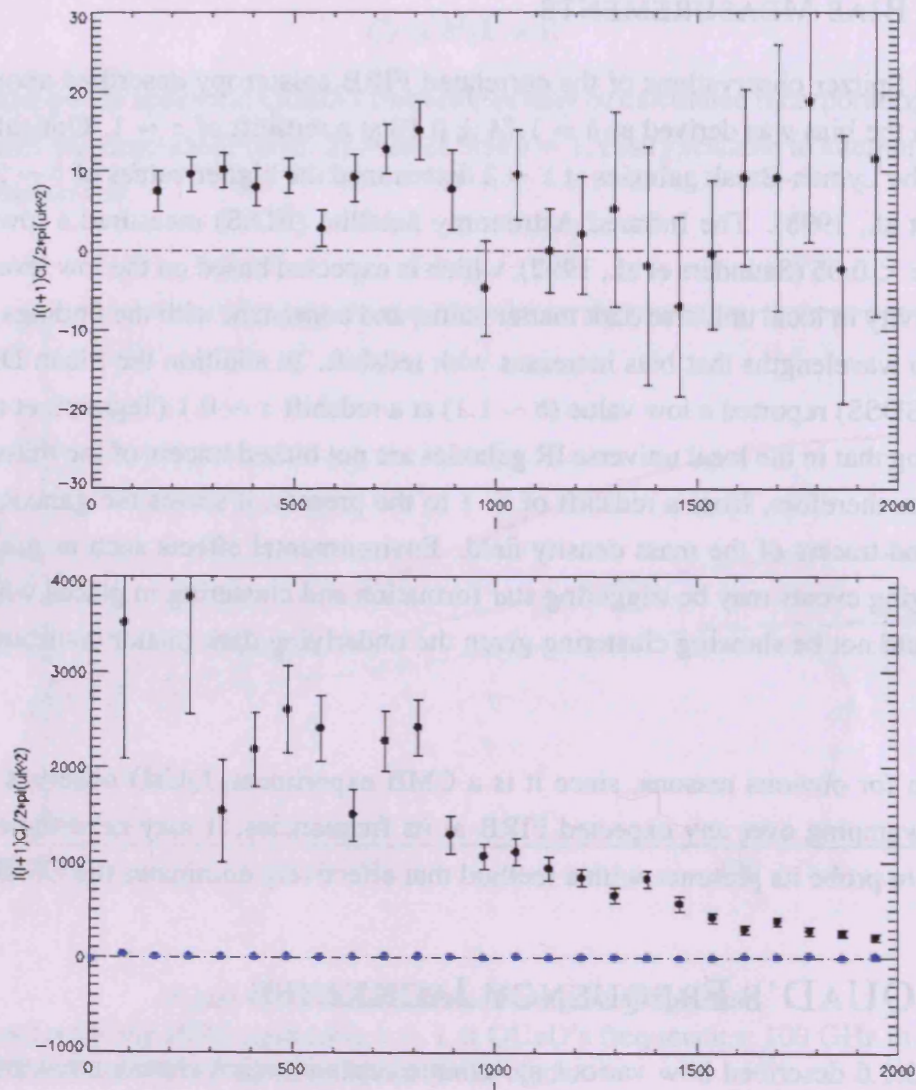


Figure 6.6: Frequency Jackknife Power Spectrum

QUaD's multi-frequency observations permit a frequency jackknife test. The resulting TT power spectrum (top) is insignificant when considered on signal spectrum scales (bottom), yet may contain some real astrophysical foreground signal.

$\chi^2$  values for the test can be calculated versus the null model:

$$\chi^2 = \mathbf{b}\mathbf{C}^{-1}\mathbf{b}^t \quad (6.9)$$

from the band powers,  $\mathbf{b}$ , and the covariance matrix,  $\mathbf{C}$ , estimated from the ensemble of signal plus noise simulations detailed in Section 3.2.4. Throughout QUaD's data analysis, in the first season data of Ade et al. (2008), the second and third season data both with field differencing (Pryke et al., 2009) and ground template subtraction techniques (Brown et al., 2009), there has consistently been a failure in the  $\chi^2$  result for the TT frequency jackknife spectrum.

Dividing each band power in the jackknife spectrum by its corresponding error bar we can investigate the contribution of each to the  $\chi^2$ . These band power deviations, as shown in Figure 6.7 reveal that for the TT frequency jackknife the source of the failure lies on angular scales below  $\ell \sim 1000$ . Beyond this the differing beam sizes for the two frequency bands lead to large error bars, as the top plot of Figure 6.6 illustrates.

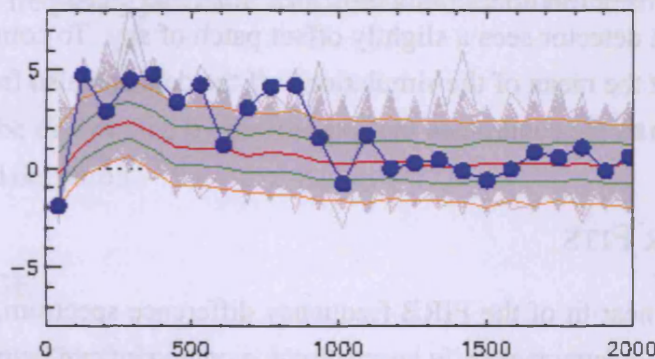


Figure 6.7: Frequency Jackknife Band Power Deviations

The blue points marking the TT frequency jackknife band power deviations from the Brown et al. (2009) results show that the failure is due to bins  $\ell \lesssim 1000$ . The grey lines represent the 600 simulations and the yellow, green and red lines mark the 2.3%, 15.9%, 50%, 84.1% and 97.7% positions of the simulation distribution.

Although in light of the fractional cancellation with the CMB spectrum the failure could be deemed irrelevant (see Figure 6.6), it may nevertheless be due to some astrophysical phenomena in the foreground of QUaD's observing region. The far infrared background, focussed on in this Chapter, is one such phenomenon. Also or alternatively we may be detecting the Sunyaev-Zel'dovich effect and/or residual radio sources. Of course the possibility remains that the failure is due to an as yet overlooked systematic or chance.

## 6.5 LOOKING FOR THE FIRB IN QUAD'S FREQUENCY JACKKNIFE

### 6.5.1 FIRB FREQUENCY DIFFERENCE

As described in the previous section, the QUaD frequency jackknife spectrum is formed by taking the difference of the 100 and 150 GHz maps, dividing by 2 and putting this map through the power spectrum estimation pipeline. Although this frequency difference spectrum therefore originates in map space we can compute an equivalent spectrum for the FIRB directly from its auto ( $C_\ell^{100}$ ,  $C_\ell^{150}$ ) and cross frequency ( $C_\ell^{cross}$ ) spectra, incorporating the band power window functions of Section 3.2.6 so as to match QUaD's binning strategy:

$$C_\ell^{diff} = \sum_{\ell} \frac{\omega_{b\ell}}{\ell} \left( \frac{C_\ell^{100} + C_\ell^{150} - 2C_\ell^{cross}}{4} \right) \quad (6.10)$$

in which  $\omega_{b\ell}$  are the band power window functions.

The mean among the 600 frequency jackknife simulations is non-zero because of the differing beam-sizes between 100 and 150 GHz at high- $\ell$  and also tile edge effects at low- $\ell$  because each detector sees a slightly offset patch of sky. To compensate for this we can simply subtract the mean of the simulations off the data and also from each simulation before construction of the covariance matrix.

### 6.5.2 LINEAR FITS

By performing a linear fit of the FIRB frequency difference spectrum,  $f$ , which scales as  $b^2$ , to the QUaD frequency jackknife spectrum,  $q$ , a constraint can be placed upon the bias accordingly. The linear fit can be done using a least squares method with inverse variance weighting. The idea behind this method is to find the gradient,  $m$ , which minimizes the chi-square statistic. The chi-square is calculated via:

$$\chi^2 = \sum (q_i - m f_i)^2 / \sigma_i^2 \quad (6.11)$$

and its minimum is then found by setting to zero the derivative with respect to  $m$ . This gives:

$$m = \frac{\sum (f_i q_i / \sigma_i^2)}{\sum (f_i^2 / \sigma_i^2)} \quad (6.12)$$

The FIRB model spectra was made assuming  $b = 1$  so given its scale factor of the square of the bias, the square root of gradient obtained is the bias value suggested by QUaD's data.

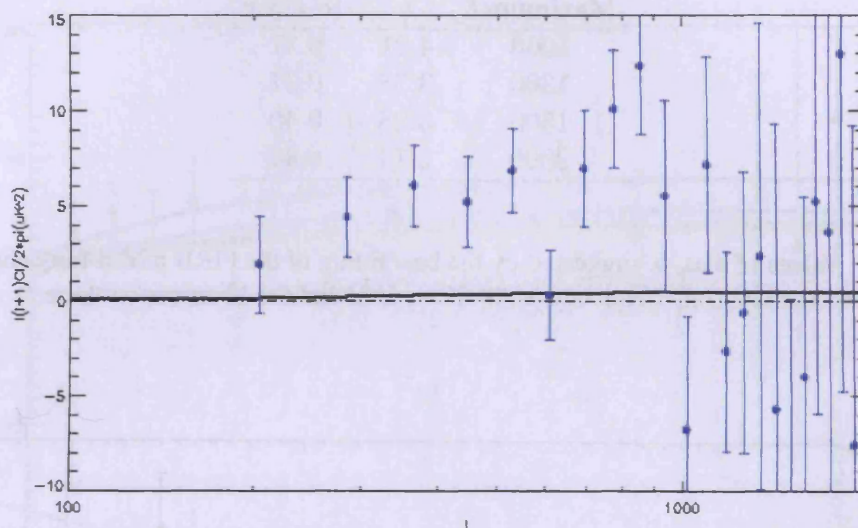


Figure 6.8: FIRB Frequency Difference Spectrum

The frequency difference power spectrum for the FIRB calculated with equation 6.10 (black line) with QUAD's frequency jackknife data after subtraction of the simulation mean (blue points).

An error on  $b$  can be determined by performing the same linear fit on each simulation and taking the standard deviation.

### 6.5.3 $l$ -RANGE

Figure 6.8 shows QUAD's frequency jackknife band powers up to  $l = 2000$ . As previously stated, (Section 4.3.3), the first two bins are not used in QUAD's analysis so are excluded leaving 22 bins. At high  $l$  ( $\gtrsim 1800$ ) the error bars become quite large. Although this is incorporated into the analysis through the inverse variance weighting we might find that constraining the fit to a particular  $l$ -range is of benefit. Figure 6.7 showed us that the jackknife failure is down to band powers less than  $\sim 1000$  so we can investigate this range in comparison to other limits. I have repeated the linear fits and determined bias values for  $l < 2000$ ,  $l < 1500$ ,  $l < 1300$  and  $l < 1000$ .

### 6.5.4 BIAS RESULTS

Table 6.1 summarizes the results across the various  $l$ -ranges considered, then Figure 6.9 shows the best fit line for  $l < 1000$ .

Maximum $\ell$	$b$	$1\sigma$ error
1000	4.21	0.37
1300	3.58	0.37
1500	3.28	0.40
2000	3.14	0.41

Table 6.1: Values of bias,  $b$ , suggested by the best fitting of the FIRB model frequency difference spectra to the QUaD frequency jackknife spectra and the  $1\sigma$  errors on these.

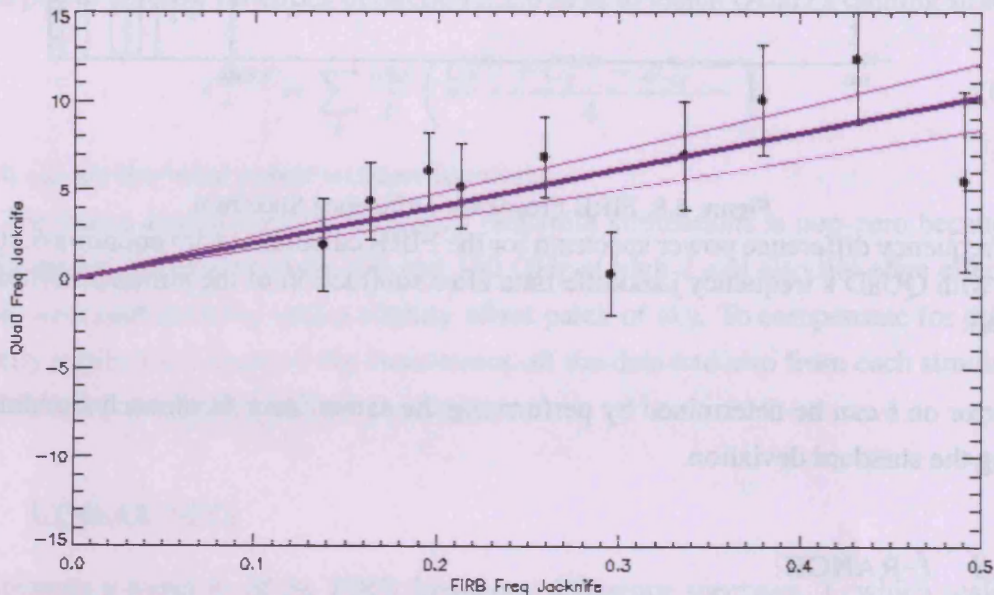


Figure 6.9: Linear Fit to the FIRB Model

The thick purple line is the best fit through the black points of QUaD's frequency jackknife against the theoretical FIRB frequency difference spectra at  $\ell < 1000$ .

The decrease in the value of  $b$  obtained as the  $\ell$ -range increases is due to the more negative values at higher  $\ell$  in the frequency jackknife, which although downweighted significantly by their larger error bars, nonetheless have an impact upon the linear fit. Figure 6.10 shows the scaled FIRB spectra for the different bias values.

Regardless of the of the angular scale considered, the value for bias is always greater than 3. This implies a biased universe in which the galaxies are a biased tracer of the mass in the universe, thus it is more widely distributed than the light suggests. The FIRB seen in QUaD data would be across all redshifts, so the findings of Brand et al. (2003) and

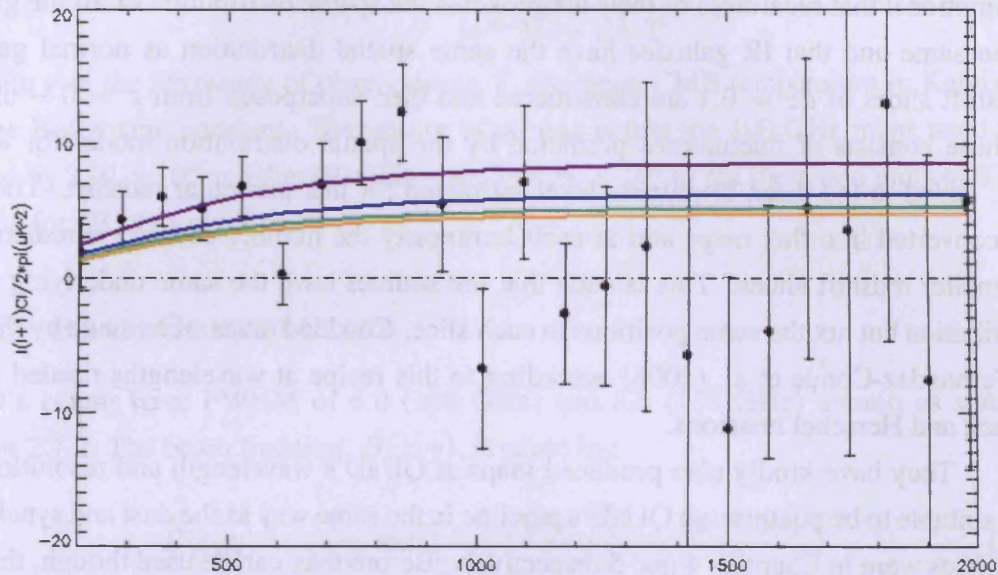


Figure 6.10: Scaled FIRB Spectra

QUaD's frequency jackknife spectra (black points) with the FIRB frequency difference spectra scaled according to  $b^2$  for the different  $l$ -ranges: purple  $< 1000$ , blue 1300, green  $< 1500$ , orange  $< 2000$ .

Marinoni et al. (2006) that bias increases with redshift might indicate that the infrared sources dominating the signal detected are from reasonably high redshift ( $z \gtrsim 3$ ). The high values also support Elbaz et al. (2007) that the star formation rates of galaxies are higher in the denser environments of clusters. They are consistent with the bias results from Lyman-Break galaxies as discussed in Section 6.3.3, but higher than the value Lagache et al. (2007) found via Spitzer's FIRB detections at  $z = 1$ .

## 6.6 INFRARED GALAXY SIMULATIONS

Rather than merely taking the FIRB power spectrum to be that given by equation 6.3, simulations can be run of infrared galaxies from which power spectra may be obtained. Fernandez-Conde et al. (2008) describes how the far infrared and submillimeter background can be simulated at CMB frequencies making use of the model in Lagache et al. (2004). This is a model of luminosity function evolution with redshift simplified to a minimal number of parameters whilst fitting all experimental data. A galaxy emissivity spatial distribution proportional to the dark matter density fluctuation distribution is then added to this model at a level defined by the bias parameter.

The same equation is used for the power spectrum, with maps created under two assumptions; that regardless of their luminosities the spatial distribution of all the galaxies is the same and that IR galaxies have the same spatial distribution as normal galaxies. Redshift slices of  $dz = 0.1$  are constructed and then superposed from  $z = 0 - 6$ . Each of these consists of fluctuations predicted by the spatial distribution model for a given bias, added to the mean brightness level estimated for that particular redshift. The maps are converted into flux maps and at each luminosity the number counts are redistributed in smaller redshift slices. This is such that the sources have the same underlying spatial distribution but not the same positions in each slice. Coadded maps were made by the team of Fernandez-Conde et al. (2008) according to this recipe at wavelengths needed for the Planck and Herschel missions.

They have kindly also produced maps at QUaD's wavelength and resolution, of a size suitable to be put through QUaD's pipeline in the same way as the dust and synchrotron templates were in Chapters 4 and 5 respectively. Before they can be used though, the maps need to be converted into CMB temperature units, convolved with QUaD's beams and repixelized into Healpix maps.

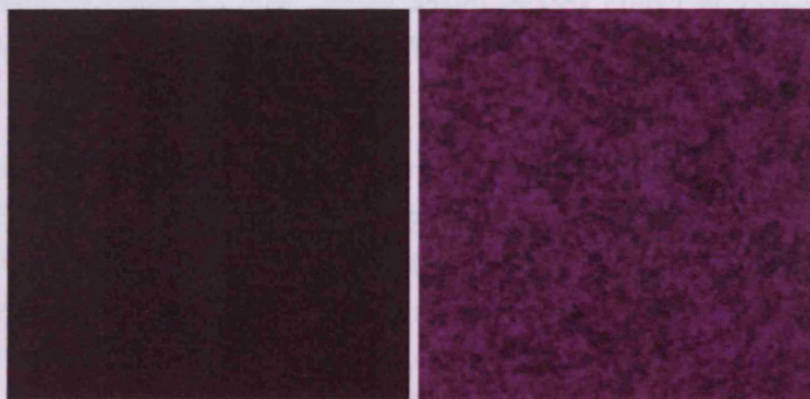


Figure 6.11: Infrared Galaxy Simulations

100 GHz (left) and 150 GHz (right) simulations of the infrared and submillimeter backgrounds with a pixel size of 72 arcsec.

### 6.6.1 UNIT CONVERSION

The maps in Figure 6.11 are in units of MJy/sr. The pixel size of the map is  $72''$ , which translates to  $0.02^\circ$  and  $1.22 \times 10^{-7}$  steradians. The conversion factor from brightness units,  $dI$ , into CMB temperature units,  $dT$ , is obtained by differentiating Planck's blackbody equation with respect to temperature:

$$dI = \frac{2h\nu^3}{c^2} \frac{h\nu/kT e^{h\nu/kT} dT}{(e^{h\nu/kT} - 1)^2 T} \quad (6.13)$$

in which  $\nu$  is the frequency of observations,  $T$  the mean CMB temperature in Kelvin and  $k$  is the Boltzmann constant. The upshot of all this is that the 100 GHz maps need to be divided by  $2.91 \times 10^4$  and the 150 GHz ones by  $4.86 \times 10^4$  to put them into units of Kelvin suitable for QUaD's pipeline.

### 6.6.2 BEAM CONVOLUTION

QUaD's beams have FWHM of 5.0 (100 GHz) and 3.5 (150 GHz) arcmin as stated in Section 2.1.2. The beam function,  $B(x, y)$ , is given by:

$$B(x, y) = \frac{1}{2\pi\sigma^2} \exp\left(-\frac{1}{2} \left[ \frac{(x - x_0)^2}{\sigma^2} + \frac{(y - y_0)^2}{\sigma^2} \right]\right) \quad (6.14)$$

where  $x_0$  and  $y_0$  is the centre of the map and  $\sigma$  is given by:

$$\sigma = \frac{FWHM}{\sqrt{8 \ln 2}} \quad (6.15)$$

A convolution is a particular type of integral transform serving to effectively blend one function with another; in this case smooth the IR galaxy maps with the QUaD beams. It is most simply accomplished by taking the Fourier transform of each function, multiplying them together in Fourier space and then transforming back to a map. Figure 6.12 shows the results of convolving the maps in Figure 6.11 with our beams and converting their units.

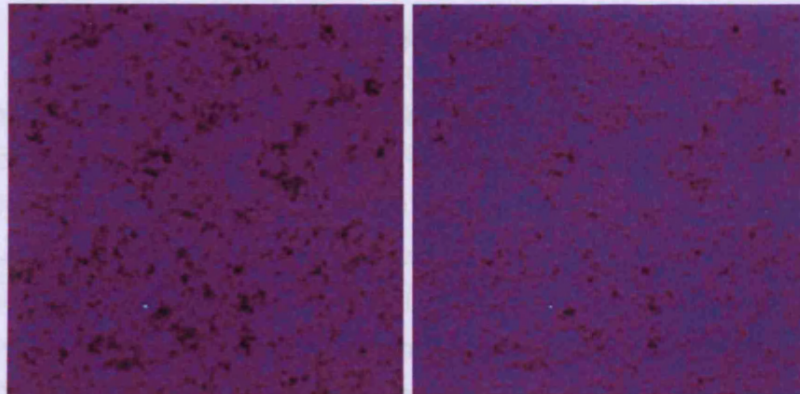


Figure 6.12: Convolved Infrared Galaxy Simulations  
100 GHz (left) and 150 GHz (right) simulations of the infrared and submillimeter back-grounds after unit conversion and beam convolution.

### 6.6.3 REPIXELIZATION

After the unit conversion and beam convolution the map remains a flat square map of  $650 \times 650$  pixels. This needs to be translated into a Healpix map of  $n_{\text{side}} 8192$  before it can be inserted into QUaD's simulation pipeline. This can be achieved by determining the RA and Dec of each Healpix pixel on an input CMB map as used in the signal simulations, fixing the bottom left-hand corner of the IR galaxy flat map to be a specific RA and Dec then knowing its pixel size fill each Healpix pixel with corresponding data. Maps such as those in Figure 6.13 are yielded, in which the area covered by the simulation sufficiently encloses QUaD's observing region.

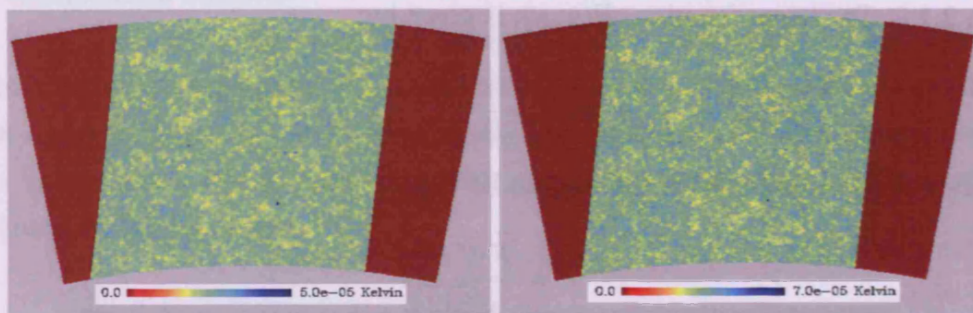


Figure 6.13: Repixelized Convolved IR galaxy Simulations

100 GHz (left) and 150 GHz (right) simulations of the infrared and submillimeter backgrounds after unit conversion, beam convolution and repixelization. These maps are now ready to go through the simulation code.

### 6.6.4 MAPS AND POWER SPECTRA

The maps are now akin to those of Figures 4.3 and 5.5 and can be run through the simulation analysis. This Chapter is however employing the non field differenced ground template subtraction technique rather than the field differencing method which Chapters 4 and 5 used, so the maps produced now have double the effective sky area. From a suite of simulated maps like Figure 6.14, mean 100 GHz, 150 GHz and cross frequency FIRB power spectra can be obtained following the method described in Section 3.2. The shape of the power spectra (Figure 6.15) look a little different to those of Figure 6.5 because now they are directly incorporating the beam and filtering effects of QUaD, and then correcting for them via the transfer function,  $F_\ell$ , of equation 3.15, rather than relying on them being compensated for later on via the band power window functions.

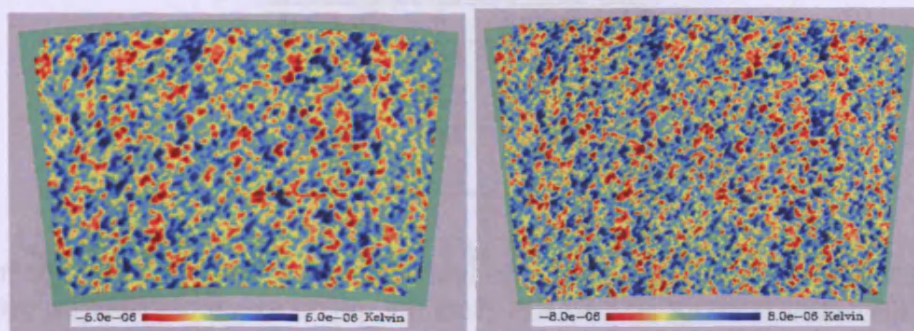


Figure 6.14: QUaD Simulated IR Galaxy Maps

The IR galaxy maps of Figure 6.13 are run through QUaD's simulation pipeline at 100 GHz (left) and 150 GHz (right).

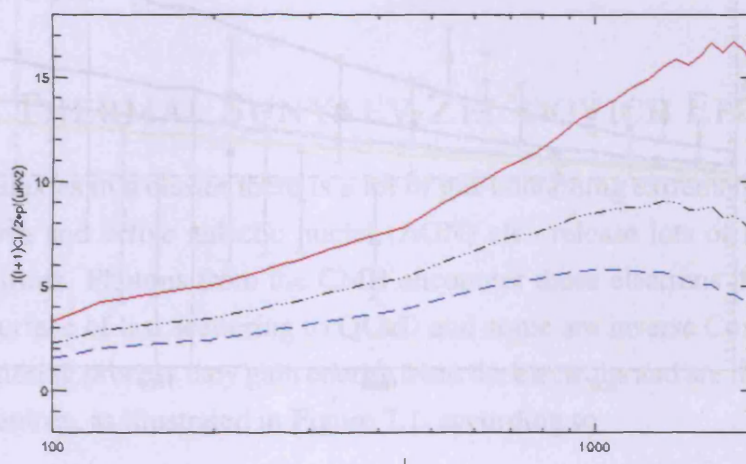


Figure 6.15: FIRB Power Spectrum from Simulations

Power spectra for the FIRB derived from the mean of  $\sim 100$  IR galaxy simulations at QUaD's frequencies; 100 GHz in blue, 150 GHz in red and the cross frequency spectrum in black.

### 6.6.5 BIAS RESULTS WITH SIMULATED SPECTRA

The linear fitting analysis of Section 6.5 can be repeated using the simulated spectra of Figure 6.15 in place of the model ones used previously. Table 6.2 presents the results of the fitting, again for various constraints on the  $\ell$ -range considered and Figure 6.16 shows the simulated spectra scaled accordingly with the frequency jackknife spectra.

We see a similar trend and similar values for  $b$ , although slighter wider spread. Any conclusions which can be drawn about the universe based on these results are therefore

Maximum $\ell$	$b$	$1\sigma$ error
1000	4.53	0.38
1300	3.26	0.39
1500	2.61	0.46
2000	2.22	0.50

Table 6.2: Values of bias,  $b$ , suggested by the best fitting of the FIRB spectra derived from IR galaxy simulations to the QUaD frequency jackknife spectra for various  $\ell$ -ranges, with their  $1\sigma$  errors.

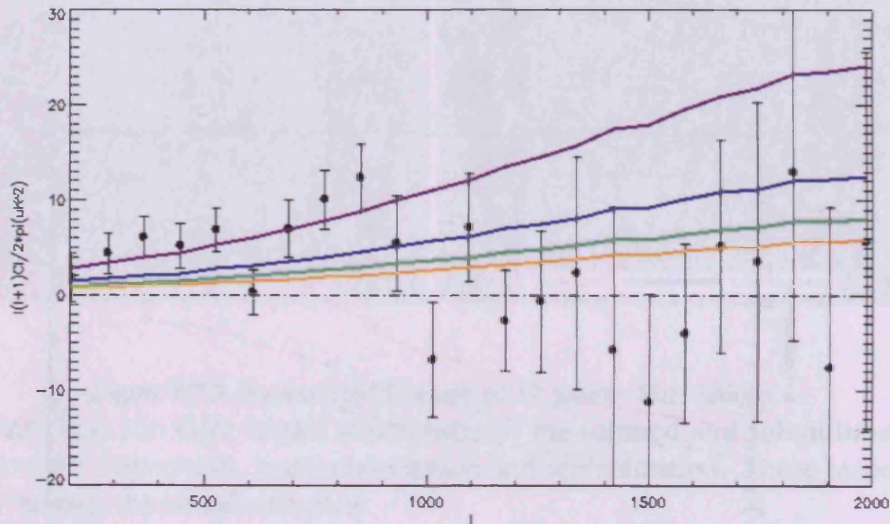


Figure 6.16: Scaled Simulated FIRB Spectra

QUaD's frequency jackknife spectra (black points) with the simulated FIRB frequency difference spectra scaled according to  $b^2$  for the different  $\ell$ -ranges: purple  $< 1000$ , blue  $1300$ , green  $< 1500$ , orange  $< 2000$ .

the same as in the previous section; that, with the assumption the FIRB is the cause of the jackknife failure, the galaxies are a strongly biased tracer of the underlying dark matter mass distribution. Even after adding the  $1\sigma$  error to  $b$  when considering only  $\ell < 1000$  it remains less than  $b = 6$ , making these results still consistent within the highest values for  $b$  determined by other experiments.

Chapter 7 will turn to one of the alternative phenomena mentioned above which may also play a role in the frequency jackknife signal observed - the Sunyaev-Zel'dovich effect.

# 7 SUNYAEV-ZEL'DOVICH EFFECT

---

“DUCT TAPE IS LIKE THE FORCE. IT HAS A LIGHT SIDE, AND A DARK SIDE, AND IT HOLDS THE UNIVERSE TOGETHER.”

CARL ZWANZIG

## 7.1 THE THERMAL SUNYAEV-ZEL'DOVICH EFFECT

Amongst the galaxies in a cluster there is a lot of gas containing extremely energetic electrons. Supernova and active galactic nuclei (AGN) also release lots of highly energetic relativistic electrons. Photons from the CMB encounter these electrons in their transmission from the surface of last scattering to QUaD and some are inverse Compton scattered. During this scattering process they gain energy from the electrons and are hence blueshifted to higher frequencies, as illustrated in Figure 7.1, according to:

$$\Delta\lambda = \lambda_0 - \lambda = \frac{h}{mc}(1 - \cos\theta) \quad (7.1)$$

in which  $\lambda_0$  is the initial wavelength and  $\theta$  the change in angle of the photon's trajectory.

In the direction of such clusters, since the scattering process conserves photon number, these blueshifted photons lead to a CMB spectrum distorted from that which cosmology would predict. This distortion is referred to as the thermal Sunyaev-Zel'dovich (SZ) effect (Zeldovich & Sunyaev, 1969) after the two scientists who first predicted it.

### 7.1.1 FREQUENCY DEPENDENCE

No photons are created or destroyed in the scattering process, they are merely moved within the CMB blackbody spectrum. Photons are shifted from a lower energetic region to a more energetic region, thus at low frequencies there is a negative temperature shift whilst at higher frequencies there is a positive shift. This gives rise to a specific shape in the CMB

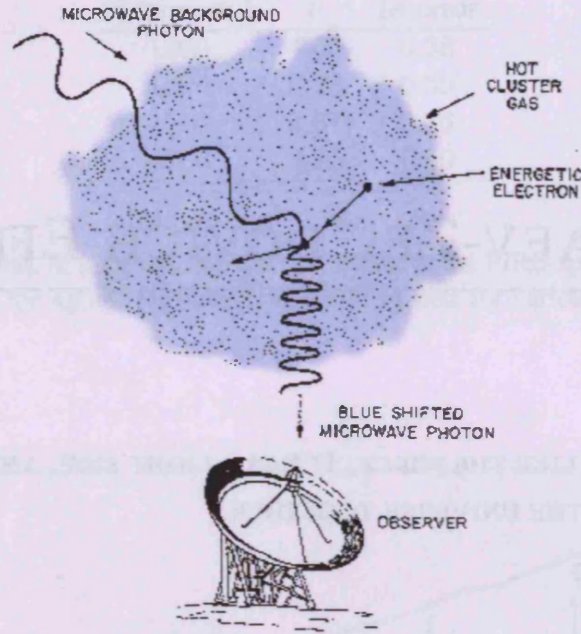


Figure 7.1: Inverse Compton Scattering

CMB photons are blueshifted upon scattering off energetic electrons in the hot gas of the intracluster medium.

(Images: SZA - <http://astro.uchicago.edu/sza>)

intensity deviation as a function of frequency, with a cross-over point at which there is no distortion at  $\sim 218$  GHz. This unique frequency dependent spectral signature, shown in Figure 7.2 provides a search technique for galactic clusters. It can be used to measure the properties of the gas in the clusters along with the motion of the cluster itself, providing an insight into the evolution of structure in the universe. In the context of CMB physics, however, it can be considered a nuisance; not so much a foreground but rather a secondary source of temperature fluctuation.

### 7.1.2 TEMPERATURE DISTORTION OF THE CMB

The distortion caused by the SZ effect depends on the average fractional frequency change of the photons, and the optical depth to the scattering event. The largest brightness change that might be expected is only of order 1 mK. Quantitatively the magnitude is proportional to a Comptonization parameter,  $y$ , which is proportional to the electron number density,  $n_e$ , and the temperature of the electrons,  $T_e$ , integrated along the line-of-sight,  $dl$ :

$$y = \frac{\sigma_T}{m_e c^2} \int dl n_e k_B T_e \quad (7.2)$$

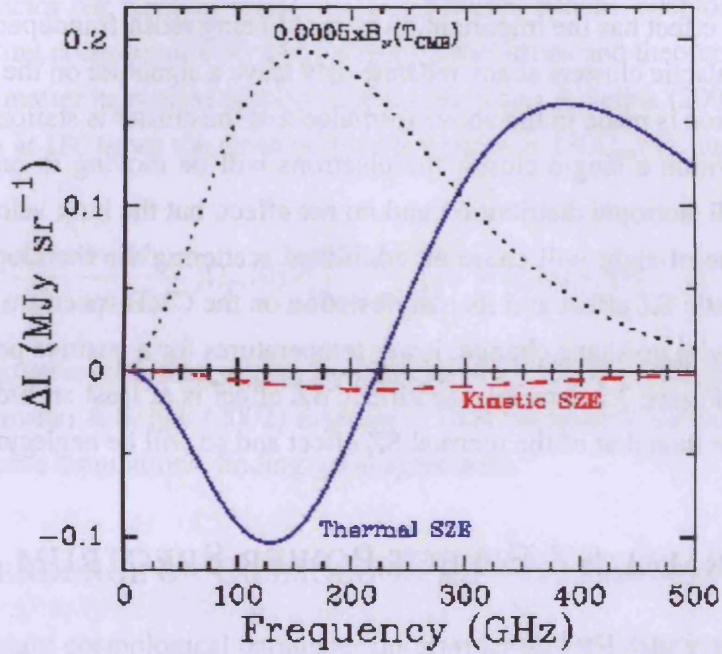


Figure 7.2: Frequency Dependence of the SZ Effect

At low frequencies there is a negative shift in the temperature of the CMB spectrum, as photons that would otherwise be observed at these frequencies have been scattered to higher energies. After a cross-over at approximately 218 GHz a positive temperature shift is seen. The dotted black line is the CMB intensity spectrum scaled by  $5 \times 10^{-4}$  (Carlstrom et al., 2002).

$\sigma_T$  is the Thomson cross section:

$$\sigma_T = \frac{8\pi}{3} \left( \frac{e^2}{4\pi\epsilon_0 m_e c^2} \right)^2 \quad (7.3)$$

and  $m_e$  the electron mass. The frequency dependent function:

$$f(x) = x \frac{e^x + 1}{e^x - 1} - 4 \quad (7.4)$$

in which  $x$  is the dimensionless frequency  $x = h\nu/k_B T_{CMB}$  is then used with the Comptonization parameter to give the temperature shift:

$$\frac{\Delta T_{CMB}}{T_{CMB}} = f(x)y \quad (7.5)$$

### 7.1.3 KINETIC SUNYAEV ZEL'DOVICH EFFECT

The thermal SZ effect has the important property of being redshift independent (Carlstrom et al., 2002). Galactic clusters at any redshift may leave a signature on the CMB spectrum, but the assumption is made in the above formulae that the cluster is stationary with respect to the CMB. Within a single cluster the electrons will be moving in random directions giving an overall isotropic distribution and no net effect, but the bulk velocity of an entire cluster in its line-of-sight will cause an additional scattering via the Doppler effect. We call this the kinetic SZ effect and its manifestation on the CMB spectrum is simply a shift in temperature with no shape change; lower temperatures for a positive peculiar motion of the cluster. As Figure 7.2 showed, the kinetic SZ effect is at least an order of magnitude smaller in power than that of the thermal SZ effect and so will be neglected.

## 7.2 THERMAL SZ EFFECT POWER SPECTRUM

### 7.2.1 ANALYTIC PREDICTION

The particular formalism typically used for the power spectrum of the SZ effect is that following the halo approach as detailed in Komatsu & Seljak (2002). Halo-halo correlations are ignored because above  $\ell \sim 300$  the one-halo Poisson term dominates. The expression given for the angular power spectrum is:

$$C_\ell = g_\nu^2 \int_0^{z_{max}} dz \frac{dV}{dz} \int_{M_{min}}^{M_{max}} dM \frac{dn(M, z)}{dM} |\tilde{y}_\ell(M, z)|^2 \quad (7.6)$$

Just as with the analytic FIRB power spectrum of equation 6.3, this equation contains many terms.  $g_\nu$  is the spectral function given in equation 7.4, for frequency  $\nu$ .  $V(z)$  is the comoving volume of the universe at redshift  $z$  per steradian.  $dn(M, z)/dM$  is the comoving dark matter halo mass function and  $\tilde{y}_\ell(M, z)$  is the two-dimensional Fourier transform of the projected Compton  $y$ -parameter of equation 7.2. The integration over redshift is carried out up to a maximum  $z$  of 10, and the mass boundaries are set as  $M_{min} = 5 \times 10^{12} h^{-1} M_\odot$  and  $M_{max} = 5 \times 10^{15} h^{-1} M_\odot$ . These masses are the Virial masses; the mass of the cluster in statistical equilibrium based on the Virial theorem in which the mean square velocity of all the galaxies in the cluster is proportional to the mass of the cluster divided by its radius.

The mass function of dark matter halos is described in Jenkins et al. (2001), with the mass of the halo evaluated in a sphere according to the spherical overdensity algorithm. The one free parameter in this model is the overdensity within the sphere relative to the critical density of the universe,  $\rho_c$ , and the mass variable used is  $\ln \sigma^{-1}(M, z)$ , derived

from the variance of the density field,  $\sigma^2(M, z)$ , extrapolated to redshift  $z$ . Use of this variable serves to factor out the mass component in different epochs, cosmologies and power spectra, permitting comparisons between various simulations and theoretical models. The comoving dark matter halo mass function used in Komatsu & Seljak (2002) fixes the mass density of halos at 180 times the mean of the universe,  $\delta = 180\Omega_m(z)$ , and has the form:

$$\frac{dn(M, z)}{dM} = \frac{dM_\delta}{dM} \frac{dn(M_\delta, z)}{dM_\delta} \Omega_m(0) \frac{\rho_c(0)}{M_\delta} \frac{d \ln \sigma^{-1}}{dM_\delta} \times 0.301 \exp\left(-|\sigma^{-1} + 0.64|^{3.82}\right) \quad (7.7)$$

Integration of equation 7.6 thus allows predictions to be made of the SZ angular power spectrum as Komatsu & Seljak (2002) discusses. They compare their analytic predictions with hydrodynamic simulations, finding good agreement.

### 7.2.2 DEPENDENCE ON COSMOLOGICAL PARAMETERS

The most important cosmological parameter upon which the SZ power spectrum depends is  $\sigma_8$ ; the root-mean-square fluctuations within a  $8h^{-1}$  Mpc sphere. This is perhaps because massive clusters are at the tail of the dark matter mass function. Section 3.1 of Zhang & Pen (2001) describes how the SZ power spectrum is proportional to the present contribution from single halo correlations to the gas pressure power spectrum in Fourier  $k$ -space,  $P_p(k)$ , which is itself proportional to the density polyspectrum,  $B_4$ . A polyspectrum is the Fourier transform of a multi-point correlation function, just as a bispectrum is the Fourier transform of the three point correlation function (Press et al., 2007). The hierarchical model used allows the higher order correlations to be expressed in terms of the product of two-point correlations, hence  $B_4 \propto P^3(k)$ , where  $P(k)$  is the gas pressure power spectrum.  $P(k) \propto \sigma_8^{2-3}$ , 2 in the linear regime and 3 in the scale clustering regime, and thus  $C_\ell \propto \sigma_8^{6-9}$ . Komatsu & Seljak (2002) find  $C_\ell \propto \sigma_8^7$  to be the best fit agreement to their analytic predictions and simulations.

In recent cosmology (e.g. Dunkley et al., 2009) the parameter  $\sigma_8$  used in analytic predictions of the SZ power spectra is set to  $0.8^3$ . This means that the power spectrum can be scaled according to:

$$C_\ell = \left(\frac{\sigma_8}{0.8}\right)^7 C_{\ell(0.8)} \quad (7.8)$$

Figure 7.3 shows the predicted angular power spectrum for the SZ effect with  $\sigma_8 = 0.8$  at QUAD's frequencies, which is scalable for different values of  $\sigma_8$  via equation 7.8.

<sup>3</sup>See [http://lambda.gsfc.nasa.gov/product/map/dr3/pow\\_sz\\_spec\\_get.cfm](http://lambda.gsfc.nasa.gov/product/map/dr3/pow_sz_spec_get.cfm)

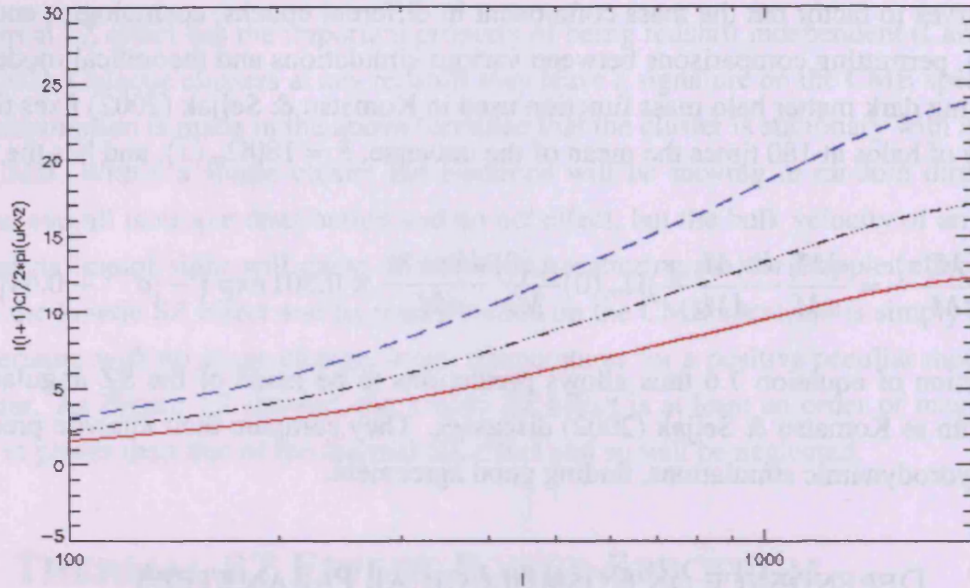


Figure 7.3: The Sunyaev Zel'dovich Spectrum

Power spectra for the SZ effect assuming  $\sigma_8 = 0.8$  at QUaD's frequencies; 100 GHz in blue, 150 GHz in red and the cross frequency spectrum in black.

The 7<sup>th</sup> power means that a 10% change in  $\sigma_8$  translates into a factor of 2 difference in the spectrum amplitude.

Komatsu & Seljak (2002) also state that they find the dependence of  $C_\ell$  upon other parameters;  $\Omega_m$ ,  $\Omega_b$ ,  $h$ ,  $n$  and  $\omega$  (the equation of state), to be very weak in comparison to that of  $\sigma_8$ . The comoving volume of the universe increases as  $\Omega_m$  decreases, cancelling out any effect that  $\Omega_m$  might have on the dark matter mass function.

Whilst virtually independent as separate parameters, the combination  $\Omega_b h$  does play a role. The amplitude of the SZ effect is proportional to  $n_e$ , the electron number density. For an isothermal cluster the total SZ flux density will therefore be proportional to the total electron count in that cluster. The intracluster gas content of a galaxy cluster is greater than the mass in the galaxies that make up the cluster and so the SZ effect can be used to provide an estimate of the baryonic mass density in the cluster.

Simply, the SZ effect will be greater for a greater density of baryonic gas in the cluster. The central gas density in a cluster scales with  $(\Omega_b h)^2$ , and the overall amplitude of the power spectrum is set by (Komatsu & Seljak, 2002):

$$\frac{\ell(\ell+1)C_\ell}{2\pi} \simeq 330\mu K^2 \sigma_8^7 \left( \frac{\Omega_b h}{0.035} \right)^2 \quad (7.9)$$

Adding data from x-ray surveys of the clusters allows the redshifts of the clusters to be determined and parameter degeneracies broken, revealing much more information from the SZ effect; in particular the Hubble constant and matter densities,  $\Omega_m$  and  $\Omega_b$  could, in principle, be more tightly constrained.

### 7.3 OBSERVATIONS AND $\sigma_8$ MEASUREMENTS

Whilst there are of course various experiments, the Sunyaev-Zel'dovich Array (SZA) for example (Muchovej et al., 2007), designed specifically to observe the SZ effect and its use to detect and study clusters, here the focus is within the context of the cosmic microwave background; the observations which can be made, and the parameters that can be determined with CMB instruments. It is only above  $\ell \sim 2000$  that the excess power due to the SZ effect could begin to dominate over the primary CMB anisotropies, but there are several experiments which have made measurements on such small angular scales, including QUaD itself (Friedman et al., 2009) as shown in Figure 7.4.

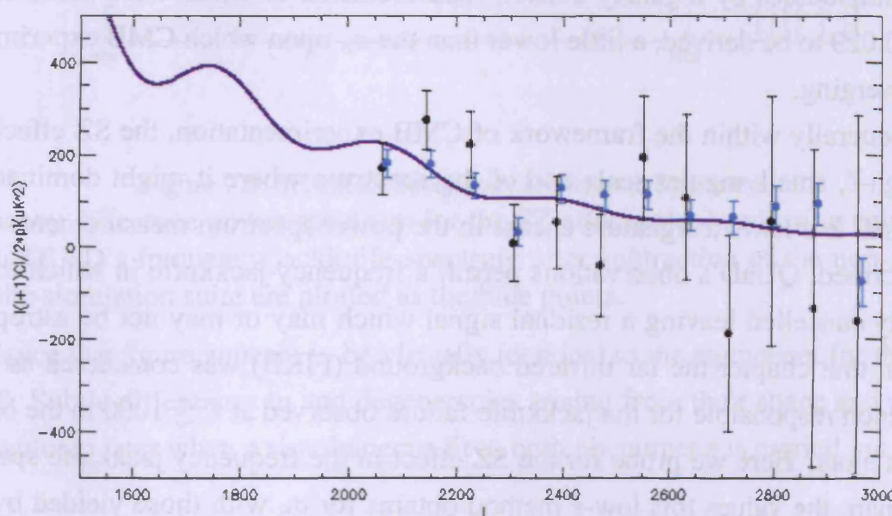


Figure 7.4: QUaD's Small Angular Scale Temperature Power Spectra

Measurements of the CMB temperature power spectrum at 100 GHz (black points) and 150 GHz (blue points) up to  $\ell = 3000$ , including a subtraction of the residual radio point sources as detailed in Friedman et al. (2009), do not show an excess over the predicted CMB anisotropies of the  $\Lambda$ CDM model (purple line).

Others include the Cosmic Background Imager (CBI) (Sievers et al., 2009) and the Berkeley-Illinois-Maryland Association (BIMA) interferometer (Dawson et al., 2006) at 30 GHz and 28.5 GHz respectively. Plus at higher frequencies the Arcminute Cosmology

Bolometer Array Receiver (ACBAR) (Reichardt et al., 2009a), Bolocam (Sayers et al., 2009) and the Atacama Pathfinder Experiment SZ (APEX-SZ) instrument (Reichardt et al., 2009b) all at 150GHz. Along with the SZA (Sharp et al., 2009) at 30 GHz and QUaD, some of these show signs of the expected excess whilst others do not.

From the excesses apparently observed by BIMA and CBI values are inferred for  $\sigma_8$  somewhat higher than the template value suggested of 0.8. CBI reports  $\sigma_8 = 1.015 \pm 0.06$  and BIMA  $\sigma_8 = 1.03^{+0.20}_{-0.29}$ . Whilst still detecting an excess ACBAR yields the lower value of  $\sigma_8 = 0.8 \pm 0.04$ . The SZA and QUaD, as Figure 7.4 illustrates, do not show an excess, whilst Bolocam and APEX-SZ are able to place upper limits of  $\sigma_8 < 1.57$  and  $\sigma_8 < 1.18$  respectively.

$\sigma_8$  may also be determined using measurements of other astrophysical phenomena, providing alternative values for comparisons. The Lyman-Alpha forest is absorptions in intergalactic gas clouds of Lyman- $\alpha$  emissions from more distant quasars. Data from the Sloan Digital Sky Survey (SDSS) of the Lyman- $\alpha$  forest suggests  $\sigma_8 = 0.85 \pm 0.02$  (Seljak et al., 2006). Fu et al. (2008) report weak lensing results based on the Canada-France-Hawaii Telescope Legacy Survey (CFHTLS). Weak lensing is a small distortion of background sources by a galaxy cluster, measurements of which have permitted a value  $0.771 \pm 0.029$  to be derived, a little lower than the  $\sigma_8$  upon which CMB experiments seem to be converging.

Generally within the framework of CMB experimentation, the SZ effect is sought at the high- $\ell$ , small angular scale end of the spectrum where it might dominate over the CMB signal and leave a signature excess in the power spectrum measurements. As Chapter 6 described, QUaD's observations permit a frequency jackknife in which the CMB is effectively cancelled leaving a residual signal which may or may not be astrophysical in origin. In that chapter the far infrared background (FIRB) was considered as a possible phenomenon responsible for the jackknife failure observed at  $\ell \lesssim 1000$  in the band power deviation plots. Here we probe for the SZ effect in the frequency jackknife spectrum and can compare the values this low- $\ell$  method obtains for  $\sigma_8$  with those yielded by the more traditional parameter estimation of Brown et al. (2009) and Gupta et al. (2009).

## 7.4 LOOKING FOR THE SZ EFFECT IN QUAD'S FREQUENCY JACKKNIFE

### 7.4.1 SZ FREQUENCY DIFFERENCE

The method followed here will be much the same as that for the FIRB in Section 6.5 of the previous chapter. The first step is to compute the SZ frequency difference spectrum from

the 100 GHz, 150 GHz and cross frequency SZ spectra as shown in Figure 7.3. Band power window functions,  $\omega_{b\ell}$ , are employed in the calculation to ensure the template spectrum is correctly binned with each  $\ell$ -value weighted accordingly:

$$C_l^{diff} = \sum_{\ell} \frac{\omega_{b\ell}}{\ell} \left( \frac{C_{\ell}^{100} + C_{\ell}^{150} - 2C_{\ell}^{cross}}{4} \right) \quad (7.10)$$

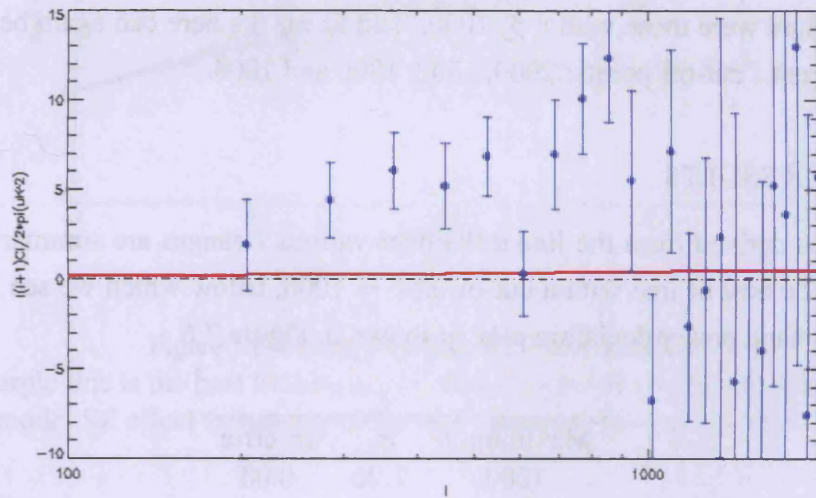


Figure 7.5: SZ Effect Frequency Difference Spectrum

The frequency difference power spectrum for the SZ effect calculated using equation 7.10 (red line). QUAD's frequency jackknife spectrum after subtraction of the non-zero mean amongst the simulation suite are plotted as the blue points.

At first glance this figure appears to be virtually identical to the equivalent for the FIRB in Figure 6.8. Subtle differences in and degeneracies arising from their shape and magnitude shall be explored later when a simultaneous fit to both phenomena is carried out.

#### 7.4.2 LINEAR FITS

The SZ frequency difference spectra of Figure 7.5 can be fit to the QUAD frequency jackknife spectrum, just as was done before with the FIRB. This time the scaled spectrum will provide a constraint on the parameter  $\sigma_8$  using the scaling function in equation 7.8. The fitting is performed using a least chi-square technique, weighting the frequency jackknife data,  $q$ , with an inverse variance weighting scheme. The chi-square is found from the QUAD data and the SZ template spectrum,  $s$ , as:

$$\chi^2 = \sum (q_i - ms_i)^2 / \sigma_i^2 \quad (7.11)$$

The best fit scaling factor is given by the gradient,  $m$ , which minimizes the  $\chi^2$ . This is found by differentiating with respect to  $m$  and setting the result to zero:

$$m = \frac{\sum (s_i q_i / \sigma_i^2)}{\sum (s_i^2 / \sigma_i^2)} \quad (7.12)$$

The best fit gradient obtained can be related back to  $\sigma_8$  by  $0.8m^{1/7}$  since the template was constructed assuming  $\sigma_8 = 0.8$  and we take  $C_\ell \propto \sigma_8^7$ . In Chapter 6 the issue of which  $\ell$ -range to use was discussed after Figure 6.7 revealed the band powers responsible for the jackknife failure were those with  $\ell \lesssim 1000$ . The linear fits here can again be repeated for several different  $\ell$  cut-off points: 2000, 1500, 1300 and 1000.

### 7.4.3 $\sigma_8$ RESULTS

The  $\sigma_8$  values derived from the linear fits over various  $\ell$ -ranges are summarized in Table 7.1 below. The best fit line with a cut-off at  $\ell = 1000$ , below which we see the jackknife failure in the band power deviation plot, is shown in Figure 7.6

Maximum $\ell$	$\sigma_8$	$1\sigma$ error
1000	1.26	0.03
1300	1.19	0.03
1500	1.15	0.04
2000	1.13	0.04

Table 7.1: The  $\sigma_8$  values with  $1\sigma$  errors suggested by the best fitting of the SZ effect frequency difference template spectrum to the QUaD frequency jackknife spectrum.

As with the FIRB we see a decrease in the  $\sigma_8$ 's derived with higher  $\ell$  cut-offs owing to the negative values in QUaD's frequency jackknife seen after  $\ell = 1000$ . Particularly after  $\ell = 1300$  these begin to have greater error bars because of the differences in beam size between 100 GHz and 150 GHz and so are downweighted accordingly. They do still however have the effect of dragging down the best fit scaling as Figure 7.7 illustrates.

Although not entirely unreasonable in light of the upper limits Bolocam and APEX-SZ place on  $\sigma_8$  of 1.57 and 1.18, the values yielded by this method are quite a bit higher than that typically obtained by a CMB experiment. This could perhaps be because whilst the residual signal left in the frequency jackknife may be due to the SZ effect, it is more likely to be the combination of SZ effect and FIRB signals than either independently. In addition there may be a third factor that has not yet been taken into consideration; a contribution from residual radio point sources, so this will be looked at first.

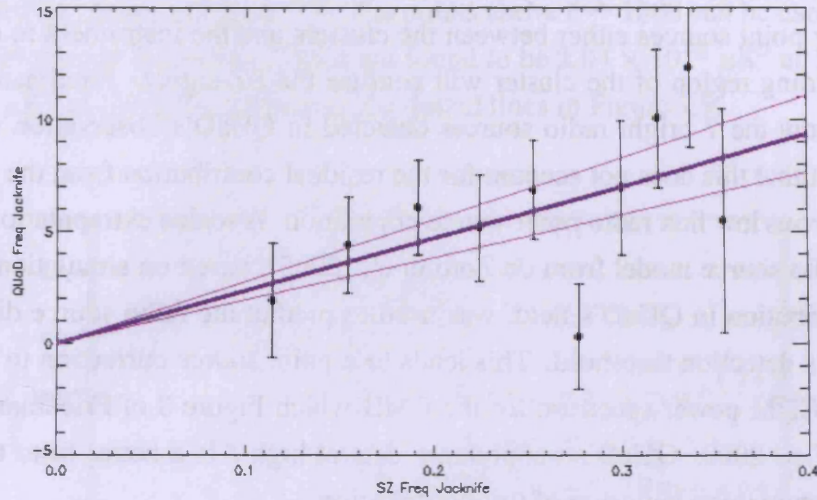


Figure 7.6: Linear Fit to the SZ Effect template

The thick purple line is the best fit through the black points of QUAD's frequency jackknife against the model SZ effect frequency difference spectrum for  $\ell$  up to 1000.

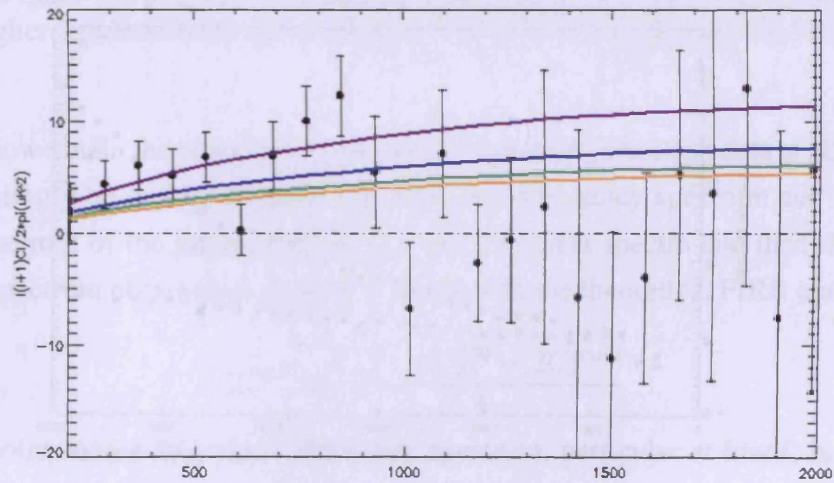


Figure 7.7: Scaled SZ Effect Spectra

QUAD's frequency jackknife spectrum (black points) with the SZ effect frequency difference spectrum scaled according to  $(\sigma_8/0.8)^7$  for the different  $\ell$ -ranges: purple  $< 1000$ , blue 1300, green  $< 1500$ , orange  $< 2000$ .

## 7.5 RADIO POINT SOURCES

Radio point sources are frequently noted as an obstacle in SZ effect detections (Holder, 2002). Any point sources either between the clusters and the instrument in question or in the surrounding region of the cluster will confuse the SZ signal. Friedman et al. (2009) describes how the 7 bright radio sources detected in QUaD's observation region can be masked, but that this does not account for the residual contribution from the exponentially more numerous low flux radio point source population. A scaled extrapolation of the extragalactic radio source model from de Zotti et al. (2005), based on simulations of the point source distribution in QUaD's field, was used to predict the radio source distribution below QUaD's detection threshold. This leads to a point source correction to the otherwise expected  $\Lambda$ CDM power spectrum for the CMB which Figure 3 of Friedman et al. (2009) shows for  $\ell > 2000$ . QUaD's temperature data at high  $\ell$  is a better fit to the theoretical power spectrum upon inclusion of this contribution.

### 7.5.1 RADIO POINT SOURCE SPECTRA

Figure 7.8 shows the radio point source correction data itself at all  $\ell$  up to 3000 for both QUaD's frequencies. As expected, since radio waves are of long wavelength, we see a larger correction required at 100 GHz than 150 GHz.

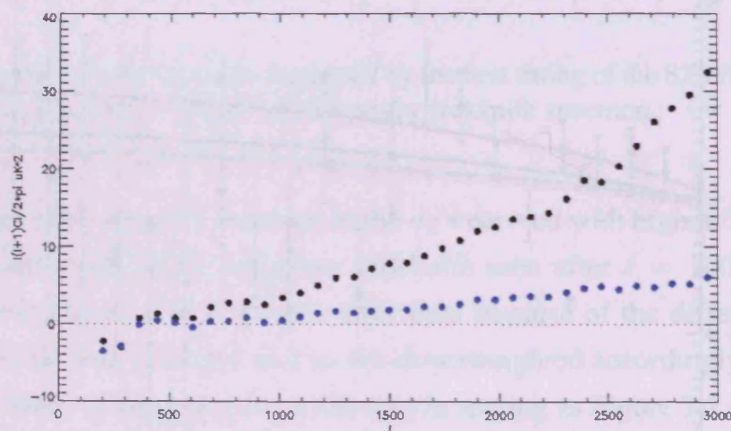


Figure 7.8: Radio Point Source Corrections

The correction added to the theoretical  $\Lambda$ CDM model to account for the correction to the CMB spectrum from residual radio point sources. 100 GHz in black and 150 GHz in blue.

The assumption can be made regarding the point sources that their Poisson distribution produces a simple white spectrum. This means it is independent of angular size and

is seen to merely rise as  $\ell^2$  in Figure 7.8 because of the way in which the power is defined on the y-axis. Dividing out the  $\ell^2/2\pi$  factor yields the expected flat spectrum at high  $\ell$  with noise at lower  $\ell$  as shown in Figure 7.9. The points above  $\ell \sim 1500$  can be used to estimate the mean level at each frequency. These are found to be  $2.04 \times 10^{-5} \mu\text{K}^2$  at 100 GHz and  $4.61 \times 10^{-6} \mu\text{K}^2$  at 150 GHz, plotted as the dotted lines in Figure 7.9.

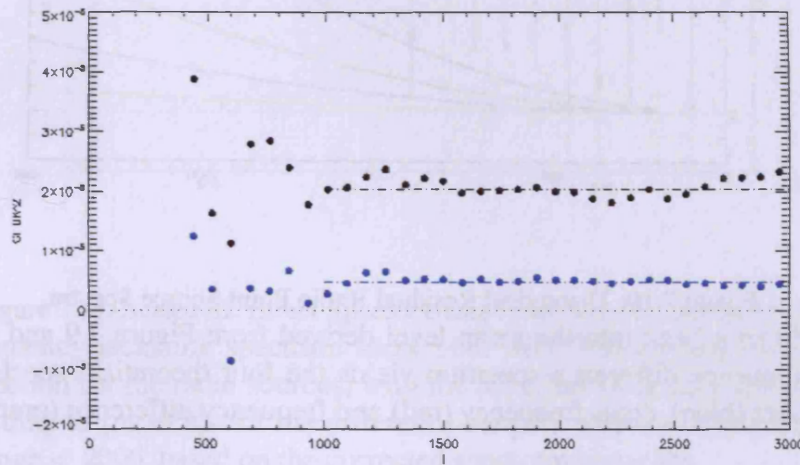


Figure 7.9: Radio Point Source White Spectra

We can assume the theoretical point source distribution to be white and hence take out the  $\ell^2$  factor in Figure 7.8 to give a flat spectrum, the mean level of which can be determined from the higher  $\ell$  points and is shown by the dotted lines at both 100 GHz (black) and 150 GHz (blue).

To now obtain the theoretical residual point source correction data at all  $\ell$ , the  $\ell^2/2\pi$  factor can simply be multiplied back in. The cross frequency spectrum can be estimated as the square root of the product of the 100 and 150 GHz spectra and then the frequency difference spectrum obtained as done previously with the theoretical FIRB and SZ spectra:

$$C_l^{diff} = \frac{C_l^{100} + C_l^{150} - 2C_l^{cross}}{4} \quad (7.13)$$

The radio point source frequency difference spectrum, particular at low  $\ell$ , is of very low magnitude ( $\sim 0.2 \mu\text{K}^2$  at  $\ell = 1000$ ), but nevertheless can be subtracted off of QUaD's frequency jackknife to account for any contribution the point sources might be making, however slight.

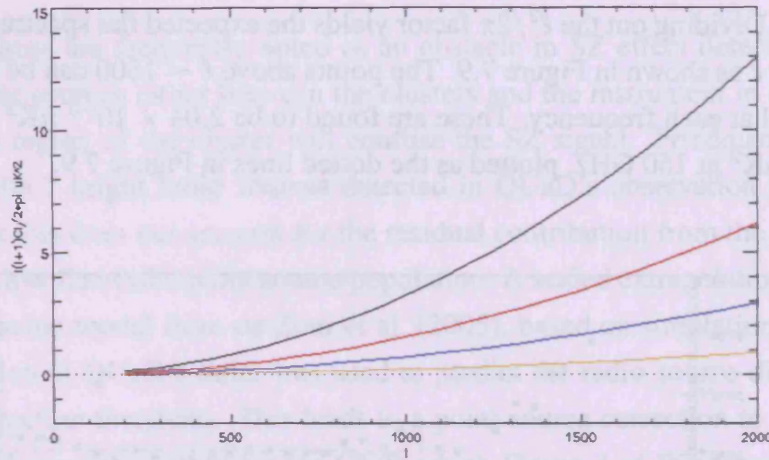


Figure 7.10: Theoretical Residual Radio Point Source Spectra

Putting the  $\ell^2$  factor back into the mean level derived from Figure 7.9 and calculating a cross and a frequency difference spectrum yields the four theoretical spectra: 100 GHz (black), 150 GHz (blue), cross frequency (red) and frequency difference (orange).

### 7.5.2 $\sigma_8$ RESULTS AFTER CORRECTING FOR RESIDUAL POINT SOURCES

The theoretical contribution from residual radio sources can be removed from each band power of the frequency jackknife spectrum before the linear fit to the SZ model is then carried out in exactly the same way as before. The results obtained are listed in Table 7.2 and illustrated below in Figure 7.11.

Maximum $\ell$	$\sigma_8$	$1\sigma$ error
1000	1.25	0.03
1300	1.18	0.04
1500	1.14	0.04
2000	1.11	0.05

Table 7.2: The  $\sigma_8$  values and  $1\sigma$  errors obtained by performing the best fit of the SZ effect frequency difference template spectrum to the QUaD frequency jackknife spectrum after first subtracting an estimate of the residual radio point source contribution.

As expected the values now yielded for  $\sigma_8$  are a little lower, and slightly more so when going up to a higher  $\ell$  where the radio contribution is greater. The values are all still on the high side though further supporting the idea that it is not just the SZ effect that needs to be considered and that a residual radio source contribution is not sufficient to explain the

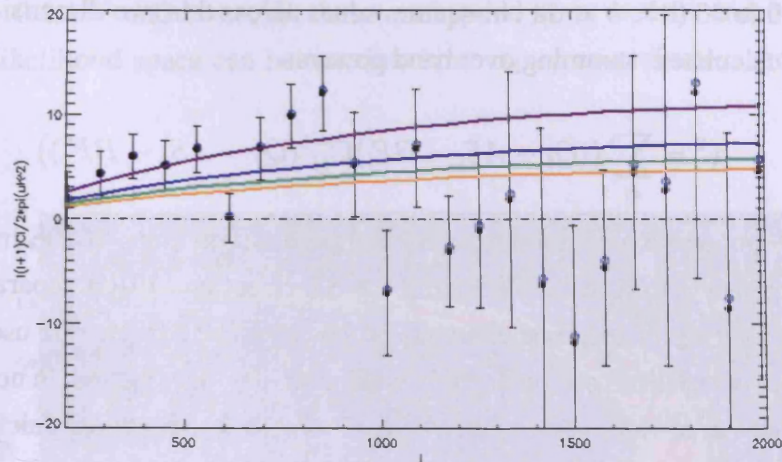


Figure 7.11: Scaled SZ Effect Spectra Using Point Source Corrected Results  
 QUaD's frequency jackknife spectrum show both with (black points) and without (blue points) correction for the radio sources, with the SZ effect frequency difference spectrum scaled according to  $(\sigma_8/0.8)^7$  for the different  $\ell$ -ranges: purple  $< 1000$ , blue  $1300 < \ell < 1500$ , green  $< 1500$ , orange  $< 2000$ , based on the corrected spectrum linear fits.

signal. We can therefore explore the possibility of including a point source correction, the SZ effect and the FIRB.

## 7.6 SIMULTANEOUSLY FITTING THE FIRB AND THE SZ EFFECT

A similar maximum likelihood technique to that which has been used to look for the FIRB and the SZ effect independently in the frequency jackknife can be employed to fit the two simultaneously. This will allow constraints to be made on both the clustering bias,  $b$ , and  $\sigma_8$  at the same time based on their individual scaling factors. The idea is to find values of  $A$ , the SZ effect amplitude and  $B$ , the FIRB amplitude to best fit:

$$Q = AS + BF \quad (7.14)$$

in which  $Q$  represents the QUaD frequency jackknife after subtraction of the residual radio point source contribution.  $S$  and  $F$  are the SZ effect and FIRB frequency difference spectra respectively. The FIRB spectra used is that derived from the simulations described in Chapter 6 rather than the analytical one and the analysis is confined to  $\ell < 1000$ , the band powers where we see the failure in QUaD's jackknife test.

Allowing the value of  $A$  to vary from 0 to 81 ( $0 < \sigma_8 < 1.5$ ) and the value of  $B$  to vary from 0 to 36 ( $0 < b < 6$ ), chi-square values across this two dimensional parameter space can be calculated, summing over band powers:

$$\chi^2 = \sum_{ij} ((Q_i - AS_i - BF_i)C_{ij}^{-1}(Q_j - AS_j - BF_j)) \quad (7.15)$$

$C_{ij}$  is the covariance matrix of the QUaD data; the equivalent of the inverse variance weighting which was used when analyzing the SZ effect and FIRB separately. Only the diagonal and first two off-diagonal elements of the covariance matrix are used; beyond this the band power correlations are sufficiently weak that they become lost in noise. The likelihood,  $\mathcal{L}$ , at each set of values across the  $A - B$  parameter space is then calculated as (Press et al., 2007):

$$\mathcal{L} = \exp(-0.5\chi^2) \quad (7.16)$$

The location of maximum likelihood corresponds to the point in  $A - B$  space with the least chi-square. On Figure 7.12 this position is marked with a star. Contours are drawn enclosing 68%, 95% and 99% of the likelihood illustrating the 1, 2 and 3 $\sigma$  deviations from maximum likelihood.

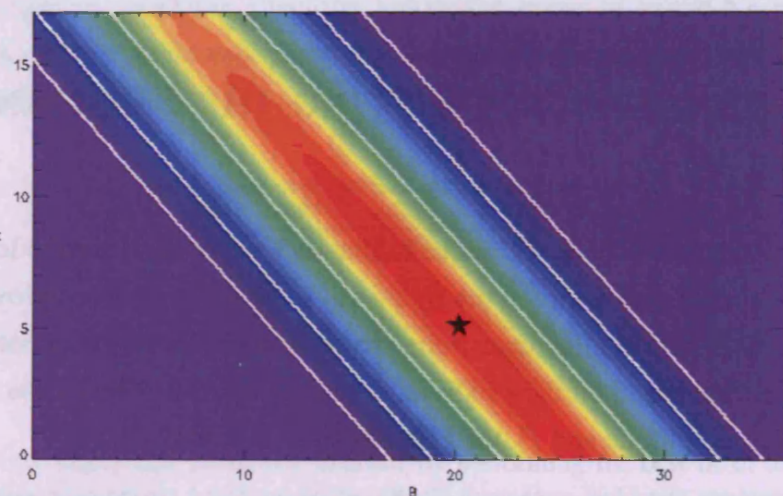


Figure 7.12: SZ Effect and FIRB Amplitude Likelihoods

Likelihoods from a simultaneous fit of the  $\ell < 1000$  QUaD frequency jackknife after subtraction of radio sources to  $A$  (the SZ amplitude) and  $B$  (the FIRB amplitude), with contours drawn at the 68%, 95%, and 99% positions and a star to mark the location of maximum likelihood.

At the point of the star the amplitudes are  $A = 5.11$  and  $B = 20.16$ . Using the relations  $\sigma_8 = 0.8A^{1/7}$  and  $b = \sqrt{B}$ , these correspond to  $\sigma_8 = 1.01$  and  $b = 4.49$ . The whole  $A - B$  likelihood space can be translated into  $\sigma_8 - b$  co-ordinates, shown in Figure 7.13.

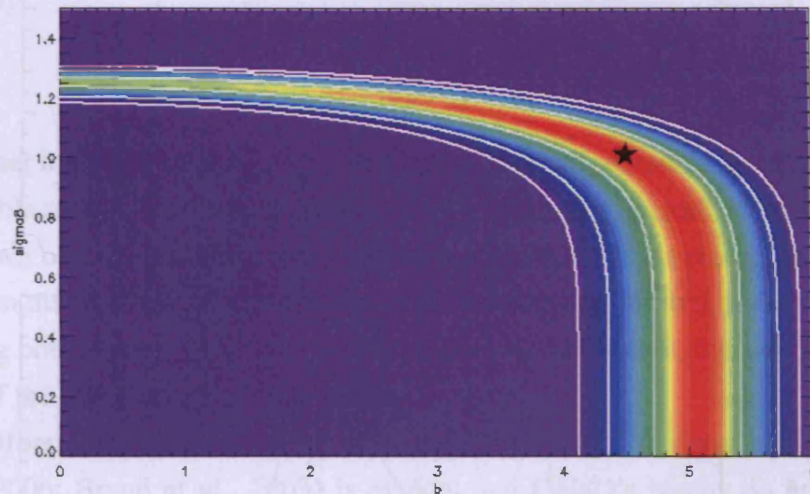


Figure 7.13:  $\sigma_8$  and  $b$  Likelihoods

The amplitude likelihood plot in Figure 7.12 translated into  $\sigma_8 - b$  parameter space. Again with a star to indicate the  $\sigma_8 = 1.01$ ,  $b = 4.49$  position of maximum likelihood and three contours enclosing 68%, 95%, and 99% of the likelihood.

The  $1\sigma$  contour line can be used to place errors on the values of the parameters derived. Because of the non-linear relationships between the amplitudes and the parameters these errors are not symmetrical about the value. The result is  $\sigma_8 = 1.01^{+0.07}_{-0.13}$  and  $b = 4.49^{+0.38}_{-0.42}$ . One dimensional slices can be taken through parameter space in either direction at any chosen value. Figure 7.14 shows slices cut across at each of the maximum likelihood values yielding the likelihood of the other parameter under the assumption that the other is correct.

### 7.6.1 DISCUSSION OF RESULTS

Unlike its previous independently derived counterpart the value now suggested for  $\sigma_8$  is more in line with those other experiments have obtained. CBI and BIMA for example, as described in Section 7.3, report  $\sigma_8 = 1.015 \pm 0.06$  and  $\sigma_8 = 1.03^{+0.20}_{-0.29}$  respectively. For other experiments and even for the traditional parameter analysis carried out by QUaD itself the  $\sigma_8$  found is much lower  $\sim 0.8$ . This is however using an entirely different method

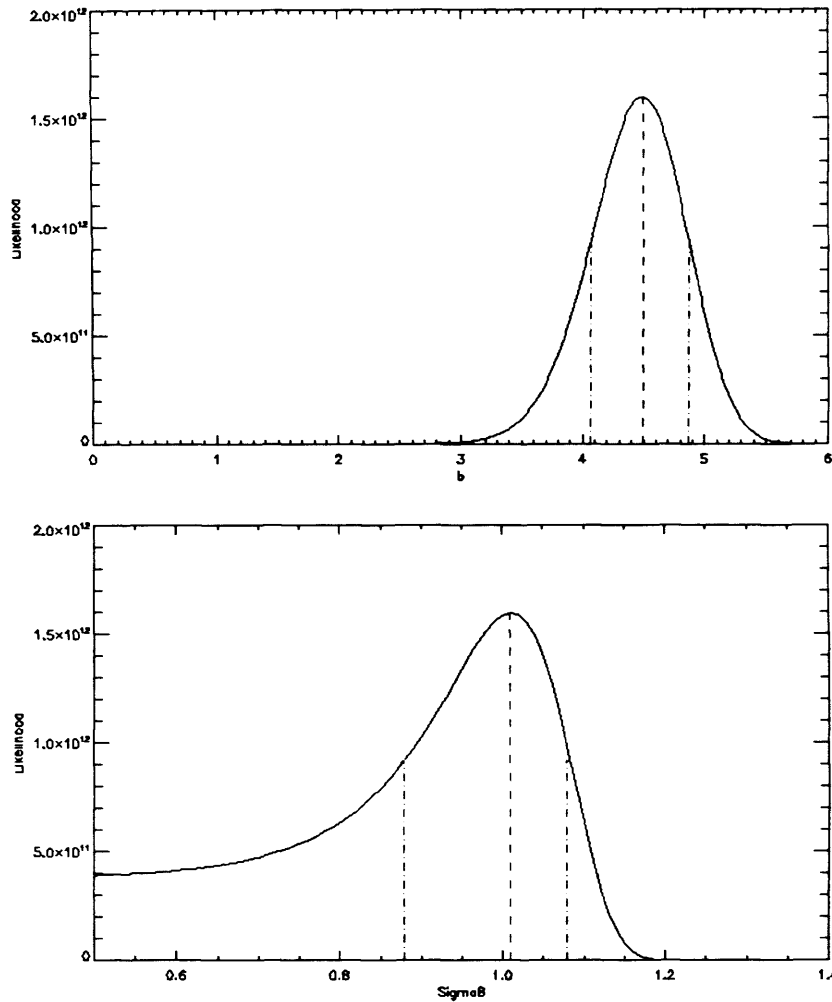


Figure 7.14: One Dimensional Likelihood Slices

A cut through parameter space at  $\sigma_8 = 1.01$  showing the resultant likelihood of  $b$  (top) and similarly at  $b = 4.49$  showing how the likelihood of  $\sigma_8$  values is then distributed (bottom). Both plots mark the maximum likelihood point of the other parameter with its  $1\sigma$  errors in blue.

so we should not expect the same results and actually a value of 0.8 is not ruled out here. The bottom panel of Figure 7.14 shows that setting  $b = 4.49$  merely sets the upper limit of  $\sigma_8 < 1.18$ , and puts 1.01 as the most likely value whilst lower values are less likely but by no means impossible.

A higher  $\sigma_8$  implies a greater mean level of matter density fluctuations on the  $8h^{-1}$  Mpc scale and therefore deeper gravitational potential wells with more clustered galaxies. The SZ effect is due to the inverse Compton scattering of CMB photons by hot electrons in the intracluster medium. Thus with more clustering there will be more highly energetic

electrons to cause a bigger SZ effect and a larger distortion of the CMB power spectrum.

There is a strong degeneracy between the two parameters,  $\sigma_8$  and  $b$ , arising from the similarities in the shapes of their spectra, particularly at low  $\ell$ . This degeneracy is very apparent in Figure 7.12. If the SZ effect amplitude were to be lower, the FIRB amplitude would be higher and vice versa. The graph reveals a straight line function between the two approximately:

$$b^2 = -(0.8\sigma_8^7) + 25 \quad (7.17)$$

Without further information or setting priors based on results obtained by other experiments it is impossible to constrain either parameter any more than permitted by the likelihood contours drawn on the plot. Fortunately there are plenty of measurements of both  $\sigma_8$  and  $b$  that have been made, many of which have been discussed earlier in this chapter and also in the preceding one. Figure 7.15 offers the likelihood plot as before, but now encompassing a selection of the other experimental results.

The aforementioned increasing of bias with redshift (Weinberg et al., 2004; Marinoni et al., 2006; Brand et al., 2003) is evident and QUaD's results do not discontinue this trend. The  $\sigma_8$ 's are less wide ranging, approximately between 0.77 and 1.17. The two curves at the bottom arise from the functions  $\sigma_8 b = 0.69$  (Saunders et al., 1992) and  $\sigma_8 b = 1.2$  (Fan et al., 1997), for which the IRAS redshift survey data and galaxy clustering data respectively have been used to constrain the  $\sigma_8 - b$  relation.

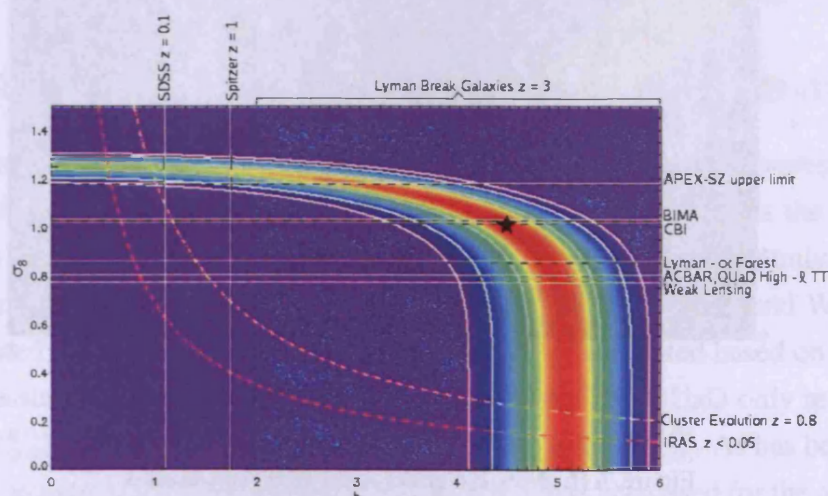


Figure 7.15:  $\sigma_8$  and  $b$  Results

The  $\sigma_8 - b$  likelihood plot of Figure 7.13 incorporating various values of the two parameters suggested by other experiments.

### 7.6.2 INCLUDING VARIATION OF $\sigma_8$ IN THE FIRB SPECTRUM

Section 6.3.1 described how the FIRB power spectrum is constructed. It mentioned that the term  $P_M(k)|_{k=\ell/r}$ , the present power spectrum of the dark matter density fluctuations, is normalized via the parameter  $\sigma_8$ . This parameter should therefore not be fixed in the FIRB spectrum if it is being allowed to vary in the SZ spectrum.

The FIRB power spectrum scales with  $\sigma_8^2$ , the variance based on smoothing within the  $8h^{-1}$  Mpc window. This will, however, introduce errors since smoothing on these scales is erasing the contribution from larger modes. It is also likely that a different  $\sigma_8$  would imply different values for other parameters, such as the matter density or the scalar spectral index, which would alter the shape and evolution of the spectrum. Nevertheless we can use this scaling as a rough first approximation.

The amplitude  $B$  in equation 7.14 is now dependent on both  $\sigma_8$  and  $b$  as:

$$B = \left(\frac{\sigma_8}{0.8}\right)^2 b^2 \quad (7.18)$$

This corresponds to a change in the likelihood plots and the maximum likelihood values derived. Figures 7.16 and 7.17 show the results of incorporating this additional dependence.

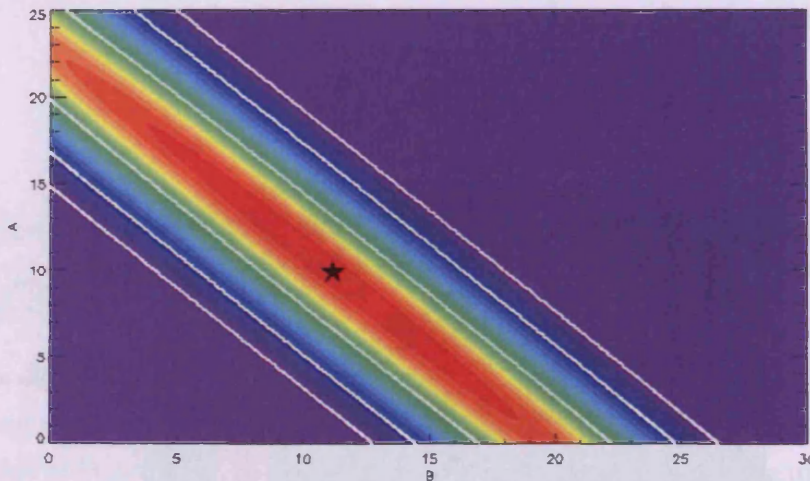
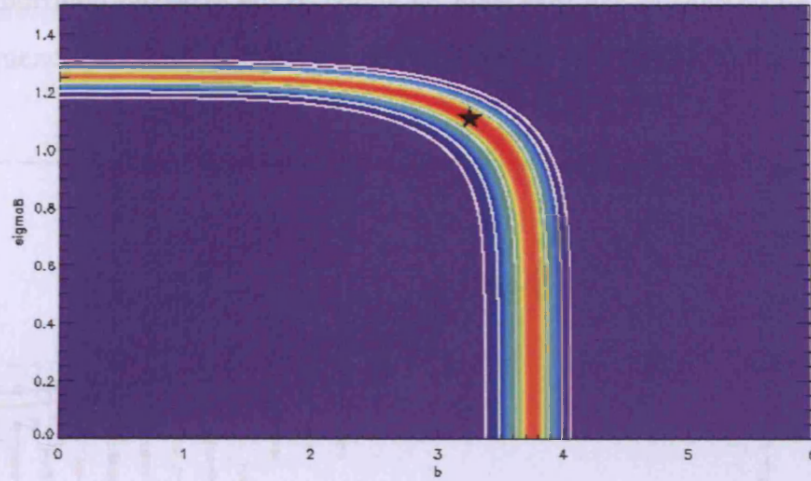


Figure 7.16: New SZ effect and FIRB Amplitudes

Results after the  $\sigma_8$  dependence of the FIRB spectrum is taken into consideration in the fitting.

As before the stars mark the points of maximum likelihood and the contour lines define the uncertainties. The results are  $A = 9.89_{-3.18}^{+2.99}$  and  $B = 11.17_{-2.83}^{+2.66}$ , which translate

Figure 7.17: New  $\sigma_8$  and  $b$ 

$\sigma_8 - b$  parameter space when the FIRB spectrum is also dependent upon  $\sigma_8$ .

to values of  $\sigma_8 = 1.11^{+0.04}_{-0.06}$  and  $b = 3.27^{+0.18}_{-0.23}$ .

This reveals that including a  $\sigma_8$  dependence on the FIRB spectrum in the analysis leads to a slight increase in the value of  $\sigma_8$  and consequently, as expected given the degeneracy between the two parameters, a decrease in the bias. Nevertheless, the results are not significantly different to all the previous ones;  $\sigma_8$  is still greater than 1, and  $b$  still greater than 3. Therefore the cosmological implications of these values remain the same.

### 7.6.3 RESULTS IN THE CONTEXT OF QUAD'S HIGH- $\ell$ DATA

QUaD's own final parameter estimation analysis in Gupta et al. (2009) presents values of the linear mass perturbation  $\sigma_8$  derived from the  $\ell < 2000$  data plus the high- $\ell$  (up to  $\ell = 3000$ ) temperature data. There are values published for a QUaD-only constraint on the parameter, and also upon inclusion of the ACBAR, CBI, BICEP and WMAP results. The estimated SZ effect power in this analysis was also simulated based on  $\sigma_8 = 0.8$  and under the assumption of scaling with the seventh power. The QUaD-only result yielded is  $\sigma_8 = 0.82^{+0.05}_{-0.06}$  and with the other datasets added is  $\sigma_8 = 0.84^{+0.04}_{-0.06}$ . As has been mentioned previously, a completely different and novel approach has been used for the analysis in this thesis, thus to expect the same results would be naive.

Nevertheless the consistency of the results obtained here with the high- $\ell$  results shown in Figure 7.4 can be investigated via an extrapolation of the template models to higher  $\ell$ . The best fit amplitudes for the FIRB and the SZ effect from the analysis in this

chapter can be applied to their respective template spectra at both 100 GHz and 150 GHz. The resulting two spectra can then both be added to the expected contribution from the CMB assuming a  $\Lambda$ CDM model (Dunkley et al., 2009).

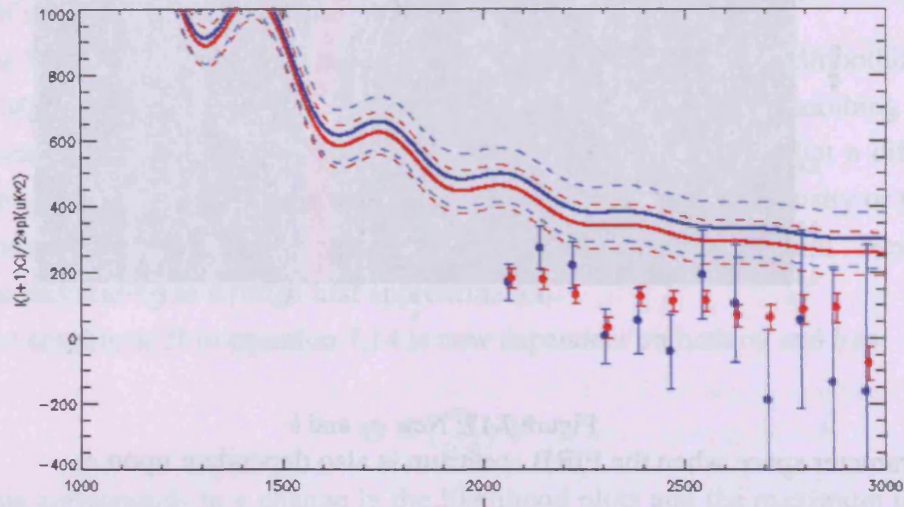


Figure 7.18: Results Compared to QUaD's High- $\ell$  Temperature Data

Spectra at 100 GHz (blue) and 150 GHz (red) suggested by the work in this chapter. Each consists of the  $\Lambda$ CDM model CMB temperature spectrum plus FIRB and SZ effect components based on their best fit amplitudes; 11.17 and 9.89 respectively. The dashed lines either side are the  $1\sigma$  errors on these spectra. The blue and red data points are the corresponding QUaD high- $\ell$  temperature data (Friedman et al., 2009) after subtraction of the residual point source contribution.

Figure 7.18 shows this combined spectra plotted with the QUaD high- $\ell$   $TT$  results from Friedman et al. (2009), which include a subtraction of the residual radio point sources.

From this it is evident that the contribution from the FIRB and the SZ effect to the data cannot be as large as the analysis based on the  $\ell < 1000$  frequency jackknife might suggest. Especially in the 150 GHz case, the prediction, even given its  $1\sigma$  error, is much above the data. This inconsistency reveals that whilst there may yet be smaller components of the FIRB and the SZ effect, the frequency jackknife signal requires them to be higher than is now shown they can be in light of high- $\ell$  results, and thus leads to the conclusion that this cannot be the end of the story. Something else more dominant at low- $\ell$ , be it an instrumental systematic, a feature of the analysis pipeline or another astrophysical phenomenon must also be at work.

So unfortunately whilst there are alternative measurements of  $\sigma_8$  and  $b$  from various experiments, the results cover a spread across parameter space and their values derived from

---

the methods here have proven to be inconclusive. The true  $\sigma_8$  and clustering bias describing the universe therefore remain somewhat irresolute and the true nature of the residual signal in QUaD's frequency jackknife remains a mystery.



# 8 CONCLUSIONS AND FUTURE WORK

---

“THE HISTORY OF MAN IS HUNG ON A TIMELINE OF EXPLORATION AND THIS IS WHAT’S NEXT.”

SAM SEABORN - THE WEST WING

## 8.1 SUMMARY OF KEY RESULTS

This thesis began by considering the very early universe to be like a bowl of soup. A hot dense opaque soup of electrons, protons, helium nuclei and neutrinos, with photons bouncing around. After  $\sim 380,000$  years it had cooled sufficiently for the primordial particles to unite, scattering the photons one last time before liberating them to journey across the now transparent universe.

Telescopes like QUaD can look out into space and see these photons everywhere, in all directions. In the billions of years since the last scattering event they’ve cooled down and are now of millimeter wavelengths with a mean temperature of 2.73K. Observing this Cosmic Microwave Background (CMB) allows us to build up a picture of the surface of the soup and map the parts that are fractionally hotter or colder. From measurements of the fluctuations in temperature across the sky and the polarization of the light this causes, we can infer much about the universe and attempt to explain why and how it has evolved into that seen today. We can thereby increase the accuracy to which we know parameters such as how much matter there is, how fast the universe is expanding and the amplitude of the density fluctuations responsible for the creation of structure.

The structures themselves however, and indeed everything else filling space between QUaD and the CMB, can hinder the experiment and contaminate the results such that they are not a true description of the universe. After first detailing the instrument and the analysis techniques used, this thesis has discussed and quantitatively analyzed a number of possible phenomena which may have affected QUaD’s success in measuring the CMB.

The main idea behind and the results from each are highlighted here.

### 8.1.1 DUST

1% of the interstellar medium is dust which absorbs photons from stars and re-emits them at lower frequencies, with a peak at  $\sim 3000$  GHz. QUaD observes at 100 and 150 GHz so we would not expect vast quantities of dust to be swamping the measurements, but nevertheless an extrapolation down to CMB frequencies can be made using a multi-component dust particle model.

After simulating QUaD's beams, filtering and scan strategy by running the dust maps through the analysis pipeline, the extent of correlation between the dust and the CMB maps was characterized via linear fits and the calculation of a correlation coefficient. Error bars were obtained on the correlation statistics by repeating the procedure with a suite of dust maps shifted around the globe from QUaD's observing region. A slight negative correlation was found that proved insignificant in light of the error bars and therefore more likely due to a chance alignment of morphologies.

A cross correlation power spectrum was then computed revealing that all band powers lay within the spread of the simulations with no extreme band power deviations. From this the conclusion was drawn that there was no evidence to suggest a dust foreground contaminating the temperature data.

If the dust grains become aligned, by a magnetic field for example, this can result in up to 5% of the light intensity becoming polarized. The correlation analysis was therefore also carried out on QUaD's  $Q$ ,  $U$  and total polarization data, but again finding no hint of any significant contamination.

The upshot of the investigation, whilst not very exciting in the context of this work, does bode well for QUaD and potentially other experiments in the future, confirming that a good choice of dust-free observing region was made and providing reassurance that the results obtained by the experiment are not influenced by dust in the interstellar medium between the CMB and the telescope.

### 8.1.2 SYNCHROTRON

Synchrotron radiation is emitted when the magnetic field associated with a supernova accelerates cosmic ray electrons passing through. The frequency of the radiation is dependent upon the strength of the magnetic field, becoming less significant than the CMB above  $\sim 50$  GHz and so at QUaD's frequencies the predicted power is negligible.

A spectral index model used to extrapolate synchrotron measurements at 408 MHz up to CMB frequencies then allowed for the same method as summarized above for the dust to be employed in the search for any hint of synchrotron radiation in the data.

The linear fitting results, correlation coefficients and cross correlations revealed that with the exception of the band power at  $\ell \sim 200$ , on all other angular scales there was no significant correlation within the spread of simulation results. This told us that the CMB power spectrum at  $\ell \sim 200$  may not be as robust as desired but certainly above  $\ell = 250$  there is no concern regarding contamination from synchrotron emissions.

The magnetic field responsible for the synchrotron radiation organizes the emission along the plane of acceleration causing it to be linearly polarized. This inherent mechanism means a higher percentage of the total intensity is polarized compared to the dust case. It is dependent upon the distribution of the magnetic field across the sky and in QUaD's observing region is  $\sim 10 - 15\%$ .

The polarization analysis again lead to the somewhat uninteresting, albeit positive for QUaD, conclusion that the polarization data is not significantly tainted by a synchrotron foreground. So overall, and certainly above  $\ell \sim 250$ , the outcome of this chapter was that there is no determining evidence for synchrotron radiation in QUaD data.

### 8.1.3 FAR INFRARED BACKGROUND

The Far Infrared Background (FIRB) comes from the thermal dust emissions of galaxies whose stars have heated interstellar dust via optical and ultraviolet radiation. The FIRB spectrum is sensitive to the distribution of these galaxies both with redshift and spatially; properties which are dependent upon the formation and evolution of the galaxies. There are anisotropies in the power spectrum arising on small scales due to the discrete nature of the sources, and on large scales because of galaxy clustering.

Large scale galaxy clustering suggests that the density fluctuations responsible for the baryonic oscillations causing the CMB were superposed on larger scale, smaller amplitude fluctuations. Such fluctuations would have been created by the total matter content of the universe, a large component of which is dark matter. The idea is then that galaxies formed in regions of extra-enhanced density creating a cluster.

We can quantify the extent of correlation between the galaxy distribution and the large scale dark matter density field by the bias parameter,  $b$ .  $b = 1$  implies an unbiased universe, but higher values mean a biased universe with total mass more widely dispersed than the light, following the underlying dark matter density distribution.

Chapter 6 included both an analytical power spectrum for the FIRB and the equivalent derived from a suite of infrared galaxy simulations that were run through QUaD's

analysis pipeline. This power spectrum scales according to the square of the clustering bias. The 100 GHz, 150 GHz and cross frequency power spectra from each were used to compute frequency difference power spectra, which was then used in a best fit analysis with QUaD's frequency jackknife.

Because QUaD operated at 100 GHz and 150 GHz, a frequency jackknife test was permitted wherein the CMB signal should be completely cancelled upon the subtraction and any residual signal either an overlooked instrumental systematic or a real astrophysical foreground. This test has persistently failed below  $\ell \sim 1000$  and so the fitting of the FIRB frequency difference spectra was investigated at these low band powers.

The bias yielded by the least chi-square linear fit procedure was  $4.21 \pm 0.37$  using the model spectra and  $4.53 \pm 0.38$  with the spectra obtained via simulations. These high values are consistent with other findings that the bias increases with redshift and imply the galaxies are a strongly biased tracer of the underlying mass distribution in the universe.

#### 8.1.4 SUNYAEV-ZEL'DOVICH EFFECT

When CMB photons encounter electrons in the hot gas surrounding a galaxy cluster, or relativistic electrons from supernovae or active galactic nuclei they can be inverse Compton scattered to higher energies. A distortion of the CMB power spectrum, the Sunyaev-Zel'dovich (SZ) effect, then arises due to the net energy gain among the photons. The predicted SZ spectrum is very sensitive to the cosmological parameter  $\sigma_8$  (the rms mass fluctuations in an  $8h^{-1}$  Mpc sphere), scaling according to  $\sigma_8^7$ .

The WMAP lambda predictions of the spectrum based on a  $\sigma_8 = 0.8$  model can be scaled up to QUaD's frequencies to permit a similar analysis as that carried out for the FIRB. In this case the aim was to place a constraint on  $\sigma_8$  by taking the seventh root of the least chi-square linear fitting of the QUaD frequency jackknife data to the frequency difference SZ effect spectrum.

The value of the parameter derived varies according to the band powers considered, but for  $\ell$  up to 1000, the range over which we see failures in the jackknife test, the result is  $\sigma_8 = 1.26 \pm 0.03$ . This is a particularly high answer in comparison to many other reports of  $\sigma_8$  measurements, from CMB experiments and otherwise (generally  $0.8 < \sigma_8 < 1.0$ ), and so the contribution that residual radio sources might be making to the jackknife data was considered.

The spectrum of low flux extragalactic point sources below QUaD's threshold was predicted from a model and used to create a correction spectrum that could be first subtracted off the data before performing any fitting analysis. The  $\sigma_8$  then yielded below  $\ell = 1000$  was not significantly different,  $1.25 \pm 0.03$ , because on these large angular scales

the power from residual point sources is negligible.

### 8.1.5 FIRB AND THE SZ EFFECT

The ultimate investigation was into the idea of QUaD's frequency jackknife spectrum being a combination of residual radio sources, the FIRB and the SZ effect. To that end an analysis was conducted wherein the point source correction spectrum was first subtracted, and then a simultaneous least chi-square linear fit performed to both the FIRB and the SZ effect frequency difference spectra. This produced a likelihood distribution across  $\sigma_8$ - $b$  parameter space with  $\sigma_8 = 1.01_{-0.03}^{+0.07}$  and  $b = 4.49_{-0.42}^{+0.38}$  emerging as the most likely set of values. Although a strong degeneracy between the two was illustrated by the likelihood plots, the maximum likelihood values suggested seem plausible and consistent with other astronomical findings. Upon inclusion of the  $\sigma_8$  dependency within the FIRB spectrum, the results changed to give best fit values of  $\sigma_8 = 1.11_{-0.06}^{+0.04}$  and  $b = 3.27_{-0.23}^{+0.18}$

However, once the implications of these results on smaller angular scales, up to  $\ell = 3000$ , were explored in light of the high- $\ell$  QUaD temperature data it was concluded that the jackknife failure could not have been entirely caused by an FIRB and SZ detection, but must have at least one other component. This could be an overlooked instrumental systematic effect or an artifact of the analysis procedure, the radio source contribution may have been underestimated or some other astrophysical phenomenon might be responsible.

## 8.2 FUTURE WORK

Rather than assuming an exact prediction for the radio source correction and simply subtracting this from the QUaD data, a three-way parameter fit could be done of the frequency jackknife data to the FIRB, the SZ effect and the radio template spectra. The trouble with this is that if only considering band powers below  $\ell = 1000$  there are a limited number of data points. The three spectra all have broadly similar shapes and so will induce a large degeneracy across the three dimensional amplitude likelihood space.

The individual 100 GHz, 150 GHz and cross frequency spectra of the FIRB, SZ effect and residual radio sources have relatively more distinct shapes and magnitudes. In the case of the FIRB spectra, unlike those of the SZ and radio, since it dominates at shorter wavelengths, the 100 GHz spectrum is of lower magnitude than the 150 GHz. These less subtle differences mean that a parameter analysis using QUaD's actual  $TT$  signal spectra rather than the jackknifed one will be more robust and permit tighter, less degenerate constraints on the parameters. Inclusion of band powers up to higher- $\ell$  in this analysis would also eliminate the possibility of arriving at values inconsistent across all angular scales.

Other effects possibly causing the frequency jackknife failure could be explored. Perhaps it could be something related to the beam's sidelobes or the absolute calibrations. Maybe for a more complete parameter analysis a marginalization over the beam uncertainties should be included. Each effect would need to be quantitatively investigated individually and then the analysis repeated in light of any findings. Most likely, however, the residual signal observed in the jackknife is made up of contributions from a number of factors, or less likely, but entirely possible, it is simply the result of chance.

THE END

## APPENDIX A: POLARIZATION MAP EXTRACTION

Beginning with the chi-square,  $\chi^2$ , defined in equation 3.12 from the difference maps,  $M_{h,\alpha_h}$ :

$$\chi^2 = \sum_{h,\alpha_h} \omega_{h,\alpha_h} (M_{h,\alpha_h} - Q \cos(2a_h) - U \sin(2a_h))^2$$

where  $\alpha_h$  is half the angle greater or less than the nominal  $\pi/2$  separating the two bolometers in a pair,  $h$ .  $a_h$  is the polarization angle and  $\omega_{h,\alpha_h}$  the weight assigned to each map. (See Section 3.1.5 for more explanation of these terms.)

This can first be differentiated with respect to  $Q$  for each pixel,  $p$ , set to zero and re-arranged.

$$\begin{aligned} \frac{\partial \chi_p^2}{\partial Q_p} &= \sum_{h,\alpha_h} -2\omega_{h,\alpha_h} \cos(2a_h) (M_{h,\alpha_h,p} - Q_p \cos(2a_h) - U_p \sin(2a_h)) \\ 0 &= \sum_{h,\alpha_h} \omega_{h,\alpha_h} \cos(2a_h) (M_{h,\alpha_h,p} - Q_p \cos(2a_h) - U_p \sin(2a_h)) \\ \sum_{h,\alpha_h} \omega_{h,\alpha_h} \cos(2a_h) M_{h,\alpha_h,p} &= \sum_{h,\alpha_h} \omega_{h,\alpha_h} \cos(2a_h) (Q_p \cos(2a_h) + U_p \sin(2a_h)) \end{aligned}$$

This can be written in matrix format:

$$\sum_{h,\alpha_h} \omega_{h,\alpha_h} \cos(2a_h) M_{h,\alpha_h,p} = \left( \sum_{h,\alpha_h} \omega_{h,\alpha_h} \cos(2a_h) \cos(2a_h) \quad \sum_{h,\alpha_h} \omega_{h,\alpha_h} \cos(2a_h) \sin(2a_h) \right) \times \begin{pmatrix} Q_p \\ U_p \end{pmatrix}$$

The same thing can then be done with respect to  $U$ :

$$\begin{aligned}
\frac{\partial \chi_p^2}{\partial U_p} &= \sum_{h,\alpha_h} -2\omega_{h,\alpha_h} \sin(2a_h) (M_{h,\alpha_h,p} - Q_p \cos(2a_h) - U_p \sin(2a_h)) \\
0 &= \sum_{h,\alpha_h} \omega_{h,\alpha_h} \sin(2a_h) (M_{h,\alpha_h,p} - Q_p \cos(2a_h) - U_p \sin(2a_h)) \\
\sum_{h,\alpha_h} \omega_{h,\alpha_h} \sin(2a_h) M_{h,\alpha_h,p} &= \sum_{h,\alpha_h} \omega_{h,\alpha_h} \sin(2a_h) (Q_p \cos(2a_h) + U_p \sin(2a_h))
\end{aligned}$$

and again it can be written in matrix format:

$$\sum_{h,\alpha_h} \omega_{h,\alpha_h} \sin(2a_h) M_{h,\alpha_h,p} = \left( \sum_{h,\alpha_h} \omega_{h,\alpha_h} \sin(2a_h) \cos(2a_h) \quad \sum_{h,\alpha_h} \omega_{h,\alpha_h} \sin(2a_h) \sin(2a_h) \right) \times \begin{pmatrix} Q \\ U \end{pmatrix}$$

The equations can now be combined into a single matrix equation:

$$\begin{pmatrix} \sum_{h,\alpha_h} \omega_{h,\alpha_h} \cos(2a_h) M_{h,\alpha_h,p} \\ \sum_{h,\alpha_h} \omega_{h,\alpha_h} \sin(2a_h) M_{h,\alpha_h,p} \end{pmatrix} = \begin{pmatrix} \sum_{h,\alpha_h} \omega_{h,\alpha_h} \cos(2a_h) \cos(2a_h) & \sum_{h,\alpha_h} \omega_{h,\alpha_h} \cos(2a_h) \sin(2a_h) \\ \sum_{h,\alpha_h} \omega_{h,\alpha_h} \sin(2a_h) \cos(2a_h) & \sum_{h,\alpha_h} \omega_{h,\alpha_h} \sin(2a_h) \sin(2a_h) \end{pmatrix} \times \begin{pmatrix} Q_p \\ U_p \end{pmatrix}$$

which can then be inverted to give the 2 x 2 matrix from which the polarization maps come:

$$\begin{pmatrix} Q_p \\ U_p \end{pmatrix} = \begin{pmatrix} \sum_{h,\alpha_h} \omega_{h,\alpha_h} \cos(2a_h) \cos(2a_h) & \sum_{h,\alpha_h} \omega_{h,\alpha_h} \cos(2a_h) \sin(2a_h) \\ \sum_{h,\alpha_h} \omega_{h,\alpha_h} \sin(2a_h) \cos(2a_h) & \sum_{h,\alpha_h} \omega_{h,\alpha_h} \sin(2a_h) \sin(2a_h) \end{pmatrix}^{-1} \times \begin{pmatrix} \sum_{h,\alpha_h} \omega_{h,\alpha_h} \cos(2a_h) M_{h,\alpha_h,p} \\ \sum_{h,\alpha_h} \omega_{h,\alpha_h} \sin(2a_h) M_{h,\alpha_h,p} \end{pmatrix}$$

as equation 3.13 declared.

## BIBLIOGRAPHY

- Ade, P., Bock, J., Bowden, M., Brown, M. L., Cahill, G., Carlstrom, J. E., Castro, P. G., Church, S., Culverhouse, T., Friedman, R., Ganga, K., Gear, W. K., Hinderks, J., Kovac, J., Lange, A. E., Leitch, E., Melhuish, S. J., Murphy, J. A., Orlando, A., Schwarz, R., O'Sullivan, C., Piccirillo, L., Pryke, C., Rajguru, N., Rusholme, B., Taylor, A. N., Thompson, K. L., Wu, E. Y. S., & Zemcov, M. 2008, *Astrophys. J.*, 674, 22
- Baccigalupi, C. 2003, *New Astronomy Review*, 47, 1127
- Balbi, A., Ade, P., Bock, J., Borrill, J., Boscaleri, A., de Bernardis, P., Ferreira, P. G., Hanany, S., Hristov, V., Jaffe, A. H., Johnson, B., Lange, A. E., Lee, A. T., Mauskopf, P. D., Netterfield, C. B., Oh, S., Pascale, E., Rabii, B., Richards, P. L., Smoot, G. F., Stompor, R., Winant, C. D., & Wu, J. H. P. 2001, *Memorie della Societa Astronomica Italiana*, 72, 849
- Bardeen, J. M., Bond, J. R., Kaiser, N., & Szalay, A. S. 1986, *Astrophys. J.*, 304, 15
- Baumann, D. & Peiris, H. V. 2008, *ArXiv Astrophysics e-prints*, astro-ph/0810.3022
- Bennett, C. L., Bay, M., Halpern, M., Hinshaw, G., Jackson, C., Jarosik, N., Kogut, A., Limon, M., Meyer, S. S., Page, L., Spergel, D. N., Tucker, G. S., Wilkinson, D. T., Wollack, E., & Wright, E. L. 2003a, *Astrophys. J.*, 583, 1
- Bennett, C. L., Hill, R. S., Hinshaw, G., Nolta, M. R., Odegard, N., Page, L., Spergel, D. N., Weiland, J. L., Wright, E. L., Halpern, M., Jarosik, N., Kogut, A., Limon, M., Meyer, S. S., Tucker, G. S., & Wollack, E. 2003b, *Astrophys. J. Suppl.*, 148, 97
- Benoît, A., Ade, P., Amblard, A., Ansari, R., Aubourg, É., Bargout, S., Bartlett, J. G., Bernard, J.-P., Bhatia, R. S., Blanchard, A., Bock, J. J., Boscaleri, A., Bouchet, F. R., Bourrachot, A., Camus, P., Couchot, F., de Bernardis, P., Delabrouille, J., Désert, F.-X., Doré, O., Douspis, M., Dumoulin, L., Dupac, X., Filliatre, P., Fosalba, P., Ganga, K., Gannaway, F., Gautier, B., Giard, M., Giraud-Héraud, Y., Gispert, R., Guglielmi, L., Hamilton, J.-C., Hanany, S., Henrot-Versillé, S., Kaplan, J., Lagache, G., Lamarre, J.-M., Lange, A. E., Macías-Pérez, J. F., Madet, K., Maffei, B., Magneville, C., Marrone,

- D. P., Masi, S., Mayet, F., Murphy, A., Naraghi, F., Nati, F., Patanchon, G., Perrin, G., Piat, M., Ponthieu, N., Prunet, S., Puget, J.-L., Renault, C., Rosset, C., Santos, D., Starobinsky, A., Strukov, I., Sudiwala, R. V., Teyssier, R., Tristram, M., Tucker, C., Vanel, J.-C., Vibert, D., Wakui, E., & Yvon, D. 2004, *Astron. & Astrophys.*, 424, 571
- Bond, J. R. 1995, *Astrophysical Letters Communications*, 32, 63
- Bowden, M. 2003, PhD thesis, Cardiff University
- Brand, K., Rawlings, S., Hill, G. J., & Lacy, M. 2003, *New Astronomy Review*, 47, 325
- Brown, M. L., Ade, P., Bock, J., Bowden, M., Cahill, G., Castro, P. G., Church, S., Culverhouse, T., Friedman, R. B., Ganga, K., Gear, W. K., Gupta, S., Hinderks, J., Kovac, J., Lange, A. E., Leitch, E., Melhuish, S. J., Memari, Y., Murphy, J. A., Orlando, A., O'Sullivan, C., Piccirillo, L., Pryke, C., Rajguru, N., Rusholme, B., Schwarz, R., Taylor, A. N., Thompson, K. L., Turner, A. H., Wu, E. Y. S., Zemcov, M., & The QUa D collaboration. 2009, *Astrophys. J.*, 705, 978
- Brown, M. L., Castro, P. G., & Taylor, A. N. 2005, *Mon. Not. Royal Astro. Society*, 360, 1262
- Carlstrom, J. E., Holder, G. P., & Reese, E. D. 2002, *Ann. Rev. Astron. Astrophys.*, 40, 643
- Castro, P. G., Ade, P., Bock, J., Bowden, M., Brown, M. L., Cahill, G., Church, S., Culverhouse, T., Friedman, R. B., Ganga, K., Gear, W. K., Gupta, S., Hinderks, J., Kovac, J., Lange, A. E., Leitch, E., Melhuish, S. J., Memari, Y., Murphy, J. A., Orlando, A., Pryke, C., Schwarz, R., O'Sullivan, C., Piccirillo, L., Rajguru, N., Rusholme, B., Taylor, A. N., Thompson, K. L., Turner, A. H., Wu, E. Y. S., Zemcov, M., & The QUa D collaboration. 2009, *Astrophys. J.*, 701, 857
- Chiang, H. C., Ade, P. A. R., Barkats, D., Battle, J. O., Bierman, E. M., Bock, J. J., Dowell, C. D., Duband, L., Hivon, E. F., Holzappel, W. L., Hristov, V. V., Jones, W. C., Keating, B. G., Kovac, J. M., Kuo, C. L., Lange, A. E., Leitch, E. M., Mason, P. V., Matsumura, T., Nguyen, H. T., Ponthieu, N., Pryke, C., Richter, S., Rocha, G., Sheehy, C., Takahashi, Y. D., Tolan, J. E., & Yoon, K. W. 2009, *ArXiv Astrophysics e-prints*, astro-ph/0906.1181
- Chiang, L.-Y., Naselsky, P. D., & Coles, P. 2008, *Modern Physics Letters A*, 23, 1489
- Church, S., Ade, P., Bock, J., Bowden, M., Carlstrom, J., Ganga, K., Gear, W., Hinderks, J., Hu, W., Keating, B., Kovac, J., Lange, A., Leitch, E., Mallie, O., Melhuish, S., Murphy,

- A., Rusholme, B., O'Sullivan, C., Piccirillo, L., Pryke, C., Taylor, A., & Thompson, K. 2003, *New Astronomy Review*, 47, 1083
- Crill, B. P., Ade, P. A. R., Battistelli, E. S., Benton, S., Bihary, R., Bock, J. J., Bond, J. R., Brevik, J., Bryan, S., Contaldi, C. R., Doré, O., Farhang, M., Fissel, L., Golwala, S. R., Halpern, M., Hilton, G., Holmes, W., Hristov, V. V., Irwin, K., Jones, W. C., Kuo, C. L., Lange, A. E., Lawrie, C., MacTavish, C. J., Martin, T. G., Mason, P., Montroy, T. E., Netterfield, C. B., Pascale, E., Riley, D., Ruhl, J. E., Runyan, M. C., Trangsrud, A., Tucker, C., Turner, A., Viero, M., & Wiebe, D. 2008, in *Society of Photo-Optical Instrumentation Engineers (SPIE) Conference Series*, Vol. 7010, Society of Photo-Optical Instrumentation Engineers (SPIE) Conference Series
- Dawson, K. S., Holzzapfel, W. L., Carlstrom, J. E., Joy, M., & LaRoque, S. J. 2006, *Astrophys. J.*, 647, 13
- de Zotti, G., Ricci, R., Mesa, D., Silva, L., Mazzotta, P., Toffolatti, L., & González-Nuevo, J. 2005, *Astron. & Astrophys.*, 431, 893
- Desert, F. X., Boulanger, F., & Puget, J. L. 1990, *Astron. & Astrophys.*, 237, 215
- Desert, F. X. & Puget, J. L. 1990, in *IAU Symposium*, Vol. 139, *The Galactic and Extragalactic Background Radiation*, ed. S. Bowyer & C. Leinert, 381–+
- Dole, H., Lagache, G., Puget, J.-L., Caputi, K. I., Fernández-Conde, N., Le Floch, E., Papovich, C., Pérez-González, P. G., Rieke, G. H., & Blaylock, M. 2006, *Astron. & Astrophys.*, 451, 417
- Dressler, A. 1980, *Astrophys. J.*, 236, 351
- Dunkley, J., Komatsu, E., Nolta, M. R., Spergel, D. N., Larson, D., Hinshaw, G., Page, L., Bennett, C. L., Gold, B., Jarosik, N., Weiland, J. L., Halpern, M., Hill, R. S., Kogut, A., Limon, M., Meyer, S. S., Tucker, G. S., Wollack, E., & Wright, E. L. 2009, *Astrophys. J. Suppl.*, 180, 306
- Efstathiou, G. & Bond, J. R. 1999, *Mon. Not. Royal Astro. Society*, 304, 75
- Elbaz, D., Daddi, E., Le Borgne, D., Dickinson, M., Alexander, D. M., Chary, R.-R., Starck, J.-L., Brandt, W. N., Kitzbichler, M., MacDonald, E., Nonino, M., Popesso, P., Stern, D., & Vanzella, E. 2007, *Astron. & Astrophys.*, 468, 33
- Fan, X., Bahcall, N. A., & Cen, R. 1997, *Astrophys. J. Letters*, 490, L123+

- Fernandez-Conde, N., Lagache, G., Puget, J.-L., & Dole, H. 2008, *Astron. & Astrophys.*, 481, 885
- Finkbeiner, D. P., Davis, M., & Schlegel, D. J. 1999, *Astrophys. J.*, 524, 867
- Fixsen, D. J., Cheng, E. S., Gales, J. M., Mather, J. C., Shafer, R. A., & Wright, E. L. 1996, *Astrophys. J.*, 473, 576
- Friedman, R. B., Ade, P., Bock, J., Bowden, M., Brown, M. L., Cahill, G., Castro, P. G., Church, S., Culverhouse, T., Ganga, K., Gear, W. K., Gupta, S., Hinderks, J., Kovac, J., Lange, A. E., Leitch, E., Melhuish, S. J., Memari, Y., Murphy, J. A., Orlando, A., O'Sullivan, C., Piccirillo, L., Pryke, C., Rajguru, N., Rusholme, B., Schwarz, R., Taylor, A. N., Thompson, K. L., Turner, A. H., Wu, E. Y. S., Zemcov, M., & QUa D collaboration. 2009, *Astrophys. J. Letters*, 700, L187
- Fu, L., Semboloni, E., Hoekstra, H., Kilbinger, M., van Waerbeke, L., Tereno, I., Mellier, Y., Heymans, C., Coupon, J., Benabed, K., Benjamin, J., Bertin, E., Doré, O., Hudson, M. J., Ilbert, O., Maoli, R., Marmo, C., McCracken, H. J., & Ménard, B. 2008, *Astron. & Astrophys.*, 479, 9
- Gold, B., Bennett, C. L., Hill, R. S., Hinshaw, G., Odegard, N., Page, L., Spergel, D. N., Weiland, J. L., Dunkley, J., Halpern, M., Jarosik, N., Kogut, A., Komatsu, E., Larson, D., Meyer, S. S., Nolta, M. R., Wollack, E., & Wright, E. L. 2009, *Astrophys. J. Suppl.*, 180, 265
- Górski, K. M., Hivon, E., Banday, A. J., Wandelt, B. D., Hansen, F. K., Reinecke, M., & Bartelmann, M. 2005, *Astrophys. J.*, 622, 759
- Gupta, S., Ade, P., Bock, J., Bowden, M., Brown, M. L., Cahill, G., Castro, P. G., Church, S., Culverhouse, T., Friedman, R. B., Ganga, K., Gear, W. K., Hinderks, J., Kovac, J., Lange, A. E., Leitch, E., Melhuish, S. J., Memari, Y., Murphy, J. A., Orlando, A., O'Sullivan, C., Piccirillo, L., Pryke, C., Rajguru, N., Rusholme, B., Schwarz, R., Taylor, A. N., Thompson, K. L., Turner, A. H., Wu, E. Y. S., & Zemcov, M. 2009, *ArXiv Astrophysics e-prints*, astro-ph/0909.1621
- Guth, A. H. 1981, *Phys. Rev. D*, 23, 347
- Haslam, C. G. T., Klein, U., Salter, C. J., Stoffel, H., Wilson, W. E., Cleary, M. N., Cooke, D. J., & Thomasson, P. 1981, *Astron. & Astrophys.*, 100, 209
- Haslam, C. G. T., Salter, C. J., Stoffel, H., & Wilson, W. E. 1982, *Astron. & Astrophys. Suppl. Ser.*, 47, 1

- Hauser, M. G. 1998, in *Bulletin of the American Astronomical Society*, Vol. 30, *Bulletin of the American Astronomical Society*, 1337–+
- Hinderks, J. R. 2005, PhD thesis, Stanford University, United States – California
- Hinshaw, G., Nolta, M. R., Bennett, C. L., Bean, R., Doré, O., Greason, M. R., Halpern, M., Hill, R. S., Jarosik, N., Kogut, A., Komatsu, E., Limon, M., Odegard, N., Meyer, S. S., Page, L., Peiris, H. V., Spergel, D. N., Tucker, G. S., Verde, L., Weiland, J. L., Wollack, E., & Wright, E. L. 2007, *Astrophys. J. Suppl.*, 170, 288
- Hinshaw, G., Spergel, D. N., Verde, L., Hill, R. S., Meyer, S. S., Barnes, C., Bennett, C. L., Halpern, M., Jarosik, N., Kogut, A., Komatsu, E., Limon, M., Page, L., Tucker, G. S., Weiland, J. L., Wollack, E., & Wright, E. L. 2003, *Astrophys. J. Suppl.*, 148, 135
- Hinshaw, G., Weiland, J. L., Hill, R. S., Odegard, N., Larson, D., Bennett, C. L., Dunkley, J., Gold, B., Greason, M. R., Jarosik, N., Komatsu, E., Nolta, M. R., Page, L., Spergel, D. N., Wollack, E., Halpern, M., Kogut, A., Limon, M., Meyer, S. S., Tucker, G. S., & Wright, E. L. 2009, *Astrophys. J. Suppl.*, 180, 225
- Hivon, E., Górski, K. M., Netterfield, C. B., Crill, B. P., Prunet, S., & Hansen, F. 2002, *Astrophys. J.*, 567, 2
- Holder, G. P. 2002, *Astrophys. J.*, 580, 36
- Jenkins, A., Frenk, C. S., White, S. D. M., Colberg, J. M., Cole, S., Evrard, A. E., Couchman, H. M. P., & Yoshida, N. 2001, *Mon. Not. Royal Astro. Society*, 321, 372
- Jones, W. C., Bhatia, R., Bock, J. J., & Lange, A. E. 2003, in *Society of Photo-Optical Instrumentation Engineers (SPIE) Conference Series*, Vol. 4855, *Society of Photo-Optical Instrumentation Engineers (SPIE) Conference Series*, ed. T. G. Phillips & J. Zmuidzinas, 227–238
- Kaiser, N. 1984, *Astrophys. J. Letters*, 284, L9
- Khoury, J., Ovrut, B. A., Steinhardt, P. J., & Turok, N. 2001, *Phys. Rev. D*, 64, 123522
- Knox, L. 1999, *Phys. Rev. D*, 60, 103516
- Knox, L., Cooray, A., Eisenstein, D., & Haiman, Z. 2001, *Astrophys. J.*, 550, 7
- Kogut, A., Dunkley, J., Bennett, C. L., Doré, O., Gold, B., Halpern, M., Hinshaw, G., Jarosik, N., Komatsu, E., Nolta, M. R., Odegard, N., Page, L., Spergel, D. N., Tucker, G. S., Weiland, J. L., Wollack, E., & Wright, E. L. 2007, *Astrophys. J.*, 665, 355

- Komatsu, E., Dunkley, J., Nolta, M. R., Bennett, C. L., Gold, B., Hinshaw, G., Jarosik, N., Larson, D., Limon, M., Page, L., Spergel, D. N., Halpern, M., Hill, R. S., Kogut, A., Meyer, S. S., Tucker, G. S., Weiland, J. L., Wollack, E., & Wright, E. L. 2009, *Astrophys. J. Suppl.*, 180, 330
- Komatsu, E. & Seljak, U. 2002, *Mon. Not. Royal Astro. Society*, 336, 1256
- Kovac, J. M., Leitch, E. M., Pryke, C., Carlstrom, J. E., Halverson, N. W., & Holzzapfel, W. L. 2002, *Nature*, 420, 772
- Lagache, G., Bavouzet, N., Fernandez-Conde, N., Ponthieu, N., Rodet, T., Dole, H., Miville-Deschênes, M.-A., & Puget, J.-L. 2007, *Astrophys. J. Letters*, 665, L89
- Lagache, G., Dole, H., Puget, J.-L., Pérez-González, P. G., Le Floc'h, E., Rieke, G. H., Papovich, C., Egami, E., Alonso-Herrero, A., Engelbracht, C. W., Gordon, K. D., Misselt, K. A., & Morrison, J. E. 2004, *Astrophys. J. Suppl.*, 154, 112
- Lagache, G. & Puget, J. L. 2000, *Astron. & Astrophys.*, 355, 17
- Lamarre, J. M. 1986, *Appl. Opt.*, 25, 870
- Leitch, E. M., Kovac, J. M., Pryke, C., Carlstrom, J. E., Halverson, N. W., Holzzapfel, W. L., Dragovan, M., Reddall, B., & Sandberg, E. S. 2002, *Nature*, 420, 763
- Lewis, A., Challinor, A., & Lasenby, A. 2000, *Astrophys. J.*, 538, 473
- Liddle, A. 2004, *The Observatory*, 124, 358
- Lisenfeld, U. & Völk, H. J. 2000, *Astron. & Astrophys.*, 354, 423
- Magneville, C. & Pansart, J. P. 2007, *ArXiv Astrophysics e-prints*, astro-ph/0708.0507
- Marian, L. & Bernstein, G. M. 2007, *Phys. Rev. D*, 76, 123009
- Marinoni, C., Le Fevre, O., Meneux, B., & the VVDS team. 2006, *ArXiv Astrophysics e-prints*, astro-ph/0612123
- Masi, S., Ade, P. A. R., Balbi, A., Bock, J. J., Bond, J. R., Borrill, J., Boscaleri, A., Cabella, P., Contaldi, C. R., Crill, B. P., de Bernardis, P., De Gasperis, G., de Oliveira-Costa, A., De Troia, G., di Stefano, G., Ganga, K., Hivon, E., Hristov, V. V., Iacoangeli, A., Jaffe, A. H., Kisner, T. S., Jones, W. C., Lange, A. E., Mausekopf, P. D., Mactavish, C., Melchiorri, A., Montroy, T., Nati, F., Natoli, P., Netterfield, C. B., Pascale, E., Piacentini,

- F., Pogosyan, D., Polenta, G., Prunet, S., Ricciardi, S., Romeo, G., Ruhl, J. E., Torbet, E., Tegmark, M., & Vittorio, N. 2003, *Memorie della Societa Astronomica Italiana Supplement*, 2, 54
- Masi, S., Ade, P. A. R., Bock, J. J., Bond, J. R., Borrill, J., Boscaleri, A., Cabella, P., Contaldi, C. R., Crill, B. P., de Bernardis, P., de Gasperis, G., de Oliveira-Costa, A., de Troia, G., di Stefano, G., Ehlers, P., Hivon, E., Hristov, V., Iacoangeli, A., Jaffe, A. H., Jones, W. C., Kisner, T. S., Lange, A. E., MacTavish, C. J., Marini Bettolo, C., Mason, P., Mauskopf, P. D., Montroy, T. E., Nati, F., Nati, L., Natoli, P., Netterfield, C. B., Pascale, E., Piacentini, F., Pogosyan, D., Polenta, G., Prunet, S., Ricciardi, S., Romeo, G., Ruhl, J. E., Santini, P., Tegmark, M., Torbet, E., Veneziani, M., & Vittorio, N. 2006, *Astron. & Astrophys.*, 458, 687
- Mather, J. C., Cheng, E. S., Cottingham, D. A., Eplee, Jr., R. E., Fixsen, D. J., Hewagama, T., Isaacman, R. B., Jensen, K. A., Meyer, S. S., Noerdlinger, P. D., Read, S. M., Rosen, L. P., Shafer, R. A., Wright, E. L., Bennett, C. L., Boggess, N. W., Hauser, M. G., Kelsall, T., Moseley, Jr., S. H., Silverberg, R. F., Smoot, G. F., Weiss, R., & Wilkinson, D. T. 1994, *Astrophys. J.*, 420, 439
- Miville-Deschênes, M.-A., Ysard, N., Lavabre, A., Ponthieu, N., Macías-Pérez, J. F., Aumont, J., & Bernard, J. P. 2008, *Astron. & Astrophys.*, 490, 1093
- Montroy, T. E., Ade, P. A. R., Bock, J. J., Bond, J. R., Borrill, J., Boscaleri, A., Cabella, P., Contaldi, C. R., Crill, B. P., de Bernardis, P., De Gasperis, G., de Oliveira-Costa, A., De Troia, G., di Stefano, G., Hivon, E., Jaffe, A. H., Kisner, T. S., Jones, W. C., Lange, A. E., Masi, S., Mauskopf, P. D., MacTavish, C. J., Melchiorri, A., Natoli, P., Netterfield, C. B., Pascale, E., Piacentini, F., Pogosyan, D., Polenta, G., Prunet, S., Ricciardi, S., Romeo, G., Ruhl, J. E., Santini, P., Tegmark, M., Veneziani, M., & Vittorio, N. 2006, *Astrophys. J.*, 647, 813
- Muchovej, S., Mroczkowski, T., Carlstrom, J. E., Cartwright, J., Greer, C., Hennessy, R., Loh, M., Pryke, C., Reddall, B., Runyan, M., Sharp, M., Hawkins, D., Lamb, J. W., Woody, D., Joy, M., Leitch, E. M., & Miller, A. D. 2007, *Astrophys. J.*, 663, 708
- North, C. E., Johnson, B. R., Ade, P. A. R., Audley, M. D., Baines, C., Battye, R. A., Brown, M. L., Cabella, P., Calisse, P. G., Challinor, A. D., Duncan, W. D., Ferreira, P. G., Gear, W. K., Glowacka, D., Goldie, D. J., Grimes, P. K., Halpern, M., Haynes, V., Hilton, G. C., Irwin, K. D., Jones, M. E., Lasenby, A. N., Leahy, P. J., Leech, J., Maffei, B., Mauskopf, P., Melhuish, S. J., O'Dea, D., Parsley, S. M., Piccirillo, L., Pisano, G., Reintsema, C. D., Savini, G., Sudiwala, R., Sutton, D., Taylor, A. C., Teleberg, G.,

- Titterton, D., Tsaneva, V., Tucker, C., Watson, R., Withington, S., Yassin, G., & Zhang, J. 2008, ArXiv Astrophysics e-prints, astro-ph/0805.3690
- O'Sullivan, C., Cahill, G., Murphy, J., Gear, W., Harris, J., Ade, P., Church, S., Thompson, K., Pryke, C., Bock, J., Bowden, M., Brown, M., Carlstrom, J., Castro, P., Culverhouse, T., Friedman, R., Ganga, K., Haynes, V., Hinderks, J., Kovak, J., Lange, A., Leitch, E., Mallie, O., Melhuish, S., Orlando, A., Piccirillo, L., Pisano, G., Rajguru, N., Rusholme, B., Schwarz, R., Taylor, A., Wu, E., & Zemcov, M. 2008, *Infrared Physics & Technology*, 51, 277
- Page, L., Hinshaw, G., Komatsu, E., Nolta, M. R., Spergel, D. N., Bennett, C. L., Barnes, C., Bean, R., Doré, O., Dunkley, J., Halpern, M., Hill, R. S., Jarosik, N., Kogut, A., Limon, M., Meyer, S. S., Odegard, N., Peiris, H. V., Tucker, G. S., Verde, L., Weiland, J. L., Wollack, E., & Wright, E. L. 2007, *Astrophys. J. Suppl.*, 170, 335
- Partridge, R. B. & Peebles, P. J. E. 1967, *Astrophys. J.*, 148, 377
- Peebles, P. J. E. 1980, *The large-scale structure of the universe*, ed. P. J. E. Peebles
- Penzias, A. A. & Wilson, R. W. 1965, *Astrophys. J.*, 142, 419
- Press, W. H., Teukolsky, S. A., Vetterling, W. T., & Flannery, B. P. 2007, *Numerical Recipes: The Art of Scientific Computing* (Cambridge University Press)
- Prunet, S., Sethi, S. K., Bouchet, F. R., & Miville-Deschenes, M.-A. 1998, *Astron. & Astrophys.*, 339, 187
- Pryke, C., Ade, P., Bock, J., Bowden, M., Brown, M. L., Cahill, G., Castro, P. G., Church, S., Culverhouse, T., Friedman, R., Ganga, K., Gear, W. K., Gupta, S., Hinderks, J., Kovac, J., Lange, A. E., Leitch, E., Melhuish, S. J., Memari, Y., Murphy, J. A., Orlando, A., Schwarz, R., Sullivan, C. O., Piccirillo, L., Rajguru, N., Rusholme, B., Taylor, A. N., Thompson, K. L., Turner, A. H., Wu, E. Y. S., & Zemcov, M. 2009, *Astrophys. J.*, 692, 1247
- Puget, J.-L., Abergel, A., Bernard, J.-P., Boulanger, F., Burton, W. B., Desert, F.-X., & Hartmann, D. 1996, *Astron. & Astrophys.*, 308, L5+
- Readhead, A. C. S., Myers, S. T., Pearson, T. J., Sievers, J. L., Mason, B. S., Contaldi, C. R., Bond, J. R., Bustos, R., Altamirano, P., Achermann, C., Bronfman, L., Carlstrom, J. E., Cartwright, J. K., Casassus, S., Dickinson, C., Holzzapfel, W. L., Kovac, J. M., Leitch, E. M., May, J., Padin, S., Pogosyan, D., Pospieszalski, M., Pryke, C., Reeves, R., Shepherd, M. C., & Torres, S. 2004, *Science*, 306, 836

- Rees, M. J. 1968, *Astrophys. J. Letters*, 153, L1+
- Reichardt, C. L., Ade, P. A. R., Bock, J. J., Bond, J. R., Brevik, J. A., Contaldi, C. R., Daub, M. D., Dempsey, J. T., Goldstein, J. H., Holzapfel, W. L., Kuo, C. L., Lange, A. E., Lueker, M., Newcomb, M., Peterson, J. B., Ruhl, J., Runyan, M. C., & Staniszewski, Z. 2009a, *Astrophys. J.*, 694, 1200
- Reichardt, C. L., Zahn, O., Ade, P. A. R., Basu, K., Bender, A. N., Bertoldi, F., Cho, H.-M., Chon, G., Dobbs, M., Ferrusca, D., Halverson, N. W., Holzapfel, W. L., Horellou, C., Johansson, D., Johnson, B. R., Kennedy, J., Kneissl, R., Lanting, T., Lee, A. T., Lueker, M., Mehl, J., Menten, K. M., Nord, M., Pacaud, F., Richards, P. L., Schaaf, R., Schwan, D., Spieler, H., Weiss, A., & Westbrook, B. 2009b, *Astrophys. J.*, 701, 1958
- Sachs, R. K. & Wolfe, A. M. 1967, *Astrophys. J.*, 147, 73
- Saunders, W., Rowan-Robinson, M., & Lawrence, A. 1992, *Mon. Not. Royal Astro. Society*, 258, 134
- Sayers, J., Golwala, S. R., Rossinot, P., Ade, P. A. R., Aguirre, J. E., Bock, J. J., Edgington, S. F., Glenn, J., Goldin, A., Haig, D., Lange, A. E., Laurent, G. T., Mauskopf, P. D., & Nguyen, H. T. 2009, *Astrophys. J.*, 690, 1597
- Schlegel, D. J., Finkbeiner, D. P., & Davis, M. 1998, *Astrophys. J.*, 500, 525
- Seljak, U., Slosar, A., & McDonald, P. 2006, *Journal of Cosmology and Astro-Particle Physics*, 10, 14
- Sharp, M. K., Marrone, D. P., Carlstrom, J. E., Culverhouse, T., Greer, C., Hawkins, D., Hennessy, R., Joy, M., Lamb, J. W., Leitch, E. M., Loh, M., Miller, A., Mroczkowski, T., Muchovej, S., Pryke, C., & Woody, D. 2009, *ArXiv Astrophysics e-prints*, astro-ph/0901.4342
- Sievers, J. L., Mason, B. S., Weintraub, L., Achermann, C., Altamirano, P., Bond, J. R., Bronfman, L., Bustos, R., Contaldi, C., Dickinson, C., Jones, M. E., May, J., Myers, S. T., Oyarce, N., Padin, S., Pearson, T. J., Pospieszalski, M., Readhead, A. C. S., Reeves, R., Shepherd, M. C., Taylor, A. C., & Torres, S. 2009, *ArXiv Astrophysics e-prints*, astro-ph/0901.4540
- Silk, J. 1968, *Astrophys. J.*, 151, 459
- Smith, K. M., Cooray, A., Das, S., Doré, O., Hanson, D., Hirata, C., Kaplinghat, M., Keating, B., LoVerde, M., Miller, N., Rocha, G., Shimon, M., & Zahn, O. 2008, *ArXiv Astrophysics e-prints*, astro-ph/0811.3916

- Smoot, G. F. 1999, ArXiv Astrophysics e-prints, astro-ph/9902201
- Smoot, G. F., Bennett, C. L., Kogut, A., Wright, E. L., Aymon, J., Boggess, N. W., Cheng, E. S., de Amici, G., Gulkis, S., Hauser, M. G., Hinshaw, G., Jackson, P. D., Janssen, M., Kaita, E., Kelsall, T., Keegstra, P., Lineweaver, C., Loewenstein, K., Lubin, P., Mather, J., Meyer, S. S., Moseley, S. H., Murdock, T., Rokke, L., Silverberg, R. F., Tenorio, L., Weiss, R., & Wilkinson, D. T. 1992, *Astrophys. J. Letters*, 396, L1
- Soifer, B. T. & Neugebauer, G. 1985, in Presented at the Society of Photo-Optical Instrumentation Engineers (SPIE) Conference, Vol. 510, Society of Photo-Optical Instrumentation Engineers (SPIE) Conference Series, ed. I. J. Spiro & R. A. Mollicone, 84–88
- Steidel, C. C., Adelberger, K. L., Dickinson, M., Giavalisco, M., & Pettini, M. 1998, ArXiv Astrophysics e-prints, astro-ph/9812167
- Tegmark, M., Eisenstein, D. J., Strauss, M. A., Weinberg, D. H., Blanton, M. R., Frieman, J. A., Fukugita, M., Gunn, J. E., Hamilton, A. J. S., Knapp, G. R., Nichol, R. C., Ostriker, J. P., Padmanabhan, N., Percival, W. J., Schlegel, D. J., Schneider, D. P., Scoccimarro, R., Seljak, U., Seo, H.-J., Swanson, M., Szalay, A. S., Vogeley, M. S., Yoo, J., Zehavi, I., Abazajian, K., Anderson, S. F., Annis, J., Bahcall, N. A., Bassett, B., Berlind, A., Brinkmann, J., Budavari, T., Castander, F., Connolly, A., Csabai, I., Doi, M., Finkbeiner, D. P., Gillespie, B., Glazebrook, K., Hennessy, G. S., Hogg, D. W., Ivezić, Ž., Jain, B., Johnston, D., Kent, S., Lamb, D. Q., Lee, B. C., Lin, H., Loveday, J., Lupton, R. H., Munn, J. A., Pan, K., Park, C., Peoples, J., Pier, J. R., Pope, A., Richmond, M., Rockosi, C., Scranton, R., Sheth, R. K., Stebbins, A., Stoughton, C., Szapudi, I., Tucker, D. L., Berk, D. E. V., Yanny, B., & York, D. G. 2006, *Phys. Rev. D*, 74, 123507
- Verde, L., Peiris, H. V., Spergel, D. N., Nolta, M. R., Bennett, C. L., Halpern, M., Hinshaw, G., Jarosik, N., Kogut, A., Limon, M., Meyer, S. S., Page, L., Tucker, G. S., Wollack, E., & Wright, E. L. 2003, *Astrophys. J. Suppl.*, 148, 195
- Weinberg, D. H., Davé, R., Katz, N., & Hernquist, L. 2004, *Astrophys. J.*, 601, 1
- Wu, J. H. P., Zuntz, J., Abroe, M. E., Ade, P. A. R., Bock, J., Borrill, J., Collins, J., Hanany, S., Jaffe, A. H., Johnson, B. R., Jones, T., Lee, A. T., Matsumura, T., Rabii, B., Renbarger, T., Richards, P. L., Smoot, G. F., Stompor, R., Tran, H. T., & Winant, C. D. 2007, *Astrophys. J.*, 665, 55
- Zeldovich, Y. B. & Sunyaev, R. A. 1969, *Astrophys. J. Suppl.*, 4, 301
- Zemcov, M. 2006, PhD thesis, Cardiff University

Zhang, P. & Pen, U.-L. 2001, *Astrophys. J.*, 549, 18

